

Optimizing the exploitation of persistent scatterers in satellite radar interferometry

Dheenathayalan, Prabu

DOI

[10.4233/uuid:aa1ef96f-4da9-41ff-bff8-30186ef2a541](https://doi.org/10.4233/uuid:aa1ef96f-4da9-41ff-bff8-30186ef2a541)

Publication date

2019

Document Version

Final published version

Citation (APA)

Dheenathayalan, P. (2019). *Optimizing the exploitation of persistent scatterers in satellite radar interferometry*. [Dissertation (TU Delft), Delft University of Technology].
<https://doi.org/10.4233/uuid:aa1ef96f-4da9-41ff-bff8-30186ef2a541>

Important note

To cite this publication, please use the final published version (if applicable).
Please check the document version above.

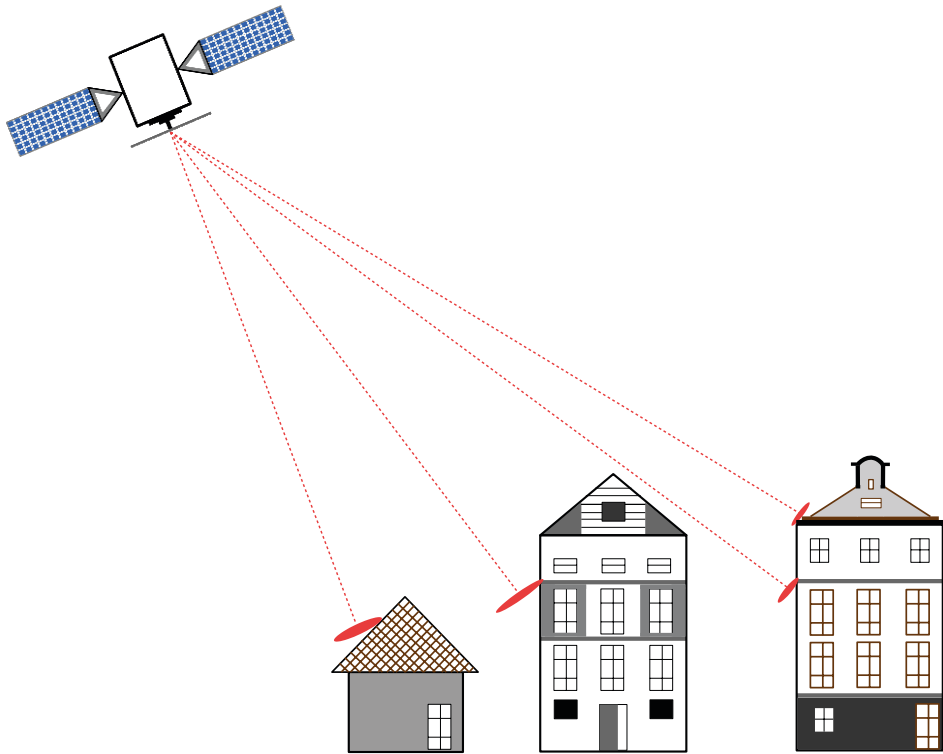
Copyright

Other than for strictly personal use, it is not permitted to download, forward or distribute the text or part of it, without the consent of the author(s) and/or copyright holder(s), unless the work is under an open content license such as Creative Commons.

Takedown policy

Please contact us and provide details if you believe this document breaches copyrights.
We will remove access to the work immediately and investigate your claim.

Optimizing the Exploitation of Persistent Scatterers in Satellite Radar Interferometry



Prabu Dheenathayalan

Optimizing the exploitation of persistent scatterers in satellite radar interferometry

Prabu Dheenathayalan

On the cover

Stylized illustration of linking persistent scatterers from radar to parts of an infrastructure using precise point positioning and error ellipsoid concept, see Figs. 4.12 and 5.16.

Optimizing the exploitation of persistent scatterers in satellite radar interferometry

Proefschrift

ter verkrijging van de graad van doctor
aan de Technische Universiteit Delft,
op gezag van de Rector Magnificus prof. dr. ir. T. H. J. J. van der Hagen,
voorzitter van het College voor Promoties,
in het openbaar te verdedigen op dinsdag 29 oktober 2019 om 10:00 uur

door

Prabu DHEENATHAYALAN

Master of Science in Electrical Engineering and Information Technologies,
Karlsruhe Institute of Technology, Germany

geboren te Madurai, India.

This dissertation has been approved by the promotor:

Prof. dr. ir. R. F. Hanssen

Composition of the doctoral committee:

Rector Magnificus	chairman
Prof. dr. ir. R. F. Hanssen	Delft University of Technology, promotor

Independent members:

Prof. dr. M. Eineder	Technical University of Munich, Germany & German Aerospace Center (DLR)
Prof. dr. A. J. Hooper	University of Leeds, UK
Prof. Dr.-Ing. O. Hellwich	Technische Universität Berlin, Germany
Prof. dr. ir. S. C. Steele-Dunne	Delft University of Technology
Prof. ir. P. Hoogeboom	Delft University of Technology
Dr. D. Small	University of Zurich, Switzerland



Keywords: spaceborne radar interferometry, surface deformation, persistent scatterers, positioning, corner reflectors, geometric calibration, infrastructure monitoring

Citation: Dheenathayalan, P. (2019), Optimizing the exploitation of persistent scatterers in satellite radar interferometry. PhD thesis, Delft University of Technology.

ISBN 978-94-6384-083-5

Copyright © 2019 by P. Dheenathayalan

All rights reserved. No part of the material protected by this copyright notice may be reproduced or utilized in any form or by any means, electronic or mechanical, including photocopying, recording or by any information storage and retrieval system, without the prior permission of the author.

An electronic version of this dissertation is available at
<http://repository.tudelft.nl/>.

Cover design: Shalini Sukumar

Printed by Ridderprint, The Netherlands

Typeset by the author with the \LaTeX documentation system

To my family

Acknowledgments

This research work would not have been possible without the help of many people and I am very grateful for their support. My quest for the synthetic aperture radar first started when I attended the lectures of Alberto Moreira (Microwaves and Radar Institute, DLR) at Karlsruhe Institute of Technology. However, this PhD-research provided me the focus and opportunity to work with radar interferometry in depth and explore its applications.

First and foremost, I would like to thank my promotor and mentor, Ramon Hanssen, for his guidance, critical feedback, and thorough reading of this manuscript. I have learned a lot from Ramon and I am immensely thankful for his kind support, trust and freedom to pursue multiple research projects.

This study has been funded by the Liander N.V., Asset Management department. During this study, I had the opportunity to collaborate with many people at Liander. I am very grateful to Ben Lambregts and Ron Janssen for the project management and enthusiastic discussions towards applying satellite radar interferometry for gas pipeline monitoring. I would also like to thank Liander for providing me access to the gas pipeline failure database which served as a validation dataset in Chapter 3. I am also pleased to have had a chance to collaborate with André Marques Arsénio and Jojanneke Dirksen in using satellite observations for other underground pipeline monitoring research.

I am grateful to David Small for the opportunity to visit University of Zurich and collaborate with him for the absolute positioning research at the Remote Sensing Laboratories. I am thankful to David Small and Adrian Schubert for guiding me with the position error corrections and the valuable contributions to our paper on high precision positioning.

I would like to express my sincere gratitude to Peter Hoogeboom for introducing me to the small reflectors concept through the Space Dikes Program (TNO). I am very grateful to Peter Hoogeboom for the design and experimentation efforts. I am thankful to Miguel Caro Cuenca for the processing assistance and the discussions. I thank Peter, and Miguel for their valuable inputs to our article on the small reflectors.

I am very grateful to Hans van der Marel for processing GNSS measurements during our corner reflector experiments. I would like to appreciate Rene Reudink for his assistance during corner reflector installation, and position measurements using GNSS and tachymetry. I would like to thank Mengshi Yang for the collaboration efforts in order to continue the current positioning research in Delft. Discussion with Paco López-Dekker, Christian Tiberius, and Roderik Lindenbergh were always instructive. I am also thankful to Andy Hooper (now at the University of Leeds) for discussions at the early stages of my research. I would like to extend my gratitude to Dian Verbunt, Lidwien de Jong, Rebeca Domingo, Debbie Rietdijk, Marjolein de Niet-de Jager, File Koot-Stomp, Danko Roozmond, and Irma Zomerdijk for their administrative support.

I have also had the pleasure of being associated with the following people of the Geoscience and Remote Sensing department who have contributed directly or indirectly to my research progress: Freek van Leijen, Peter de Bakker, Jochem Lesparre, Sami Samiei Esfahany, Bram te Brake, Ramses Molijn, Gertjan van Zwieten, Petar Marinkovic, Taco

Broerse, Pooja Mahapatra, Peter Buist, Raluca Ianoschi, Olga Didova, Shizhuo Liu, Manu Delgado Blasco, Piers van der Torren, Ling Chang, Ali Mousivand, Gert Mulder (Gert helped me with the Dutch translation of the summary of this dissertation), Ece Ozer, Floris Heuff, Hamid Reza Ghafarian Malamiri, Marcel Kleinherenbrink, Naresh Soni, Alexandru Lepadatu, Saygin Abdikan, Ricardo Reinoso Rondinel, Reenu Toodesh, Karen Simon, Stephanie Rusli, Dimitra Mamali, Siavash Shakeri, Davide Imparato, Yanqing Hou, Karsten Spaans, David Bekaert, and several other students, and researchers. I am thankful to my office mates Kaixuan Zhou and Elyta Widyaningrum for coffee-table talks and machine learning related discussions. I have had a chance to advise Deirdre Bosch, Adriaan Visser, Jelte Van Oostveen, during their MSc/BSc research and I have learned a lot from their work. Special thanks to Joana Martins, Mahmut Arıkan, Sylvie Dijkstra-Soudarissanane, Lorenzo Iannini, Enayat Hosseini Aria, and Anneleen Oyen with whom I share and cherish moments personally and professionally discussing a range of topics.

I would also like to express my deepest appreciation to my defense committee: Michael Eineder, Andy Hooper, Olaf Hellwich, Susan Steele-Dunne, Peter Hoogeboom, and David Small, for their thorough reading of this work and their valuable comments.

I am deeply indebted to my parents, Amirthaa and Dheenathayalan Chakrapani, who have always trusted, inspired, and supported me unconditionally in all my endeavors right from my childhood. Many thanks to my brother Kousik Dheena Thayalan and sister-in-law Shobana Kousik for the wonderful memories together, family vacations and fun discussions. I am also thankful to my parents-in-law Kalavathi and Sukumar Srinivasan for their moral support and sharing their work and life experiences.

Finally, very special thanks to Shalini Sukumar for reading parts of my thesis and pushing me to finish my thesis. Shalini, it would not have been possible without your pragmatic ideas, patience, and selfless support.

Prabu Dheenathayalan
Delft, September 2019

Summary

Time-series synthetic aperture radar interferometry (InSAR) has evolved into a widely preferred geodetic technique for measuring topography and surface deformation of the earth. In the last decades, time-series InSAR methodologies were developed to extract information from persistent scatterers (PS) and distributed scatterers (DS). Methodologies based on DSs extract information from pixels from the natural terrain. Persistent Scatterer Interferometry (PSI) extracts information from PSs, which are found in abundance in areas with man-made infrastructure. However, a satisfactory geodetic application of these methodologies requires a complete understanding of the measurement principles, an identification of radar scatterers in the physical world, and an interpretation of the estimated deformation. Moreover, for areas not suitable for coherent imaging adding new measurements is not trivial.

In consideration of the above challenges, the two main objectives of this study are: (i) to develop a systematic method to decode PSI measurements, *i.e.*, identify PSs in the object space in order to interpret the estimated deformation (kinematics), and (ii) to assess the feasibility of encoding artificial radar scatterers, *i.e.* adding new measurements using radar reflectors, at places where there exists no coherent InSAR measurements.

We review the contents of SAR resolution cell and the time-series processing methodologies with special focus on the Delft implementation of PSI processing. A physical interpretation of the time-series InSAR results is shown possible by decoding what the radar has measured and understanding the deformation phenomena. We employ two approaches to perform this decoding. First is to identify the source of the radar reflection by characterizing and associating PSs to a target type. By using only InSAR data, we apply an iterative classification method to discriminate radar scatterers between the ground level and elevated infrastructure. We combine the limited classification output with deformation rate and identify various deformation phenomena such as shallow compaction, no relative motion, autonomous structural motion, local land subsidence, and inter-structural deformation. In particular, we introduce a parameter known as RDI (Relative Deformation Index) to detect, quantify and analyze the regions subject to relative deformation for infrastructural stability analysis. The feasibility of this approach is successfully demonstrated with underground gas-pipe and water-pipe network monitoring applications over Amsterdam and The Hague, respectively.

Second, a point-level (object or sub-object level) linking of radar reflections to real-world objects. For this step, a precise 3D position of the scatterers is derived. Applying corrections for various position error sources, accurate 3D position of scatterers is achieved for high-resolution and medium-resolution SAR imagery. A standard Gauss-Markov approach is applied to facilitate error propagation and quality assessment and control. The 2D and 3D position capabilities are validated using trihedral corner reflector field experiments. In order to precisely associate radar scatterers to physical objects, we introduce an approach to use a 3D building model of the physical objects. Linking of scatterers to parts of infrastructure is demonstrated for high-resolution and medium-resolution imagery.

Finally, we propose the concept of small radar reflectors to introduce new coherent reflections. The small reflectors are designed such that they are visible from both ascending and descending imaging directions, enabling vector decomposition of deformation measurements. These small radar reflectors act as weak point scatterers. To achieve a desired SCR (Signal to Clutter Ratio), many small reflectors are distributed over an area and averaged. The detection of small reflectors is achieved by distributing them in a predefined spatial pattern. In this study, a new interferometric phase expression is derived to estimate a phase standard deviation for low-SCR and high-SCR targets. The proposed concept is experimentally validated using X-band satellite data over a grassy terrain in the Netherlands. The results indicate that distributed corner reflectors can provide deformation measurements with millimeter precision.

Samenvatting (Summary in Dutch)

Het gebruik van tijdreeksen van synthetic aperture radar interferometry (InSAR) is geëvolueerd tot een breed toegepaste geodetische techniek voor het meten van topografie en deformatie van de aardoppervlak. In de afgelopen decennia zijn technieken voor InSAR tijdreeksen ontwikkeld om informatie te extraheren uit Persistent Scatterers (PS) en distributed scatterers (DS). Technieken op basis van DS's halen informatie uit pixels uit het natuurlijke terrein. Persistent Scatterer Interferometry (PSI) haalde informatie uit PS's, die in overvloed aanwezig zijn in bebouwde gebieden. Een goede geodetische toepassing van deze methodologieën vereist echter een volledig begrip van de meetprincipes, een correcte identificatie van radar scatterers in de fysieke wereld en een interpretatie van de geschatte deformatie. Bovendien is de toepasbaarheid van nieuwe metingen voor gebieden die ongeschikt zijn voor conventionele metingen niet triviaal.

Rekening houdend met de bovenstaande uitdagingen, zijn de twee hoofddoelstellingen van deze studie: (i) het ontwikkelen van een systematische methode voor het decoderen van PSI-metingen, dat wil zeggen het identificeren van PS's in de objectruimte om de geschatte vervorming (kinematica) te interpreteren, en (ii) om de haalbaarheid te beoordelen van het coderen van kunstmatige radar scatterers, ofwel het toevoegen van nieuwe metingen, op plaatsen waar geen coherente InSAR-metingen bestaan.

We bekijken de inhoud van de SAR-resolutie cel en de verwerkingsmethoden voor tijdseries met speciale aandacht voor de Delftse implementatie van PSI-verwerking. Een fysieke interpretatie van de InSAR-resultaten van de tijdreeks wordt mogelijk gemaakt door te decoderen wat de radar heeft gemeten en de verschillende oorzaken voor deformatie te begrijpen. We gebruiken twee benaderingen om deze decodering uit te voeren. Allereerst moet het reflectiepunt van het radarsignaal worden geïdentificeerd door PS's te karakteriseren en te associëren met verschillende typen reflectiepunten. Enkel gebruikmakend van InSAR-gegevens, passen we een iteratieve classificatiemethode toe om radar scatterers te onderscheiden in punten op maaiveld en verhoogde infrastructuur. Vervolgens identificeren we met behulp van deze eenvoudige classificatie en deformatiesnelheden verschillende deformatietypes zoals ondiepe verdichting, afwezigheid van relatieve beweging, onafhankelijke structurele deformatie, lokale bodemdaling en afhankelijke structurele deformatie. Daarbij introduceren we de parameter RDI (Relative Deformation Index) voor het detecteren, kwantificeren en analyseren van de regio's die onderhevig zijn aan relatieve deformatie, voor analyse van de stabiliteit van de infrastructuur. De haalbaarheid van deze aanpak is aangetoond met het gebruik voor netwerkcontroles van ondergrondse gas- en waterpijpleidingen in respectievelijk Amsterdam en Den Haag.

Ten tweede een koppeling radarreflecties per radar punt aan objecten (of delen van objecten) in de echte wereld. Voor deze stap wordt de precieze 3D-positie van de scatterers afgeleid. Door correcties toe te passen voor verschillende bronnen van lokalisatiefouten, wordt een nauwkeurige 3D-positie van scatterers bereikt voor SAR-afbeeldingen met hoge resolutie en gemiddelde resolutie. Daarbij is een standaard Gauss-Markov-methode toegepast om foutpropagatie en kwaliteit van de resultaten te kunnen analyseren en beoordelen.

De mogelijke 2D- en 3D-posities worden gevalideerd met behulp van corner reflector experimenten. Om radar scatterers nauwkeurig te koppelen aan fysieke objecten, introduceren we een benadering om een 3D model van de fysieke objecten te gebruiken. Het koppelen van scatterers aan verschillende delen van infrastructuur is aangetoond voor beelden met een hoge resolutie en een gemiddelde resolutie.

Ten slotte willen we het concept van kleine radarreflectoren voor nieuwe coherente reflecties introduceren. Deze kleine reflectoren zijn zodanig ontworpen dat ze zichtbaar zijn vanuit zowel noord-zuid als zuid-noord satellietbanen, waardoor vectordecompositie van deformatiemetingen mogelijk wordt. Deze kleine radarreflectoren fungeren als zwakke point scatterers. Om een gewenste SCR (Signal to Clutter Ratio) te bereiken, worden veel kleine reflectoren over een gebied verdeeld en gemiddeld. De detectie van kleine reflectoren wordt bereikt door ze in een vooraf bepaald ruimtelijk patroon te verdelen. In deze studie wordt een nieuwe formule voor de interferometrische fase afgeleid om een standaardafwijking voor lage en hoge SCR-doelen te schatten. Het voorgestelde concept is experimenteel gevalideerd met behulp van X-band satellietgegevens over grasland in Nederland. De resultaten geven aan dat gespreide corner reflectors deformatiemetingen kunnen leveren met millimeter precisie.

Contents

Acknowledgments	vii
Summary	ix
Samenvatting	xi
Nomenclature	xvii
1 Introduction	1
1.1 Motivation	1
1.2 Background	1
1.3 Problem formulation	4
1.4 Research questions and limitations	6
1.4.1 Research questions	6
1.4.2 Methodology	7
1.4.3 Research scope and limitations	8
1.5 Thesis outline	8
2 A review of InSAR and persistent scatterers	11
2.1 Radar	11
2.2 Side looking Real Aperture Radar	11
2.3 Synthetic Aperture Radar	12
2.4 Synthetic Aperture Radar Interferometry	15
2.4.1 The range-related phase	15
2.4.2 Atmospheric phase	17
2.4.3 Scattering-related phase	18
2.4.4 Phase noise	19
2.5 InSAR processing chain	20
2.5.1 Azimuth and range filtering	21
2.5.2 Coregistration and resampling	21
2.5.3 Flat earth and topographic phase removal	22
2.5.4 Multilooking	22
2.5.5 Unwrapping	22
2.6 Point and distributed targets	23
2.6.1 The effective phase center	24
2.6.2 Time-series processing	28
2.7 Persistent Scatterer Interferometry	29
2.8 Encoding and decoding SAR measurements	31
2.9 Summary	34

3	Target classification and deformation interpretation applied to infrastructure monitoring	35
3.1	Introduction	35
3.2	Taxonomy of urban targets	40
3.3	Methodology	42
3.3.1	Height based classification.	42
3.3.2	Performance analysis of target classification	46
3.3.3	Applications	53
3.4	Deformation classification	56
3.4.1	Deformation type classification method	58
3.4.2	Relative deformation index	62
3.4.3	Performance analysis of deformation interpretation	65
3.5	Case study: Gas pipe network monitoring over Amsterdam	65
3.6	Summary and conclusions	69
4	Positioning and target association in high resolution imagery	73
4.1	Introduction	73
4.2	Scatterer positioning	74
4.2.1	In the dimensionless 2D radar datum	75
4.2.2	To the temporal 1D radar datum	76
4.2.3	To the geometric 2D radar datum	78
4.2.4	To the geometric 3D radar datum	80
4.2.5	To the ellipsoidal 3D TRF datum and local 3D coordinate system	83
4.3	Scatterer position validation	86
4.3.1	2D accuracy	86
4.3.2	3D accuracy	87
4.4	Experiment setup	89
4.4.1	Configuration	89
4.4.2	Computation of the higher-order positioning terms	90
4.5	Results	91
4.5.1	2D absolute CR position accuracy	91
4.5.2	2D absolute position accuracy of CR using stochastic information.	93
4.5.3	3D absolute positioning and its uncertainty for CR	94
4.5.4	3D absolute positioning and its uncertainty for (non-CR) coherent scatterers	96
4.6	Summary and conclusions	96
5	Positioning and target association in medium resolution imagery	99
5.1	Introduction	99
5.2	Positioning and target association	102
5.2.1	Mitigate errors in 2D position of radar scatterers.	102
5.2.2	Cross-range positioning of radar scatterers	107
5.2.3	Geocoding and datum transformation from radar to local coordinates	109
5.2.4	Linking radar scatterers to objects	110

5.3	Experiment setup and results	111
5.3.1	Setup.	112
5.3.2	Empirical computation of 2D residual calibration offsets	114
5.3.3	3D position accuracy for reflectors.	114
5.3.4	Linking coherent scatterers to objects	115
5.4	Summary and conclusions	119
6	Distributed Corner Reflectors - an alternative method to introduce PS	121
6.1	Introduction	121
6.2	Signal to clutter ratio and the phase statistics	122
6.2.1	Phase precision of radar targets	122
6.2.2	Radar cross-section of reflector tiles	126
6.2.3	Radar cross-section of the background.	127
6.3	Small reflectors for ground motion monitoring	127
6.3.1	Bidirectional reflector tiles design	128
6.3.2	Expected SCR	130
6.3.3	Reflector tiles deployment	130
6.3.4	Filtering	131
6.4	Experimental results	132
6.4.1	Setup.	132
6.4.2	SCR estimation	132
6.4.3	LOS deformation results	133
6.4.4	Decomposition of LOS deformation	134
6.4.5	Discussion	136
6.5	Summary and conclusions	136
7	Conclusions and Recommendations	137
7.1	Conclusions.	137
7.1.1	Decoding via target classification	137
7.1.2	Decoding via 3D positioning and target association	140
7.1.3	Encoding via distributed corner reflectors	142
7.2	Main contributions	144
7.3	Recommendations for future work	147
	Bibliography	151
A	Higher-order positioning terms	173
A.0.1	Radar satellite instrument effects	173
A.0.2	Signal propagation effects: Atmospheric path time delay	174
A.0.3	Geodynamic effects	174
A.0.4	Coordinate conversion effects: Tectonic plate motion	175
B	Pipe failure predictions in drinking water systems using satellite radar interferometry	177
B.1	Introduction	177
B.2	Materials and methods	179
B.2.1	Soil deformation data	179
B.2.2	Failure registration data	180
B.2.3	Study area	180

B.2.4	Data analysis.181
B.3	Results and discussion182
B.3.1	Failure registration data182
B.3.2	Pixel-based analysis183
B.3.3	Cell-based analysis.184
B.4	Conclusions.190
About the author		193

Nomenclature

List of acronyms

1D	One dimensional
2D	Two dimensional
3D	Three dimensional
AC	Asbestos Cement
AHN	Actueel Hoogtebestand Nederland
ASAR	Advanced Synthetic Aperture Radar
BLUE	Best Linear Unbiased Estimation
CI	Cast Iron
CoM	Center of Mass
CR	Corner Reflector
CSK	Cosmo-Skymed
DC	Doppler Centroid
DEM	Digital Elevation Model
DePSI	Delft's implementation of PSI
DGPS	Differential Global Positioning System
Doris	Delft Object-oriented Radar Interferometric Software
DORIS	Doppler Orbitography and Radio-positioning Integrated by Satellite
DS	Distributed Scatterer
DSM	Digital Surface Model
DTM	Digital Terrain Model
EM	Electromagnetic
ENVISAT	Environmental Satellite
ERS	European Remote Sensing satellite
ETRF89	European Terrestrial Reference Frame 1989
ETRS	European Terrestrial Reference System
EUREF	IAG Regional Reference Frame sub-commission for Europe
FFT	Fast Fourier Transform
GIS	Geographic Information System
GNSS	Global Navigation Satellite System
GPS	Global Positioning System
HM	High Movement
IAG	International Association of Geodesy

IMS	Imaging Mode Single Look Complex
InSAR	Synthetic Aperture Radar Interferometry
ITRF	International Terrestrial Reference Frame
LiDAR	Light Detection And Ranging
LM	Low Movement
LO	Local Oscillator
LOS	Line-of-Sight
MM	Medium Movement
NAP	Normaal Amsterdams Peil (Dutch vertical reference system)
NETPOS	Netherlands Positioning Service
OMT	Overall Model Test
PDF	Probability Density Function
PDM	Probability of Differential Motion
PRF	Pulse Repetition Frequency
PRI	Pulse Repetition Interval
PS	Persistent Scatterer
PSc	Persistent Scatterer candidates
PSI	Persistent Scatterer Interferometry
PVC	Polyvinyl Chloride
RAR	Real Aperture Radar
RCS	Radar Cross-Section
RD	Rijksdriehoekstelsel (Dutch horizontal reference system)
RDI	Relative Deformation Index
RSF	Range Sampling Frequency
RTK	Real Time Kinematic
SAR	Synthetic Aperture Radar
SCR	Signal to Clutter Ratio
SCNR	Signal to Clutter plus Noise Ratio
SET	Solid Earth Tides
SLC	Single Look Complex
SM	Stripmap
SNR	Signal to Noise Ratio
SRTM	Shuttle Radar Topography Mission
SWST	Sampling Window Start Time
TDX	TanDEM-X
TEC	Total Electron Content
TRF	Terrestrial Reference Frame
TSX	TerraSAR-X
UTC	Universal Time Coordinated
VC	Variance Covariance
VCE	Variance Component Estimation

List of symbols

a	Azimuth; a constant value; a side of a trihedral reflector
A	SLC amplitude of a pixel; design matrix; area of a resolution cell
a_e	Secondary positioning components in azimuth
A_{effec}	Effective aperture of a trihedral reflector
a_{cal}	Azimuth calibration offset
a_{tect}	Tectonic plate motion projected in azimuth direction [m]
a_{set}	Solid earth tide projected in azimuth direction [m]
A_D	Amplitude contribution from distributed scatterer
A_P	Amplitude contribution of a point scatterer
b	Baseline [m]; breath of rectangular plate; semi-minor axis; a side of a reflector
B	Design matrix; spatial baseline [m]
B_{\perp}^c	Critical perpendicular baseline
B_{DC}^c	Critical Doppler centroid baseline
B_T^c	Critical temporal baseline
B_{\parallel}	Parallel baseline [m]
B_{\perp}	Perpendicular baseline [m]
B_v	Boolean variable to indicate significant deformation
B_D	Doppler bandwidth [Hz]
B_R	Bandwidth of the transmitted radar pulses [Hz]
c	Cross-range; a constant value
d	Polynomial degree; distance offset; a constant value
d_{asc}	Displacement observed in ascending mode
d_{desc}	Displacement observed in descending mode
D_{LOS}	Light of sight deformation [m]
D_A	Amplitude dispersion
D_e	Surface deformation in East [m]
D_n	Surface deformation in North [m]
d_s	Diameter of a scatterer [m]
D_u	Surface deformation in Up [m]
e	East coordinate
f_{ϕ}	Local fringe frequency [Hz]
f_{DC}	Doppler centroid
f_D	Doppler frequency [Hz]
G	Design matrix
h	Up coordinate; height
h_g	Local ground height [m]
H	Height of a scatterer above reference surface [m]
H_R	Height of a reference point above reference surface [m]
H_0	Height of a scatterer in the reference surface [m]; null hypothesis
I	Complex interferogram; identity matrix
I_{ϵ}	Intensity due to noise
I_D	Intensity of distributed scatterer
I_P	Intensity of point scatterer
k	A constant value
K	Critical value

l	Coregistration polynomial coefficients; length of a plate; semi-major axis
L_a	Effective target size in azimuth; length of radar antenna in azimuth
L_c	Effective target dimension in cross-range
m	Coregistration polynomial coefficients
M	Master image antenna position; number of PSs in neighborhood
N	Number of SLC images; number of small reflectors
n	Refractive index; north coordinate
n_μ	Multilooking factor in range
n_ν	Multilooking factor in azimuth
N_{hydro}	Refractivity related to hydrostatic delay
N_{iono}	Refractivity related to ionosphere
N_{liq}	Refractivity related to cloud liquid delay
N_{wet}	Refractivity related to wet delay
N_D	Number of distributed scatterers
N_P	Number of point scatterers
P	Position of an arbitrary scatterer on the ground
P_0	Position of scatterer in the reference surface
P_C	Power reflected due to clutter
P_E	Estimated position of a scatterer
P_H	Position of scatterer at a height H above reference surface
P_P	Power reflected by a reflector
P_T	Ground truth position of a scatterer
Q_{rac}	Covariance matrix of radar coordinates a , r , and c
Q_{xyz}	Covariance matrix of terrestrial coordinates x , y , and z
Q_y	Covariance matrix of observations
r	Range (slant-range)
R	Range to a target [m]; rotation matrix
r_ϵ	Secondary positioning components in range
r_{pd}	Range path delay
r_{cal}	Range calibration offset
r_{far}	Far range
r_{near}	Near range
r_{tect}	Tectonic plate motion projected in range direction [m]
r_{set}	Solid earth tides projected in range direction [m]
R_p	Fresnel reflection coefficient
R_d	Mean relative deformation rate [m/s]
R_d^c	Critical relative deformation rate [m/s]
$\text{RCS}_{\text{clutter}}$	Radar cross-section of clutter
$\text{RCS}_{\text{reflector}}$	Radar cross-section of reflector
s	A constant value
S	Slave image antenna position; position vector of the spacecraft [m]
t	Slow (azimuth) time coordinate
t^{rx}	Time of receiving backscattered echo
t^{tx}	Time of transmitting radar pulses
t_{bi}	Bistatic timing correction

t_{lo}	Azimuth local oscillator drift
t_{omt}	Overall model test statistic
V	Vertical deformation component
H	Horizontal (East) deformation component
$v_{s/c}$	Platform velocity along the orbit [m/s]
v_0	Velocity of microwaves in vacuum [m/s]
w	Width of street canyon
x	A constant value; unknown variables; position in x-coordinate
y	Vector of observations; position in y-coordinate
z	SLC pixel value; $z \in \mathbb{C}$; position in z-coordinate
α	Baseline orientation angle [deg]; a vector
α_h	Satellite heading angle [deg]
β	Orientation of orbit error; a vector
χ^2	Chi-square distribution
Δf_{conv}	Azimuth spectral shift due to non-parallel orbits [Hz]
δ	Small reflector depression angle
Δ	Oversampling factor
ϵ	Residues between model and observations
γ	Complex coherence; ratio of position error ellipsoid axis lengths
γ^s	Stack coherence
γ_{DC}	Doppler centroid decorrelation
$\gamma_{thermal}$	Thermal noise decorrelation
γ_{total}	Total decorrelation
γ_{vol}	Volumetric decorrelation
γ_B	Baseline decorrelation
γ_T	Temporal decorrelation
κ	Wavenumber
κ_{\parallel}	Orbit convergence angle [rad]
λ	Radar wavelength [m]
\mathbb{B}	Bhattacharyya metric
\mathcal{E}	Error in baseline
\mathcal{E}_{\perp}	Error in perpendicular baseline
\mathcal{E}_{\parallel}	Error in parallel baseline
μ	Sub-pixel position in range
μ_A	Temporal mean pixel amplitude
ν	Sub-pixel position in azimuth
ω	A constant value
ϕ	Interferometric phase of a pixel [rad]
ϕ^{model}	Modeled interferometric phase [rad]
$\phi_{\Delta atmo}$	Phase due to change in atmospheric contribution
$\phi_{\Delta range}$	Interferometric phase due to change in range [rad]
$\phi_{\Delta scat}$	Phase due to change in scattering
ϕ_{topo}	Topographic phase [rad]
$\phi_{\Delta topo}$	Topography with respect to the reference surface [rad]
ϕ_{defo}	Phase due to deformation [rad]
ϕ_{ref}	Flat-earth phase [rad]

$\phi_{\text{topo_ref}}$	Reference topography phase [rad]
ψ	SLC phase of a pixel [rad]
ψ^w	Wrapped-phase [rad]
ψ_ε	Phase noise
ψ_{atmo}	Phase contribution due to atmospheric path delay [rad]
ψ_{range}	Phase due to distance between antenna and the target [rad]
ψ_{scat}	Phase contribution due to scattering [rad]
ψ_D	Phase contribution from distributed scatterer
ψ_P	Phase contribution from point scatterer
σ	Standard deviation
σ_{corb}^2	Cross-range position variance due to orbit errors
σ_{cSCR}^2	Cross-range position variance due to signal to clutter ratio
σ_{cR}^2	Cross-range position variance due to height error of the reference
σ_ϕ	Interferometric phase standard deviation
σ_ψ	SLC phase standard deviation
$\sigma_{\hat{h}_{\text{lg}}}$	Standard deviation of local ground height [m]
σ_v	Threshold for linear deformation rate [m/s]
σ_0	Radar backscatter coefficient
σ_A	Temporal standard deviation pixel amplitude
σ_a	Standard deviation azimuth coordinate
σ_c	Standard deviation cross-range coordinate
σ_d	Standard deviation of line of sight deformation
σ_r	Standard deviation range coordinate
τ	Fast (range) time coordinate
τ_{sys}	Unmodeled sensor internal electronic delay
τ_{lo}	Range local oscillator drift
τ_0	Sampling Window Start Time (SWST)
LO_{drift}	Local oscillator drift
θ	Radar look angle [rad]
θ_{bw}	Antenna beamwidth [rad]
θ_{inc}	Radar incidence angle [rad]
θ_p	Maxima of the cardinal sine in cross-range [rad]
ϕ	Differential polarization phase [rad]
$\phi_{\text{HH-VV}}$	Polarization phase difference between HH and VV [rad]
v	Linear deformation rate [m/s]
ϑ	Squint angle [rad]
ϑ_p	Maxima of the cardinal sine in Doppler [rad]
ζ	Terrain slope [rad]
Δ_a	Azimuth resolution of synthetic aperture radar [m]
Δ_a^{rar}	Azimuth resolution of real aperture radar [m]
Δ_c	Cross-range resolution [m]
Δ_r	Range resolution of radar [m]
$\hat{\gamma}_{\text{ens}}$	Ensemble coherence

List of operators and functions

$\{\cdot\}$	Stochastic variables
$ \cdot $	Determinant of a matrix or absolute of a variable
$\{\cdot\}^{-1}$	Inverse
$\{\cdot\}^T$	Transpose
$\{\cdot\}^*$	Complex conjugate
$\langle \cdot \rangle$	Multilooping operator; estimator operator
$D\{\cdot\}$	Dispersion
$d(\cdot, \cdot)$	Euclidean distance
$\text{Diag}\{\cdot\}$	Diagonal of a matrix
$e(\cdot)$	Exponential function
$E\{\cdot\}$	Expectation
$\text{erf}(\cdot)$	Gauss error function
$f(\cdot)$	Function operator
$g(\cdot)$	Function operator
Im	Imaginary part
$\text{mod}\{\cdot\}$	Modulo operator
$N(\cdot)$	Normal distribution
$\text{pdf}_{(\cdot)}(\cdot)$	Probability density function
Re	Real part
$\text{Tr}\{\cdot\}$	Trace of a matrix
$\text{vec}\{\cdot\}$	Vector of a matrix
$W\{\cdot\}$	Phase wrapping operator

1

Introduction

1.1. Motivation

In interferometric SAR, a measurement may represent signal contributions from one or more objects (radar scatterers) on the ground, which hampers unambiguous interpretation. Here, we propose methods towards associating radar measurements to physical objects, and understand the underlying deformation phenomena.

1.2. Background

Geodesy

Geodesy is defined as the science of determining the Earth's geometric shape, orientation in space, and its gravity field — as well as their changes with time (Helmert, 1880, 1884; Baarda et al., 1967; Vaníček and Krakiwsky, 1982). During the last 60 years with the launch of artificial satellites¹, geodesy has advanced with the following developments: mapping of large spatial extent in national, continental, and global scales; improved point positioning; measuring the dynamics of earth's surface such as plate tectonics, sea-level, ocean currents, ice sheets, climate change, sea-level rise, deformation induced by natural processes and anthropogenic activities; and capability to perform repeated, accurate and reliable measurements. These advancements were made possible by space-based geodetic techniques such as VLBI (very long baseline interferometry), spaceborne laser and radar altimetry, satellite optical remote sensing, Global Navigation Satellite Systems (GNSS), satellite-based gravity sensors, satellite-based scatterometers, and spaceborne radar interferometry. Though not intended for this purpose, techniques such as VLBI, Global Positioning Systems (GPS), and radar altimetry also contributed in understanding the Earth's atmosphere. Geodesy is a well-established field with contributions in geodynamics, geophysics, meteorology, glaciology, tectonics, volcanology, hydrology, and deformation monitoring. Well positioned in this line-up is spaceborne Interferometric Synthetic Aperture Radar (InSAR) — a cost-effective geodetic technique capable of providing precise repeated (temporal sampling in the order of days) measurements of the terrain in both local (high-resolution) and continental (wide-area coverage) scales.

¹From here on the term satellite is used to refer to artificial satellites.

InSAR and data processing

InSAR performs interferometry between two Synthetic Aperture Radar (SAR) images acquired simultaneously (single-pass interferometry) or with a time-lapse (repeat-pass interferometry) to extract information about changes of the Earth's surface and the atmosphere through which the electromagnetic waves travel (Zebker and Goldstein, 1986; Gabriel et al., 1989). SAR interferometry applications include earthquake monitoring (Massonnet et al., 1993; Zebker et al., 1994a); land cover classification (Askne and Hagberg, 1993; Dobson et al., 1995; Alberga, 2007); glacier motion estimation (Goldstein et al., 1993; Hartl et al., 1994; Rott et al., 1998); crustal changes and volcanism (Rosen et al., 1996; Sigmundsson et al., 1997); atmosphere estimation (Hanssen et al., 1999b); DEM generation (Massonnet et al., 1995); infrastructure monitoring (Massonnet, 1997; Amelung et al., 1999); and landslide analysis (Fruneau et al., 1996; Achache et al., 1996; Strozzi et al., 2005; Colesanti and Wasowski, 2006), just to name a few.

Each SAR measurement is a complex number and has two layers of information namely amplitude and phase (or in other representation real and imaginary parts). Amplitude provides the signal strength of the reflecting object while phase is sensitive to the distance between the radar antenna and the target. InSAR measures deformation as a change in distance via differential phase measurements using satellite images acquired over time in a monostatic configuration or simultaneously in a bistatic configuration. InSAR phase measurements are disturbed by the atmosphere and its variability; geometrical decorrelation due to change in satellite to target viewing angles; temporal decorrelation due to a change in the backscattering characteristics of the target; and the noise inherent in the radar (thermal, and phase noise) and data processing. By defining the signal of interest, and using some *a priori* knowledge of the noise and/or signal, processing methodologies have emerged to discriminate the underlying signal of interest from the noise by exploiting a time-series of InSAR images (Ferretti et al., 2001; Hanssen, 2001a; Hooper et al., 2004; Kampes, 2005). In addition, depending of the content of a SAR resolution cell, the processing methods can be discriminated.

A resolution cell or a pixel represents an area on the ground. It has signal contributions from a set of elementary reflecting objects from that area. The usability of a pixel is determined by the composition and physical nature of objects imaged in a resolution cell. Broadly, radar scatterers within a resolution cell are classified as point-like and distributed scatterers (DS) (Huynen, 1970; Taket et al., 1991; Nasr and Vidal-Madjar, 1991; Bamler and Hartl, 1998; Rice, 1951). Where the first one, usually a very few in number in a resolution cell (only one being dominant is the most exploited case), is described by a deterministic backscattering process; and the latter, usually many in number in a resolution cell is described by a stochastic process. Point-like scatterers exhibiting a constant backscattering response over time are commonly referred to as persistent scatterers (PS) (Ferretti et al., 2001). This discriminating factor led to two main branches of time-series processing approaches. First, Persistent Scatterers InSAR (PSInSAR) is introduced for pixels with has one dominant PS and are less-affected by decorrelation. Given N SAR images, PSInSAR approaches generally operate on $N - 1$ interferograms using one of the acquisition as a master reference image. This approach is called single-master PSInSAR or more commonly referred to as Persistent Scatterers Interferometry (PSI) (Ferretti et al., 2001; Kampes, 2005; van Leijen, 2014; Crosetto et al., 2016). The second branch of techniques are developed to process pixels with DS characteristics, here their main focus is to combat decorrelation

effects and they usually use spatial averaging as a tool to improve the SNR (Berardino et al., 2002). Small baseline subsets (SBAS) is a well-known technique in this category which utilizes multi-master configuration to exploit interferometric image pairs such that there is a smaller spatial separation (spatial baseline) between satellite positions and/or a smaller temporal separation (temporal baseline) between image acquisition times (Berardino et al., 2002; Schmidt and Bürgmann, 2003; Mora et al., 2003; Berardino et al., 2004; Pepe et al., 2015). Recent developments are being made in the hybrid techniques which processes both PS and DS together, see *e.g.*, extended SBAS exploiting both single-look and multi-looked interferograms (Lanari et al., 2004), multi-temporal approach combining PS with small baselines method (Hooper et al., 2004), and SqueeSAR approach which aims to extract information from all possible $N*(N-1)/2$ interferogram combinations (Guarnieri and Tebaldini, 2008; Ferretti et al., 2011). In all the above cases, information extraction, *e.g.* deformation, and topography estimation, is only possible when a pixel (or a group of homogeneous pixels averaged) provides a sufficient SNR and a consistent reflection over the InSAR measurement period.

Focus shift from terrain to infrastructure

In recent years, measuring deformation in a local-scale *i.e.* at infrastructure and sub-infrastructure levels over a wide-area *i.e.* at a city level, is gaining more importance (Jensen and Cowen, 1999; Strozzi et al., 2009; Stramondo et al., 2008; Colesanti et al., 2003; Prati et al., 2010; Adam et al., 2009; Zhu and Bamler, 2010; Lan et al., 2012; Barzaghi et al., 2018). This is a paradigm shift from the traditional geodesy where measuring and understanding natural terrain dynamics served their key interest. Driven by the world's population, infrastructure aging, and change in the ground/soil dynamics it is necessary to maintain a safe standard of living, and hence attention is on the rise towards monitoring the infrastructure eco system. The world's population is increasingly urban with more than half living in urban areas today, a proportion that is expected to increase to 66% by 2050 (United Nations, Department of Economic and Social Affairs, Population Division, 2015). As a result, the existing cities are becoming bigger-and-bigger, and new (mega) infrastructure are being constructed. Infrastructure are vulnerable to human and nature induced deformation processes. The underground mineral/hydrocarbon extraction, ground water pumping, and tunnel construction are some of the anthropological activities. The natural processes inducing deformation include global warming, sea-level rise, sinkholes, earthquakes, volcanic activity, tectonic and so forth. Monitoring infrastructure encompasses measuring the deformation of the infrastructure and the supporting ground due to aging, anthropological and nature induced events. Continuous monitoring by repeatedly measuring every high-rise infrastructure and parts of it using standard point-by-point geodetic surveying is bluntly considered to be time-and-cost inefficient (Strozzi et al., 2001; Cascini et al., 2007; Karila et al., 2013). We believe that in the future, periodic deformation monitoring will become a prerequisite for a safe and sustainable infrastructural projects development and maintenance. In this aspect, an active remote sensing technique such as spaceborne radar interferometry, suitable in yielding weather-and-sunlight independent repeated measurements covering larger spatial extent, is hypothesized to play a pivotal role. In this work, we focus on measuring the Earth's surface deformation and that of the infrastructure, and its variations over time via PSs.

1 1.3. Problem formulation

In the last decade, PSI has emerged as a matured remote sensing technique to perform cost-effective geodetic measurements with a high spatio-temporal sampling, supplementing or even substituting other standard in-situ terrestrial measurements. Nevertheless, in order to fully exploit the estimated deformation the object on the ground contributed to the radar measurements needs to be identified. In addition, for the locations where coherent radar measurements are not naturally available, a method to artificially introduce radar reflectors needs to be investigated. Given these issues, the following are a number of attributes of the InSAR measurement process that shapes this research.

Encoding and decoding

SAR is a side-looking imaging system which utilizes the flight path to create a synthetic antenna extent to enhance resolution in the flight direction. Though the side-looking ranging helps to improve the resolution in range direction, the SAR system suffers from geometric distortions, such as layover, foreshortening, and shadow (Schreier, 1993a). These distortions are pronounced when there is significant topography and/or tall infrastructure. Therefore, the resolution cell may comprise a complex mixture of reflecting objects from the 3D and their distinct signals encoded in a single radar measurement due to the slant-looking imaging process, the geometry of the objects on ground, and the resolution of radar instrument². As a result, associating each radar measurement to a specific object needs decoding. In traditional geodetic surveying, the points to be measured are known in advance and a geodetic measurement network is constructed *a priori* (Alberda, 1973; Grafarend and Sansò, 2012; Schmitt, 1982), while what InSAR offers is a reverse geodetic surveying problem. That is, one has to **decode the InSAR observations to know what it has measured**.

Opportunistic character

Though PSI is capable to detect millimeter-level (relative) surface changes from several hundred kilometers in space, it is an *opportunistic* measurement technique (Gernhardt, 2010; Crosetto et al., 2016). InSAR is opportunistic in the sense that the feasibility of measuring an object of interest is not just determined by the radar and satellite configuration, but also heavily depends on the size, shape, orientation, dielectric property (material) and surface roughness of the objects on the ground. It means InSAR cannot guarantee measuring a specific point on Earth without *a priori* knowledge of the measurement terrain. In order to measure a specific deformation phenomena the physical properties of PSs are to be known (Ketelaar, 2008). Once the physical object that gives rise to a PS in the SAR image is identified, a PS displacement may be used to interpret a deformation phenomena, such as structural instability, shallow ground compaction, or deep-layer ground compaction. Therefore, **there is a need to classify PSs in order to improve the interpretation of the estimated deformation**.

Resolution

A SAR resolution cell covers a voxel on the ground which extends in 3D defined by a resolution in range, azimuth, and cross-range. In 2D, a resolution cell depending on

²Here, the term encoding is used to represent the process of combining or manipulating the contributions from one or many physical objects on the ground into one resolution cell measurement of the slant-looking radar.

the azimuth and range resolution covers a fixed area on ground, about $3 \times 3 \text{ m}^2$ for TerraSAR-X and $5 \times 20 \text{ m}^2$ for Sentinel-1. The resolution attainable in the cross-range is determined by the baseline configuration of the time-series (Zhu and Bamler, 2010; Tebaldini, 2010). Assuming one dominant scatterer per resolution cell model, PSI is able to estimate deformation and topography provided the dominant radar reflection is stronger than the noise floor and coherent (Ferretti et al., 2001; Kampes, 2005). However, the main challenge here is to locate precisely in the 3D voxel where the persistent radar reflection arises from. For this purpose, **the 3D positioning capability of scatterers is studied in detail. The studies related to the error sources impacting 3D positioning, its quality description in a geodetic framework, and associating PSs to objects in the voxel are addressed.**

Information about the objects in the terrain

To identify and understand the physical object related to the scatterer, the geometrical information about the objects present in the measured terrain and its microwave scattering characteristics play a crucial role. Information could be retrieved either from the SAR measurements itself and/or could be obtained from an external source. A set information can be obtained externally, such as, 3D model of the objects or infrastructure, surface roughness, dielectric properties and its temporal variations. Effective use of every such detailed external data will certainly improve the accuracy of decoding one can attain. However, such a level of external information in high spatial and temporal resolution is not always fully available everywhere. On the other hand, retrieval of object properties from InSAR such as scatterer extent, height, polarization signature could enhance our understanding of the type of object being measured by a PS. This may also **make PSI a self-sufficient technique by decoding**. However, this is (only) possible provided the InSAR and a full polarization data-set are available and are able to accurately retrieve those object properties. Hence, alternate methods need to be developed to address this issue.

Not all pixels are usable

InSAR is capable of measuring surface variations of every illuminated resolution cell for most of the measurement terrains, such as, mountainous, desert, urban, and agricultural fields. But, the deformation and topography estimation is restricted only to a subset of pixels which remain coherent. In other cases, where pixels having contributions from natural scatterers or man-made targets or their combination as a whole represented by a coherent sum of individual contributions exhibiting a lower SNR remain less useful in the deformation studies. Such pixels, usually but not always originate from the natural terrain such as crop fields, forest, and other vegetated areas. Man-made infrastructure which does not have an optimum orientation and scattering properties also suffers with this problem. In these cases, the use of an artificial radar target such as a passive reflector (trihedral corner reflector) or an active transponder is necessary (Sarabandi and Chiu, 1996; Russo et al., 2005; Haynes et al., 2004; Mahapatra et al., 2014). An artificial radar target or a group of such targets distributed over several resolution cells can improve spatial sampling and also aid in selectively adding a (or even removing an existing) critical point (object) of interest into the InSAR measurement network which are otherwise not measured. Hence, **it can be useful to alter the object space on the ground to bring in extra InSAR measurements, this step we refer as encoding.**

Multiple scatterers

During a SAR imaging process, a 3D scene is captured into a 2D image composed of resolution cells defined by azimuth and range. During this process, apart from azimuth and range resolution the cross-range³ extent determined by slant-range resolution and local incidence angle over the imaging terrain might collect contributions from more than one dominant scatterer. As a result, resolution cells having contributions from more than one dominant scatterer need not be always coherent and might not be detected as PS during PSI. In such cases, tomographic processing methods utilizing the spatial separation of satellite positions can be used to separate scatterer contributions (Reigber and Moreira, 2000; Fornaro and Serafino, 2006; Lombardini, 2005; Zhu and Bamler, 2010; Tebaldini, 2010). Tomographic processing techniques will increase SAR measurement density by bringing in a new set of resolution cells which are untouched by PSI. In addition, application of **tomographic methods can significantly improve the quality of positioning and deformation estimation of the individual scatterers** when applied to pixels which were already detected as PS but contain more than one dominant scatterer.

1.4. Research questions and limitations

Based on the properties and problems discussed in the previous section, the two main objectives of this study are: (i) to develop a systematic method to decode PSI measurements identify PSs in the object space and to interpret the estimated deformation (kinematics), (ii) to assess the feasibility of encoding artificial radar scatterers at places where there exist no coherent measurements.

1.4.1. Research questions

Given these objectives, three main research questions and their sub-questions are addressed in this work.

1. How can we identify each coherent radar scatterer on the ground and relate InSAR-derived displacements to stress on the infrastructure?

Most of the PSs come from the infrastructure and it is vital to establish the link between PSs and infrastructure to fully exploit the estimated deformation and to perform asset management efficiently. Though interconnected, there are two types of man-made assets: underground infrastructure and above-ground infrastructure. The below-ground part consists of water pipes, gas pipes, sewer lines, tunnels, electricity/internet lines, and so forth. The above-ground infrastructure includes buildings, bridges, roads, railways lines, highways, dams, dikes, lamp poles, just to name a few. It is to be noted that the underground infrastructure is not directly measured by radar. However, the surface deformation measured by the radar can be used to assess the impact on the underground infrastructure. In this aspect the following three sub-questions are derived.

- 1.1. How can we attribute radar scatterers to different types of infrastructure?
- 1.2. How can we classify different deformation phenomena in order to relate them to stress on underground infrastructure?

³This third dimension is also called elevation (Zhu and Bamler, 2010).

- 1.3. How can we detect, quantify, and analyze potential stress on infrastructure so that asset maintenance can be prioritized?
2. How can we precisely associate each coherent radar scatterer to a physical object on the ground?

One of the salient features of InSAR is its measurement point density, usually in the order of thousands per square kilometer, enabling to monitor even parts of individual infrastructure. To demonstrate geodetic capability and in order to fully exploit the capacity of InSAR, precise point positioning is necessary to quantitatively associate radar measurements to parts of infrastructure. In addition this step not only helps to measure very local-scale deformation but also helps in integrating and comparing the PS results with other SAR sensors and geodetic data. Here, we address the following sub-questions.

- 2.1. How can we pinpoint very-localized deformation?
- 2.2. How can we systematically model error contributions and estimate 3D position of a radar scatterer, with a proper quality description?
- 2.3. How can we establish a link between the radar scatterers and the physical objects on the ground?
3. How can we monitor a specific infrastructure (or a point of interest) by artificially encoding coherent SAR measurements?

In order to include (a specific part of) an infrastructure into InSAR measurement network, the infrastructure should be consistently measured by a SAR sensor with favorable geometrical and electromagnetic properties. This is not always the case. So, in order to monitor an infrastructure or a terrain which does not possess favorable conditions, artificial radar reflectors can be deployed. However, artificial reflector deployment for deformation monitoring often comes with a set of constraints like low visual impact, size, and expense, which are in contradiction to attain a sufficient SNR and phase quality. These contradictions lead us to a new concept of distributing many small passive corner reflectors (CR). We attend the following sub-questions in order to employ distributed CRs.

- 3.1. How can we distribute and detect small artificial reflectors for infrastructure monitoring?
- 3.2. How can we describe the phase statistics of small artificial reflectors?
- 3.3. How do the distributed CRs perform over a vegetated region?

1.4.2. Methodology

The first set of research questions are addressed in two key steps: classify the coherent radar reflectors in the object space and interpret the deformation experienced by them. For this purpose, different types of information such as polarization, amplitude, and phase are studied and an approach is developed by utilizing the most commonly available InSAR dataset. Here, the use of any external information about the terrain is avoided. With a height based approach, scatterers from above-ground and below-ground are discriminated. Using this target classification approach, a method is developed to classify deformation

phenomena. In order to access the stress on infrastructure, a relative deformation metric is derived and the results are validated with ground-truth data. The target and deformation classification method developed here will be applied for the gas-pipe network monitoring in the Netherlands.

The second set of research questions regard a systematic geodetic procedure to perform error propagation and to precisely estimate the position of radar scatterers in 3D. The 3D positioning capabilities will be studied for both the high-resolution (using TerraSAR-X) and medium resolution (using ENVISAT) imagery. The proposed positioning and target association will be assessed using CR field campaigns. In the end, the association of scatterers to parts of real-world objects will be demonstrated. For this purpose, external information such as a 3D building model of the infrastructure will be used.

The third set of research questions helps to develop, and examine the suitability of small CR for InSAR monitoring. The main complication arises in detecting small CR and in their phase quality. Moreover, the existing interferometric phase statistics derived for strong targets needs to be changed for the low SCR (signal to clutter ratio) small reflectors. Towards this purpose, a distributed CR concept will be studied and a new interferometric phase expression addressing both low and high SCR radar targets will be derived. The proposed distributed CR concept will be tested with a field experiment.

1.4.3. Research scope and limitations

In this work, we will apply our methods only on the coherent scatterers which are identified as PS and processed by PSI methodology. Nevertheless our approach can also be applied to DS (Samiei Esfahany, 2017; Goel and Adam, 2014; Even and Schulz, 2018). The SAR interferograms are generated by Doris (Delft Object-oriented Radar Interferometric Software) and PSI processing is performed by DePSI (Delft's implementation of PSI) software (Kampes and Usai, 1999; Kampes, 2006; van Leijen, 2014). Here, we will not study the processing stages, such as image co-registration (Kampes, 1999a; Arikan et al., 2008), interferogram generation (Kampes, 1999a), PS detection, atmospheric phase screen (APS) removal (Hanssen, 2001a; Liu, 2012), PS densification, and phase unwrapping (Kampes and Hanssen, 2004b; Cuenca et al., 2011). Neither do we study the recursive PSI processing (Marinkovic et al., 2005), deformation model selection using hypothesis testing theory (Chang, 2015), satellite orbit error correction (Bähr, 2013). Moreover, we will only consider the PS which remain coherent over the entire stack duration: the temporally coherent PS will not be used. Finally, we will assume that the coherent radar scattering emanates from only one dominant scatterer, therefore scatterer separation using tomographic techniques is not considered here.

1.5. Thesis outline

The research objectives addressed above are sub-divided into research questions and each of them are answered in the following chapters.

Chapter 2 is a review of InSAR fundamentals mainly focused on applications to infrastructure monitoring. This chapter is intended to provide sufficient foundation needed to build the subsequent chapters.

Chapter 3 provides a state of the art survey of the radar target classification options and details the method employed in this study to perform first level discrimination to use InSAR for monitoring the impact of deformation on the infrastructure and the utilities underground. Here, the monitoring is studied with application to gas pipe networks in the

Netherlands as an example. An application of our methods for the water pipe network asset management can be found in *the Structure and Infrastructure Engineering* article published in July 2014.

Chapters 4 and 5 comprise a systematic geodetic procedure to model and estimate the position and positioning errors of the radar scatterers. The method is applied to both high resolution TerraSAR-X and medium resolution ENVISAT ASAR satellite data both validated with corner reflector experiments. A methodology is demonstrated to associate radar scatterers to objects on the ground. Chapters 4 and 5 are based on *the Journal of Geodesy* article published in February 2016 and *the IEEE Transactions on Geoscience and Remote Sensing* article published in November 2018 respectively. Further, predicting the occurrence and location of PSs using 3D city models and ray-tracing method is studied in *the IEEE Transactions on Geoscience and Remote Sensing* article published in March 2019 (Yang et al., 2019b). The methods related to the study of tie-points usage and sub-pixel positioning are addressed in separate articles under preparation (Yang et al., 2019c,a).

Chapter 6 is devoted to ‘encoding’ SAR resolution cells with small and distributed radar reflectors and study its phase stability for InSAR deformation monitoring. This will aim to provide new InSAR measurements at places where coherent reflections are naturally not available. This chapter is based on *the IEEE Transactions on Geoscience and Remote Sensing* article published on December 2017.

Chapter 7 provides the conclusions and a set of recommendations for future research.

A schematic outline of this research is illustrated in Fig. 1.1.

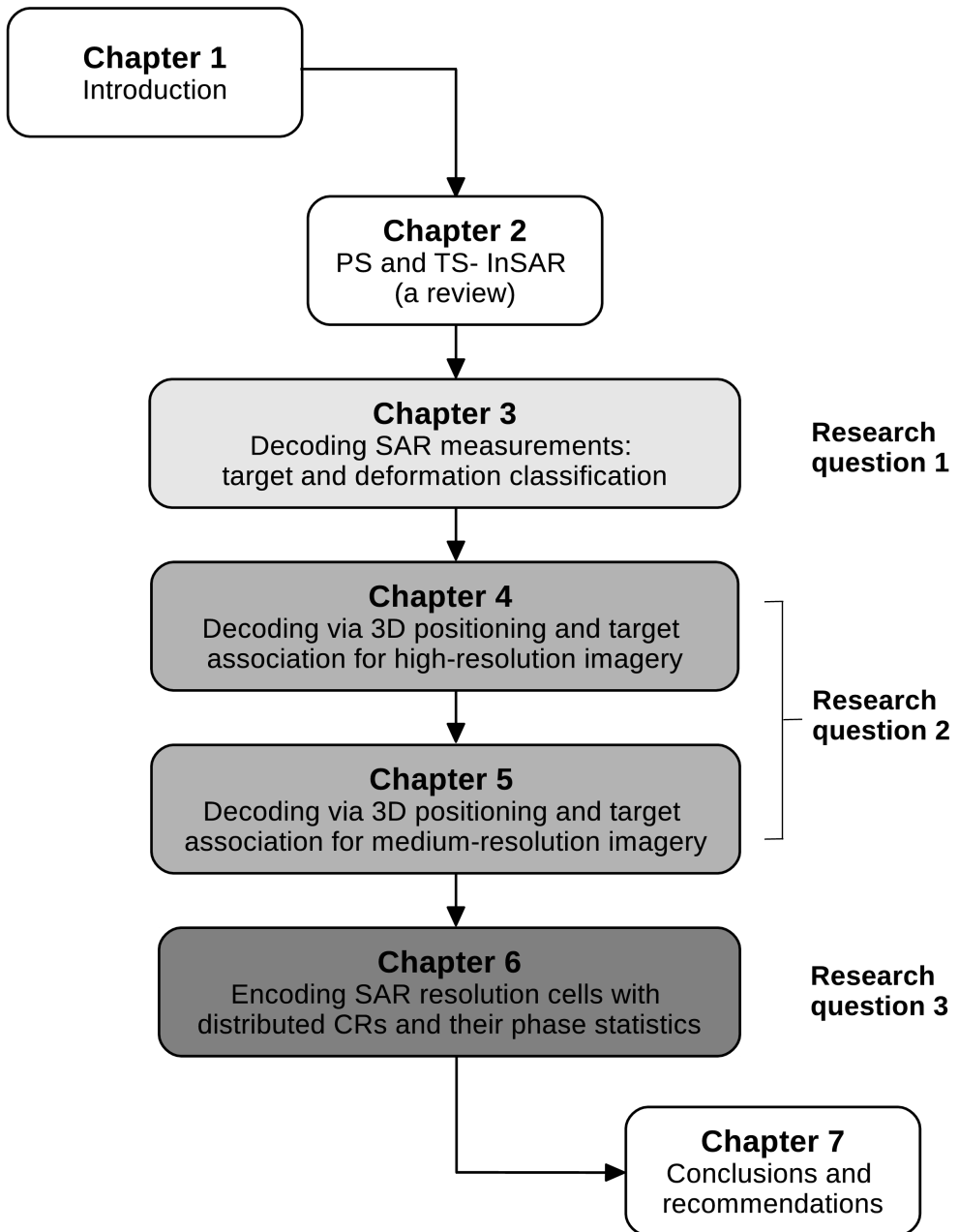


Figure 1.1: A quick-look at the chapters, contributions are highlighted in grey.

2

A review of InSAR and persistent scatterers

In this chapter a brief overview of real-aperture radar, Synthetic Aperture Radar (SAR), and Interferometric SAR (InSAR) are given in secs. 2.1–2.5. The SAR images cover various types of resolution cells. Based on the contents of the resolution cells, the InSAR time-series data processing and interpretation of measurements will vary, this is described in sec. 2.6. Processing a time-series of radar images is found to be extremely beneficial in extracting deformation and height for a dense set of measurement points using Persistent Scatterer Interferometry (PSI), see sec. 2.7. This is followed by a discussion in sec. 2.8 on the need to understand the origin of radar scatterers to physically interpret the deformation.

2.1. Radar

Radar, an acronym for RADIO Detection And Ranging, is a remote sensing technique to measure distance, and velocity of target by illuminating via radio waves and measuring the reflected signal. Radio waves are a subset of electromagnetic waves with a frequency range between 3 kHz (100 km wavelength) and 300 GHz (1 mm wavelength). A list of the most common frequency bands allotted for remote sensing is given by Tab. 2.1 (Lillesand et al., 2014). Unlike measurements from optic and infrared providing chemical properties of the objects, radar measures the dielectric properties (Ulaby et al., 1982; Fung, 1994; Skolnik, 2002; Elachi, 1988).

2.2. Side looking Real Aperture Radar

Side-looking Real Aperture Radar (RAR) is an active remote sensing technique, where a moving platform (satellite, or airborne or ground-based) carrying a radar transceiver transmits radar pulses towards targets on the Earth and records the backscattered echo (Skolnik, 1980). The motion of platform along a desired path makes it possible to create a 2D image of the 3D surface of the Earth. The resolution of such radar images is defined by azimuth and slant-range directions. Azimuth is defined by the direction of platform motion. Range is defined in the direction in which the radar pulses are transmitted towards the Earth, known as line of sight (LOS) direction. The range refers to the slant-range distance

Table 2.1: Remote sensing radar frequency bands and their labels according to the IEEE standard (Lillesand et al., 2014). Frequency bands and satellite missions highlighted in bold are used in this study. The launch year is mentioned next to the satellite mission in parenthesis.

Band label	Frequency range [GHz]	Wavelength range [cm]	Satellite SAR missions
Ka	26.5 – 40	0.75 – 1.1	–
K	18 – 26.5	1.1 – 1.67	–
Ku	12.5 – 18	1.67 – 2.4	–
X	8 – 12.5	2.4 – 3.75	TerraSAR-X (2007), Cosmo-Skymed (2007-2010), TanDEM-X (2010), PAZ (2018)
C	4 – 8	3.75 – 7.5	ERS-1/2 (1991/1995), ENVISAT (2002), Radarsat-1/2 (1995/2007), Sentinel-1A/1B (2014/2016)
S	2 – 4	7.5 – 15	NISAR (planned 2021)
L	1 – 2	15 – 30	Seasat (1978), JERS-1 (1992), ALOS-1/2 (2006/2014), SAOCOM 1A/1B (2018/planned 2019), NISAR (planned 2021)
P	0.3 – 1	30 – 100	Biomass (planned 2021)

between the radar and the target, unless explicitly defined otherwise. The resolution of radar in range (Δ_r) is limited by the bandwidth B_R of the transmitted pulses which is a radar design criteria. The range resolution is given by (Curlander and McDonough, 1991),

$$\Delta_r = \frac{v_0}{2 \cdot B_R}, \quad (2.1)$$

where v_0 is the velocity of microwaves in vacuum. The resolution in azimuth is proportional to the antenna-to-target range R and the antenna beamwidth θ_{bw} ,

$$\Delta_a^{\text{rar}} = R \cdot \theta_{bw} = R \cdot \frac{\lambda}{L_a}, \quad (2.2)$$

where λ is the radar wavelength, and L_a is the length of the radar antenna in azimuth. The azimuth resolution of real-aperture radar is in the order of several hundred meters in an airborne case and several kilometers in the spaceborne case.

2.3. Synthetic Aperture Radar

In the 1950s, to increase the resolution in azimuth possibly with a smallest physical antenna size, a post processing technique known as Doppler beam sharpening (nowadays called strip-mapping or stripmap) was first introduced by Wiley (1954). Only in 1978, the first satellite "Seasat" with a SAR payload was launched, which was coincidentally the same

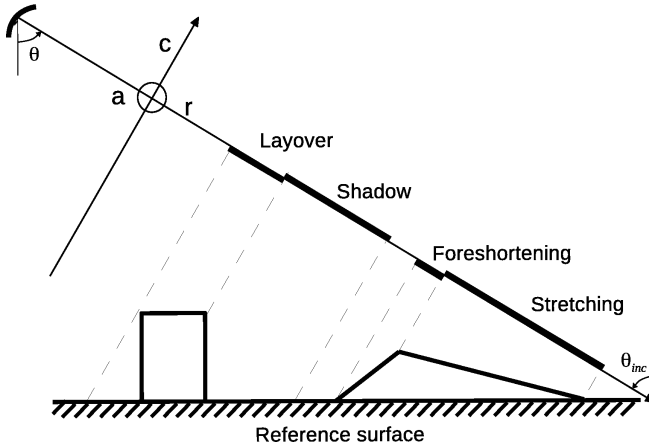


Figure 2.1: Distortions in side-looking SAR imaging. SAR imaging geometry is defined by azimuth a , range r , and cross-range c directions. θ and θ_{inc} are the radar look and incidence angles respectively. Azimuth is perpendicular to the plane.

year for the launch of the first GPS (Global Positioning System) satellite (NSSDCA, 1978; BORN et al., 1979; Carver et al., 1985). A SAR system gains resolution in azimuth by collecting signals in flight direction according to the Doppler frequency shift. For this purpose, pulses are transmitted and collected when a radar antenna mounted orthogonal to the flight direction passes the target. Each of these successive radar returns are then combined during post processing in order to form a larger synthetic aperture, hence the resolution improvement in azimuth. The azimuth resolution can be written by (Curlander and McDonough, 1991),

$$\Delta_a = \frac{v_{s/c}}{B_D} = \frac{L_a}{2}, \quad (2.3)$$

where $v_{s/c}$ is the platform velocity along the orbit, and B_D is the Doppler bandwidth. Unlike Eq. (2.2), in SAR Δ_a is independent of the antenna-to-target distance, see Eq. (2.3). The imaging geometry of SAR systems is side-looking in nature which improves the range resolution of the system. But, this oblique imaging geometry introduces several distortions based on the local slope of the target in relation to the side-looking angle of the platform, see Fig. 2.1. The distortions are shadow, foreshortening, stretching, and layover. Shadow occurs when the radar illumination does not reach the target. Such pixels do not produce backscattering and are exempt from speckle¹. For a terrain with topography or high-rise infrastructure, larger radar look angles will increase the shadow regions. Foreshortening occurs when the slope is facing towards the radar while stretching occurs when the slope is facing opposite to the radar look direction. Layover is a special scenario which occurs when the slope is larger than the incidence angle (θ_{inc}), see Fig. 2.1.

The earth is made-up of 3D terrain and infrastructure, also referred as the object-space. A SAR SLC (Single Look Complex) image maps the earth's 3D object-space with

¹ Speckle is a phenomenon where adjacent pixels representing a single surface type (*i.e.*, homogeneous regions) show high variability in radar backscattering. It is due to the interference of waves reflected from many tiny elementary scatterers in a resolution cell (Lee et al., 1994).

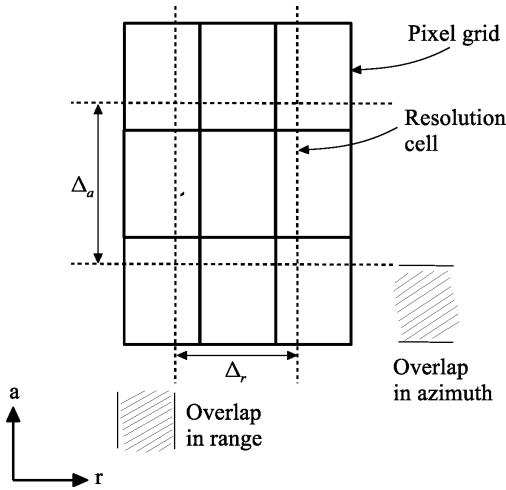


Figure 2.2: SAR Single Look Complex (SLC) product resolution cell and pixel grid posting in an imaging plane defined by azimuth (a) and range (r) directions.

finite bandwidths onto azimuth (flight path) and (slant) range (image acquisition) direction, which is 2D. Finite bandwidths of the SAR sensor namely, Doppler bandwidth (B_D) and chirp bandwidth (B_R) translate into a resolution of the radar sensor in azimuth (Δ_a) and range (Δ_r), respectively, see Eqs. (2.3) and (2.1). The area illuminated from radar described by physical dimensions Δ_a and Δ_r defines a resolution cell (Curlander and McDonough, 1991). Objects from neighboring resolution cells can be distinguished. But in practice, a 2D SAR image is given in pixels which results in SAR processing to achieve Nyquist criteria for the system bandwidth, overlapping adjacent resolution cells. As a result, a pixel size posting is smaller than a resolution cell size as illustrated in Fig. 2.2.

Like all electromagnetic signal systems, a radar echo stored in every SAR SLC image pixel provides two “layers” of measurement—amplitude (A) and phase (ψ), expressed by,

$$A \cdot e^{j\psi}. \quad (2.4)$$

Amplitude A is a digital number representative of the RCS (Radar Cross-Section) of the target². The fractional phase ψ_ε wrapped in $[-\pi, \pi)$ varies with the distance or travel time between the target and the SAR sensor, given by,

$$\psi^w = W\{\psi_{\text{range}} + \psi_{\text{atmo}} + \psi_{\text{scat}} + \psi_\varepsilon\}, \quad (2.5)$$

where, W is the modulo- 2π wrapping operator, and ψ_{range} represents the distance between the phase-center of the radar antenna and the effective phase-center of a resolution cell on the ground. The contribution due to backscattering from the scatterers in a SAR resolution cell is represented by ψ_{scat} , see sec. 2.6 for further details. The phase delay due to propagation of radiowaves in the earth’s atmosphere is denoted by ψ_{atmo} . The final term ψ_ε in Eq. (2.7) represents the noise from processing, thermal and sensor local oscillator

²The relation between amplitude A and RCS can be given by $\text{RCS} = k_1 \cdot A^2 + k_2$, where k_1 and k_2 are scaling and shift factors, respectively (Fritz, 2007; Hajduch et al., 2018).

phase jitter, which are common to all resolution cells for a given SAR acquisition. Since the SLC phase ψ is wrapped, it is not possible to extract information from the phase in a single SLC image.

2.4. Synthetic Aperture Radar Interferometry

InSAR exploits the changes between SAR images to generate an interferogram using amplitude and phase measurements. SAR interferograms provide an interference pattern containing all the information on relative geometry (Massonnet and Feigl, 1998; Bamler and Hartl, 1998; Gabriel et al., 1989). SAR images acquired simultaneously with a different platform position are applied for single-pass interferometry and images acquired with a difference in time are applied for multi-pass interferometry. SAR pixel phases from two images are only comparable after a careful image registration. A SAR interferogram I_{MS} between a master image M and a slave image S is generated by a pointwise complex conjugate multiplication operation (denoted by the $(\cdot)^*$ operator), written as,

$$I_{MS} = (A_M \cdot e^{j\psi_M})(A_S \cdot e^{j\psi_S})^* = A_M A_S e^{j\phi_{MS}}, \quad (2.6)$$

where A_M , A_S , ψ_M , and ψ_S are the pixel amplitudes and phases for master and slave images respectively. Useful information can be obtained from the interferometric phase difference,

$$\phi_{MS} = \text{mod}\{\psi_M - \psi_S + \pi, 2\pi\} - \pi = W\{\phi_{\Delta\text{range}} + \phi_{\Delta\text{atmo}} + \phi_{\Delta\text{scat}} + \phi_{\epsilon}\}. \quad (2.7)$$

where $\phi_{\Delta\text{range}}$, $\phi_{\Delta\text{atmo}}$, $\phi_{\Delta\text{scat}}$, and ϕ_{ϵ} are the interferometric phase contributions due to a change in range, atmospheric path delay, target scattering, and noise in imaging a target with a master and a slave acquisition. The modulo operator is denoted by $\text{mod}\{\cdot\}$.

2.4.1. The range-related phase

The change in range measured via the differential phase can be sub-divided into four components, written by,

$$\phi_{\Delta\text{range}} = \phi_{\text{defo},MS} + \underbrace{\phi_{\Delta\text{topo}} + \phi_{\text{topo_ref}}}_{\phi_{\text{topo}}} + \phi_{\text{ref}}. \quad (2.8)$$

The first component $\phi_{\text{defo},MS}$ measures the deformation seen at the surface during a time-gap between the master and the slave acquisitions, expressed by,

$$\phi_{\text{defo},MS} = \frac{-4\pi}{\lambda} D_{\text{LOS}}, \quad (2.9)$$

where D_{LOS} is the surface deformation of a target projected onto the 1D radar Line of Sight (LOS) direction. The actual 3D deformation of the surface is represented by D_e , D_n and D_u in East, North and Up directions respectively. For a satellite platform with an orbit heading angle of α_h and a local incidence angle of θ_{inc} , the 3D to 1D projection is given by Hanssen (2001a),

$$D_{\text{LOS}} = D_u \cos(\theta_{\text{inc}}) - \sin(\theta_{\text{inc}}) [D_n \cos(\alpha_h - 3^k \pi/2) + D_e \sin(\alpha_h - 3^k \pi/2)], \quad (2.10)$$

$$= D_u \cos(\theta_{\text{inc}}) - \sin(\theta_{\text{inc}}) [-D_n \sin(\alpha_h) + D_e \cos(\alpha_h)],$$

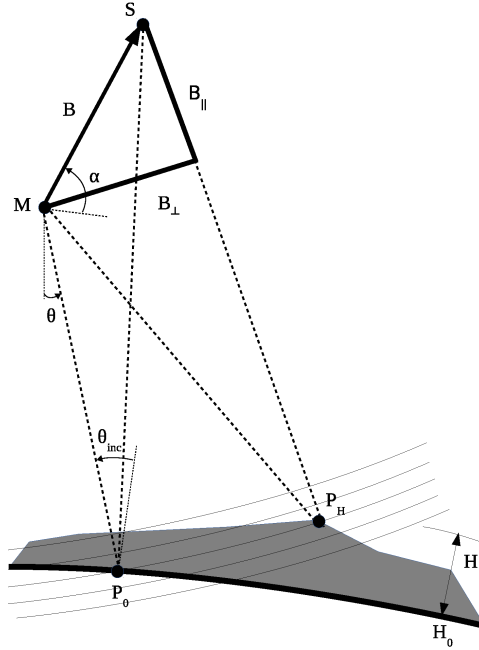


Figure 2.3: InSAR acquisition geometry of a target P_H at a height H above reference surface while point P_0 is its equivalent with height H_0 . P_H and P_0 share the same range to the master M . The master M and slave S acquisitions are separated by a spatial baseline B with orientation α . B is decomposed into parallel baseline B_{\parallel} and perpendicular baseline B_{\perp} . The B_{\parallel} and B_{\perp} vary across the image and are dependent on the local incidence angle θ_{inc} and α . θ is the look angle of the satellite. After Hanssen (2001a); van Leijen (2014).

where D_{LOS} is the projection for the most common right-looking satellite case with $k = 1$ and the $(\alpha_h - 3\pi/2)$ represents the angle perpendicular to the satellite orbit, known as the azimuth look direction. In the case of a left-looking satellite, the projection can be written by substituting $k = 0$ in Eq. (2.10) (van Leijen, 2014).

The second and third term in Eq. (2.8) are related to the topography. ϕ_{topo} is the target topography with respect to a reference surface such as an ellipsoid (see Fig. 2.3), given by,

$$\phi_{\text{topo}} = \frac{-4\pi}{\lambda} \left((d(M, P_H) - d(S, P_H)) - (d(M, P_0) - d(S, P_0)) \right), \quad (2.11)$$

where, $d(\cdot, \cdot)$ is Euclidean distance operator. Using the far-field approximation, ϕ_{topo} can be written as (Hanssen, 2001a; Zebker and Goldstein, 1986),

$$\phi_{\text{topo}} = \frac{-4\pi}{\lambda} \frac{B \cos(\theta_{\text{inc}} - \alpha)}{R \sin(\theta_{\text{inc}})} H = \frac{-4\pi}{\lambda} \frac{B_{\perp}}{R \sin(\theta_{\text{inc}})} H, \quad (2.12)$$

where B , and B_{\perp} are the baseline and perpendicular baseline separation between master and slave satellite positions respectively. The baseline orientation angle is denoted by α , see Fig. 2.3.

In the presence of a reference DEM (Digital Elevation Model) of the terrain, such as the SRTM (Shuttle Radar Topography Mission) (Farr et al., 2007), $\phi_{\text{topo_ref}}$ is computed and removed from ϕ_{topo} to get $\phi_{\Delta\text{topo}}$. In this case, only the residual topography component

$\phi_{\Delta\text{topo}} = -\frac{4\pi}{\lambda} \frac{B_{\perp}}{R \sin(\theta_{\text{inc}})} \Delta H$ remains to be estimated. The height difference of the target with respect to a reference DEM given by ΔH is also known as DEM error. When a reference elevation model is not available or not used, then H from ϕ_{topo} is directly estimated. Here, the larger the perpendicular baseline, the larger the sensitivity of phase to topography. Therefore, for a better topography estimation interferograms with a larger baseline are preferred.

The fourth component in Eq. (2.8), called the flat-Earth phase ϕ_{ref} , is a contribution attributed to the distance between the satellite and an ellipsoid such as the WGS84 or a local Bessel. The flat earth phase of P_H is computed at P_0 on the reference surface which shares the same range to master antenna position, written as,

$$\phi_{\text{ref}} = \frac{4\pi}{\lambda} B \sin(\theta_{\text{inc}} - \alpha) = \frac{4\pi}{\lambda} B_{\parallel}, \quad (2.13)$$

where B_{\parallel} is the parallel baseline. A removal of ϕ_{ref} , decreases the fringe rate, which improves the visibility of interferometric phase due to topography and deformation components.

2.4.2. Atmospheric phase

Radio waves are not strongly attenuated by the atmosphere in terms of their signal magnitude and hence the day-and-night imaging is possible by radars. However, during signal propagation, the phase of the radio signal is delayed due to velocity variations and the ray bending effects. The bending of radio waves can be neglected for SAR missions with incidence angles (θ_{inc}) less than 75° (Mendes, 1999; Liu, 2012). Therefore, SAR acquisitions are disturbed only by the path delays (r_{pd}) due to refractive index n variations in the ionosphere and the troposphere, expressed by Hanssen (2001a); Davis et al. (1985),

$$r_{\text{pd}} = \frac{10^{-6}}{\cos(\theta_{\text{inc}})} \left\{ \int_h^H N_{\text{iono}} dz + \int_h^H N_{\text{hydro}} dz + \int_h^H N_{\text{wet}} dz + \int_h^H N_{\text{liq}} dz \right\}, \quad (2.14)$$

where h is the height of the target, H is height of the satellite, and the factor $1/\cos(\theta_{\text{inc}})$ is the mapping function from zenith to slant-range. The four refractivity components are the ionospheric component N_{iono} , the hydrostatic component N_{hydro} , the wet component N_{wet} and the cloud liquid component N_{liq} . The multiplier 10^{-6} is used to convert the refractive index n into refractivity $N = (n - 1)10^6$. The integrals with N_{iono} , N_{hydro} , N_{wet} , and N_{liq} describe the ionosphere delay, the hydrostatic delay, the wet delay and the cloud liquid delay, respectively. Typical total delay due to ionosphere and troposphere is about 2.7 m (Dheenathayalan et al., 2014).

The differencing operation in an interferogram largely cancels the constant parts of the ionospheric and tropospheric delays. Still, the differential path delay exhibits a strong variability, written as,

$$\phi_{\Delta\text{atmo}} = \frac{-4\pi 10^{-6}}{\lambda \cos(\theta_{\text{inc}})} \left\{ \int_h^H \Delta N_{\text{iono}} dz + \int_h^H \Delta N_{\text{hydro}} dz + \int_h^H \Delta N_{\text{wet}} dz + \int_h^H \Delta N_{\text{liq}} dz \right\}, \quad (2.15)$$

where Δ symbolizes the change in the refractivities in Eq. (2.14) between the two SAR acquisitions. The interferometric atmospheric phase variability is mainly due to the following factors (Hanssen, 2001a; Goldstein, 1995).

1. **Turbulent mixing:** Turbulent processes such as water vapor distribution (causing the wet delay), solar heating of the earth's surface, and differences in wind direction/velocity generates a phase delay, which is heterogeneous and non-linear in nature. Such signals are spatially correlated for shorter distances and can be described by a power-law behavior (Hanssen, 2001a). Turbulent mixing effects exhibit limited correlation in time, may be for upto a few hours.
2. **Vertical stratification:** This effect is only seen when a scene contains topography and its vertical refraction profile is varying between acquisitions. Stratification effects are correlated with the height and can be ignored for a flat terrain.
3. **Total electron content variation:** The phase delay in ionosphere is characterized by the free electron density in the upper atmosphere quantified by the TEC (Total Electron Content) (Meyer et al., 2006).

2.4.3. Scattering-related phase

A significant change in the scattering phase between acquisitions resulting in $\phi_{\Delta\text{scat}} \neq 0$ is not desirable and is considered to be a source of decorrelation. The phase contribution $\phi_{\Delta\text{scat}}$ due to a change in scattering between the two acquisitions can be attributed to two categories: sensor-side effects and target-side effects. The degree of decorrelation is usually expressed by the coherence (γ) (Zebker and Villasenor, 1992). The target-side effects include temporal decorrelation (γ_T), and volumetric decorrelation (γ_{vol}). The sensor-side effects include baseline (γ_B) decorrelation and Doppler centroid decorrelation (γ_{DC}).

Temporal decorrelation γ_T occurs due to an implicit change in the scattering properties of the surface. This can be due to a variation of the physical position of (elementary) scatterers in a resolution cell, and/or a change in dielectric properties of the scattering surface. A volumetric decorrelation γ_{vol} is an extension of temporal decorrelation where the scatterers are distributed in a 3D volume rather than a 2D surface and hence it is different from γ_T . γ_{vol} includes scattering changes above the surface (*e.g.* forests, vegetated areas) and below the surface (*e.g.* sandy desserts) when the radar signal penetrates a medium. Here, the signal penetration is dependent on the radar wavelength and the surface/volume characteristics. Describing γ_T and γ_{vol} using analytical expressions is difficult since the range of possible temporal and volume changes is too wide to be described quantitatively (Hanssen, 2001a).

Due to a change in satellite positions during repeated acquisitions, a SAR sensor in a given satellite pass direction (ascending or descending) may look at a target from a different viewing geometry. Baseline decorrelation γ_B occurs due to a change in incidence angles of the satellites looking at a same target, given by Zebker and Villasenor (1992); Gatelli et al. (1994),

$$|\gamma_B| = \begin{cases} \frac{B_{\perp}^c - B_{\perp}}{B_{\perp}^c}, & |B_{\perp}| \leq B_{\perp}^c, \\ 0, & |B_{\perp}| > B_{\perp}^c, \end{cases} \quad (2.16)$$

where B_{\perp} is the perpendicular baseline, B_{\perp}^c is the critical baseline causing a spectral shift equal to the bandwidth B_R , written as,

$$B_{\perp}^c = \lambda \frac{B_R R}{c} \tan(\theta_{\text{inc}} - \zeta) \quad (2.17)$$

where, ζ is the topographic slope, and R is a distance between the radar antenna and target. Similarly, in azimuth, Doppler decorrelation is caused by a change in azimuth squint angle³ between acquisitions, given by Hanssen (2001a),

$$|\gamma_{DC}| = \begin{cases} 1 - \frac{\Delta f_{DC}}{B_A}, & |\Delta f_{DC}| \leq B_A, \\ 0, & |\Delta f_{DC}| > B_A, \end{cases} \quad (2.18)$$

where, Δf_{DC} is the differential Doppler centroid between acquisitions, and B_A is the bandwidth in azimuth.

2.4.4. Phase noise

The final component in Eq. (2.7) is the noise term ϕ_ϵ , which includes all the remaining decorrelation effects. It includes thermal noise induced decorrelation γ_{thermal} , and the SAR and interferogram image processing induced noise sources γ_{proc} . The thermal noise can also be expressed using the thermal signal-to-noise ratio (SNR). The thermal noise (also known as the system noise) for a SAR image includes the noise related to the oscillator phase jitters. The SNR is expressed as a ratio between the average received signal power from a target and the radar receiver thermal noise power. SNR includes both the parameters from the sensor and the reflection characteristics of the target. The thermal decorrelation of a SAR image is given by (Foster and Guinzy, 1967; Zebker and Villasenor, 1992; Zebker et al., 1994b), as

$$\gamma_{\text{thermal}} = \frac{SNR}{1 + SNR}. \quad (2.19)$$

In addition, an error in the orbital state vectors can introduce additional unwanted phase ramps. The estimation and removal of orbital effects are addressed in Bähr (2013).

In summary, the different decorrelation effects can be combined in a multiplicative manner to a total coherence value (γ_{total}), expressed by (Zebker and Villasenor, 1992),

$$\gamma_{\text{total}} = \gamma_T \cdot \gamma_{\text{vol}} \cdot \gamma_B \cdot \gamma_{DC} \cdot \gamma_{\text{thermal}} \cdot \gamma_{\text{proc}}. \quad (2.20)$$

Here, the information extraction, *e.g.* deformation, topography or atmosphere estimation, is better for pixels having a higher coherence value. The complex coherence of a pixel in two SLC images $z_M = A_M \cdot e^{j\psi_M}$ and $z_S = A_S \cdot e^{j\psi_S}$ reads (Born et al., 1959; Foster and Guinzy, 1967; Papoulis, 1991),

$$\gamma = \frac{E\{z_M \cdot z_S^*\}}{\sqrt{E\{|z_M|^2\} \cdot E\{|z_S|^2\}}}, 0 \leq |\gamma| \leq 1. \quad (2.21)$$

The computation of coherence using Eq. (2.21) is possible when the expectation values (*e.g.* $E\{|z_M|^2\}$, $E\{|z_S|^2\}$) can be computed using a large set of observations acquired for a single pixel under the same circumstances. In the space-borne InSAR case, a pixel is observed only once during each SAR acquisition. Therefore, assuming ergodicity, the expectation operation is replaced with a spatial averaging over N surrounding pixels, expressed by (Seymour and Cumming, 1994),

$$\hat{\gamma} = \frac{\sum_{i=1}^N z_{M,i} z_{S,i}^*}{\sqrt{\sum_{i=1}^N |z_{M,i}|^2 |z_{S,i}|^2}}. \quad (2.22)$$

³An angle between the actual pointing direction of the antenna and the perpendicular direction (zero-Doppler line) to the flight path

Achieving a value of $|\hat{\gamma}|$ close to 1 is a favorable condition for interferometric processing algorithms, and is dependent on the type of scatterers in the resolution cell. Depending on the contents of a resolution cell, the radar back-scattering characteristics vary. In the following section a procedure for interferogram generation is described followed by a quick overview of SAR resolution cells in sec. 2.6.

2

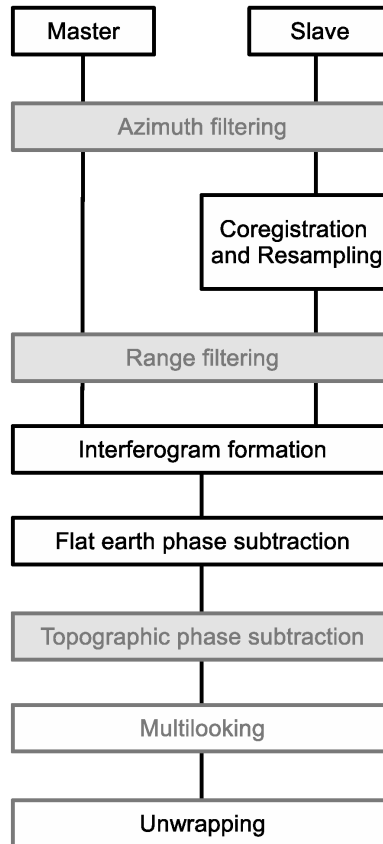


Figure 2.4: Interferometric processing chain (Kampes, 1999b). Optional steps are in gray.

2.5. InSAR processing chain

In order to create an interferogram between a master and a slave image according to Eq. (2.6), a set of processing steps are required as illustrated in Fig. 2.4. There exists various InSAR processors and in this section the processing steps are explained based on the Delft Object-oriented Radar Interferometric Software (Doris) developed at Delft University of Technology since 1998 (Kampes and Usai, 1999; Kampes et al., 2003).

2.5.1. Azimuth and range filtering

Azimuth and range filtering are optional steps which help in reducing the phase noise in the interferogram due to a non-identical viewing geometry of the master and slave satellite positions. The spectral filtering is useful mainly for the resolution cells dominated by distributed targets, while for point targets the filtering is not necessary.

In azimuth, a change in squint angles (Doppler centroids) and non-parallel orbits between master and slave satellite trajectory results in decorrelation. Filtering the images for the Doppler shift enhances coherence. Generally, Doppler centroid shifts are significantly reduced by a zero-Doppler steering. The non-parallel orbits results in an additional spectral shift in azimuth, given by (Bähr, 2013),

$$\Delta f_{\text{conv}} = -\frac{2\kappa_{\parallel} v_{s/c}}{\lambda}, \quad (2.23)$$

where, κ_{\parallel} is the orbit convergence angle, and $v_{s/c}$ is the velocity of the spacecraft.

In range, a change in the satellite look angle between two acquisitions results in a shift in the ground reflectivity spectrum (object spectrum), resulting in decorrelation during interferogram formation. A bandpass range filtering can be designed based on the local fringe frequency f_{ϕ} which is identical to the spectral shift, written as (Hanssen, 2001a),

$$f_{\phi} = \frac{v_0}{2\pi} \frac{\delta\phi}{\delta R} = -\frac{v_0 B_{\perp}}{\lambda R \tan(\theta_{\text{inc}} - \zeta)}. \quad (2.24)$$

For a flat topography, f_{ϕ} is computed from the satellite state vectors and assuming a constant terrain slope, *i.e.*, $\zeta = 0$. However, for a rough terrain, f_{ϕ} is estimated locally for small regions (Hanssen, 2001a). For this approach, a temporary interferogram is required and generated using a resampled slave image (Kampes and Usai, 1999).

2.5.2. Coregistration and resampling

Coregistration is a key step in aligning both acquisition start times and sampling window start times between the master and slave images. Moreover, due to a change in sampling grids of slave and master images, a coregistration polynomial of degree d is often estimated to capture higher order distortions, written as (Bähr, 2013; Kampes and Usai, 1999),

$$\begin{pmatrix} \mu_S \\ \nu_S \end{pmatrix} = \begin{pmatrix} \mu_M \\ \nu_M \end{pmatrix} + \sum_{i=0}^d \sum_{j=0}^{d-i} \begin{pmatrix} l_{i,j} \mu_M^i \nu_M^j \\ m_{i,j} \mu_M^i \nu_M^j \end{pmatrix}, \quad (2.25)$$

where $l_{i,j}$ and $m_{i,j}$ are the polynomial coefficients between the pixels in the master (μ_M, ν_M) and slave (μ_S, ν_S) images. Usually a polynomial of degree d of 2 may be sufficient to achieve a misregistration threshold of $1/8^{\text{th}}$ of a pixel which results in a negligible (4%) loss of coherence (Just and Bamler, 1994; Nitti et al., 2011; Hanssen, 2001a, p. 46).

After the coregistration, the resampling operation is carried out in two steps to map the complex values of slave image to the the pixel positions of the master image. First, a continuous signal is reconstructed from sampled values of the slave image using an interpolation kernel (Laakso et al., 1996; Hanssen et al., 1999b). In the second step, the reconstructed continuous signal is sampled at the master grid locations.

2.5.3. Flat earth and topographic phase removal

The flat earth phase is computed using a reference phase of a mathematical body such as an ellipsoid and is subtracted point-wise from the complex interferogram I ,

$$I = I \cdot e^{-j\phi_{\text{ref}}}, \quad (2.26)$$

where the flat earth phase ϕ_{ref} is computed for all pixels in the master image using Eq. (2.13). For this computation, a pixel position on the ground is necessary, which is obtained through a step called geocoding (Schreier, 1993b; Schwäbisch, 1995a; Madsen et al., 1993; Geudtner et al., 1996; Small et al., 1996), see the equations in sec. 4.2.5 for details. The image pixel numbers are usually referenced to one of the five positions of a pixel, *viz.*, lower-left, lower-right, center, upper-left and upper-right. However, the actual position of the scatterer determined at sub-pixel level might vary significantly from these fixed positions. Therefore, the ϕ_{ref} computed using sub-pixel position is more accurate. The larger the size of the pixel, the larger the impact of sub-pixel position on the ϕ_{ref} computation. Apart from high-resolution images, medium and low-resolution imagery benefits the most from sub-pixel computations (Kampes, 2005).

Topographic phase removal is another optional step to reduce the phase contribution due to a known topography $\phi_{\text{topo_ref}}$ which might improve the phase unwrapping operation. The known topographic information can be obtained from an available DEM such as SRTM. The topographic phase $\phi_{\text{topo_ref}}$ is computed as in Eq. (2.12) and applied after flat earth phase reduction step as,

$$I = I \cdot e^{-j\phi_{\text{topo_ref}}}. \quad (2.27)$$

Similar to the flat earth contribution, the topographic phase computed using sub-pixel positions can be beneficial (Yang et al., 2019a). An improvement in topographic phase due to sub-pixel position depends on the DEM resolution and the local topography over a pixel.

2.5.4. Multilooking

Multilooking is an optional step performed to reduce phase noise in the interferograms by complex averaging adjacent pixels (Lee et al., 1994; Goldstein et al., 1988; Rodriguez and Martin, 1992). The complex averaging operation improves phase quality provided the signal is constant over the averaged area and the noise is statistically homogeneous (Lee et al., 1994; Hanssen, 2001a). The multilooked interferogram pixel reads,

$$\langle I(v, \mu) \rangle = \frac{1}{n_v n_\mu} \sum_{v=1}^{n_v} \sum_{\mu=1}^{n_\mu} I(v, \mu), \quad (2.28)$$

where $\langle \cdot \rangle$ is the multilooking operator, n_v and n_μ are the multilook factors in azimuth and range directions, respectively. The multilook factors are chosen such that a necessary noise reduction is achieved and in consideration to the spatial wavelength of the signal of interest. The multilook operation might not be beneficial for pixels with point scatterers since it might reduce coherence when added with other pixels with distinct signals.

2.5.5. Unwrapping

Phase unwrapping is one of the most important and challenging step in the estimation of the unknown absolute phase from the wrapped SAR measurements. Since unwrapping operation is under-determined in nature, the solution is non-unique and requires assumption

or a-priori knowledge about the signal of interest. The most general assumption is that the phase of adjacent pixels varies less than half a cycle. This assumption is not valid for a scene with mountainous terrain or high deformation gradient. In such locations, additional information is mandatory to resolve the 2π phase ambiguities. Phase unwrapping applied to an interferogram is referred to as 2D unwrapping (Goldstein et al., 1988; Ghiglia and Pritt, 1998; Bamler et al., 1998; Eineder and Holzner, 1999; Chen, 2001). Stack processing of interferograms extends the concept to the temporal domain resulting in a 3D (2D space and 1D time) unwrapping operation (Hooper and Zebker, 2007; van Leijen et al., 2006).

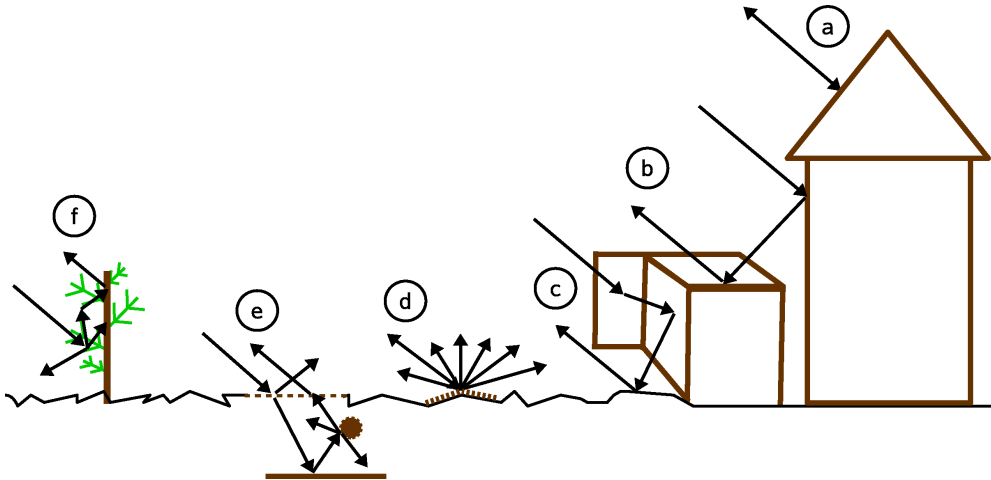


Figure 2.5: Radar targets and their backscattering processes. (a), (b) and (c) undergo specular reflection backscattering process from point targets with a single (monohedral), double (dihedral) and triple (trihedral) bounces, respectively. (d), (e), and (f) undergo a diffuse reflection from distributed targets at the surface, sub-surface, and in a volume, respectively.

Table 2.2: Typical radar targets types and their backscattering processes, refer to Fig. 2.5 for the cases from (a) to (f).

Case	Backscattering	Target type	Reflection type
(a)	Specular	Point	Single bounce
(b)	Specular	Point	Double bounce
(c)	Specular with specular	Point	Triple bounce
(c)	Specular with diffuse	Composite	Triple bounce
(d)	Diffuse at surface level	Distributed	Surface scattering
(e)	Diffuse with penetration into subsurface	Distributed	Volume scattering
(f)	Diffuse over a volume	Distributed	Volume scattering

2.6. Point and distributed targets

A radar scene is complicated as far as scattering is concerned. It contains a variety of geometric scales, ranging from much greater to much less than a wavelength in size. The largest scales are provided by the ground and buildings, while the smallest are provided

by the surface roughness of the buildings and the ground themselves. Based on the target dimension when compared to radar wavelength, the radar target types can vary between the two extremes of scattering (Huynen, 1970; Taket et al., 1991; Nasr and Vidal-Madjar, 1991):

2

- Point target

Radar targets, usually man-made objects, appearing smooth on the scale of wavelength of the incident radar signal are referred to as point-like or point targets (Maffett, 1965; Taket et al., 1991; Nasr and Vidal-Madjar, 1991; Dong and Ticehurst, 1997; Bamler and Hartl, 1998). The root mean squared height of the surface details is much smaller than the radar wavelength. Here, the radar signal exhibits a definite specular (mirror-like) reflection (as shown in (a), (b) and (c) in Fig. 2.5) when incident on such smooth surfaces.

- Distributed target

A vast majority of surfaces, synthetic or natural, appearing rough (or very rough) on the scale of the wavelength are referred to as distributed radar targets (Rice, 1951; Goodman, 1976; Kozma and Christensen, 1976; Madsen, 1986; Fung, 1994). The root mean squared height of the surface details is larger or comparable to the radar wavelength. In this case, the backscattered signal is a function of the surface characteristics, see (d), (e), and (f) in Fig. 2.5.

The radar signal undergoes a different backscattering process based on the type of target and surface properties from where the signal is reflected as tabulated in Tab. 2.2. Point targets reflect the radar signal depending on the angle of incidence of the radar signal. It can vary from a single, double, triple to multiple-bounce scenario. The cases of single and double bounce are shown in Fig. 2.5 (a) and (b). Since the reflectivity of dielectric surfaces (given by the Fresnel reflection coefficient) is always less than 1, the lower the number of reflections (bounces) the higher the backscattered power (Ruck, 1970; Dong and Ticehurst, 1997). Likewise, narrow reflections of dominant targets are stronger compared to wide-spread diffuse reflection (scattering) of distributed targets. In (c), the specular reflection from a smooth surface (in this case a building) may get reflected back to the radar either from a dominant target (smooth ground, as drawn in the figure) or a distributed target (rough ground-surface), and thereby it might exhibit a composite backscattering process. Cases (d)-(f) are due to diffuse scattering from distributed targets, see Fig. 2.5.

2.6.1. The effective phase center

The effective phase center is a virtual point given by the complex summation operation of signal contributions from many elementary scatterers along with one or more dominant scatterers within a resolution cell. The 2D (azimuth and range) position of a scatterer object within a resolution cell can be determined by oversampling the back-scattered response given in Eq. (2.4) and detecting the amplitude maximum. However, a resolution cell might comprise the back-scattered contributions from multiple scatterers, which can be

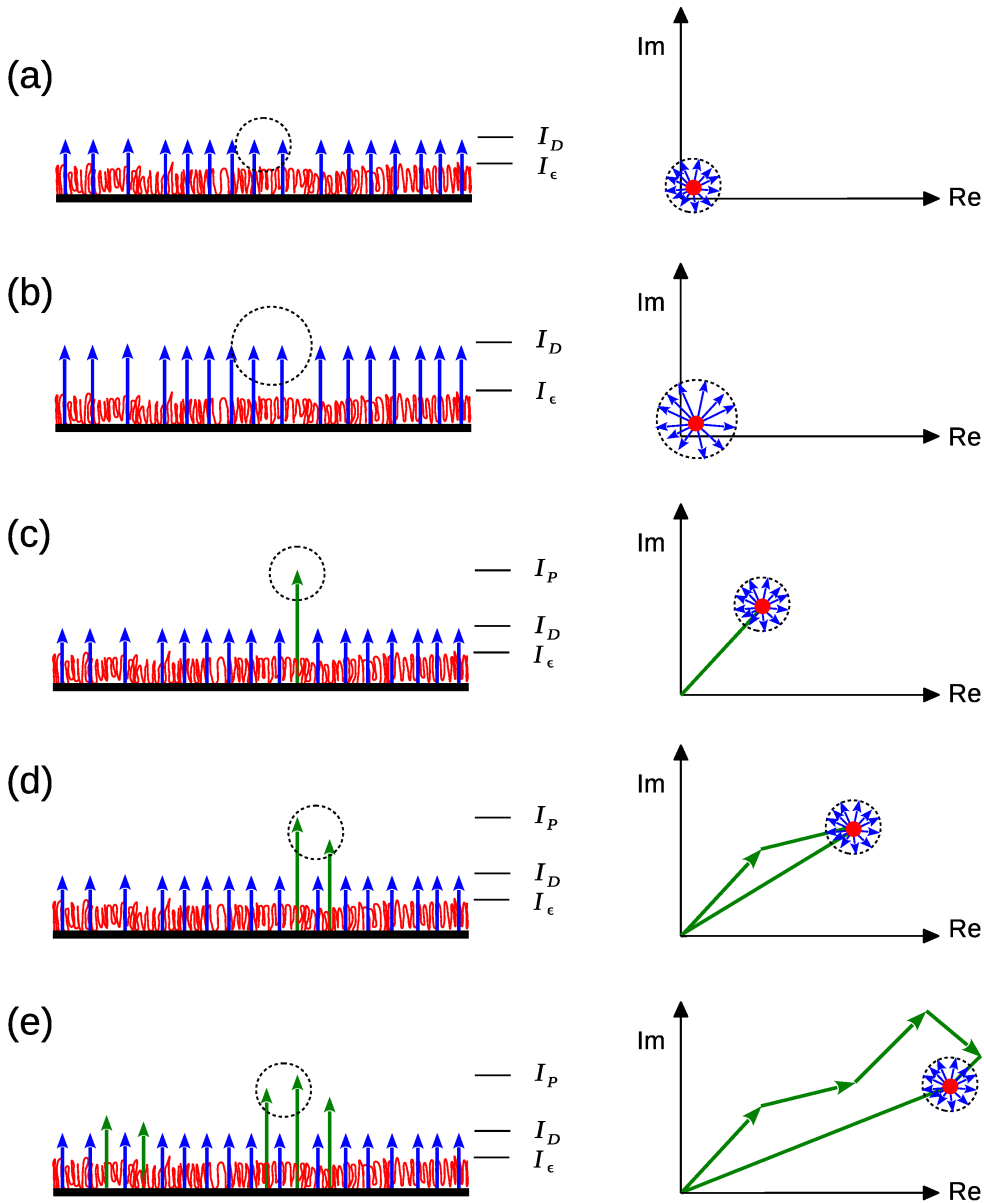


Figure 2.6: Representation of a SAR resolution cell (from side view) for different configurations, see (a) to (e). The second column is the corresponding representation in the real (Re) and imaginary (Im) planes, see Eqs. (2.30) and (2.31). The dotted circle represents the effective phase center of a resolution cell. ϵ represents the noise floor (in red), which is a combination of thermal noise, sensor oscillator phase jitter, and SAR processing noise sources. I_P , I_D , and I_ϵ represent the signal (in intensity or power units) contribution of the dominant targets (in green), distributed targets (in blue), and noise floor (in red), respectively. The dotted circle (in black) represents a region where the position of the effective phase-center could be located. The symbols such as dotted circle in the right-hand side are not strictly equivalent to the left-hand side, but they are used to exemplify the concept.

approximated as:

$$\begin{aligned}
 A \cdot e^{j\psi_{\text{scat}}} &= \underbrace{\sum_{i=0}^{N_P} a_i \cdot e^{j\psi_i}}_{\text{Point scatterers}} + \underbrace{\sum_{j=1}^{N_D} a_j \cdot e^{j\psi_j}}_{\text{Distributed scatterers}}, \\
 &= A_P \cdot e^{j\psi_P} + A_D \cdot e^{j\psi_D}, \\
 &\text{with } A, a_i \geq 0, \psi \in [-\pi, \pi), N \in \mathbb{Z}, a_i > a_j.
 \end{aligned} \tag{2.29}$$

The first term in Eq. (2.29), $A_P \cdot e^{(j\psi_P)} = \sum_{i=0}^{N_P} a_i \cdot e^{(j\psi_i)}$ is the effective contribution from one or more point scatterers (denoted with subscript P), where N_P (typically $N_P \leq 3$) is the number of point scatterers in a resolution cell. The circumference ($\pi \cdot d_s$) of these scatterers are much larger than the radar wavelength λ , where d_s is the diameter of a scatterer. Here, the radar signal exhibits a definite specular (mirror-like) reflection (as shown in (a), (b) and (c) in Fig. 2.5) when incident on such smooth surfaces, as a result a dominant scatterer's phase center does not change inherently and exhibits a relatively high RCS.

Table 2.3: Contribution of the targets types (point and distributed) in a resolution cell. N_P , and N_D are the number of point and distributed scatterers in a resolution cell.

N_P	N_D	pdf	SNR	Configuration	Position of effective phase-center	Time-series processing technique
0	++	Eq. (2.30) modifies to a χ^2 -distribution	$\frac{I_D}{I_\epsilon}$	Fig. 2.6 (a)	Center [‡] of multilooked resolution cell	DS with multilooking to improve SNR
0	++	Eq. (2.30)	$\frac{I_D}{I_\epsilon}$	Fig. 2.6 (b)	Center [‡] of original resolution cell	DS without multilooking
1	†	Eq. (2.31)	$\frac{I_P}{I_D + I_\epsilon}$ *	Fig. 2.6 (c)	At the dominant scatterer	PSI
2	†	Eq. (2.31)	$\frac{I_P}{I_D + I_\epsilon}$ *	Fig. 2.6 (d)	Vary between the two dominant scatterers	Tomography
$\gg 2$	†	Eq. (2.31)	$\frac{I_P}{I_D + I_\epsilon}$ *	Fig. 2.6 (e)	Vary across N_P dominant scatterers	Unable to extract information

++ very large contribution

† does not matter

‡ for a homogeneous DS resolution cell

* here, SNR is sometimes referred as SCNR (Signal to Clutter plus Noise Ratio)

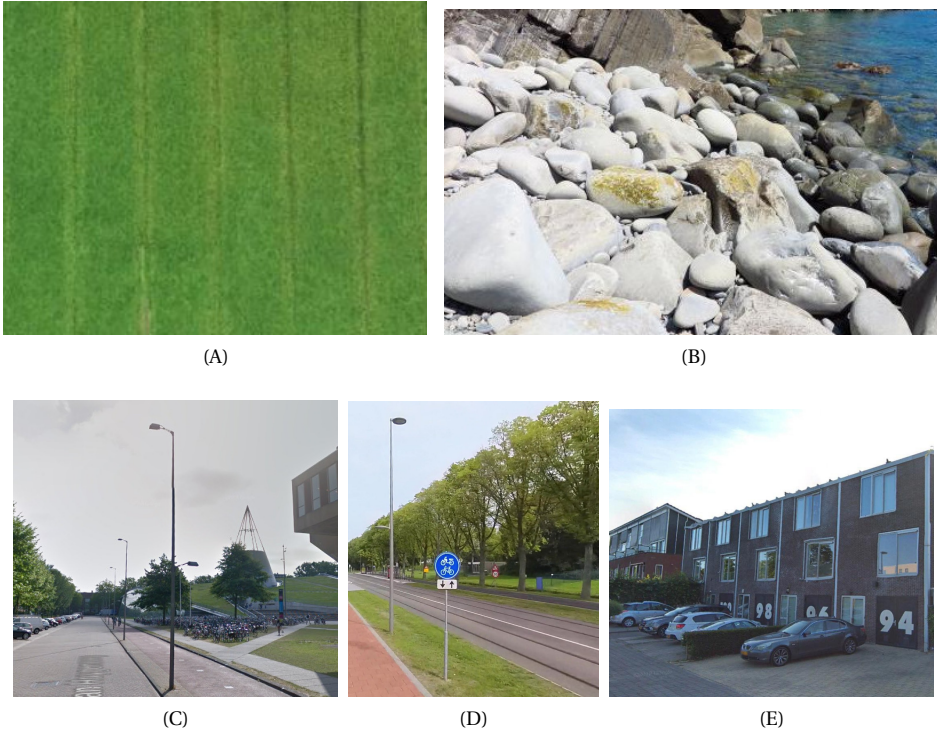


Figure 2.7: Examples of resolution cells shown in Fig. 2.6. (a) A distributed scatterer cell consisting of weak elementary scatterers from a grassy terrain (Fig. 2.6 (a)). (b) A distributed scatterer cell consisting of strong elementary scatterers (Fig. 2.6 (b)). (c) Single point scatterer cell with a lamppost in each resolution cell (Fig. 2.6 (c)). (d) Two point scatterer cell containing a lamp post and a pole (Fig. 2.6 (d)). (e) Multiple point scatterer cell (Fig. 2.6 (e)).

The second term in Eq. (2.29), $A_D \cdot e^{j\psi_D} = \sum_{j=1}^{N_D} a_j \cdot e^{j\psi_j}$ is the effective contribution of distributed scatterers (denoted with subscript D) usually referred as distributed scatterers, with N_D (typically $N_D \rightarrow \infty$) denoting the number of elementary distributed scatterers in a resolution cell. The circumference of these scatterers $\pi \cdot d_s$ are smaller or comparable to the radar wavelength λ , and exhibit low RCS due to their diffuse scattering phenomenon. In this case, the backscattered signal is a function of the surface characteristics (see (d), (e), and (f) in Fig. 2.5) and treated statistically. Such distributed scatterers in a resolution cell (see Fig. 2.6 (a) and (b)) are characterized by a pdf (Probability Density Function) :

$$\text{pdf}(A \cdot e^{j\psi_{\text{scat}}}) = \text{pdf}(A_D \cdot e^{j\psi_D}) = \text{pdf}(y) = \frac{1}{2\pi\sigma^2} \cdot e^{-\frac{(\text{Re}\{y\})^2 + \text{Im}\{y\}^2}{2\sigma^2}}$$

$$\text{with } \sigma^2 = \sigma_{\text{Re}\{y\}}^2 = \sigma_{\text{Im}\{y\}}^2 = \frac{E\{|y|^2\}}{2}, \quad (2.30)$$

where $y = A_D \cdot e^{j\psi_D}$ is a complex random variable, and $E\{\cdot\}$ is the expectation operator. The amplitude A_D is Rayleigh distributed, and phase ψ_D follows a uniform distribution. Under

Central limit theorem⁴, the pdf of a distributed scatterer resolution cell can be expressed by a zero-mean circular Gaussian distribution, see Eq. (2.30). The zero-mean refers to the real and imaginary components of y . For homogeneous areas, the circular Gaussian bi-variate pdf in Eq. (2.30) holds true (Dainty, 1975; Goodman, 1976; Tur et al., 1982; Madsen, 1986; Davenport and Root, 1987; Molesini et al., 1990; Just and Bamler, 1994; Bamler and Hartl, 1998; Argenti et al., 2013). For the case where the circular Gaussian assumption does not hold, the pdf is given by Ohtsubo and Asakura (1977); Tuthill et al. (1988); Goodman (2007). When the SNR from a single resolution cell is not sufficient, a multilooking operation is performed. For the case of multilooked resolution cells, the pdf in Eq. (2.30) is replaced by a chi-square (χ^2) distribution (Raney, 1998).

The pdf of a resolution cell in Eq. (2.30) is modified to include the point scatterers:

$$\text{pdf}(A \cdot e^{j\psi_{\text{scat}}}) = A_P \cdot e^{j\psi_P} + \frac{1}{2\pi\sigma^2} \cdot e^{-\frac{(A_D \cos(\psi_D))^2 + (A_D \sin(\psi_D))^2}{2\sigma^2}}, \quad (2.31)$$

where A_P and ψ_P represent the cumulative contribution of point scatterers. The inclusion of point scatterers shifts the pdf in Eq. (2.30) by an amplitude A_P and phase ψ_P to yield Eq. (2.31), see illustration in Fig. 2.6 (c) to (e). When a resolution cell contains point scatterers, the contribution of speckle (I_D) is also considered as a noise source. In these cases, the term SNR is used interchangeably with the SCNR, as indicated in Tab. 2.3.

Eq. (2.31) enables an explanation of different types of SAR resolution cells in a single expression. See Tab. 2.3 and Fig. 2.6 for the types of resolution cells and their processing characteristics. The PS technique to process the InSAR stack varies based on the number of dominant point scatterers (N_P) in a resolution cell and their overall SNR. It should be noted, when N_P is very large, then the resolution cell exhibits distributed scatterer properties. For high SNR distributed scatterers spatial averaging is not necessary, while for the low SNR case spatial averaging is mandatory. Fig. 2.7 (a) to (e) shows real-world examples of the resolution cells described in Fig. 2.6.

2.6.2. Time-series processing

In order to combat atmosphere, scattering changes, and other noise sources, and to precisely estimate deformation and topography, a time-series of interferograms from the same scene is exploited. The feasibility of deformation and topography estimation and the choice of a time-series processing technique depends on the resolution cell type as listed in Tab. 2.3.

There are four main classes of processing techniques.

- First is distributed scatterer processing techniques, here $\phi_{\Delta\text{scat}} \neq 0$ in Eq. (2.7). DS-based processing techniques use a small baselines multi-master configuration known as small baseline subsets (SBAS) to reduce decorrelation effects (Berardino et al., 2002; Schmidt and Bürgmann, 2003; Mora et al., 2003; Berardino et al., 2004; Pepe et al., 2015). In DS processing, to achieve sufficient SNR, usually pixels are spatially averaged using a predefined window or by adaptively selecting a neighborhood polygon (Ferretti et al., 2011; Parizzi and Brcic, 2011; Jiang et al., 2015; Lee, 1983). The DS-based techniques are applied over regions containing natural terrain.

⁴A pdf of the summation of n independent random variables approaches a normal distribution when n is very large ($n \rightarrow \infty$), even if the original random variables themselves are not normally distributed.

- The second class of processing techniques collectively referred as PSI (see sec. 2.7) is devoted to single PS resolution cells. These techniques exploit dominant PSs and use single-master interferogram configuration. PSI was first introduced by Ferretti et al. (2001). PSs are usually, but not necessarily always, strong reflectors and remain coherent over longer temporal and larger spatial baselines. As a result, the decorrelation effects are negligible, and hence the scattering contribution in Eq. (2.7) is given by $\phi_{\Delta\text{scat}} \approx 0$ (Kampes, 2005). The PS-based techniques are applied for areas containing man-made objects.
- The tomographic processing methodology is used to identify and separate scatterer contributions for the resolution cells containing multiple dominant point scatterers (Reigber and Moreira, 2000; Fornaro and Serafino, 2006; Lombardini, 2005; Zhu and Bamler, 2010; Tebaldini, 2010).
- The fourth class of techniques called as hybrid technique is developed to process both PS and DS together, such as modified small baselines, multi-temporal PS with small baselines, and Squee-SAR approach (Hooper et al., 2004; Guarnieri and Tebaldini, 2008; Ferretti et al., 2011; Lanari et al., 2004).

A detailed review of various time-series InSAR techniques can be found in Crosetto et al. (2016); Samiei Esfahany (2017); Ansari (2019). In principle, the positioning capability and interpretation of deformation required the position of effective phase-center for a given type of resolution cell (see Tab. 2.3 and Fig. 2.6).

2.7. Persistent Scatterer Interferometry

Since the identification of long-time phase-coherent pixels (Usai and Hanssen, 1997; Usai and Klees, 1999; Ferretti et al., 1999), PSI was introduced to extract information from a set of scatterers subject to negligible geometrical and temporal decorrelation called persistent scatterers (PS) (Ferretti et al., 2001; Kampes, 2005). This technique is developed for a single dominant scatterer resolution cell, *i.e.*, $N_p = 1$ in Eq. (2.31). Here, the effective phase-center typically represents one (dominant) point scatterer as shown in Fig. 2.6 (c).

In the following the generic processing steps followed by the DePSI (Delft's implementation of PSI) software implementation is described as follows (Kampes, 2005; van Leijen, 2014), see Fig. 2.8:

• Single master interferogram generation

Given a stack of N SLC images, a single image is selected as master (m) such that the expected overall stack coherence (γ^m) is maximum. The expected stack coherence for a master image m is defined by (Kampes, 2005),

$$\gamma^m = \frac{1}{N-1} \sum_{s=1}^{N-1} f(B_{\perp}^s, B_{\perp}^c) \cdot f(B_T^s, B_T^c) \cdot f(B_{DC}^s, B_{DC}^c),$$

$$\text{given } f(x, c) = \begin{cases} 1 - \frac{|x|}{c} & \forall |x| < c \\ 0 & \text{otherwise,} \end{cases} \quad (2.32)$$

where B_{\perp}^s , B_T^s , and B_{DC}^s are the perpendicular baseline, temporal baseline, Doppler baseline between master m and slave s image, respectively. The respective critical

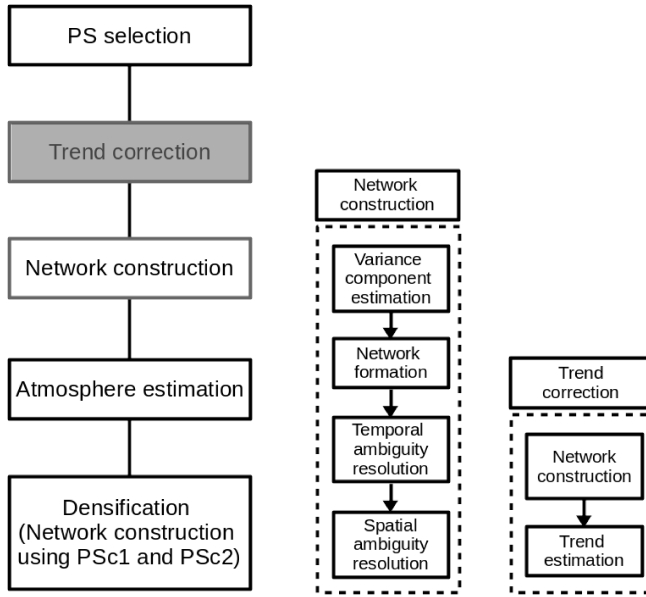


Figure 2.8: Processing modules of DePSI (left). Optional steps are in gray. The network construction module consists of four sub-tasks (center). The trend estimation module has two sub-tasks (right).

baselines are B_{\perp}^c , B_T^c , and B_{DC}^c , values larger than critical baselines are expected to cause a complete decorrelation for DS in the interferograms. Once the master image is selected, all slave images are resampled, and coregistered to the master grid. Subsequently, interferograms are generated and flat earth and topography phase subtraction steps are carried out. The interferogram generation procedure is performed using Doris as described in sec. 2.5.

• PS selection

PS selection step selects a set of pixels which are expected to remain phase coherent over the entire time-series. These selected PS candidates (PSc) are highly suited for processing and can provide reliable deformation and topography estimates. Since the interferometric phase is wrapped, the PS candidates are first selected based on the temporal amplitude stability of pixels. For this purpose, Ferretti et al. (2001) introduced the normalized amplitude dispersion index (D_A) as an approximation of the expected phase precision (σ_{ϕ}), given by,

$$\sigma_{\phi} \approx \tan(\phi) \approx \frac{\sigma_A}{\mu_A} = D_A, \quad (2.33)$$

where μ_A , and σ_A are the mean and standard deviation of the pixel amplitude over time. Here, the noise is expected to follow a circular Gaussian distribution. By applying thresholds on D_A , PS candidates are selected in this study. Alternatively, different PS selection criteria such as the SCR, and spatial phase stability are also used (Hooper et al., 2004; Adam et al., 2004). In order to reduce computational complexity, an iterative implementation is performed where PSc are selected in two

levels: coarsely sampled first order (PSc1) selected with a stringent threshold (usually $D_A = 0.25$ is used) and a finely sampled second order (PSc2) selected with a relaxed threshold (e.g. $D_A = 0.4$).

- **Trend correction**

This is an optional step performed to estimate a two-dimensional trend per interferogram. This trend mainly accounts for a low frequency signal in the interferograms due to orbit errors. The estimated orbital phase trend is then subtracted per interferogram.

- **Network construction**

Once the PSc are selected, a reference network based on PSc is established in order to estimate orbital and atmospheric phase screen, and perform a densification of the PSs. Network construction consists of 4 steps. 1) Estimate the precision of the double-difference phase observations using Variance Component Estimation (VCE). The single-difference phase observations are the phase differences obtained either in time or space. The double-difference phase observations are the differences obtained in time and space. 2) Based on the selected PSc, using PSc1 a (Delaunay or spider) network is created to form a grid of arcs. An arc is an interconnection between two PS points resulting in their phase difference. 3) Using PSc1 candidates, the arcs are first unwrapped in time and then 4) unwrapped (integrated) in space.

- **Atmosphere estimation**

During 3D unwrapping (1D in time and 2D in space), deformation, topography, atmosphere components are separated. The estimated atmosphere signal called as Atmospheric Phase Screen (APS) is interpolated to a wider grid using PSc2 points and subtracted from the wrapped time-series.

- **PS densification**

Now, a larger network is constructed using both PSc1 and PSc2 points, and they are unwrapped in time and space using an assumed temporal deformation model. A final selection of PS is determined based on the unwrapped phase quality. The most common selection criterion is the ensemble coherence γ_{ens} , defined as,

$$\hat{\gamma}_{\text{ens}} = \frac{1}{N-1} \left| \sum_{k=1}^{N-1} e^{j(\hat{\phi}_k - \phi_i^{\text{model}})} \right|, \quad (2.34)$$

where $\hat{\phi}_k$ and ϕ_i^{model} are the unwrapped phase and model based phase time-series, respectively. The number of single-master interferograms is denoted by $N - 1$.

As a result, PSI provides deformation time-series, deformation rates, atmosphere time-series, and relative topography of each PS as its output relative to a reference point and reference epoch. Further details about the individual processing stages can be found in Kampes and Hanssen (2004b); Kampes (2005); van Leijen (2014).

2.8. Encoding and decoding SAR measurements

Due to the slant-looking imaging of the SAR system, a resolution cell is a 3D voxel containing a complex mixture of one to many reflecting objects and their distinct signals coherently

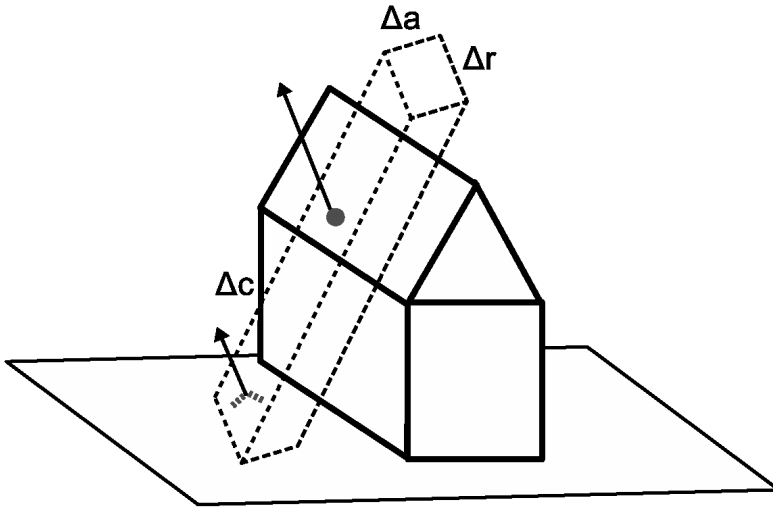


Figure 2.9: SAR imaging is an encoding process: translating physical properties of the illuminated area to a complex radar observation. A SAR resolution voxel is defined by a resolution in range (Δr), azimuth (Δa), and cross-range (Δc). The voxel here encodes information (geometry and scattering properties) of two targets: a point scatterer with a strong reflection from a roof and a weak distributed scatterer from the ground.

summed in a single radar measurement, see the illustration in Fig. 2.9. Such packing of object information into a voxel we conceptually refer to as *encoding*: the translation of physical properties of the illuminated area into the complex radar observation of a focused SAR image. The object information includes position, back-scattering properties and their variations when SAR images are acquired over time. If the objects and their information per voxel would be known *a priori* it would be less cumbersome to interpret the SAR observation. However, in reality, such a high level of detail is not known, hence SAR observations are interpreted after the measurement process. Once coherent scatterers are detected, a set of SAR images can be processed using PSI to estimate their position and deformation per voxel. Here, the main challenge is to identify an object within the SAR resolution voxel which is responsible for the coherent reflection, and to interpret the estimated relative deformation. We refer to this step as *decoding*.

On the other hand, for the resolution voxels in which there are no significant coherent scatterers available, it is possible to artificially encode radar scatterers of a specific geometry and back-scattering characteristics, to produce a new coherent measurement. Artificial encoding can also be considered as a step to selectively add or hide a specific point of interest on the ground. An artificial target can be an active transponder or a passive reflector. Passive reflectors are cheap, have fixed back-scattering characteristics and they do not require additional power. On the other hand, transponders require a power source but they are compact and able to manipulate their back-scattering properties. In summary, decoding and encoding can be considered as steps to understand (the existing) and facilitate (new) InSAR measurements, respectively.

A series of studies has laid the basic foundation in the understanding of radar target types, and their scattering behavior for multi-frequency and multi-polarization radar

signals (Feinberg, 1944; Rice, 1951; Huynen, 1970; Van Zyl, 1986; Zebker et al., 1987; Evans et al., 1988). Polarimetric data are adding information related to the scattering mechanism in performing classification compared to single-pol radar images (Ulaby and Elachi, 1990). Most of these studies, aimed at scene classification by separating types of land cover.

In the 1990's, individual objects became recognizable due to high spatial resolution (~ 1 m) of airborne SAR imagery. Owing to this improvement in resolution, the focus of the image interpretation shifted from radiometric to geometric properties of objects and identifying key urban targets (Soergel et al., 2004). Three dominant specular reflection scenarios are studied by Dong and Ticehurst (1997): single, double and triple bounce reflections from a building roof, building-ground and building-ground-building, respectively. These same three dominant scattering scenarios were examined further by deriving a closed-form solution but now by including the distributed nature of the ground surface, building orientation angle and building structures with non-perfectly conducting material (Franceschetti et al., 2002). The electromagnetic scattering is found to be only sensitive to the building orientation when terrain roughness is small and the incidence angle is greater than about 30° (Franceschetti et al., 2002).

The applications of using radar for infrastructure monitoring have also emerged, predominantly exploiting the amplitude measurements from multi-view SAR acquisitions. For example, the use of SAR images to detect changes related to urban infrastructural damage with particular emphasis on changes caused by destructive earthquakes was studied by Shinozuka et al. (2000) and Matsuoka and Yamazaki (2004). For urban areas not impacted by occlusion and layover, reconstruction of buildings using SAR/InSAR data is studied by Soergel et al. (2003) and Stilla et al. (2003b). Perceptual grouping of point scatterers is shown useful in detecting regular structures of man-made objects (Stilla et al., 2003a). The perceptual grouping is a concept developed by a group of psychology researchers to describe the tendency of human vision to group objects based on their similarity, proximity, symmetry, closure, and continuity (Wertheimer, 1938). This concept is used in computer vision to solve problems such as object segmentation and search optimization during grouping. Grouping using contextual information is computationally efficient, since it can constraint the possible locations and orientations, see Stilla et al. (2003a). Here, *e.g.*, the contours of the building cues are used as context information to group PSs. Using layover and shadow boundaries, a reconstruction of simple building structures is shown by Bolter (2000). By applying a modified machine vision approach to InSAR measurements, the 3D structure of large buildings is detected and reconstructed by Gamba et al. (2000). Using polarimetric and interferometric SAR data from an airborne campaign, a method based on the unsupervised Wishart H-A- α classification and Estimation of Signal Parameters via Rotational Invariance Techniques (ESPRIT) is presented by Guillaso et al. (2005) to identify buildings and estimate their height. A data clustering approach based road network identification is presented for the characterization of streets with different width and shape (Dell'Acqua and Gamba, 2001; Dell'Acqua et al., 2003). Using medium resolution ERS images, building densities estimation is shown possible by Dell'Acqua and Gamba (2003).

In our approach, we perform encoding and decoding steps to address different research interests, see a pictorial representation in Fig.2.10. Based on the intent to associate coherent scatterers at an object level or a point level, the decoding approach can be discriminated. The object-level association is useful and sufficient to link PSs to infrastructure as a whole and under-ground infrastructure. The point-level association is beneficial towards

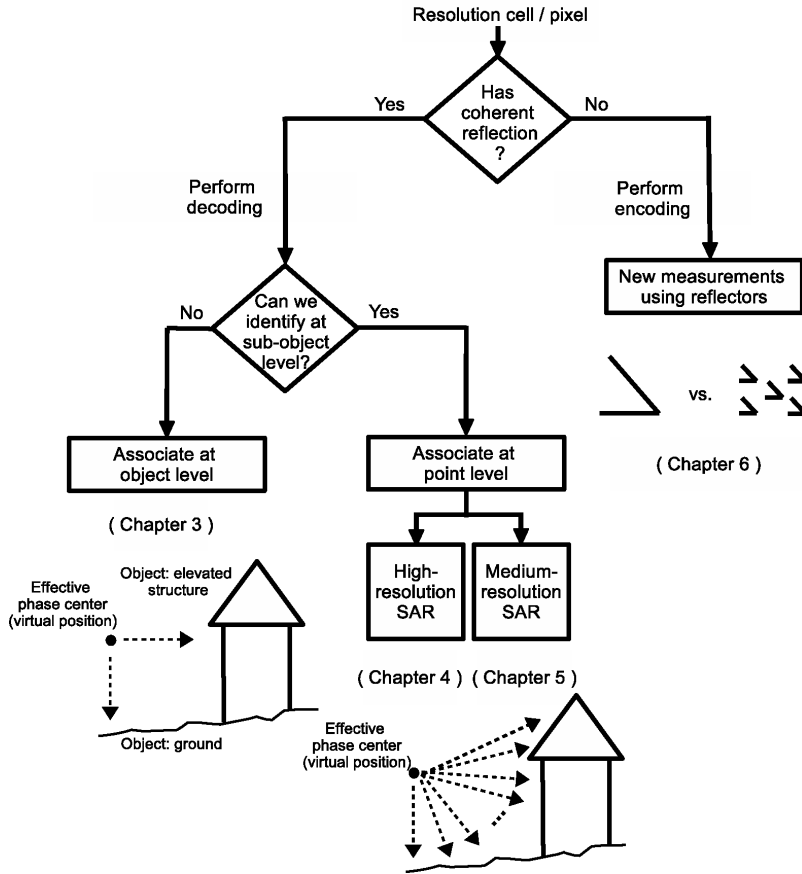


Figure 2.10: An overview of this study addressing different research aspects are described using the decoding and encoding steps in chapters. 3–6. A sub-object level target association links PSs to parts of an elevated infrastructure.

linking PSs to specific parts of an elevated infrastructure. Further, the performance of the point-level approach requires investigation based on the resolution of the SAR imagery. On the absence of coherent reflection at a pixel location, we develop a method to introduce new measurements using artificial radar reflectors.

2.9. Summary

In this chapter, we reviewed the basic concepts of SAR, InSAR, and PSI. We presented a generic framework consisting of point and distributed scattering in understanding the SAR resolution cells and their processing approaches. In the following, we will focus on the resolution cells where the effective phase-center typically represents one (dominant) point scatterer, see Fig. 2.6 (c). In the following chapter, InSAR measurements are decoded to obtain target classification and deformation interpretation, with a case study devoted to gas pipe-network monitoring application.

3

Target classification and deformation interpretation applied to infrastructure monitoring

This chapter starts with a review of a set of opportunities to classify radar scatterers (sec. 3.1). These different opportunities are studied and a methodology is developed for infrastructure monitoring using persistent scatterers. The proposed methodology has two key steps: target classification (sec. 3.3) and deformation classification (sec. 3.4); and is validated with simulated and real data (secs. 3.3.2 and 3.4.3). A case study over Amsterdam, the Netherlands to monitor underground infrastructure to assess stress on the gas pipe networks demonstrates the efficacy of the proposed method (sec. 3.5).

3.1. Introduction

InSAR provides regular measurements via a cloud of millions of data points across a given area. However, it is necessary to identify the origin of each single radar scatterers to understand the usability of these measurements. In this chapter, we enhance our understanding of the radar point cloud measurements through a classification procedure. Here, the main challenges are (i) to understand where the radar reflections stem from, not only from which object, but also from which location on the object, and (ii) to understand displacement signal relative to other objects. We propose to solve these challenges in two phases: (i) target classification - associating radar reflections to real-world objects (Perissin, 2006), and (ii) deformation classification - comparing and/or grouping deformation from different real-world objects to further characterize the estimated deformation signal. The point cloud data comes in from radar scatterers which remain coherent (stable signal to noise ratio) over a period of time. Such coherent scatterers, or PS (Persistent Scatterers), are

Parts of this chapter have been published in the proceedings of the 5th International Workshop on Science and Applications of SAR Polarimetry and Polarimetric Interferometry (POLInSAR), Frascati, Italy, 2011 (Dheenathayalan and Hanssen, 2011), the proceedings of the 8th International Workshop on Advances in the Science and Applications of SAR Interferometry (FRINGE), Frascati, Italy, 2011 (Dheenathayalan et al., 2011), and the proceedings of the IEEE International Geoscience and Remote Sensing Symposium (IGARS), Melbourne, Australia, 2013 (Dheenathayalan and Hanssen, 2013).

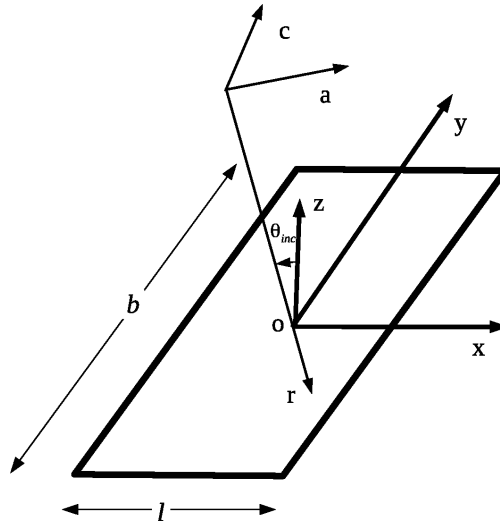


Figure 3.1: Rectangular flat plate of dimension $l \times b$ with radar angle of incidence θ_{inc} . a , r , and c are the azimuth, slant-range and cross-range directions, respectively. z is the normal to the plate plane surface defined by x and y .

detected using a set of SLC SAR images and processed to estimate relative displacement and height per radar scatterer (Ferretti et al., 2001; Kampes and Hanssen, 2004a). We therefore implicitly assume that: 1) there is only one dominant radar scatterer in a resolution voxel, and 2) the target classification for distributed scatterers can be ignored.

In general, there are 4 sources of information to characterize a radar target from the radar data:

- multi-angle amplitude observation - provides target dimensions,
- multi-temporal amplitude observations - provide target integrity,
- polarimetric phase data - provides scattering properties of the target, and
- interferometric phase - provides height and line-of-sight displacement estimates of the target.

Multi-angle amplitude observation The RCS (Radar Cross-Section) of a dielectric flat rectangular plate can be given based on the physical optics approximation (Ruck, 1970; Colwell et al., 1983; Dong and Ticehurst, 1997):

$$RCS_{pp} = \frac{4\pi}{\lambda^2} \cdot R_p^2 \cdot l^2 \cdot b^2 \cdot \cos^2(\theta_{inc}) \cdot |\text{sinc}(2\pi/\lambda \cdot l \cdot \sin(\theta_{inc}))|^2 \quad \forall L_a, L_c \gg \lambda \quad (3.1)$$

where λ is the radar wavelength, the subscript p stands for polarization, R_p is the Fresnel reflection coefficient for a given polarization p (Ruck, 1970), and θ_{inc} is the incidence angle. The length and breadth of the rectangular plate are given by l and b , respectively, see Fig. 3.1. From Fig. 3.1, when a target is imaged from viewing geometries varying in Doppler and perpendicular baseline directions, then the respective dimensions of the radar target

in azimuth and cross-range can be estimated. This method of target size estimation is performed for medium-resolution SAR sensors such as ERS and ENVISAT (Perissin and Ferretti, 2007). Now, considering only the scatterers which prevail the whole data-set period *i.e.*, partially coherent PS are not selected. Under these conditions the scattering amplitude response of the extended radar target in a low-clutter environment from Perissin and Ferretti (2007) can be simplified to:

$$A_i^{\text{model}}(\Delta\theta_i, \Delta\vartheta_i, \Delta T_i) \approx \text{RCS}_{\text{max}} \cdot \left| \text{sinc}\left(\frac{2}{\lambda}L_c(\theta_p - \Delta\theta_i)\right) \cdot \text{sinc}\left(\frac{2}{\lambda}L_a(\vartheta_p - \Delta\vartheta_i)\right) \right| \cdot (1 - \kappa_T \cdot \Delta T_i) \quad \forall L_a, L_c \gg \lambda, \quad (3.2)$$

where A_i^{model} is the modeled backscattered amplitude response for acquisition i , RCS_{max} is the maximum Radar Cross Section (RCS) in amplitude units (not intensity) for the given radar of wavelength λ , and L_c and L_a are the effective target dimensions obtained by projecting l and b in Fig. 3.1 in cross-range and azimuth, respectively. The location of maxima of the cardinal sines θ_p and ϑ_p depends on the target orientation with respect to the radar. A difference in temperature of acquisition i relative to the master image is given by ΔT_i and κ_T represents the amplitude temperature coefficient. The first cardinal sine term modulates the impulse response amplitude based on the changes in normal baseline (expressed by $\Delta\theta$) and the second cardinal sine term accounts for the variation in Doppler Centroid (expressed by $\Delta\vartheta_i$). For small variations in look angle relative to the nominal orbit, the cross-track angle can be found from the normal baseline $B_{\perp,i}$ and the sensor-to-target distance at the master acquisition R_m :

$$\Delta\theta_i = \frac{B_{\perp,i}}{R_m}. \quad (3.3)$$

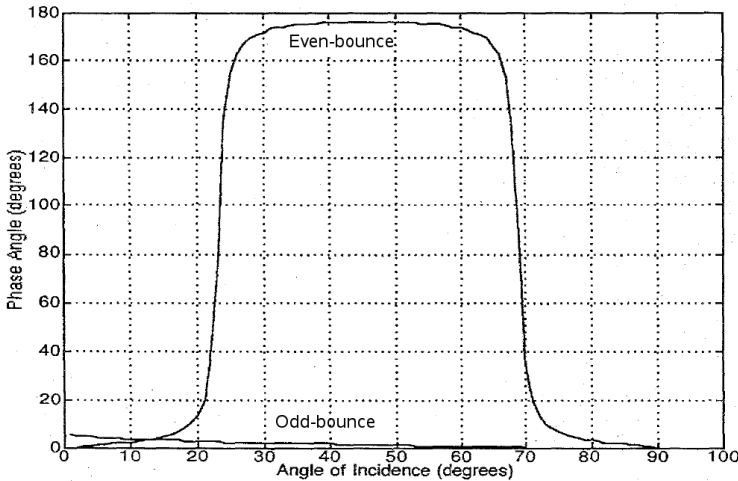


Figure 3.2: The phase angle between HH and VV polarization channels ($\phi_{\text{HH-VV}}$) as a function of incidence angle (θ_{inc}) for odd and even bounce mechanisms after Cloude and Pottier (1996).

The squint(along-track) angle $\Delta\vartheta_i$ is given by

$$\Delta\vartheta_i = \frac{\lambda}{2\delta_a \text{PRF}} \Delta f_{DC,i}, \quad (3.4)$$

where δ_a is the azimuth sampling interval, PRF is the pulse repetition frequency, and $\Delta f_{DC,i}$ is the DC (Doppler Centroid) frequency difference of image i relative to zero-Doppler direction. By solving the non-linear system given in Eq. (3.2), the rough target dimensions can be estimated.

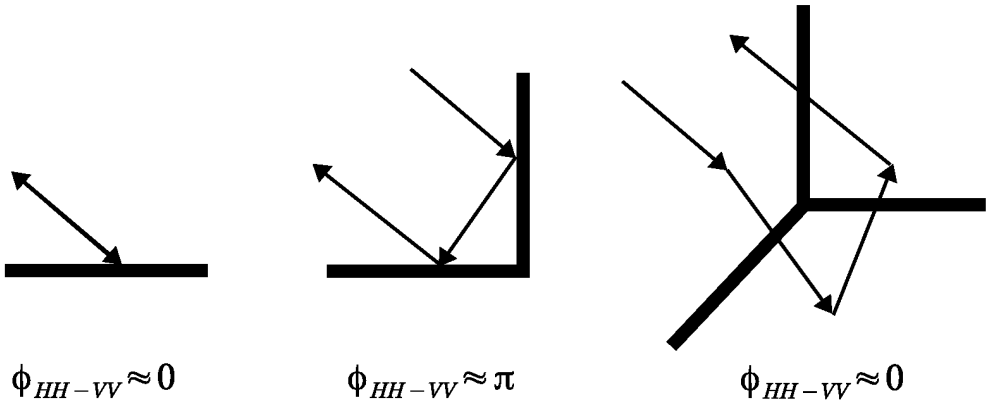


Figure 3.3: Impact of backscattering mechanism on differential polarization phase. An even number of bounces leads to a phase shift of π radians in the difference between HH and VV.

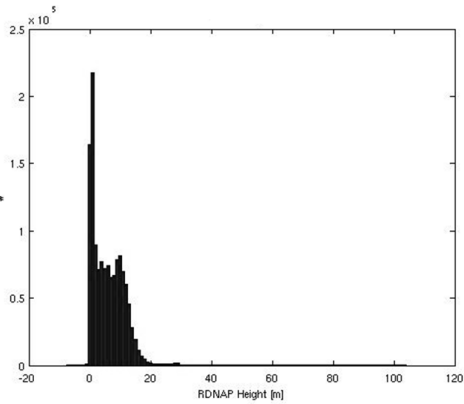
Polarimetry Multi-polarization SAR data can be decomposed to understand the scattering properties of the radar target (Cloude and Pottier, 1996). For a wide range of incidence angles (see Fig. 3.2), the phase angle between HH and VV polarization channels is approximately equal to 0 and π for odd and even number of bounces, respectively (Van Zyl, 1989; Hoekman and Quiñones, 1998; Inglada et al., 2004). However, for steep ($\theta_{\text{inc}} < 15^\circ$) and very large incidence angles ($\theta_{\text{inc}} > 75^\circ$), the exact angles depends on the Brewster angle¹ of the dielectric materials of the reflecting surfaces, the separability is limited, see Fig. 3.2. Using the two orthogonal co-polarization channels as shown in Fig. 3.3, the odd and even bounce scattering mechanisms can be separated.

¹Brewster angle is an angle of incidence at which light with a particular polarization is fully transmitted through a dielectric surface without any reflection.

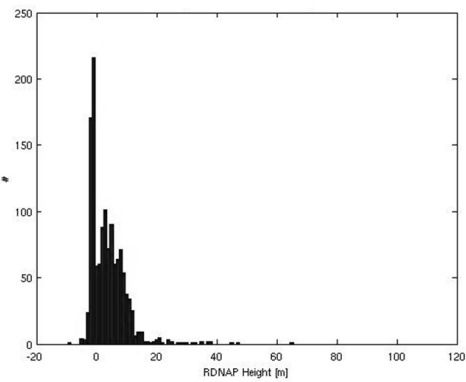


(A) Ascending

(B) Descending



(C)



(D)

Figure 3.4: Comparison of TSX PS height separation with AHN2 (Actueel Hoogtebestand Nederland), see Rijkswaterstaat-AGI (1996); van der Sande et al. (2010). Red points: radar reflections with height ≥ 3 m, white dots: radar reflections with height ≤ 3 m and background AHN2 (red region ≥ 3 m, (clipped) white region ≤ 3 m). Red points and white dots of radar mostly match with the red and white regions of lidar respectively. (A) PS from TSX ascending track over Delft. (B) PS from TSX descending track over Delft. We used the TSX ascending and descending tracks covering an area of about 49 km^2 and only the Delft city centre region is shown in (A) and (B). (C) Height distribution of AHN2 points. (D) Height distribution of PSs from TSX descending orbit. There are about 60% of points from the AHN2 (C) above 3 m (RDNAP height) when compared to $\sim 48\%$ from TSX descending track (D). The height estimated from InSAR is comparable to lidar and can be used to discriminate radar reflections from above and below the ground level.

Interferometry The final source of information of a radar target comes from the interferometric phase. Interferometric phase measurements are processed using the PSI technique to extract the relative displacement and position (height) information of time-coherent radar targets. By looking in ascending and descending viewing geometries, the PS spatial sampling of an urban area is different (see Fig. 3.4) since they sample different sides of urban infrastructure. The scatterer height is a vital parameter to characterize radar targets. For example, a separation of PS heights (after correcting for 3D offsets using tie-points) is shown in Fig. 3.4, where the PS heights above-and-below the 3 m level are compared with AHN (Actueel Hoogtebestand Nederland) for both the ascending ($\theta_{\text{inc}} = 39.3^\circ$) and the descending ($\theta_{\text{inc}} = 24^\circ$) track. It can be noted that the PS height separation is similar to the one obtained from the lidar dataset (AHN) (Rijkswaterstaat-AGI, 1996)), as the white dots from radar mostly lie over the white region and similarly red points over the red region of the lidar dataset. Comparing Figs. 3.4C and 3.4D, there are about 60% of points from the AHN2 above 3 m (RDNAP height) when compared to $\sim 48\%$ from the TSX descending track.

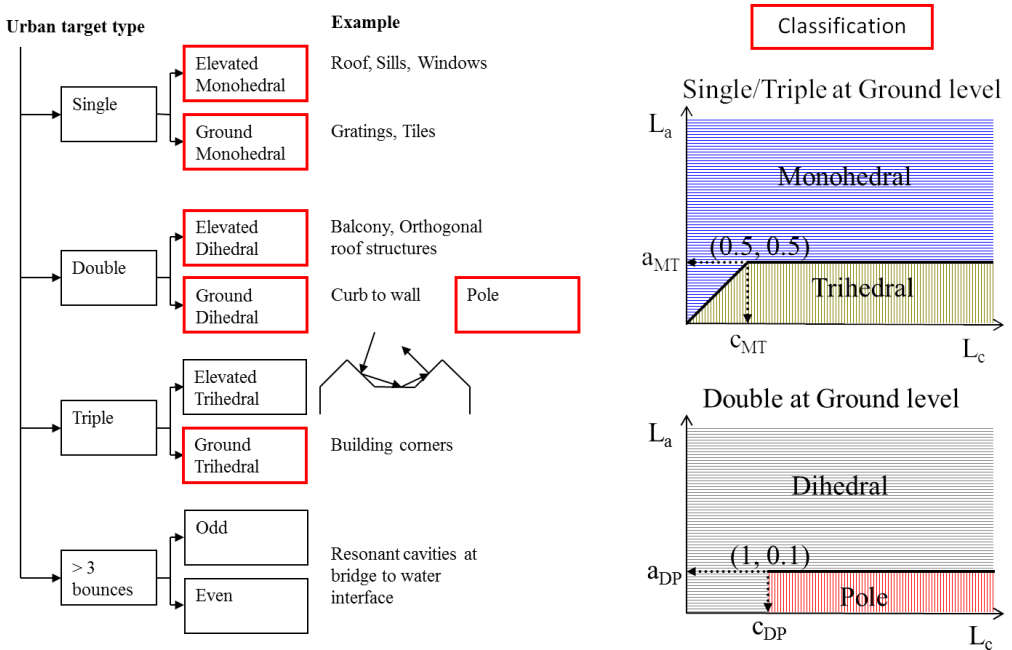


Figure 3.5: (Left) Taxonomy of urban target types. Target types identified are highlighted in red. (Right) Thresholds used for target classification using the scatterer extent estimated from amplitude scattering data. Threshold for monohedral and trihedral discrimination in azimuth and cross-range are a_{MT} , and c_{MT} respectively. Similar thresholds for dihedral and pole target discrimination are given by a_{DP} and c_{DP} .

3.2. Taxonomy of urban targets

We combined the parameters obtained from amplitude data, PS processing and polarization data to derive a taxonomy of target types. Fig. 3.5 illustrates a taxonomy of dominant target types seen in an urban environment. Based on the number of reflections (bounces)

we group targets into single bounce (called as monohedral), double bounce (dihedral), triple bounce (trihedral) and multi-bounce (when the number of bounces is greater than three). Using the height of the scatterers, we classified targets into ground level (height < 3 m) and elevated (height ≥ 3 m) types.

A scatterer with an odd number of bounces at ground level can be monohedral or trihedral. The trihedrals provide a flat amplitude response for a wide range of angles in cross-range and azimuth. As a result, we expect a negligible cross-range and azimuth extension for the trihedrals. This property is used to differentiate between monohedrals and trihedrals. In our analysis, trihedrals such as wall-ground-wall reflections are detected with a negligible effective extension in azimuth ($L_a < 0.5$ m), and a non-negligible extension in cross-range ($L_c > 0.5$ m). We hypothesize that this is due to the sensitivity of trihedral targets in the cross-range direction. Then the scatterers with an even number of bounces at ground level such as dihedral, and pole are differentiated. The poles exhibit barely a small extension in azimuth ($L_a < 0.1$ m) compared to cross-range ($L_c > 1$ m) while the dihedrals such as wall-ground reflections show a large extension in azimuth compared to poles. Identical classification strategy is applied for scatterers which are elevated. Here, the target type classification is restricted to the following six groups highlighted in red in Fig. 3.5 (Left): Ground Monohedral, Elevated Monohedral, Ground Dihedral, Elevated Dihedral, Dihedral Pole and Ground Trihedral. In the next section, we compare the information sources and propose a classification method based on the most important and available information.

Selection of information for classification

Various types of information such as (i) relative height estimated from PSI, (ii) size of scatterer estimated from the amplitude variation over various incidence and squint angles, and (iii) scattering type estimated from polarimetric information are found to be useful to perform target classification (Perissin and Ferretti, 2007). However, due to the limited variation in the baseline distribution (orbital tube) from ERS-1/2, ENVISAT, TerraSAR-X to Sentinel-1, target size estimation is difficult. In addition, the multi-polarization data (HH and VV channels) are not available everywhere and at all times, this can further limit the use of scattering type estimations in the classification process. Therefore, in order to identify the most important information source, different methods such as: (i) height; (ii) height, and amplitude; and (iii) height, amplitude, and polarization are proposed for target classification and deformation interpretation. Using these methods each PS is associated to a specific radar target type and then the estimated deformation in urban areas is interpreted.

A case study region with known deformation phenomena such as Diemen, the Netherlands is selected and the deformation interpretation from each of the methods are compared. In order to relatively compare the methods and to find the influence of information used, the method which used all the available information (method (iii)) is considered as reference method. Therefore, the interpretation obtained from method (i) and method (ii) are compared piece-wise with method III. The height based interpretation (method (i)) exhibits 89% agreement with height, amplitude and polarization based interpretation (method (iii)), while height with amplitude information (method (ii)) yields 91% agreement. The height with amplitude (method (ii)) performs only marginally better than interpretation only with height (method (i)). Therefore, for urban deformation scenarios, we found the height information to play a significant role in the deformation interpretation compared

to amplitude and/or polarization information.

3.3. Methodology

Given the importance and availability of data (see sec. 3.2), here only the height information is exploited in our method to address the main challenge of associating a PS to an actual target type. Once a target is classified then deformation type classification or interpretation is performed to understand in detail the underlying deformation phenomena, see sec. 3.4.

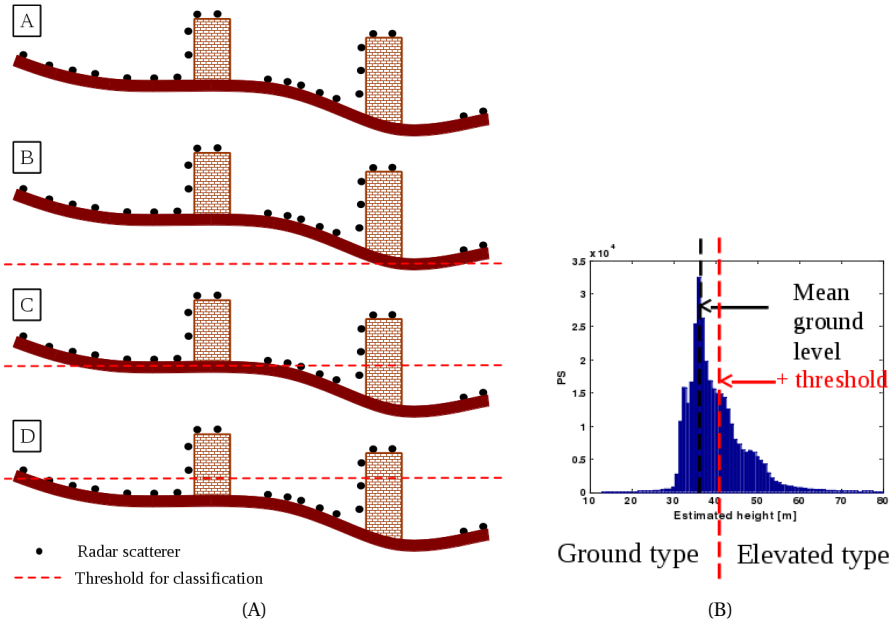


Figure 3.6: Identification of mean ground level from PS heights and determine a threshold for classification. (A) Separation of scatterers (black dots) based on threshold (red dashed line). (B) Estimating mean ground level and setting a threshold for classification (considered as a reference method, see sec. 3.3.2).

3.3.1. Height based classification

A stack of Single Look Complex (SLC) images is processed by PSI to estimate parameters such as displacement and height relative to a reference point for each of these PS (Ferretti et al., 2001; Kampes, 2005; van Leijen, 2014). Estimated heights and their standard deviations are considered the preliminary inputs to our target classification. Using height, two classes of radar targets can be separated: ground-type and elevated-type. In order to perform this classification, one should note that: 1) the PS heights are relative, and 2) the urban terrain is not perfectly flat. Usually mean ground height is inferred from the histogram of PS heights over a certain area and by using a threshold (say ≥ 3 m), ground-and-elevated scatterer classes are separated, see Fig. 3.6B. However, depending on the choice of the threshold and the presence of a local topography, classification results vary as shown in Fig. 3.6A (B)-(D). This problem can be solved if a local height estimate at each PS location is available. This local height information can also be obtained from an

external DEM (Digital Elevation Model)/DSM (Digital Surface Model) such as AHN. In our study, height information from PS is used stand-alone to derive the local ground height.

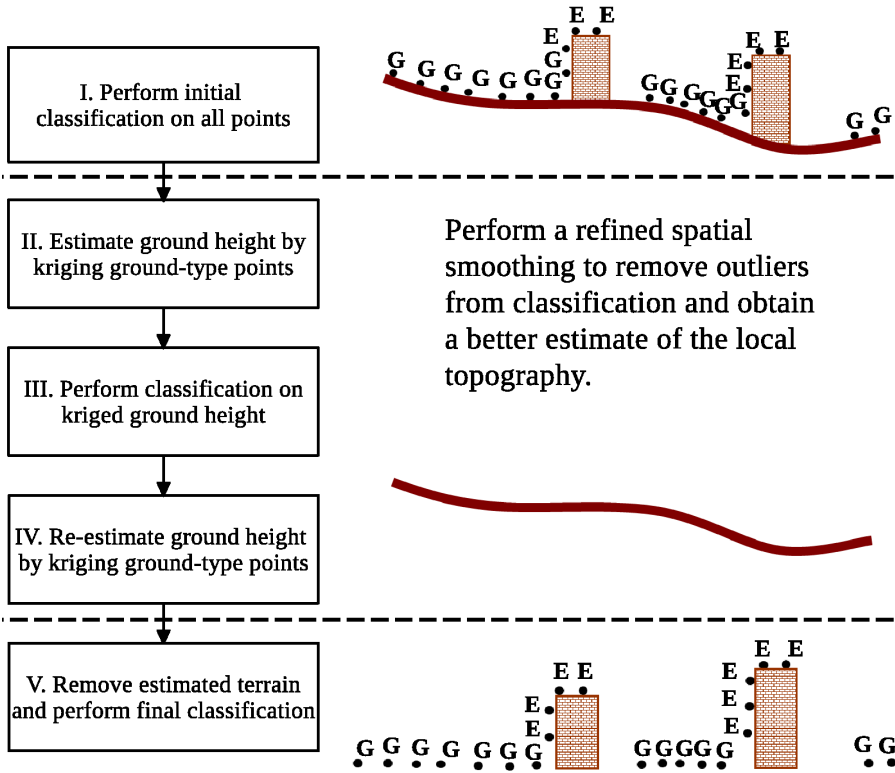


Figure 3.7: Methodology for target type classification using height. Radar scatterers are classified into two classes: ground-type (G) and elevated-type (E).

Fig. 3.7 sketches a methodology to estimate this local ground height and subsequently perform target classification to separate radar reflections from-and-above ground level. The method is divided into five main steps. Steps I, III and V perform classification, while steps II and IV refine the ground height estimation by kriging. The mathematical operation performed in step I is the same as in steps III and V, however, with improved (filtered) inputs as explained below.

I Initial classification

The initial classification step is performed iteratively. A circular region with radius R around a point of interest (red dot) is selected, see Fig. 3.8 [A]. The radius of the circular region R is adaptively scaled based on the PS spatial density and the nature of the terrain. For example, the radius of region R is increased gradually until there are a sufficient number of points to determine the ground height. Based on the topography, the maximum value for the radius of circular region R will be adopted. Typical values of R range from 50 m to 250 m. During the first iteration, we use all M points selected in region R for the ground height computation. Now, from all the points selected in region

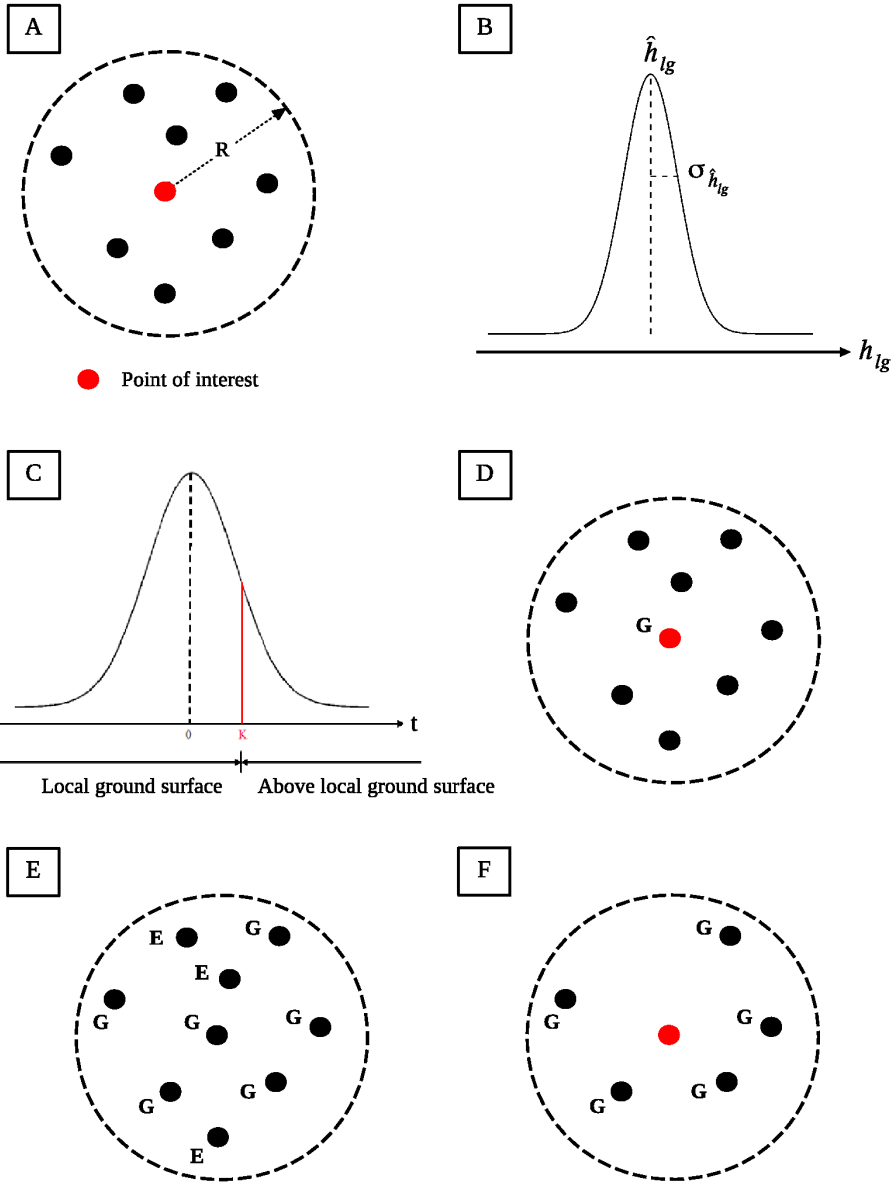


Figure 3.8: Classification process input and output. G and E stand for ground-type and elevated-type, respectively. Subscript lg represents the local ground height. **A** shows a circular region R around a point of interest (red dot) used for local ground height estimation. The estimated local ground height distribution is shown in **B**. **C** describes the t-distribution with threshold K employed for height classification. **D** is a result of classification for a given point of interest. **E** shows the result of classification after the first iteration. Points identified as a ground type in the current iteration, as indicated in **F**, is only used to estimate the local ground height distribution in the subsequent iteration.

R the local ground height distribution as shown in Fig. 3.8 [B] at the location of the point of interest is obtained using Best Linear Unbiased Estimation (BLUE) (Teunissen et al., 2005):

$$\hat{\underline{h}}_{\text{lg}} = (A^T Q_y^{-1} A)^{-1} A^T Q_y^{-1} \underline{y} \text{ and } \sigma_{\hat{\underline{h}}_{\text{lg}}}^2 = (A^T Q_y^{-1} A)^{-1}, \quad (3.5)$$

given the following functional and stochastic models

$$E\{\underline{y}\} = A \underline{h}_{\text{lg}}, \text{ with } \underline{y} = \begin{bmatrix} \underline{h}_1 \\ \underline{h}_2 \\ \vdots \\ \underline{h}_m \end{bmatrix}, \quad A = \begin{bmatrix} 1 \\ 1 \\ \vdots \\ 1 \end{bmatrix}, \text{ and } Q_y = \begin{bmatrix} \sigma_{h_1}^2 & & & \\ & \sigma_{h_2}^2 & & \\ & & \ddots & \\ & & & \sigma_{h_M}^2 \end{bmatrix}, \quad (3.6)$$

where $[\underline{h}_1, \underline{h}_2, \dots, \underline{h}_m]$, and $[\sigma_{h_1}^2, \sigma_{h_2}^2, \dots, \sigma_{h_M}^2]$ are the heights and their variances of M PS points in the neighborhood of the point of interest, respectively. The underline (e.g., \underline{y} , $\hat{\underline{h}}_{\text{lg}}$) represents that the terms are random variables. The local height at the location of a radar scatterer is given by a Gaussian distribution with mean $\hat{\underline{h}}_{\text{lg}}$ and variance $\sigma_{\hat{\underline{h}}_{\text{lg}}}^2$.

Hypothesis testing, Eq. (3.7) is conducted to see if the height of point of interest \underline{h}_i is significantly different from the local ground distribution estimated from Eq. (3.5). The test statistic is given by (Fisher et al., 1925)

$$\frac{\hat{\underline{h}}_{\text{lg}} - \underline{h}_i}{\sqrt{\sigma_{\hat{\underline{h}}_{\text{lg}}}^2 + \sigma_{h_i}^2}} \sim t(N + M - 2) \quad (3.7)$$

where N is number of SLC images used in PSI, the test statistic t is student-t distributed with $(N + M - 2)$ degrees of freedom (see Fig. 3.8 [C]), and subscript i represents the point of interest. Based on a desired level of significance (α), the threshold K for classification is chosen. Depending on the outcome of this hypothesis testing, the point of interest is classified as either ground type ($t \leq K$) or elevated type ($t > K$), see Fig. 3.8 [D]. This procedure is repeated for all the PS points in the area of interest to get Fig. 3.8 [E]. Hence, we know the target class type for all the PS. Now, we iterate this procedure ([A] \rightarrow [E]) to re-assign the class type, but during the subsequent iterations, PS that are of the ground class type alone as shown in Fig. 3.8 [F] are selected for local ground height distribution estimation. These iterations can be continued until there are no significant changes in either target class type or local terrain height interpolated. In our study, we limit the number of iterations to 2.

II Estimate local ground height by kriging ground-type points

The points classified as ground-type in step I are selected and Universal kriging is performed to interpolate the local ground height at each location of PS point.

III Perform classification on the kriged ground-type points

The classification process explained in step I is repeated using the kriged local ground height estimated from step II.

IV Re-estimate local ground height by kriging ground-type points

Here, the classification process (explained in step I) is again repeated only for the ground-type points obtained from step III.

V Remove estimated terrain and perform final classification

To eliminate the impact of the terrain, the local ground topography estimated from step IV is removed from the PS heights, and then the classification (see step I) is performed again in step V.

In the end, the method yields two key outcomes. First, the target type (G or E type) which helps us in understanding where the reflections come from as illustrated on the bottom right of Fig. 3.7. Second, as a result of classification, an estimate of the local ground height or DEM of the terrain and local height of the target above ground are obtained.

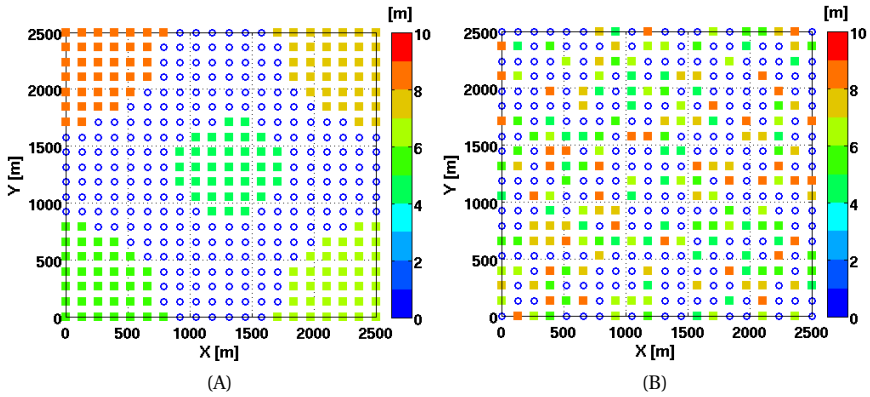


Figure 3.9: A scenario of simulation for a (A) grouped and (B) random distribution of building and ground points. Points on building and ground are marked as squares and circles, respectively. (A) Height map showing the building (elevated) points being distributed in five building groups viz. left top, right top, right bottom, left bottom and center. Ground points are distributed in the space between these building groups. (B) Height map showing a random distribution of buildings and ground points. Color represents the height of the simulated points in metres. In both simulation scenarios and in all simulations, a conservative point density of 64 PS per km^2 is maintained.

3.3.2. Performance analysis of target classification

Analysis using simulated data

In order to analyze the performance of the target type classification method, predefined values for location, height and class type of scatterers are simulated and fed as input. The resulting target class is compared with the simulated (predefined) input to obtain the success rate of target classification.

To emulate different urban scenarios, the simulation is repeated for different spatial distributions of ground and elevated (also referred as building for convenience) points, different building heights and also for different percentages of points on ground versus building. In reality an urban or a semi-urban environment can be represented by a mix of spatially grouped and random distributed buildings and the ground with a certain point

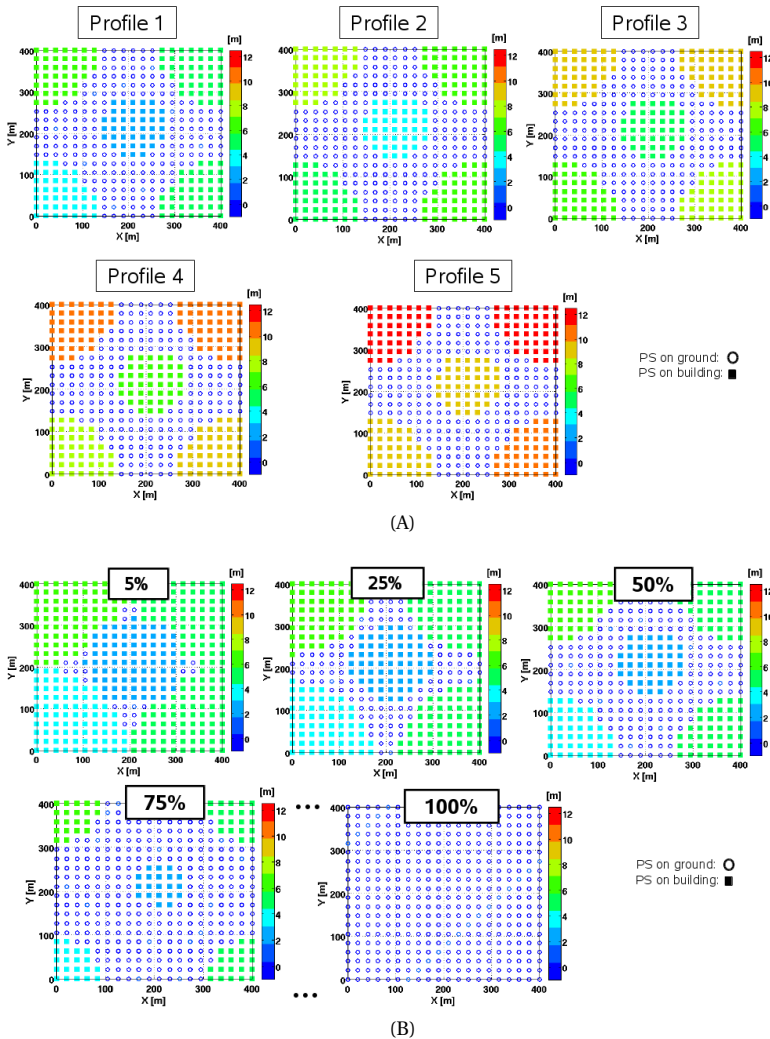


Figure 3.10: Simulation for the grouped distribution of points. (A) With different building profiles. (B) With different number of points on ground versus building. The ratio between the number points on the ground and the total number of points on the ground and building combined is expressed in %. For example, a 100% represents a scenario where all the reflections are from the ground level.

density. Hence these two distinct spatial distributions of building and ground points (grouped (Fig. 3.9A), and random (Fig. 3.9B)) are simulated. Each marker (square or circle) in Fig. 3.9A and Fig. 3.9B represents a PS point. Each square marker represents a PS on a building (elevated type) and each circle represents a PS lying on a ground level (ground-type). For each spatial distribution, the simulation is repeated for different building heights, which is achieved through five building (height) profiles. The term *building profile* refers to height of all building points distributed in either a grouped or a random pattern. For example, building profile 2 is obtained by adding a constant height increment to all building

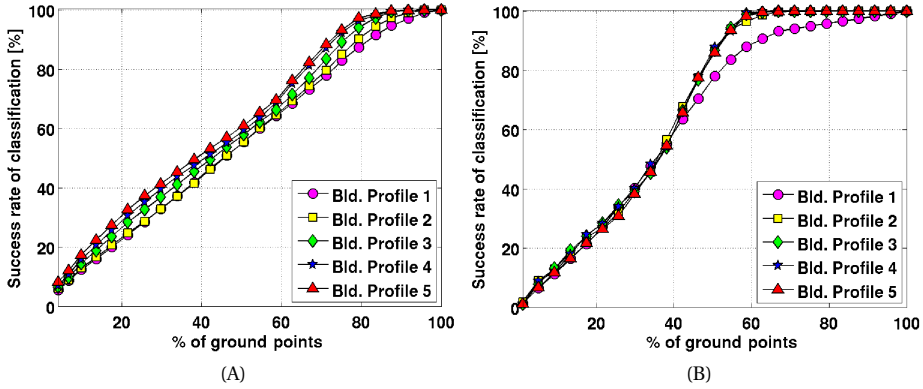


Figure 3.11: Target classification results for (A) grouped and (B) random distribution of building and ground points. (A) Classification results for simulation of grouped distribution of points. (B) Classification results for simulation of random distribution of points. Shown are the results of target classification for different building profiles (1 to 5) and percentages of points on ground versus building.

points in building profile 1. Similarly, building profiles 3 to 5 are obtained such that the heights of building points are increased in the following order: Building profile 1 < Building profile 2 < Building profile 3 < Building profile 4 < Building profile 5. Fig. 3.10A shows a simulation scenario of grouped distribution of points for 5 different building profiles. Finally, for each spatial distribution (grouped and random) and building profile (1 to 5), the entire simulation is repeated by gradually increasing the percentage of points on ground versus building from 0% (no points on the ground but only on the buildings) to 100% (no points on the buildings but only on the ground). Fig. 3.10B shows a few simulation scenarios for grouped distribution of points for a building profile.

The simulation results are shown in Fig. 3.11A and 3.11B. The performance of our classification relies mainly on the number of points lying on the ground to estimate the local ground height. It can be observed from Fig. 3.11A and Fig. 3.11B that the success rate of classification increases with an increasing number of points on the ground. Especially for a random distribution of points (Fig. 3.9B) the quality of classification (Fig. 3.11B) is above 80% when the percentage of points on ground reaches 50% or higher. This is because when the ground points are randomly distributed and higher in number, the availability of ground points in the vicinity of the target to be classified is higher. This ensures a better local ground height estimation process, and subsequently improves the classification between the building and the ground points. It is also evident from the simulation results that the higher the ground versus building height differences, the better the target classification results. For example, building profile 5 exhibits higher success rate compared to building profile 4, building profile 4 is better than building profile 3 and so on. Independent of the sensor used, the above simulation scenarios and their results provide us an insight into the performance of the developed target classification method under a variety of different urban environments.

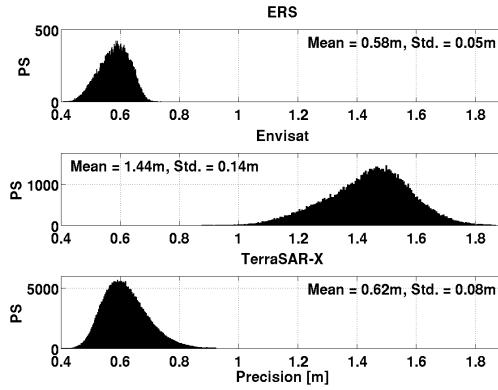


Figure 3.12: Histogram of the estimated height standard deviation for ERS in Imaging Mode (top), ENVISAT ASAR Imaging Mode in IS7 swath (center) and TerraSAR-X in stripmap mode (bottom). ERS, ENVISAT, and TerraSAR-X images were acquired in the ascending direction with an incidence angle (at scene center) of about 23° , 44° , and 31° respectively.

Analysis using real data

Since we do not know the target type beforehand for each of the PS in a real data set, the success rate of classification is indirectly obtained by comparing the height of the ground estimated from our method with highly precise (5 cm RMS (Root Mean Square)) elevation data obtained from airborne laser altimetry. The data set named “Actueel Hoogtebestand Nederland” (AHN) (Rijkswaterstaat-AGI, 1996) with a specific version filtered to have only ground surface was used in our study as ground truth elevation information. Therefore the quality of classification on a real dataset is judged based on the accuracy of the ground height estimated. For this purpose, data acquired from 1992 to 2012 with multiple spaceborne satellites such as ERS-1/2, ENVISAT, and TerraSAR-X covering about 240 km^2 over Amsterdam, the Netherlands are processed and their results are analyzed. Images acquired in right look ascending direction from satellites such as ERS-1/2 in Imaging Mode from May-1992 to Dec-2000, ENVISAT in Imaging Mode (IS7 swath) from Dec-2002 to June-2010, and TerraSAR-X (TSX) in stripmap mode from Feb-2009 to Mar-2012 were used for this study. Each track was processed individually using PSI (Kampes, 2005; van Leijen, 2014) to estimate height and deformation per PS.

Fig. 3.12 shows the standard deviation of the estimated PS heights from ERS, ENVISAT and TerraSAR-X. It can be seen that the precision is poor in case of ENVISAT compared to ERS and TerraSAR-X. This is due to the following factors. (i) First, the number of images available in case of ENVISAT was 42, which is much less compared to the 74 images for ERS and the 86 images for TerraSAR-X. The higher the number of images the lower the height standard deviation. (ii) The sensitivity of height measured changes with respect to incidence angle of the radar beam. ENVISAT images were acquired in IM with an incidence angle of approximately 44° while ERS (in Imaging Mode) and TerraSAR-X (in stripmap mode) were acquired with incidence angles of approximately 23° and 31° respectively. From Hanssen (2001b) the change in height as a function of incidence angle can be written by

$$\frac{\delta h}{\delta \theta} = \beta \cdot \cos \theta, \quad \text{with } \beta = \frac{\lambda R \Delta \phi}{4\pi B_{\perp}}, \quad (3.8)$$

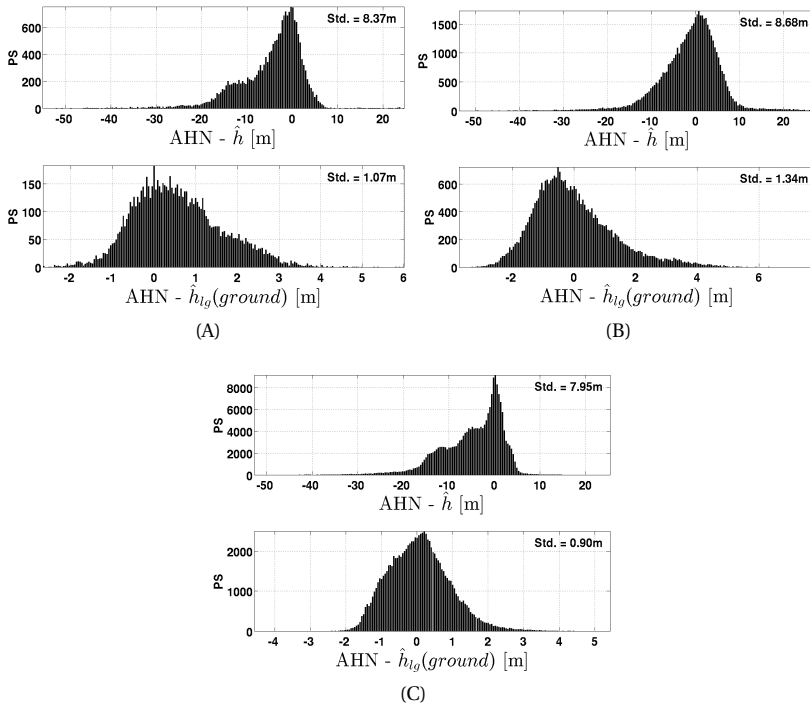


Figure 3.13: Target type classification results and validation for (A) ERS, (B) ENVISAT, and (C) TerraSAR-X datasets. Top: height error between AHN and PS. Bottom: height error between AHN and estimated local ground height for PS with ground target type.

where h is the height, θ is the incidence angle, λ is radar wavelength, R is the slant range distance from the platform to the scatterer, $\Delta\phi$ is the interferometric phase, and B_{\perp} is the perpendicular baseline. For incidence angles of 23° and 44° , $\frac{\delta h}{\delta\theta}$ is given by 0.92β and 0.72β , respectively.

A large incidence angle lowers the sensitivity to the height measured from a slant-looking spaceborne platform, and hence it lowers the precision of the estimated height. (iii) Finally, due to the relatively large incidence angle the atmospheric path length increases, thereby increasing the atmospheric noise which in-turn can lead to poor height estimation variance.

PSs with the estimated heights (and its precision) from PSI are classified and the resulting local ground topography is compared with AHN heights. Here the PS reference point bias and linear trend component, both with respect to AHN, are calculated and removed in our validation. Fig. 3.13A displays the target type classification results for the ERS dataset. Fig. 3.13A (top) shows the height error between AHN and PS without classification. In this case we obtain a height error standard deviation of 8.37m . Since scatterers lying on ground and above ground surfaces are not separated we obtain a rather high dispersion.

Now the result of target classification such as target type and local ground height estimated are used to get the precise local elevation information of the ground type targets.

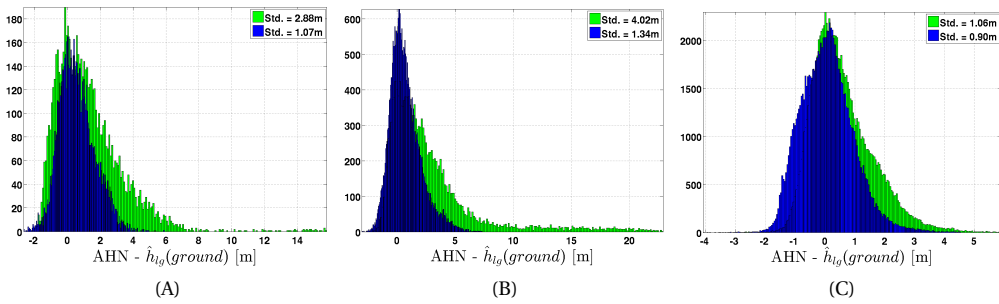


Figure 3.14: Variation of local ground height estimated from the reference method (green) and the proposed method (blue) with AHN for (A) ERS, (B) ENVISAT, and (C) TerraSAR-X.

Fig. 3.13A (bottom) shows the error between the local ground height per PS filtered for ground target type and AHN. Here we obtained a height error standard deviation of 1.07 m with respect to AHN, Similar explanations hold for the ENVISAT and the TerraSAR-X results shown in Fig. 3.13B and Fig. 3.13C respectively. Based on the comparison with AHN, the generated DEM precision of the ground is nearly sub-metric in case of ERS, ENVISAT, and TerraSAR-X as shown in Fig. 3.13A (bottom), Fig. 3.13B (bottom), and Fig. 3.13C (bottom) respectively, which supports our target classification method.

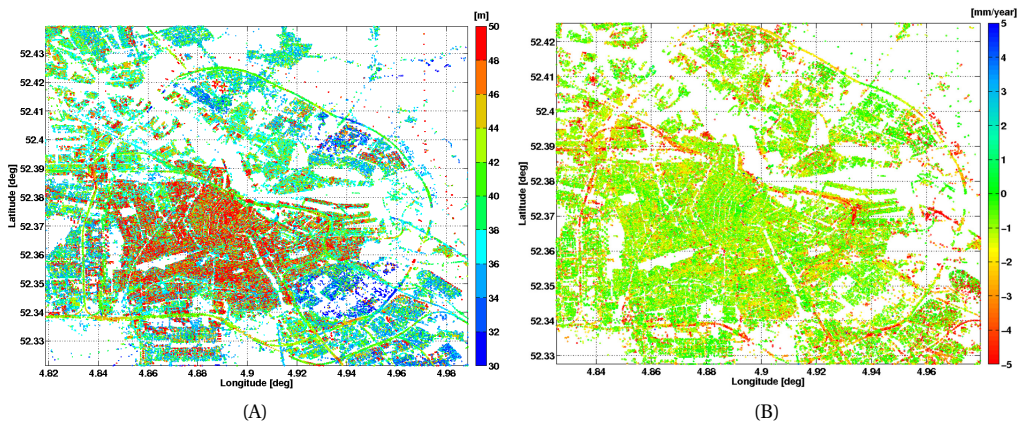


Figure 3.15: Estimated height (A) and velocity (B) from PSI using TerraSAR-X covering Amsterdam.

Comparison with a reference height classification method

For comparison, a height-based classification performed using a single fixed-elevation threshold as shown in Fig. 3.6B is considered as our reference method. The local ground height estimated (a by-product of classification) from the proposed method and the reference method are compared with AHN2 in Fig. 3.14. A lower spread with respect to AHN (see horizontal axis in Fig. 3.14) in these graphs indicates a better estimate of the ground level. The results from ERS, ENVISAT and TerraSAR-X validate the performance of the proposed classification method.

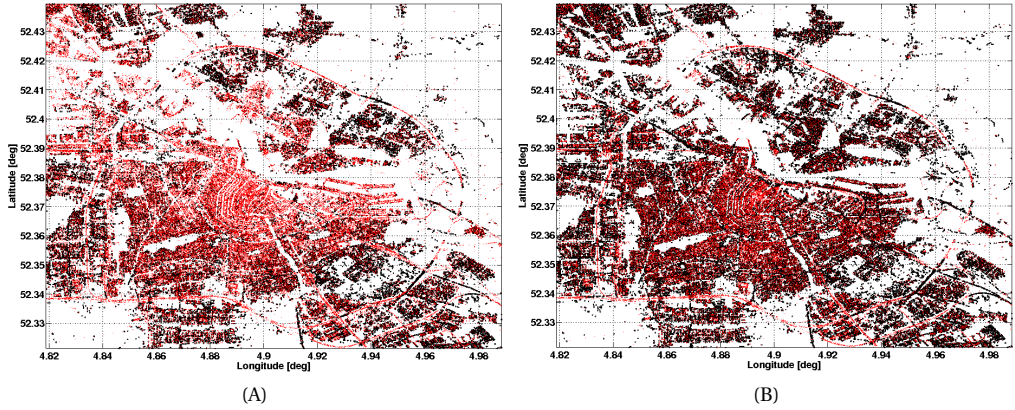


Figure 3.16: Comparison of classification results from a single threshold reference method (A) with the proposed local ground height based classification method (B). PS classified into ground-type (black dots) and elevated-type (red dots). The proposed method provides a better classification due to a better estimation of the local ground height, see Fig. 3.14C.

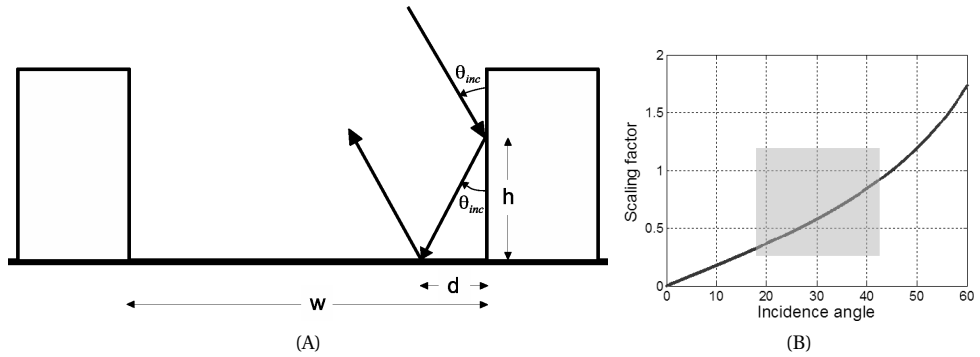


Figure 3.17: Impact of geometry on reflections from the ground. (A) Incidence angle (θ_{inc}) versus distance from building (d). (B) Incidence angle (θ_{inc}) is related to the distance from building (d) by a scaling factor, see Eq. (3.9). Typical SAR incidence angles are highlighted in gray.

For further analysis, we present the results from TerraSAR-X in detail. The PS heights estimated from TerraSAR-X over Amsterdam are shown in Fig. 3.15A. The central part seen with PS having higher heights indicate the main built-up region of Amsterdam. The results of target classification from both methods for the TerraSAR-X dataset are shown in Fig. 3.16. Comparing Fig. 3.16A with Fig. 3.16B, the proposed method assigns relatively more points to the ground level in the central part which is due to a better estimation of ground level as a result of improved classification, see Fig. 3.14C. A relatively higher number of ground points in Fig. 3.16B resembles the PSs with a low elevation in Fig. 3.15A. The higher the points from the ground, the better the ground level estimation and target classification. The higher density of points from ground level is favored by the steep incidence angles of the TerraSAR-X acquisitions of approximately 31° (Gernhardt, 2010). In addition, the width of the street canyon (w) and the height (h) at which the reflection emanates also plays a role,

see Fig. 3.17A. The radar incidence angle θ_{inc} , and distance from building d can be related by,

$$d = h \cdot \tan(\theta_{\text{inc}}), \quad (3.9)$$

where $\tan(\theta_{\text{inc}})$ is a scaling factor, see Fig. 3.17B. From Fig. 3.17B, for a reflection starting from $h = 10$ m, the clearance needed for a successful curb-to-wall reflection are $d = 4.2$ m and $d = 6.0$ m for $\theta_{\text{inc}} = 23^\circ$ (ERS ascending track) and $\theta_{\text{inc}} = 31^\circ$ (TerraSAR-X/TanDEM-X ascending track) respectively. Therefore, the lower the incidence angles the closer we measure to buildings and vice-versa. Similarly, the narrower the streets, the lesser the curb-to-wall reflection possibilities even with steep incidence angles.

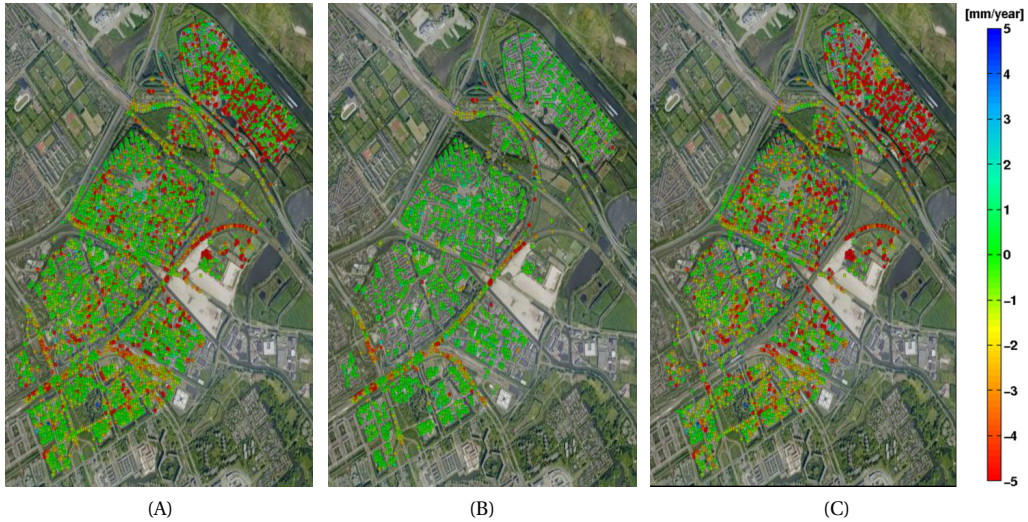


Figure 3.18: Application of target height classification in Diemen, the Netherlands. (A) Deformation rates in mm/year are displayed over an optical image for PSs before (A) and after (B and C) classification. Applying our classification, the deformation behaviors of the elevated-type PSs (B), and the ground-type PSs (C) are discriminated. Except the road networks, PSs from the building (B) are stable while the ground (C) undergoes subsidence. Our interpretation is confirmed by the ground truth. The ground truth from municipality reveals that the buildings in this neighborhood have strong foundation while the ground experiences deformation due to peat compaction, see Fig. 3.19.

3.3.3. Applications

An application of target classification is demonstrated over Diemen, see Fig. 3.18. The estimated deformation (see Fig. 3.18 (A)), and the separation of deformation from two regimes namely ground level (Fig. 3.18 (C)) and elevated structures (Fig. 3.18 (B)) helps in understanding where the deformation stems from, in this case from the ground level, as shown in Fig. 3.18 (C).

The local information from the municipality validates our interpretation that the ground in this region experiences subsidence due to soil compaction and here the sub-regions were re-filled with sand to maintain the ground level. Fig. 3.19 shows the year in which each sub-region was re-filled. The above application illustrates the feasibility of the proposed height-based classification.

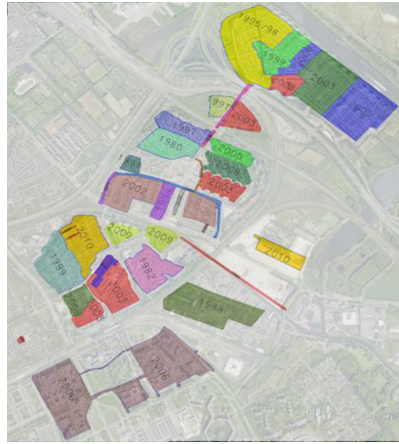


Figure 3.19: Year of ground suppletion per sub-region in the area of Diemen, the Netherlands, data of Diemen municipality (obtained from SkyGeo).

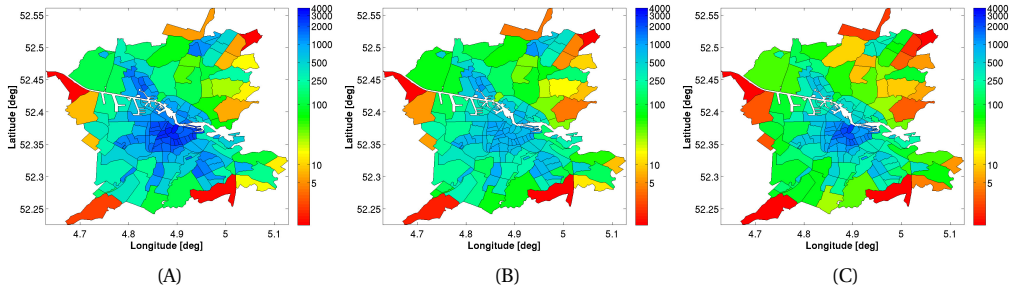


Figure 3.20: Interpretation of PS density (PSs per km^2) per postcode before and after a height-based scatterer classification over Amsterdam. The height-based classification is performed using the method described in sec. 3.3.1.1. (A) PS density of all scatterers, colors are in log scale. (B) PS density of the scatterers from the ground level. (C) PS density of the scatterers from elevated structures. In the central part of the Amsterdam city, PSs from the elevated structures (C) dominate the scatterers from the ground level (B).

In general, the target classification can be applied to segregate estimated height and velocity to aid in interpretation. The results of target classification can be presented in many ways — point based, polygon/window (square, postcode, quadtree) based and asset (infrastructure like pipelines, buildings, bridges, dikes) based. Results displayed in points are shown in Figs. 3.16 and 3.18. Here, we explored the postcode-based presentation to get a first-level interpretation of the results, see Fig. 3.20. Fig. 3.20A shows the number of PS density (number of PS per km^2) per postcode, while Fig. 3.20B and Fig. 3.20C show PS density for elevated and ground type targets respectively. It is evident from Figs. 3.20C and 3.20B that a large set of PS (approximately 2700 out of 3500 PS/ km^2) from the central part of the city emanates from the infrastructure. Outside heavily urbanized areas (away from the center), PS density varies from 100/ km^2 to 1000/ km^2 . It is to be noted that the polygons at the edges exhibit lower point density since the processed TSX track spatially covers those postcodes partially.

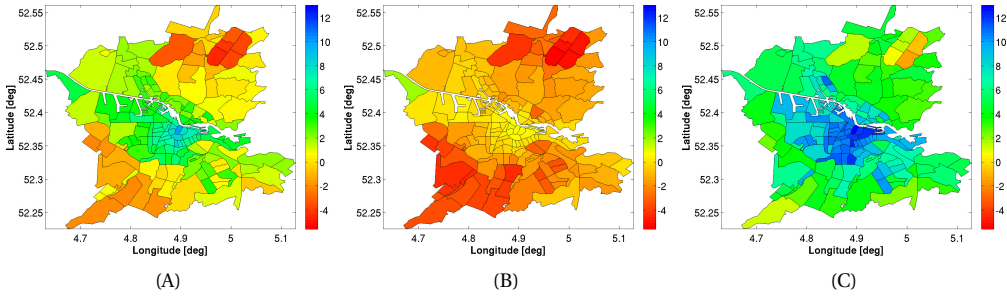


Figure 3.21: Interpretation of mean PS heights (in m) per postcode before and after a height-based scatterer classification over Amsterdam. The PS heights are given relative to a reference point. (A) Mean PS heights. (B) Mean PS heights from the ground level scatterers. (C) Mean PS heights of scatterers from elevated structures. Separation of scatterers into (B) and (C) helps in the identification of the local ground level and built-up regions. The elevated structures in the city centre have a mean height of about 10 m to 12 m.

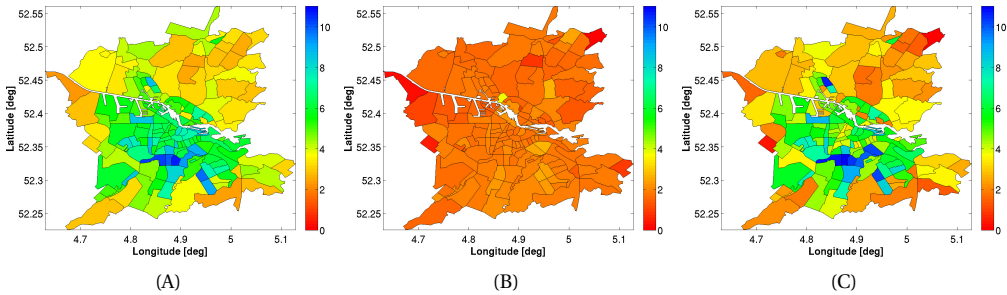


Figure 3.22: Interpretation of PS height variation (in m) per postcode before and after a height-based scatterer classification over Amsterdam. (A) Std PS heights of all scatterers. (B) Std PS heights of the scatterers from the ground level. (C) Std PS heights of the scatterers from elevated structures. A majority of the height variation in (A) is represented by a variation of the scatterer's height from the elevated structures (C). Here, the ground level shows a minimal variation (B), which can be expected for a flat terrain like Amsterdam.

Figs. 3.21A, 3.21C, and 3.21B illustrate a mean of PS heights per polygon (postcode) for all scatterers, scatterers from ground, and elevated scatterers respectively. Similarly, the standard deviation of PS heights are shown in Figs. 3.22A, 3.22C, and 3.22B. Compared to Figs. 3.21A and 3.22A, after classification, Figs. 3.21B and 3.22B indicate a flat and a smooth ground level in the city centre. Figs. 3.21C and 3.22C represent the magnitude and variety of infrastructure built-up in the area. As one would expect, infrastructure (buildings) show a larger height variation than the ground, see Figs. 3.22C and 3.22B.

Figs. 3.23 and 3.24 display the mean and standard deviation of PS velocity (per postcode), respectively. Figs. 3.23A and 3.24A display PS velocities for all scatterers (*i.e.* without classification). Figs. 3.23B and 3.24B show only for the scatterers from ground level, while Figs. 3.23C and 3.24C display for the elevated scatterers. Comparing Figs. 3.23A, 3.23B, and 3.23C, infrastructure appear to be relatively more stable than the ground. A similar interpretation can be derived by looking at their standard deviation plots, see Fig. 3.24, where the variation in velocity is mainly from the ground when compared to

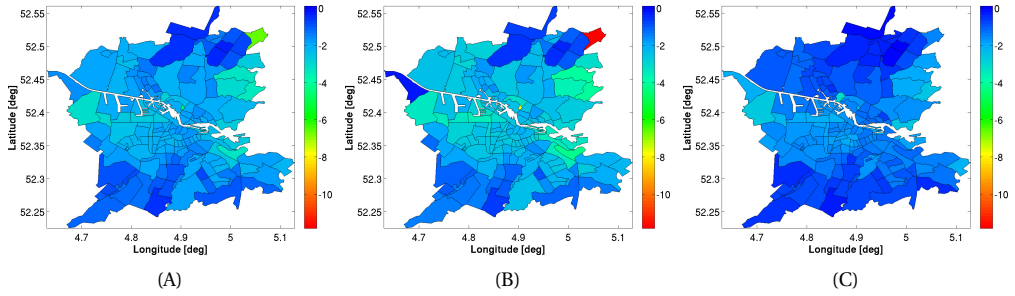


Figure 3.23: Interpretation of mean PS velocity per postcode before and after a height-based scatterer classification over Amsterdam as described in sec. 3.3.1. (A) Mean PS velocity (in mm/yr) of all scatterers. (B) Mean PS velocity of the scatterers from the ground level. (C) Mean PS velocity of the scatterers from elevated structures. Comparing (B) and (C), the ground exhibits more subsidence when compared to elevated structures such as buildings, and other infrastructure.

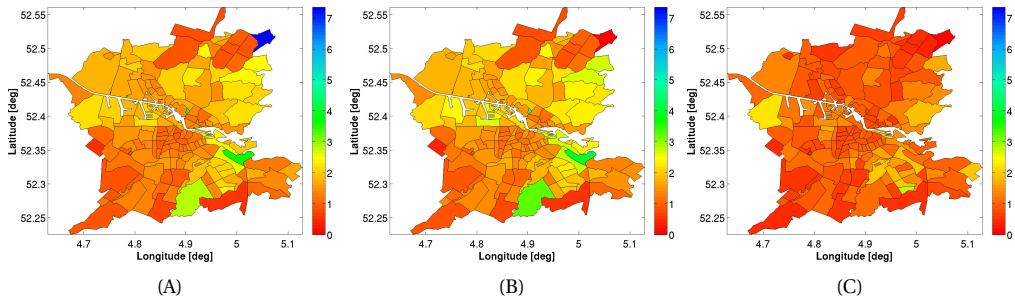


Figure 3.24: Interpretation of PS velocity variation (in mm/yr) per postcode before and after a height-based scatterer classification over Amsterdam. (A) Std PS velocity of all scatterers. (B) Std PS velocity of the scatterers from the ground level. (C) Std PS velocity of the scatterers from elevated structures. A majority of velocity variation is exhibited by the ground (B) when compared to the elevated structures (C).

elevated structures.

3.4. Deformation classification

Once a PS has been classified, with its target type information and displacement rate of each scatterer (relative to a reference point), it is possible to identify the deformation phenomena shown in Fig. 3.25. For a typical building infrastructure, the reflections from buildings, ground, and the building-to-ground interfaces have to be separated (Ketelaar and Hanssen, 2006). Consider three scatterers (PS points) where one is an elevated monohedral, the second one is a ground dihedral and the third one is a ground monohedral as portrayed in Fig. 3.26. Let v_1, v_2, v_3 be the estimated linear displacement rates (velocity) of the scatterers ①, ② and ③ respectively and let K_v represent the threshold on the displacement rate including thermal noise limitations to detect whether a target experienced significant displacement. From the three individual target types and their displacement rates only the following interpretations are possible:

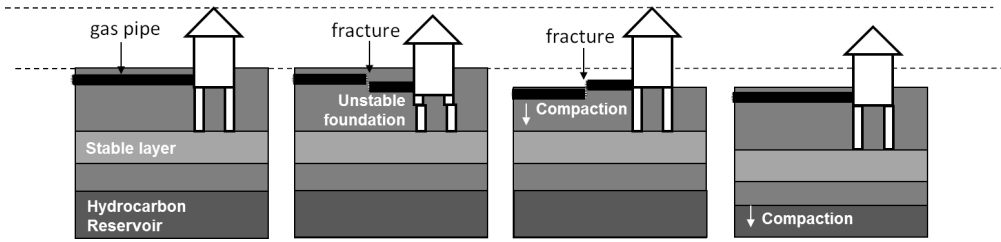


Figure 3.25: Typical deformation scenarios adapted from Ketelaar et al. (2006): stable ground and building (left), stable ground and unstable building (second left), unstable ground and stable building (second right), and unstable ground and unstable building (right). The impact of deformation acting on an underground infrastructure is illustrated using gas pipeline as an example. A fracture in the gas pipeline may develop when the pipeline experiences a relative deformation as shown in the middle two plots. The two horizontal dashed lines represent stable building and ground levels respectively.

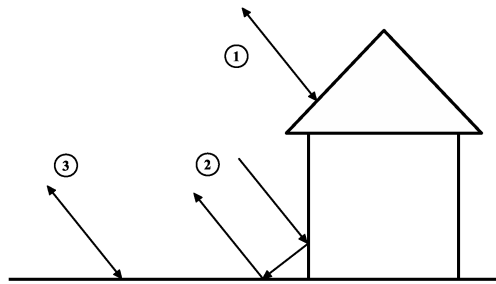


Figure 3.26: PS after target classification: ① - Elevated Monohedral, ② - Ground Dihedral and ③ - Ground Monohedral. In our approach, we use a height-based target classification, as a result ground dihedral ② will be classified as ground monohedral ③, see sec. 3.4.

Table 3.1: Deformation Type (Defo-Type) interpretation. Boolean variable B_v is set to 1 when a scatterer experiences a significant displacement ($|v| > K_v$). It is assumed here that the displacement of the reference point is known.

B_{v_1}	B_{v_2}	B_{v_3}	Defo-Type
0	0	0	All objects are stable
0	0	1	Not a possible condition
0	1	0	Not a possible condition
0	1	1	Ground not stable causing relative motion (Shallow deformation)
1	0	0	Building not stable, difference with Ground leads to relative motion (Structural deformation)
1	0	1	Both Building and Ground not stable, difference causes relative motion (Deep deformation)
1	1	0	Building not stable, difference with Ground leads to relative motion (Structural deformation)
1	1	1	Both Building and Ground not stable, difference leads to relative motion (Deep deformation)

1. When $|v_1| > K_v$, it can be interpreted that the building is deforming or building is deforming together with ground.
2. When $|v_2| > K_v$, it represents either the relative motion between the ground and the building or both building and ground deforming together. But it is not clear at this stage whether the building is stable or the ground is deforming, or vice-versa.
3. When $|v_3| > K_v$, it represents the ground deformation rate and no information is available about the building or building vs ground relative motion.

3

However, by combining these three individual target types, the deformation classification can be obtained. Let B_{v_1}, B_{v_2} , and B_{v_3} denote the probability of occurrence of cases $|v_1| > K_v$, $|v_2| > K_v$, and $|v_3| > K_v$ respectively. For the sake of simplicity B_v can be assumed as a boolean variable (a target undergoes significant displacement or it does not undergo significant displacement). From boolean algebra the following deformation types as given in Tab. 3.1 can be derived.

- All Stable: all targets are found stable.
- Shallow deformation: the case of a building being strongly founded and hence stable, while the local ground level changes, *i.e.*, because of local water level changes or peat compaction. Typical examples would be underground tunnel construction projects performed nearby buildings.
- Deep deformation: in this case, both building and ground are being unstable, while their relative motion represents the magnitude of the building instability possibly caused by deep foundation. Typical examples would be a hydrocarbon extraction from a deep layer.
- Structural deformation: the case where the structural foundation (pillar) of a building is weak and is creating an instability on stable ground. The building versus ground deformation represents the magnitude of the building instability caused by structural problems.

From these four interpretations, the deformation in urban environments can be well understood and the critical problems causing such deformations can also be inferred. The above interpretation is possible when the displacement of the reference point is known in an absolute sense. However, in practice we do not have this information. Hence, in sec. 3.4.1 we develop a deformation classification method using relative displacement.

3.4.1. Deformation type classification method

Based on the methodology proposed in sec.3.3.1, targets are classified into two main classes: elevated (B) scatterers are the reflections from a building or any other elevated structure, and ground level (G) scatterers. The elevated and ground level scatterers are depicted in Fig. 3.26 as type ① and ③ respectively. Here, the reflections from building-to-ground dihedral reflections, *i.e.* type ② in Fig. 3.26, are detected as a ground-type ③. This has no consequences (assuming only vertical deformation) because the ground dihedrals detect deformation signal only when the ground is deforming.

Table 3.2: Detection and classification of deformation for a scatterer of interest i . The deformation rate of scatterer i and j are given by v_i and v_j , respectively. Boolean variable $B_{v_{i,j}}$ is set to 1 when the relative displacement between scatterers i and j is significant, see Eq. (3.11). The target class G represents the scatterers from the ground-level while B represents the elevated type. The last row can be of type intra-structural (i and j are from the same structure) deformation or inter-structural deformation (i and j are from different structure). Since we do not have information whether i and j are from the same structure, inter-structural deformation type is assumed here.)

$B_{v_{i,j}}$	Target type of scatterer i	Target type of scatterer j	Relative deformation type classification
0	G/B	G/B	No relative motion
1	G	G	Local land subsidence
1	G	B	$\begin{cases} v_i - v_j > 0 & \text{Shallow compaction} \\ v_i - v_j < 0 & \text{Autonomous structural motion} \end{cases}$
1	B	G	$\begin{cases} v_i - v_j > 0 & \text{Autonomous structural motion} \\ v_i - v_j < 0 & \text{Shallow compaction} \end{cases}$
1	B	B	Inter-structural deformation

In the following, a methodology is introduced to perform four tasks: detect, classify, quantify, and prioritize areas based on relative deformation. The detection and classification steps are explained here while the quantification and prioritization steps will be described in sec. 3.4.2. The detection and classification are performed using relative deformation of a scatterer of interest i with respect to its surrounding neighborhood. The surrounding neighborhood for a point of interest is defined by a circular window of radius R , identical to sec. 3.3.1.

For every arc between a scatterer of interest (i) and another scatterer (j) in the neighborhood, hypothesis testing is conducted to detect if there is any significant relative deformation. The null hypothesis of an arc not undergoing any significant motion is assumed to have a Gaussian probability density function,

$$H_0 : N(0, \sigma_v^2), \quad (3.10)$$

where σ_v is set based on the precision of velocity estimation from PSI, experience, and/or external user input. Now, similar to Eq. (3.7), the student-t test statistic for relative motion detection is given by,

$$\frac{|v_i - v_j|}{\sqrt{\sigma_{v_i}^2 + \sigma_{v_j}^2}} \sim t(2N - 2), \quad (3.11)$$

where $\sigma_{v_i}^2$, and $\sigma_{v_j}^2$ are the estimated velocity precision of scatterer i and j , respectively. For a given significance level, the null hypothesis H_0 is either sustained or rejected. Depending on the test outcome, a boolean variable $B_{v_{i,j}}$ is accordingly set to either 0 (when H_0 is sustained) or 1 (when H_0 is rejected), and by using the algorithm proposed in Tab. 3.2 the deformation type classification is achieved. In addition, by combining scatterer i with M arcs in the neighborhood region R , a percentage of arcs showing of each deformation class

type (shallow compaction, no relative motion, autonomous structural motion, local land subsidence, or inter-structural deformation) is computed and a dominant deformation behavior at each scatterer location can be arrived.

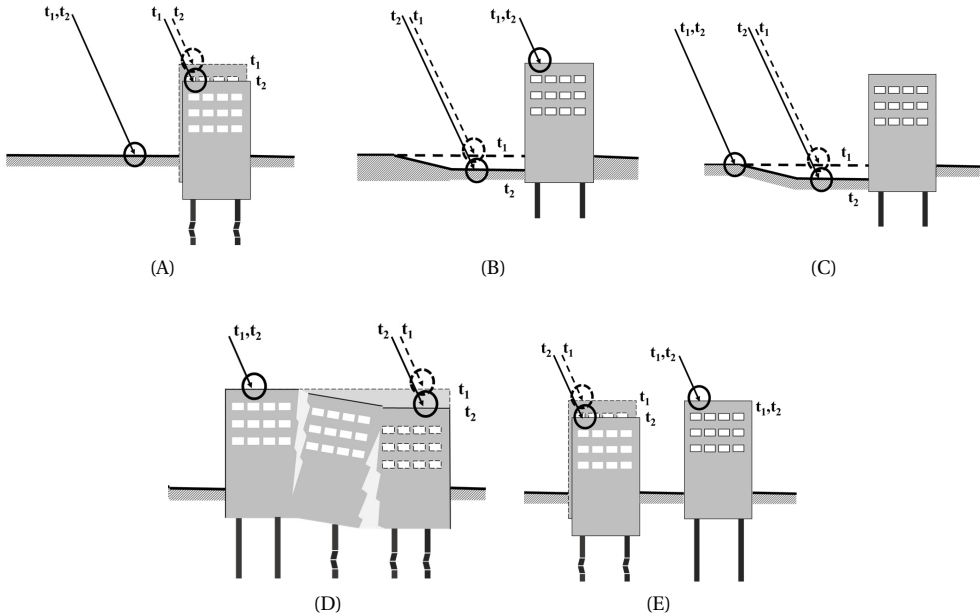


Figure 3.27: Relative deformation types derived by comparing displacement rates, and target classification results of PSs, see Tab. 3.2. Several relative deformation possibilities of the ground and elevated structure between epochs t_1 and t_2 are illustrated and five deformation regimes are identified. (A) Autonomous structural motion - significant deformation of the building relative to the stable ground. (B) Shallow compaction - the ground moves near a stable elevated structure. (C) Local land subsidence - local relative motion between the ground. (D) Intra-structural deformation - relative motion between parts of an elevated infrastructure. (E) Inter-structural deformation - relative motion between two elevated infrastructure.

A 'no relative motion' type in Tab. 3.2 is detected when there is no significant relative motion between scatterers i and j . This could be an indication that both the scatterers (irrespective of their target types B or G) are experiencing the same deformation together driven by a mechanism from a deep layer, see Fig. 3.25. A shallow compaction is identified when the ground shows significant displacement relative to the elevated infrastructure (see Fig. 3.27B) and vice-versa for a autonomous structural motion (see Fig. 3.27A). Local land subsidence (see Fig. 3.27C) and inter-structural motion (see Fig. 3.27E) captures inter-relative motion between the ground and the buildings, respectively.

The proposed deformation classification method is applied for a TerraSAR-X dataset over Amsterdam and the results are presented using postcode polygons, see Fig. 3.28. Using a number of PSs present in the polygon, a percentage of different deformation types is computed per polygon. By comparing, individual polygons in Figs. 3.28A– 3.28E, interpretation of the regions subject to a deformation phenomenon can be arrived. For example, by comparing the red polygon in Fig. 3.28E with the blue polygon in Fig. 3.28C, we infer that the relative motion in this region is due to shallow compaction. Similarly,

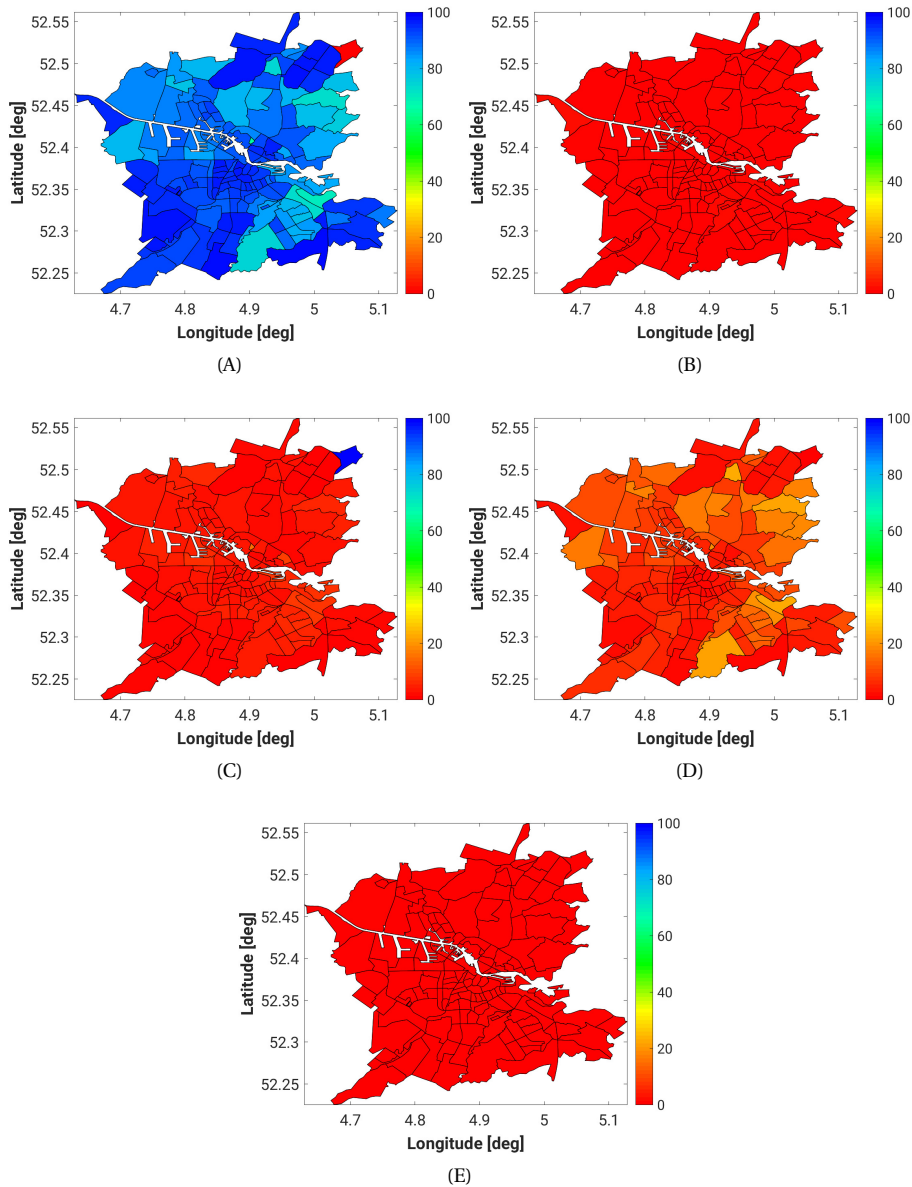


Figure 3.28: Relative deformation classification results per postcode obtained using TerraSAR-X data over Amsterdam. Relative deformation classification is performed using Tab. 3.2 and a percentage of arcs subject to a specific deformation type is obtained per polygon. The summation of each polygon from (A) to (E) adds up to 100%. (A) No relative motion. (B) Autonomous structural motion. (C) Shallow compaction. (D) Local land subsidence. (E) Inter-structural deformation. The regions (polygons) subject to relative motion can be identified in (A) with a high value. For example, a polygon highlighted in red in (A) experiences a strong relative motion. Comparing (A) with (B) to (E), it can be inferred that, this polygon with relative motion is due to a strong shallow compaction phenomena, see the blue polygon in (C). A similar strategy can be employed to interpret the other regions. Comparing (B), (D) and (E), we can infer that the most of the relative deformation seen here comes from the local land subsidence rather than from the elevated structures, see pale orange (>15%) regions in (D) and red regions (~0%) in (E).

by comparing orange regions in Fig. 3.28D with the corresponding polygons in Figs. 3.28C and 3.28E, we infer that the local land subsidence is the main type of deformation in the Amsterdam region. In the following section, we combine several relative deformation types such as shallow compaction, local land subsidence, inter-structural motion, and autonomous structural motion into one parameter in order to quantify, and prioritize areas subject to relative deformation.

3.4.2. Relative deformation index

Recent studies have shown that the relative deformation in urban areas is a key problem for infrastructural stability, and therefore a metric expressing the relative deformation is useful. Towards this goal, the parameter (R^d) is introduced to quantify the mean relative deformation of a scatterer i (point of interest) relative to the surrounding M scatterers in the region R . Here, the point i is connected via M arcs and each arc is tested to detect significant relative motion as given by Eq. (3.11). Then, R^d is computed as:

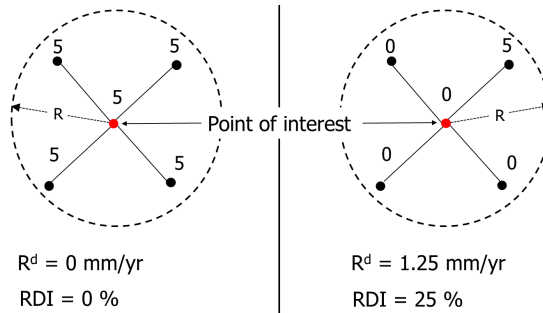


Figure 3.29: RDI computed for a scatterer of interest (in red) for two scenarios given a threshold on the deformation rate of $\sigma_D = 2 \text{ mm/yr}$ and a critical threshold of $R_c^d = 5 \text{ mm/yr}$, see Eqs. (3.14) and (3.15). Here, scatterers are displayed along with their deformation rate in mm/yr.

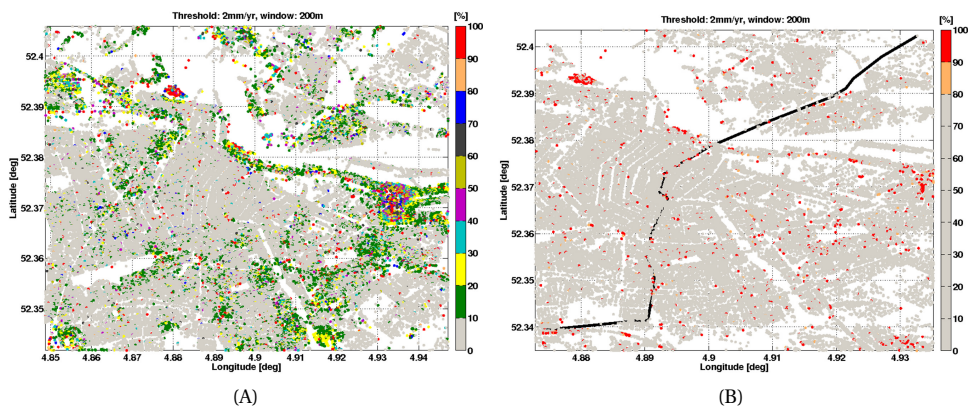


Figure 3.30: RDI computed over Amsterdam using TerraSAR-X dataset. (A) RDI (values in %) over Amsterdam. (B) $\text{RDI} > 80\%$ are highlighted, and a thick black line indicates the passage of the Amsterdam North-South metro tunnel construction.

$$R^d(i) = \frac{\sum_{j=1}^M B_{v_{i,j}}}{M} \cdot \frac{\sum_{j=1}^M B_{v_{i,j}} \cdot |v_i - v_j|}{\sum_{j=1}^M B_{v_{i,j}}}, \quad (3.12)$$

where the first term in Eq. (3.12) indicates the possibility of relative deformation in the neighborhood and the second term provides a mean relative deformation with respect to its surrounding when a significant relative motion is detected. Eq. (3.12) can be simplified as,

$$R^d(i) = \frac{M'}{M} \cdot \sum_{j=1}^M \frac{B_{v_{i,j}} \cdot |v_i - v_j|}{M'} = \frac{1}{M} \cdot \sum_{j=1}^M B_{v_{i,j}} \cdot |v_i - v_j|, \quad (3.13)$$

where $M' = \sum_{j=1}^M B_{v_{i,j}}$ is the number of arcs showing significant relative deformation (see Tab. 3.2). Eq. (3.13) is reformulated as,

$$R^d(i) = \frac{1}{M} \cdot \sum_{j=1}^{M'} |v_i - v_j|, \quad (3.14)$$

since $B_{v_{i,j}} = 1$ for all M' arcs. In order to quantitatively pin-point a location to signal alarm and prioritize detection of critically deforming locations, we introduce the relative deformation index (RDI). RDI (expressed in %) at a location i is given by

$$RDI(i) = \frac{R^d(i)}{R_c^d} \cdot 100 \%, \quad (3.15)$$

where, R_c^d is a threshold critical value to signal alarm which is obtained based either on experience or on external user input. It should be noted that the impact of the actual deformation of the reference point (assumed stable in most cases though not always true) in deformation interpretation is eliminated by R^d and RDI. For example, given a $\sigma_v = 2$ mm/yr and $R_c^d = 5$ mm/yr, the RDI computation is illustrated for a point of interest (in red) surrounded by scatterers in the window R in Fig. 3.29. R^d and RDI values are independent of the deformation of the reference point.

The RDI computed for the TerraSAR-X dataset is shown in Fig. 3.30. It is evident from Fig. 3.30A that most of the area is relatively stable and if we only highlight the scatterers experiencing $RDI > 80\%$, the relatively unstable areas show-up as illustrated in Fig. 3.30B. The location of Amsterdam North-South tunnel constructed underground is drawn as a thick black line in Fig. 3.30B. The traces of relative deformation along the tunnel location can be noticed. Measurements and data reported from the ground also support our RDI-based interpretation that along the metro lines some of the buildings displayed a subsidence signal (van Outeren, 2009). Similarly, here, every unstable point indicated in Fig. 3.30 can be investigated to explore the cause of relative motion. It should be noted that, the RDI computation depends on the number of PSs available in the neighborhood region (within radius R from the point of interest). When the number of PSs in region R is small, RDI values should be interpreted taking the number of PSs used in the computation into account.

The R^d and RDI parameters are compared with the deformation rates in Fig. 3.31. From Fig. 3.31A, the deformation rate has a higher concentration of points around -1 mm/yr and

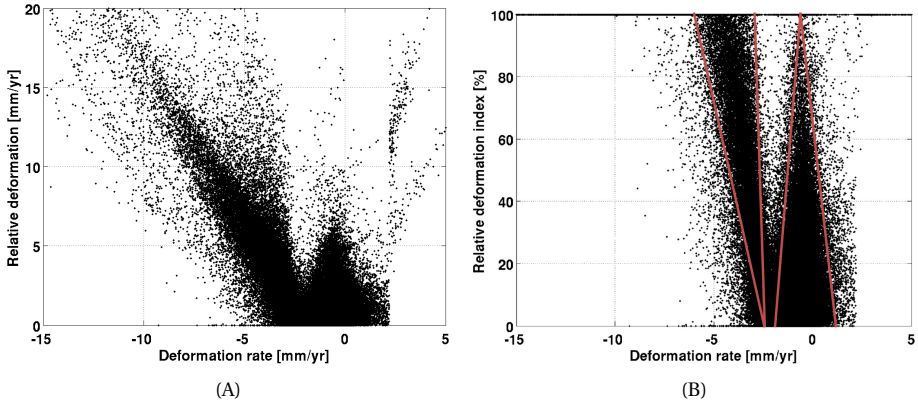


Figure 3.31: R^d and RDI compared with deformation rate over Amsterdam using TerraSAR-X dataset. (A) $|R^d|$ (values in mm/yr) versus deformation rate. (B) RDI (values in %) versus deformation rate. The two cones marked in brown are explained in the text below.

points less than -2 mm/yr tend to show a correlation with $|R^d|$. Similarly, in Fig. 3.31B we can clearly identify two regions (cones marked in brown): one (cone) centered around -1 mm/yr which has only a few points (with higher RDI) needing attention, and the other cone sloping towards relatively high RDI values. Regions highlighted by high R^d and RDI are not always cautioned by a higher deformation rate. This wealth of additional insights can be very useful for monitoring infrastructure, urban development projects, underground pipeline networks, and so on.

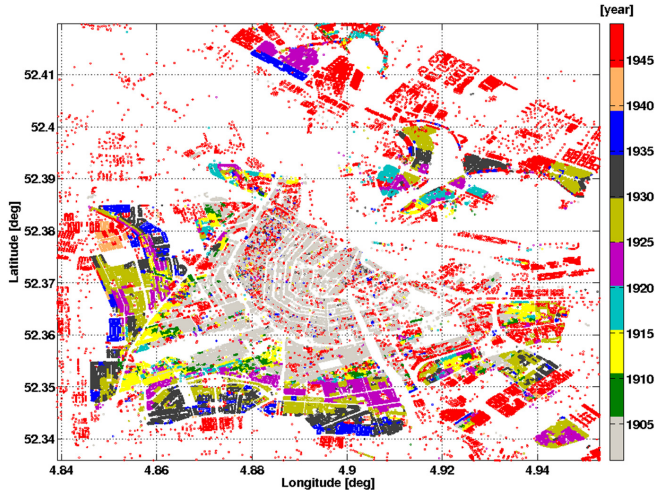


Figure 3.32: Year of building construction for the city of Amsterdam.

Table 3.3: Building construction and foundation information over Amsterdam (gem, 2012). Over the years, construction practices improved leading to a more stable building structures.

Year of construction (Bouwjaar)	Pillars	Foundation
< 1925	Wooden poles	Wood
1925 to 1950	Wooden poles	Concrete
1950 to 1990	Concrete poles	Concrete
1990 <	Concrete poles anchored 19 m deep in the second sand layer	Concrete

3.4.3. Performance analysis of deformation interpretation

In order to validate the relative deformation index (RDI) computed per PS, high density (in the order of 100–1000 points per square kilometer) deformation information of the area is needed preferably from an independent measurement system which covers the same time period as PS dataset. However, in practice, such dense ground-truth deformation measurements are not available. As an alternative, in our approach, we exploited the building construction data to perform an indirect validation. Fig. 3.32 shows the year of construction (“Bouwjaar” in Dutch) of buildings in the Amsterdam region. The anthropogenic development expanding from the center (old city) to the sides (newer parts) can be seen here. Based on the period of construction, the buildings applied different materials for the foundation and pillars (poles) as given in Tab. 3.3.

For every building foundation, we identify a nearby building PS using the method from sec. 3.3.1. The PS deformation rate and the RDI are grouped under four different construction categories as shown in Fig. 3.33. From Fig. 3.33A, the deformation rate spread of the buildings reduced ‘after 1990’ (top left) when compared to construction ‘before 1925’ (bottom right). This reaffirms the fact that the newer buildings are more stable due to improved construction practices, as indicated by the ground-truth data in Tab. 3.3. Similar plots are made using the RDI and the relative deformation spread increases gradually from groups ‘before 1925’ (top left) to ‘after 1990’ (bottom right). This result demonstrates that due to strong foundation of the buildings (over the years), the relative deformation increases due to differential motion between the stable buildings and a deforming ground. These inferences, apart from being useful, also provide an indirect validation of RDI in differential motion detection.

3.5. Case study: Gas pipe network monitoring over Amsterdam

In many countries, underground infrastructure is made up of a complex maze of water, gas, sewer, electric, and telecommunications pipelines, which are several decades to even centuries old requiring regular maintenance, repair, and upgrades. In addition, civil infrastructure built on soft clay and/or peat layers, predominantly in the western parts of the Netherlands, are prone to subsidence related damages (Van den Born et al., 2016; Brus and Van Den Akker, 2018; Van-Camp et al., 2004; Bakker and Bezuijen, 2008). The

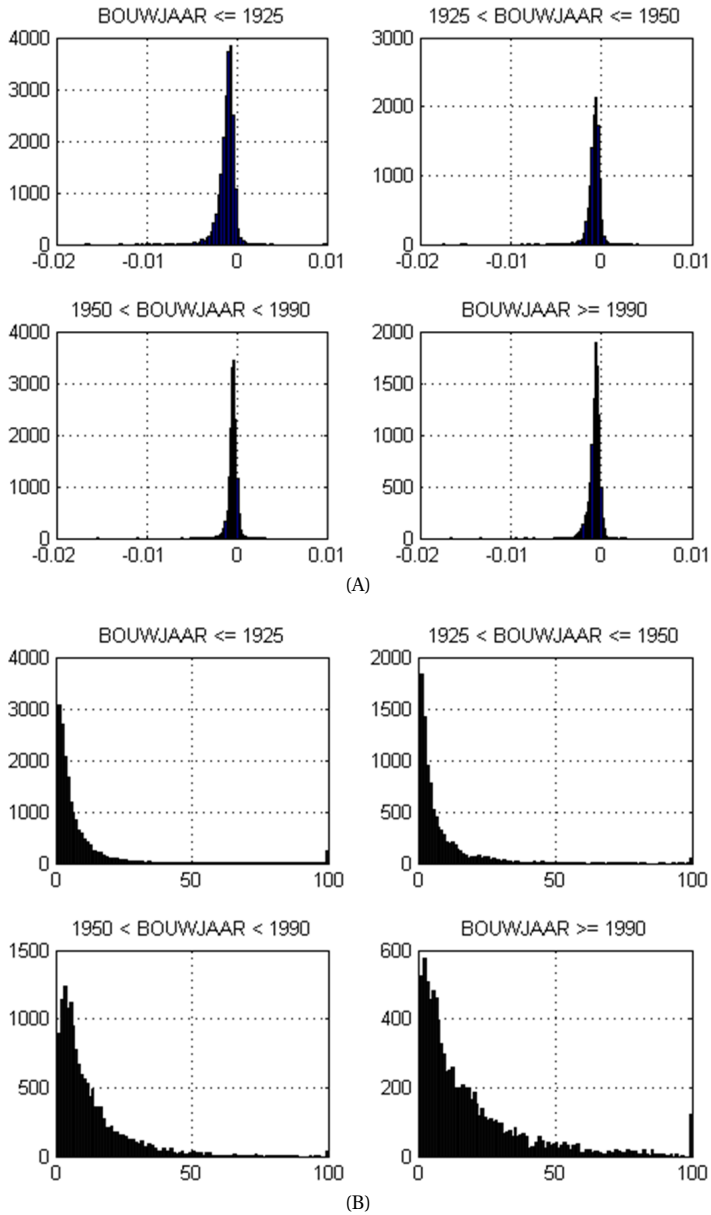


Figure 3.33: Comparison of deformation rate and relative deformation index of elevated-type PS grouped as per the year of building construction (Bouwjaar). The vertical axis shows the number of elevated PS per group. (A) Deformation rate (in m/yr) on the horizontal axis. (B) RDI (in %) on the horizontal axis.

subsidence acting on the below-ground assets especially with gas pipelines is posing an ever greater strain on businesses and residents due to pipe breakage resulting in gas explosions and fatalities, see Fig. 3.34.

On 15 August 2001, there was a gas explosion in Amsterdam, see Fig. 3.34A. An

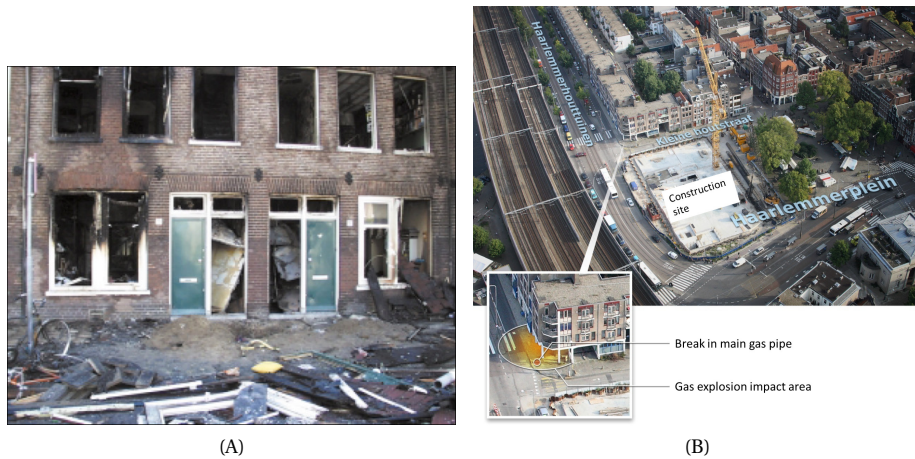


Figure 3.34: Gas explosion accidents in Amsterdam (van Vollenhoven et al., 2002; van Vollenhoven et al., 2009). (A) Czaar Peterstraat on 15 Aug 2001. (B) Haarlemmer Houttuinen on 09 Mar 2008.

investigation team found a fresh fracture of approximately 5 mm width in the main gas pipeline (made of gray cast iron) which had led to the gas explosion (van Vollenhoven et al., 2002). Similarly, on 9 March 2008, another gas explosion took place on the corner of the streets between Haarlemmer Houttuinen and the Kleine Houtstraat in Amsterdam, see Fig. 3.34B. It was determined that the fracture in the main gas pipe made of gray cast iron (with an inner diameter of 150 mm) led to the gas leakage and subsequent explosion (van Vollenhoven et al., 2009). In both cases people were injured, their houses were burnt and had to be displaced.

An investigation made by The Dutch Safety Board showed that when a differential tension acting on a pipeline exceeds its bending stress, the pipe fractures (van Vollenhoven et al., 2002; van Vollenhoven et al., 2009). For older pipes made of brittle materials, such as gray cast iron, the problem is more prone to occur. The differential stress could be accumulated over time as shown from left to right in Fig. 3.35. Two scenarios are possible: a fixed pipe with local ground motion as seen in Fig. 3.35A or an uneven tension from the surface bending the pipeline as shown in Fig. 3.35B. In such scenarios timely detection and repair of pipe lines subject to differential stress might help in mitigating natural gas pipe leakage. The danger associated to gas pipe fracture is not just limited to the Netherlands. Between 1970 and 2008, there have been multiple accidents in the natural gas chain sector with more than 2800 fatalities reported all over the world (Burgherr et al., 2012; Burgherr and Hirschberg, 2014).

According to the figures supplied by the network operators, the total length of the main pipelines is approximately 122,956 km in the Netherlands (van Vollenhoven et al., 2009). 70% of those main pipelines consist of non-brittle materials (steel, PE (Polyethylene) and impact-resistant PVC (Polyvinyl chloride)) and thirty percent of them consist of relatively brittle materials, see Fig. 3.36. Most of the brittle pipes were made of hard PVC (21%), gray cast iron (6%), ductile cast iron (2%) and asbestos cement (1%). About 40% of the main lines were built before 1976 and 81% of the brittle pipes were built before 1976. Since 1976,

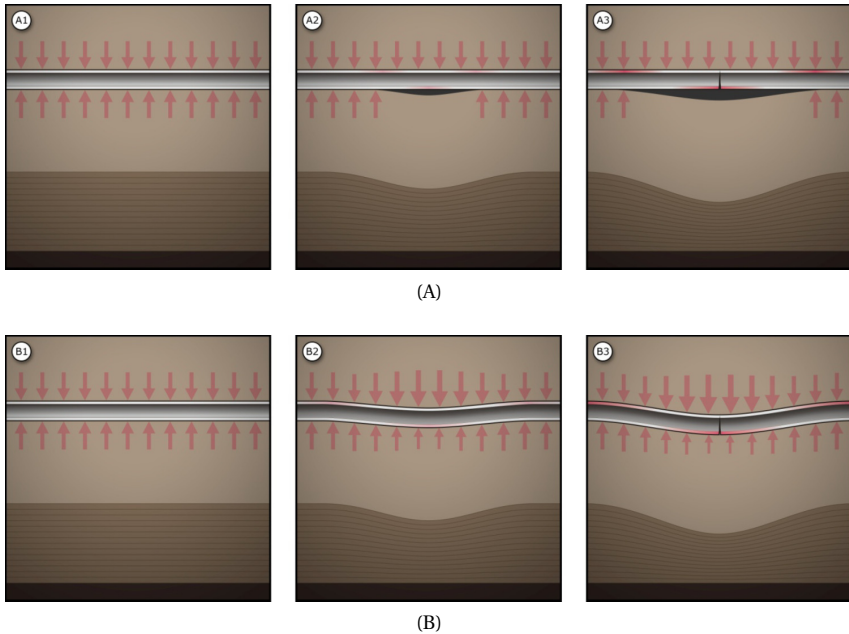


Figure 3.35: Two mechanisms of cumulative stress build-up (left to right) on underground pipelines (longitudinal section) leading to differential stress which results in pipe fracture, pictures from van Vollenhoven et al. (2009). (A) Constant tension build up on the pipe subject to a local ground motion. (B) Uneven tension acting on the pipe where both the ground and the pipe move along.

non-brittle materials were in usage for main pipelines.

In our case study, we focus on pipes made of brittle materials especially gray cast iron, which are posing a higher risk in the Amsterdam region (van Vollenhoven et. al., 2002; van Vollenhoven et al., 2009). As of 2010, there was about 6972 km of (6% of 122,956) gray cast iron pipe that needs replacement. From that count Liander² possesses 2700 km of pipe lines, most of them located in Amsterdam. The pipe network companies are working with the municipalities to replace brittle pipes, and they typically replace about 0.1-1 km per day. Therefore, it is necessary to detect areas prone to differential motion which (when combined with the below-ground asset information such as material type and age) could help prevent potential accidents.

In order to reduce risk and successively replace the vulnerable pipes, it is necessary to pin-point relatively deforming areas and prioritize the pipe replacement. For this purpose, we applied the methodology proposed in secs. 3.3 and 3.4 using a case study over Amsterdam and the result is shown as relative deformation index map in Fig. 3.37A. The colors indicate the degree of relative deformation with grey being the lowest impact and red being the highest impact on the below-ground assets. The utility companies can prioritize their asset management activities by inspecting areas with a higher RDI before inspecting areas with a lower RDI, *i.e.* from red, orange, blue to light gray dots in Fig. 3.37A. Fig. 3.37A is computed with threshold deformation rate $\sigma_v = 2$ mm/yr and alarm threshold $R_c^d = 6$

²Liander is a regional gas and electricity grid operator, mainly in northern, eastern, and western Netherlands.

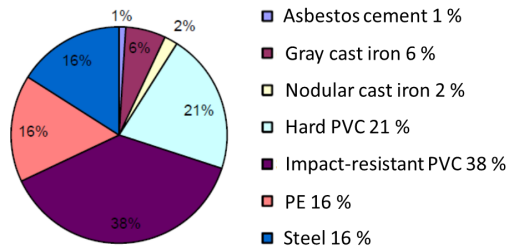


Figure 3.36: Overview (in %) of main pipe materials in the Netherlands (van Vollenhoven et al., 2009). There are about 122,956 km of gas pipelines (distribution and transmission lines) in the Netherlands. As of 2010, about 6972 km of gray cast iron gas pipes need to be replaced.

mm/yr. The choice of the σ_v value is critical in RDI computation. For instance, a higher σ_v threshold value brings-in a higher risk (by ignoring high relatively deforming regions) but it saves cost by attending only the most critical regions. On the other hand, a lower σ_v threshold could be rather expensive but it also lowers the risk of an undetected potential of a gas explosion. Therefore, we recommend that σ_v value is to be chosen in close consultation with the utility asset managers and government agencies such that there is a fair trade-off between the risk and the cost involved.

In order to validate our approach in identifying potential risk zones, we compared RDI with the gas pipe failures data over Amsterdam between 2009 and mid-2012. The natural gas pipeline fracture can be caused by several factors: corrosion of pipes, bending stress due to deformation (caused by natural settlement, heavy traffic loads, settlement due to anthropocentric activities such as digging for building construction and tunnels), faulty connections, and third party damages due to (unreported) mechanical digging activities. Therefore, we filtered gas pipe failures data to retain only failures related to deformation, see Fig. 3.37B. Comparing with RDI, we notice that in most of the cases there is a high RDI within 50 m radius from a gas pipe failure as shown in Fig. 3.37C. From Fig. 3.37D, it is evident that most of the failures were from the high relative-deformation areas. We also confirm that not all high-relative deformation areas have reported failures, see Figs. 3.37C and 3.37D. This, we hypothesize, could be due to: i) variation in health of brittle-pipes due to quality, age, and corrosion level differences, ii) surface deformation not fully acting on pipeline, and iii) unreported failures. We also successfully demonstrated our methodology for monitoring drink water pipe networks over the Hague, the Netherlands, and the relative deformation metric was found useful towards managing water pipe assets (Arsénio et al., 2014), see Appendix B.

3.6. Summary and conclusions

We introduced a method for limited classification of radar targets using height information. The main advantages of this method are: self-reliant on PS (no use of external DEM), estimation of ground DEM as a by-product, and inclusion of height estimates' quality descriptor in its classification process. Through a simulation study, we have shown that the height-based target classification performs better when there are more PS from the ground-level. The main drawback of this method is its capacity to discriminate ground level when the number of scatterers from the ground level is minimum. However, this

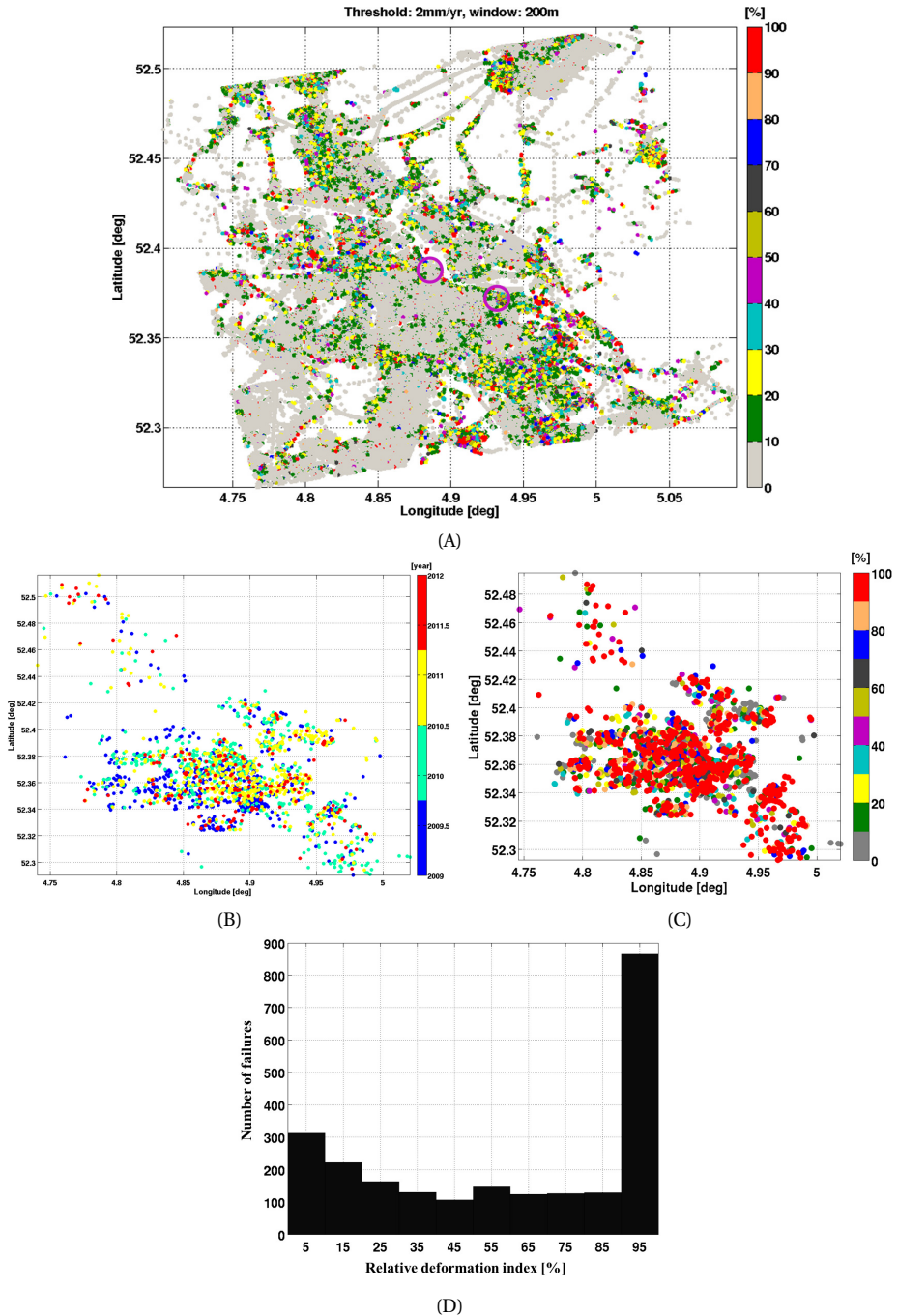


Figure 3.37: Gas pipeline failures data from Amsterdam compared with relative deformation index. In most of the cases gas pipeline failure is located nearby a PS with a relatively high RDI. (A) A scene covering Amsterdam region showing RDI per scatterer. RDI (in %) is computed with a $\sigma_v = 2$ mm/yr, $R_C^d = 6$ mm/yr and $R = 200$ m. The location of the two gas explosion sites are marked in magenta. (B) Gas pipe failures registered between 2009 and 2012 in Amsterdam. (C) RDI value within 50 m of the location of gas pipe failures. (D) Relation of number of gas pipe failures with RDI. For very high RDI (above 90%), there are a high number of gas pipeline failures.

issue can be ignored since the InSAR satellites usually acquire images with (moderately) steeper incidence angles which guarantee a sufficient point density from the ground level. The performance of our classification method is tested with 20 years of real data over Amsterdam from ERS (1992-2000), ENVISAT (2002-2010), and TerraSAR-X (2009-2012). The DEM generated from the classification is found to be about 1 m accurate when validated with a high-quality lidar dataset. Applying the proposed deformation classification method, we are able to classify deformation into five deformation regimes: autonomous structural motion, shallow compaction, local land subsidence, inter-structural deformation, and no relative motion. Further, we have introduced a new parameter RDI to quantify relative deformation and its usefulness for infrastructure monitoring is validated with building age data and gas pipeline failure data. The proposed deformation classification approach has been applied to a stack of interferograms over Amsterdam and the monitoring of the below-ground gas pipeline assets are successfully demonstrated.

4

Positioning and target association in high resolution imagery

Remote sensing radar satellites cover wide areas and provide spatially dense measurements, with millions of scatterers. Knowledge of the precise position of each radar scatterer is essential to identify the corresponding object and interpret the estimated deformation. The absolute position accuracy of SAR (Synthetic Aperture Radar) scatterers in a 2D radar coordinate system, after compensating for atmosphere and tidal effects, is in the order of centimeters for TerraSAR-X (TSX) spotlight images. However, the absolute positioning in 3D and its quality description are not well known. Here, we exploit time-series Interferometric SAR to enhance the positioning capability in three dimensions. The 3D positioning precision is parameterized by a variance-covariance matrix and visualized as an error ellipsoid centered at the estimated position. The intersection of the error ellipsoid with objects in the field is exploited to link radar scatterers to real world objects.

We demonstrate the estimation of scatterer position and its quality using 20 months of TSX stripmap acquisitions over Delft, the Netherlands. Using trihedral corner reflectors (CR), the accuracy of absolute positioning in 2D is about 7 cm. In 3D, an absolute accuracy of up to ~66 cm is realized, with a cigar-shaped error ellipsoid having centimeter precision in azimuth and range dimensions, and elongated in cross-range dimension with a precision in the order of meters (the ratio of the ellipsoid axis lengths is 1/3/213, respectively). The CR absolute 3D position, along with the associated error ellipsoid, is found to be accurate and agree with the ground truth position at a 0.01 level of significance. For other non-CR coherent scatterers, the error ellipsoid concept is validated using 3D building models. In both cases, the error ellipsoid not only serves as a quality descriptor but can also help to associate radar scatterers to real world objects.

4.1. Introduction

Interferometric Synthetic Aperture Radar (InSAR) has evolved towards an effective tool for measuring the Earth's topography and surface deformation. Persistent Scatterer Interferometry (PSI) is one of the techniques to process a set of images in order to identify phase-

This chapter has been published in the Journal of Geodesy, 2016 (Dheenathayalan et al., 2016).

coherent scatterers known as Persistent Scatterers (PS) (Ferretti et al., 2001; Kampes, 2005). These PS are a random subset of scatterers in the imaged scene, usually but not necessarily man-made objects, that are phase-coherent over time. Deformation and location of these PS are estimated. The relative deformation is estimated with millimeter-level precision, but the *positioning* precision is usually in the order of decimeters or even meters. This hampers the interpretation of the deformation signal, as it is unclear which object is associated with the measurements.

In previous studies (Small et al., 2004a; Schubert et al., 2010; Eineder et al., 2011; Schubert et al., 2012a) the absolute positioning capabilities of SAR systems were validated in the 2D (azimuth and range) radar geometry by measuring the phase center of CR with DGPS (Differential Global Positioning System) to centimeter accuracy and predicting their respective positions in the radar image. The absolute position accuracy of ENVISAT (Small et al., 2004a,b, 2007) and Sentinel-1A (Schubert et al., 2014) images were computed to be in the order of several decimeters at best both in azimuth and range directions. Recently, for TSX the absolute geo-location accuracy after compensating for atmospheric and tidal effects, was reported to be in the order of a few centimeters in azimuth and range directions (Schubert et al., 2010; Eineder et al., 2011; Schubert et al., 2012a; Balss et al., 2013). The accuracy of PS heights was indirectly validated by Perissin (2008) (for ERS and ENVISAT) and Dheenathayalan and Hanssen (2013) (for ERS, ENVISAT and TSX), both by making a Digital Terrain Model (DTM) from smoothed PS heights and comparing this with precise elevation data obtained from airborne lidar. 3D positioning was presented for TSX stereoSAR by Gisinger et al. (2015), and for PSI the absolute 3D positioning and quality assessment by Dheenathayalan et al. (2013, 2014). In this paper we: (i) present a systematic geodetic procedure to precisely estimate the position, (ii) perform error propagation to estimate the position quality, and as a result, (iii) demonstrate the association of scatterers by intersecting error ellipsoids to real world objects.

This paper is structured as follows. Section 4.2 presents the definition of different coordinate systems, and the sequence of mapping operators used to estimate the position and describe their stochastic properties. The discussions related to computing the 2D and 3D positioning accuracy are briefed in Section 4.3. The experimental setup to demonstrate our approach is explained in Section 4.4. The 2D and 3D positioning results for corner reflectors and other coherent scatterers are presented in Section 4.5. Section 5.4 is devoted to the conclusions.

4.2. Scatterer positioning

Using a single SAR image, the position of a scatterer can only be described in two dimensions, namely azimuth and (slant) range. In order to estimate the third dimension, cross-range, InSAR observations are necessary. The position of a scatterer in the radar geometry (azimuth, range and cross-range) is mapped to a 3D TRF (Terrestrial Reference Frame) reference system using a non-linear mapping transformation. This transformation, known as geocoding, is based on the range, Doppler, and ellipsoid/DEM (Digital Elevation Model) equations (Schreier, 1993b; Small et al., 1996).

However, the radar measurements are composed of several higher-order positioning terms which impact the position estimation, see Appendix A. Some of the higher-order

¹Applicable when we position scatterers in a TRF.

Table 4.1: Higher-order positioning terms, and their impact in azimuth and range for TSX images (Balss et al., 2013; Dheenathayalan et al., 2013). Dominant terms are highlighted in bold.

Higher-order terms	Impact in azimuth	Impact in range
Azimuth shift	dm to cm	Nil
Path delay (iono+tropo)	Nil	m
Solid earth tides	cm	dm
Tectonics ¹	dm	dm
Atmosphere pressure loading	mm	< cm
Ocean tidal loading	mm	< cm
Pole loading	mm	mm
Ocean pole tides	mm	mm
Atmosphere tidal loading	mm	mm

positioning terms and their magnitude of impact are tabulated in Tab. 4.1. Dominant terms such as atmospheric delay, Solid Earth Tides (SET), tectonics, and timing errors (azimuth shift) can cause position improvements ranging from centimeters to even several meters. In the following, precise scatterer positioning in radar, time, and geodetic coordinate systems and their transformations are discussed, including error propagation.

Scatterer positioning is the procedure that maps a position in radar image coordinates (dimensionless sample units) to a corresponding point in a TRF, an Earth-centered Earth-fixed reference system (datum) with units in meters. This mapping procedure is subdivided into a number of steps. We apply a standard Gauss-Markov approach, where we use the output estimators of the previous mapping step as input observations for the subsequent step. This facilitates error propagation and quality assessment and control. In the end, this leads to an estimated position in a (Cartesian) TRF, with units in meters, and associated “precision” expressed via the variance-covariance (VC) matrix of the estimator.

4.2.1. In the dimensionless 2D radar datum

The initial amplitude measurements refer to a target, or scatterer, in the focused radar image. The local two-dimensional datum is expressed in pixels in range and azimuth, with sample units. The origin of the datum is the location $(0,0)^2$ for range and azimuth, respectively. To determine the estimated sub-pixel position (μ_P, ν_P) of target P in range and azimuth direction respectively, the measurement involves reconstruction of a sinc-function (Cumming and Wong, 2005), by performing complex FFT oversampling and detecting the sub-pixel location of the target by finding the maximum peak. This peak position represents the effective phase center of the radar scatterer. In case of an isolated ideal point scatterer, such as a trihedral corner reflector, the effective phase center is the apex of the reflector. But, in a complex urban environment, containing many dominant scatterers, depending

²Represents the lower-left corner of the pixel.

on the distribution of scatterers, the effective phase center may be less well-defined.

Quality description

The quality of the sub-pixel position is dependent on (i) shifting of the peak position due to clutter or more than one dominant scatterer, a function of the Signal to Clutter Ratio (SCR), and (ii) the oversampling factor Δ . Therefore, the variance of the peak (in azimuth or range) position estimate of a target P in i -th image can be approximated as:

$$\sigma_{\mu_{P,i}}^2 = \sigma_{\nu_{P,i}}^2 = \frac{3}{2 \cdot \pi^2 \cdot \text{SCR}_{P,i}} + \frac{1}{12 \cdot \Delta_{P,i}^2}, \quad (4.1)$$

where the first term of the above equation provides the Cramér-Rao Bound for a change in peak position due to clutter in a given SLC (Single Look Complex) image (Stein, 1981; Bamler and Eineder, 2005). The SCR value is the ratio between the peak intensity and the background, calculated by averaging the intensity values in the oversampled area excluding the cross-arm pattern produced by the side lobes of the scatterer of interest. The second term in Eq. (4.1) represents the error due to quantization introduced by a chosen oversampling factor (Bennett, 1948). Increasing the oversampling factor does not necessarily always yield a better sub-pixel position, there is a saturation point beyond which the position doesn't improve significantly for any significant increase in oversampling factor. In addition to oversampling, an optional 2D quadratic interpolation is usually performed for computational efficiency (Press et al., 1992).

The observed subpixel position is considered to be unbiased, $(\mu_P, \nu_P) = E\{\underline{\mu}_P, \underline{\nu}_P\}$, with its quality expressed by the pixel variances from Eq. (4.1) in range and azimuth, $(\sigma_{\mu}^2, \sigma_{\nu}^2)$. The underline (e.g., $\underline{\mu}_P, \underline{\nu}_P$) denotes that the quantities are stochastic in nature and $E\{\cdot\}$ is the expectation operator. The range and azimuth position observations are considered to be uncorrelated, as they are derived independently.

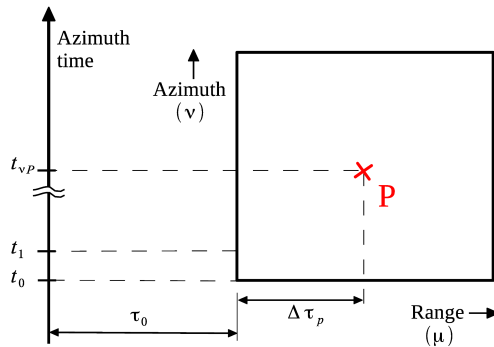


Figure 4.1: Slow (t) and fast (τ) time coordinates.

4.2.2. To the temporal 1D radar datum

The first mapping operator transforms the pixel-positions to time-units. Slow-time (azimuth direction), t , and fast-time, τ , refer to the azimuth and range timing, respectively (Bamler and Schättler, 1993), but the time coordinate is inherently one-dimensional. The

absolute time in the satellite system is given by the onboard GPS receiver. GPS time is like an atomic clock time, however not identical to the Universal Time Coordinated (UTC). The corrections from GPS time to UTC, e.g., leap seconds, is implemented in the Level-1 SAR data processing chain or in the GPS instrument. The absolute time, annotated in the SAR header files, is usually provided with a resolution of one microsecond³ (ENVISAT (Kult et al., 2007) and TSX/TDX (Fritz, 2007)).

The internal relative timing for radar positioning requires more precise numbers⁴. The relative time is obtained from the local oscillator (Massonnet and Vadon, 1995). This relative time determines the SWST (Sampling Window Start Time), also known as the near-range time \underline{t}_0 , the sampling frequency, which determines the pixel spacing or posting, and the PRF (Pulse Repetition Frequency) or PRI (Pulse Repetition Interval).

The mapping from the pixel coordinates $(\underline{\mu}_P, \underline{\nu}_P)$ to the fast (\underline{t}_{μ_P}) and slow (\underline{t}_{ν_P}) time coordinates can be expressed as, see Fig. 4.1,

$$\underline{t}_{\mu_P} = \underline{t}_0 + \underline{\mu}_P \cdot \underline{\Delta t} \quad (4.2)$$

$$\underline{t}_{\nu_P} = \underline{t}_0 + \underline{\nu}_P \cdot \underline{\Delta t}, \quad (4.3)$$

where $\underline{t}_P = \underline{t}_{\nu_P} + \underline{t}_{\mu_P}$ is the time of receiving the zero-Doppler signal corresponding to target P , \underline{t}_0 is the time of emitting the first pulse of the (focused) image, \underline{t}_{ν_P} is the time of emitting the pulse that contains P in the focused image (azimuth time), \underline{t}_0 is the time to the first range pixel, or SWST, $\underline{\Delta t} = \text{PRI} = \text{PRF}^{-1}$, and $\underline{\Delta t} = f_s^{-1}$ is the range sample interval, the inverse of the range sampling frequency (RSF).

Quality description

The quality of the time-units in Eqs. (4.2) and (4.3) is dependent on (i) the absolute time given by GPS, and (ii) the local oscillator. The observed fast and slow time coordinates of a scatterer are given by linearizing Eqs. (4.2) and (4.3) with initial values $(t_0^o, \nu_P^o, \Delta t^o, \tau_0^o, \mu_P^o, \Delta \tau^o)$:

$$\sigma_{\tau_{\mu_P}}^2 = [1, \Delta \tau^o, \mu_P^o] \begin{bmatrix} \sigma_{\tau_0}^2 & & \\ & \sigma_{\mu_P}^2 & \\ & & \sigma_{\Delta \tau}^2 \end{bmatrix} [1, \Delta \tau^o, \mu_P^o]^T \quad (4.4)$$

$$\sigma_{\tau_{\nu_P}}^2 = [1, \Delta t^o, \nu_P^o] \begin{bmatrix} \sigma_{t_0}^2 & & \\ & \sigma_{\nu_P}^2 & \\ & & \sigma_{\Delta t}^2 \end{bmatrix} [1, \Delta t^o, \nu_P^o]^T, \quad (4.5)$$

where $\sigma_{t_0}^2$ is based on the quality of the absolute timing from GPS, and pixel variances $(\sigma_{\mu_P}^2, \sigma_{\nu_P}^2)$ are given by Eq. (4.1). $\sigma_{\Delta t}^2, \sigma_{\Delta \tau}^2$, and $\sigma_{\tau_0}^2$ represent the respective precisions of PRF, RSF, and SWST given by the local oscillator. The quality of the observed slow and fast time coordinates is influenced by the accuracy and precision of timing information provided in the metadata.

Recently, Marinkovic and Larsen (2013); Bähr (2013) reported a systematic frequency decay of the ENVISAT ASAR instrument which was claimed to originate from the deterioration of local oscillator performance over time. This could introduce a time-dependent-timing error, and as a consequence the time coordinate and positioning capability would

³In case of TSX and TDX (TanDEM-X), an additional parameter record namely 'timeGPSFraction' provides seconds with up to 19 significant digits.

⁴Timing expressed in seconds with 10^{-10} (for ENVISAT) up to 10^{-20} (for TSX) significant decimal digits.

drift over time. If this drift is known *a priori*, it can be compensated, otherwise it has to be estimated empirically over a period of time using calibration targets. In that case, a time-dependent-timing-calibration is mandatory. In our study, the timing information (from the metadata) expressed with a given number of decimal digits is assumed to reflect their precision.

4.2.3. To the geometric 2D radar datum

The second mapping operator transforms the time coordinate t_P or its 2D equivalent (τ_{μ_P}, t_{v_P}) for point P to distances in range and azimuth, (r, a) respectively. To discriminate between time and space, we refer to these coordinates as range-distance, r and azimuth-distance, a , acknowledging the pleonasm. The coordinate system has its origin in the phase center of the antenna. The range distance r_P is expressed as

$$\begin{aligned} r_P &= \frac{v_0}{2} \cdot (\underline{\tau}_{\mu_P} + \underline{\tau}_{\text{sys}}) + r_{\epsilon}, \\ &= \frac{v_0}{2} \cdot (\underline{\tau}_0 + \underline{\mu}_P \cdot \underline{\Delta\tau} + \underline{\tau}_{\text{sys}}) + r_{\epsilon}, \end{aligned} \quad (4.6)$$

where $\underline{\tau}_{\text{sys}}$ is an offset representative of unmodeled internal electronic delays in the system, and r_{ϵ} represents the higher-order positioning terms in range with $E\{r_{\epsilon}\} \neq 0$. Note that the atmosphere is not vacuum, but the true velocity along the path is unknown. Therefore, we use v_0 instead of the mean propagation velocity v (incorporating potential bending effects along the path between the antenna phase center and the target) of the radio signal. Also, in practice, $\underline{\tau}_{\text{sys}}$ is either not known and/or not explicitly given in the metadata. Frequently, during the commissioning phase of the mission, the process of Eq. (4.6) is inverted: instead of deriving r_Q from accurate timing measurements, r_Q is empirically measured from some calibration target Q , $\underline{\tau}_{\mu_Q}$ is measured in the commissioning phase, and a correction bias $\underline{\tau}_{\text{sys}}$ is estimated, often even using the velocity of light in vacuum, v_0 , instead of the actual velocity v . From inverting Eq. (4.6)

$$\underline{\tau}_{\text{sys}} = \frac{2 \cdot r_Q}{v_0} - \underline{\tau}_{\mu_Q}, \quad (4.7)$$

is estimated and hence Eq. (4.6) becomes

$$r_P = \frac{v_0}{2} \cdot (\underline{\tau}_0 + \underline{\mu}_P \cdot \underline{\Delta\tau} + \frac{2 \cdot r_Q}{v_0} - \underline{\tau}_{\mu_Q}) + r_{\epsilon}. \quad (4.8)$$

Then, instead of explicitly stating this correction factor in the metadata, the timing information may be corrected directly during the generation of the product annotations. Such corrections were described for the case of ENVISAT by Small et al. (2004a), and Dheenathayalan et al. (2014).

This also holds for the distance from the radar antenna phase center to the instantaneous center-of-mass (CoM) of the satellite, and the position of the independent positioning device (GNSS receiver, retro-reflector, or equivalent device). For highly accurate positioning (geo-localization) of targets, the reported state-vectors should point at the antenna phase center. However, conventionally the state-vectors are defined to the CoM of the satellite, which may shift during the lifetime of the mission due to depletion of consumables. Even if the CoM was once calibrated at the start of the mission, a mismatch

(as a drift over time) should be given due consideration during the lifespan of the mission. Similarly, variability of $\underline{t}_{\text{sys}}$ over time should be considered due to aging effects of the electronics on board.

From Appendix A, we know that the slant range measurement also includes the higher-order terms such as path delay, tectonics and SET. Therefore, the range position \underline{r}_P in Eq. (4.8) can be written as:

$$\underline{r}_P = \frac{v_0}{2} \cdot (\underline{t}_0 + \underline{\mu}_P \cdot \underline{\Delta t} + \frac{2 \cdot \underline{r}_Q}{v_0} - \underline{t}_{\mu_Q}) + \underline{r}_{\text{pd}_P} + \underline{r}_{\text{tect}_P} + \underline{r}_{\text{set}_P}, \quad (4.9)$$

where $\underline{r}_{\text{pd}_P}$, $\underline{r}_{\text{tect}_P}$, and $\underline{r}_{\text{set}_P}$ are the modeled position correction factors in range. $\sigma_{\underline{r}_{\text{pd}_P}}^2$, $\sigma_{\underline{r}_{\text{tect}_P}}^2$, and $\sigma_{\underline{r}_{\text{set}_P}}^2$ (see Appendix A) are set to their respective *a priori* precisions.

Now in the along-track dimension, the geometric azimuth distance \underline{a}_P is expressed as:

$$\begin{aligned} \underline{a}_P &= \underline{v}_{s/c} \cdot (\underline{t}_{v_P} + \underline{t}_{\text{sys}}) + \underline{a}_\epsilon, \\ &= \underline{v}_{s/c} \cdot (\underline{t}_0 + \underline{v}_P \cdot \underline{\Delta t} + \underline{t}_{\text{sys}}) + \underline{a}_\epsilon, \end{aligned} \quad (4.10)$$

where $\underline{v}_{s/c}$ is the local velocity of the spacecraft, $\underline{t}_{\text{sys}}$ is an offset due to instrument timing errors, and \underline{a}_ϵ represents the higher-order positioning terms in azimuth with $E\{\underline{a}_\epsilon\} \neq 0$, see Appendix A. $\underline{t}_{\text{sys}}$ is also estimated and corrected during the commissioning phase to yield

$$\underline{a}_P = \underline{v}_{s/c} \cdot (\underline{t}_0 + \underline{v}_P \cdot \underline{\Delta t} + \frac{\underline{a}_Q}{\underline{v}_{s/c}} - \underline{t}_{v_Q}) + \underline{a}_\epsilon. \quad (4.11)$$

Radar satellites are often zero-Doppler steered, and the raw data is then focused to produce a SLC image. In this study, the offsets emanating from the Doppler (usually zero-Doppler) image processing (SAR focusing) are assumed to be already compensated by the processor during focusing and hence not considered.

From Appendix A, the azimuth measurements are influenced by timing ($\underline{a}_{\text{shift}_P}$), tectonics ($\underline{a}_{\text{tect}_P}$) and SET ($\underline{a}_{\text{set}_P}$). Then, Eq. (4.11) can be rewritten by:

$$\underline{a}_P = \underline{v}_{s/c} \cdot (\underline{t}_0 + \underline{v}_P \cdot \underline{\Delta t} + \frac{\underline{a}_Q}{\underline{v}_{s/c}} - \underline{t}_{v_Q}) + \underline{a}_{\text{shift}_P} + \underline{a}_{\text{tect}_P} + \underline{a}_{\text{set}_P}, \quad (4.12)$$

where $\underline{a}_{\text{shift}_P}$, $\underline{a}_{\text{tect}_P}$, and $\underline{a}_{\text{set}_P}$ are the modeled position correction factors in azimuth and $\sigma_{\underline{a}_{\text{shift}_P}}^2$, $\sigma_{\underline{a}_{\text{tect}_P}}^2$, and $\sigma_{\underline{a}_{\text{set}_P}}^2$ are set to their respective *a priori* precisions.

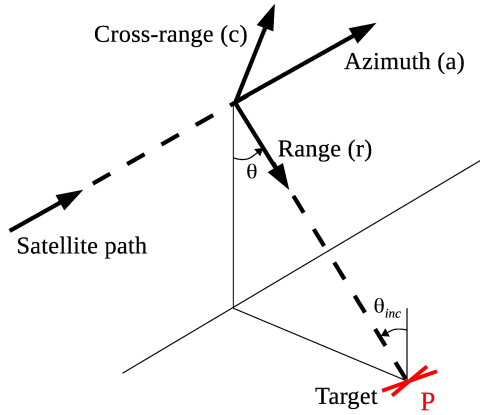


Figure 4.2: 3D radar geometry: range (r), azimuth (A), and cross-range (C) dimensions.

Quality description

The observed range and azimuth distances are, (r_p, a_p) , with their quality expressed by the variances in range $\sigma_{r_p}^2$ and azimuth $\sigma_{a_p}^2$ with initial values $(\tau_0^o, \mu_p^o, \Delta\tau^o, \tau_{\text{sys}}^o, \nu_{s/c}^o, t_0^o, \nu_p^o, \Delta t^o, t_{\text{sys}}^o)$ determined by:

$$\sigma_{r_p}^2 = \alpha^T \cdot A \cdot \alpha \quad (4.13)$$

$$\sigma_{a_p}^2 = \beta^T \cdot B \cdot \beta, \quad (4.14)$$

where

$$\alpha = \left[\frac{\nu_0}{2}, \frac{\nu_0}{2} \cdot \Delta\tau^o, \frac{\nu_0}{2} \cdot \mu_p^o, \frac{\nu_0}{2}, 1, 1, 1 \right],$$

$$\beta = \left[t_0^o + \nu_p^o \cdot \Delta t^o + t_{\text{sys}}^o, \nu_{s/c}^o, \nu_{s/c}^o \cdot \Delta t^o, \nu_{s/c}^o \cdot \nu_p^o, \nu_{s/c}^o, 1, 1, 1 \right],$$

$$\text{diag}\{A\} = [\sigma_{\tau_0}^2, \sigma_{\mu_p}^2, \sigma_{\Delta\tau}^2, \sigma_{\tau_{\text{sys}}}^2, \sigma_{r_{\text{pd}p}}^2, \sigma_{r_{\text{rect}p}}^2, \sigma_{r_{\text{set}p}}^2], \text{ and}$$

$$\text{diag}\{B\} = [\sigma_{\nu_{s/c}}^2, \sigma_{t_0}^2, \sigma_{\nu_p}^2, \sigma_{\Delta t}^2, \sigma_{t_{\text{sys}}}^2, \sigma_{a_{\text{shift}p}}^2, \sigma_{a_{\text{rect}p}}^2, \sigma_{a_{\text{set}p}}^2].$$

The range and azimuth distance estimates are considered to be uncorrelated, neglecting any covariance as a result of timing, and other common error sources.

4.2.4. To the geometric 3D radar datum

Range, azimuth, and cross-range⁵ distances form a 3D orthogonal Cartesian coordinate system in a radar geometry as shown in Fig. 4.2. With a single SLC image, the third dimension, namely cross-range (c) cannot be derived, but interferometric SAR observations can be utilized to estimate it. Therefore, unlike azimuth and range distances, cross-range distance is expressed relative to a spatial (reference point R) and a temporal (reference master image M) reference.

⁵This is also sometimes called elevation in the literature, even though it is not in the vertical direction.

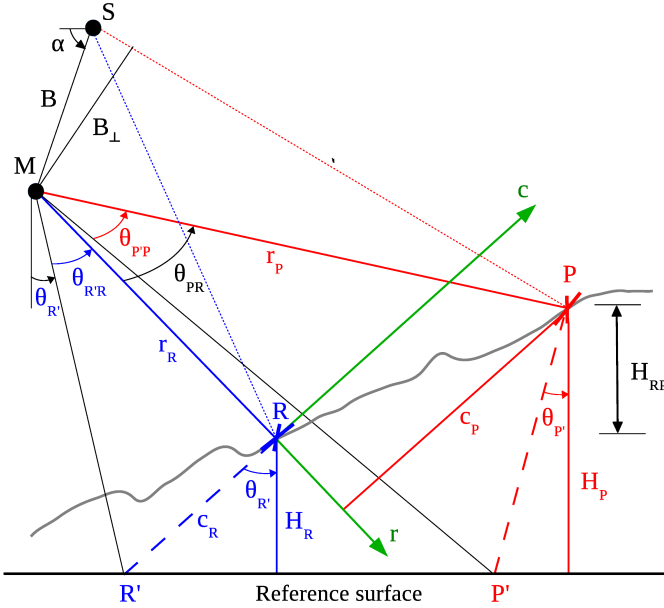


Figure 4.3: Cross-range (c) component estimated from interferometry. R is the reference point and P is the scatterer of interest. The reference surface can be considered to be either a flat surface (as drawn here), an ellipse, or a DEM.

From Fig. 4.3, the cross-range component is estimated from the change in look-angle θ_{PR} , and the distance between the sensor and the scatterer r_P (from Eq. (4.9)). The change in look angle θ_{PR} is estimated from the interferometric phase change. Under the far-field approximation (Zebker and Goldstein, 1986), the cross-range becomes

$$\begin{aligned}
 c_P &= r_P \cdot \theta_{PR}, \\
 &= -\frac{\lambda}{4\pi} \frac{r_P}{B_1 \cos(\theta_{R'} - \alpha_1)} \phi_{PR,1}, \\
 &= -\frac{\lambda}{4\pi} \frac{r_P}{B_{\perp,1}} \phi_{PR,1},
 \end{aligned} \tag{4.15}$$

where λ is the radar wavelength. B_1 , $B_{\perp,1}$, $\phi_{PR,1}$, and α_1 are the baseline, perpendicular baseline, the unwrapped interferometric phase, and the baseline angle between a master M and slave S acquisition, respectively.

Each interferometric pair provides a derived observation of change in look-angle (θ_{PR}) (Hanssen, 2001a, pp. 34–40). When a radar scatterer is measured from a stack of m repeat-pass acquisitions with different baselines $[B_{\perp,1}, B_{\perp,2}, \dots, B_{\perp,m-1}]$, then θ_{PR} and hence \hat{c}_P and its precision $\sigma_{\hat{c}_P}^2$ can be better estimated using BLUE (Best Linear Unbiased Estimation)

(Teunissen et al., 2005):

$$\begin{aligned}\hat{c}_p &= \hat{x}(1) \text{ and } \sigma_{\hat{c}_p}^2 = \sigma_{\hat{x}}^2(1,1), \text{ with} \\ \hat{x} &= (G^T Q_y^{-1} G)^{-1} G^T Q_y^{-1} y \text{ and } \sigma_{\hat{x}}^2 = (G^T Q_y^{-1} G)^{-1},\end{aligned}\tag{4.16}$$

given the following functional and stochastic models with initial values $(r_p^o, B_{\perp,1}^o, B_{\perp,2}^o, \dots, B_{\perp,m-1}^o)$,

$$E\left\{ \begin{bmatrix} \phi_{PR,1} \\ \phi_{PR,2} \\ \vdots \\ \phi_{PR,m-1} \\ \underline{B}_{\perp,1} \\ \underline{B}_{\perp,2} \\ \vdots \\ \underline{B}_{\perp,m-1} \\ \underline{r}_p \end{bmatrix} \right\} = \begin{bmatrix} \frac{-4\pi \cdot B_{\perp,1}^o}{\lambda \cdot r_p^o} \\ \frac{-4\pi \cdot B_{\perp,2}^o}{\lambda \cdot r_p^o} \\ \vdots \\ \frac{-4\pi \cdot B_{\perp,m-1}^o}{\lambda \cdot r_p^o} \\ 1 \\ & 1 \\ & & \ddots \\ & & & 1 \\ & & & & 1 \end{bmatrix} \begin{bmatrix} c_p \\ B_{\perp,1} \\ B_{\perp,2} \\ \vdots \\ B_{\perp,m-1} \\ r_p \end{bmatrix}$$

$\underbrace{\hspace{10em}}_y \quad \underbrace{\hspace{15em}}_G \quad \underbrace{\hspace{5em}}_x$

and diagonal matrix $D\{y\} = Q_y$ with entries

$$\left[\sigma_{\phi_{PR,1}}^2, \sigma_{\phi_{PR,2}}^2, \dots, \sigma_{\phi_{PR,m-1}}^2, \sigma_{B_{\perp,1}}^2, \sigma_{B_{\perp,2}}^2, \dots, \sigma_{B_{\perp,m-1}}^2, \sigma_{r_p}^2 \right],\tag{4.17}$$

where $E\{\cdot\}$ is the first moment, $D\{\cdot\}$ is the second moment, $\sigma_{r_p}^2$ is given by Eq. (4.13), $\left[\sigma_{\phi_{PR,1}}^2, \sigma_{\phi_{PR,2}}^2, \dots, \sigma_{\phi_{PR,m-1}}^2 \right]$ is from interferometry, and $\left[\sigma_{B_{\perp,1}}^2, \sigma_{B_{\perp,2}}^2, \dots, \sigma_{B_{\perp,m-1}}^2 \right]$ takes into account the baseline quality due to orbit inaccuracies in $(m-1)$ interferometric pairs.

Quality description

The quality of the range $\sigma_{r_p}^2$ and azimuth $\sigma_{a_p}^2$ distances is derived as explained in Section 4.2.3. The cross-range precision $\sigma_{\hat{c}_p}^2$ depends on: (i) sub-pixel positions (of both reference point R and scatterer P), (ii) temporal phase stability of the reference point R , (iii) phase unwrapping, (iv) the number of images, (v) the perpendicular baseline distribution, and (vi) phase noise. In this work, (i) and (ii) are handled, while (iii) is assumed to be error-free, and factors (iv) to (vi) are subject to data availability and not discussed here.

Since we use PSI to obtain the cross-range component, our 3D position estimates viz. range, azimuth, and cross-range are relative in nature. Therefore, the higher-order (azimuth and range) positioning terms are applied with respect to a master image. In order to obtain the absolute 3D position for scatterers, we choose a scatterer with known 3D position as a reference point during PSI processing. Then, from Eqs. (4.13), (4.14), and (4.16), the uncertainty in positioning a scatterer P in 3D radar geometry is expressed using the following VC matrix:

$$Q_{rac} = \begin{bmatrix} \sigma_{r_p}^2 & & \\ & \sigma_{a_p}^2 & \\ & & \sigma_{\hat{c}_p}^2 \end{bmatrix}.\tag{4.18}$$

From this VC matrix, the 3D position error ellipsoid per scatterer can be drawn. Though the error in azimuth and range positions will have some influence in cross-range estimation, in our study, the error covariances are assumed to be negligible and hence the 3D VC matrix is considered to be diagonal.

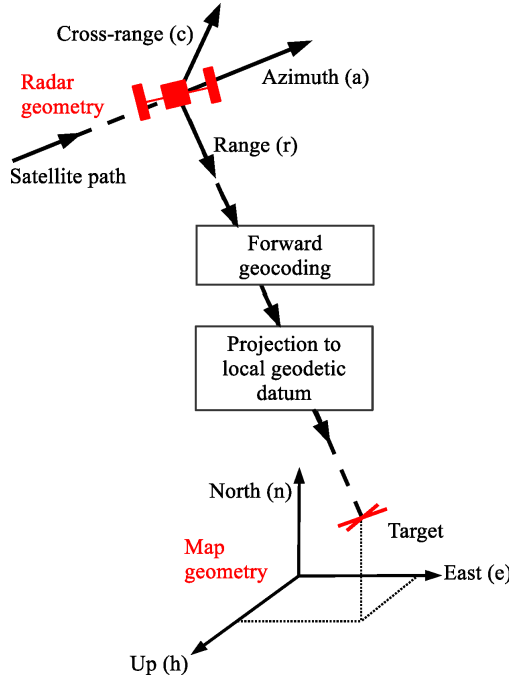


Figure 4.4: Radar to map geometry.

4.2.5. To the ellipsoidal 3D TRF datum and local 3D coordinate system

A scatterer in the 3D radar geometry (r_p, a_p, c_p) is transformed to a 3D TRF reference system expressed in (x_p, y_p, z_p) using a non-linear mapping transformation known as geocoding is described by the following equations (Schwäbisch, 1995b; Small et al., 1996; Hanssen, 2001a):

$$\text{Doppler: } \underline{V}_{s/c}(\underline{a}_p) \cdot \left(\frac{P - \underline{S}(\underline{a}_p)}{|P - \underline{S}(\underline{a}_p)|} \right) - \frac{\lambda}{2} \cdot \underline{f}_D(\underline{a}_p) = 0,$$

$$\text{Range: } (P - \underline{S}(\underline{a}_p)) \cdot (P - \underline{S}(\underline{a}_p)) - r_p = 0,$$

$$\text{Ellipsoid: } \frac{x_p^2}{(l + \underline{H}_p)^2} + \frac{y_p^2}{(l + \underline{H}_p)^2} + \frac{z_p^2}{(b + \underline{H}_p)^2} - 1 = 0,$$

Height of scatterer P above reference surface and its precision:

$$\begin{aligned} \underline{H}_p &= \underline{H}_R + \hat{c}_p \cdot \sin(\theta_{inc,p}), \\ \sigma_{H_p}^2 &= \sigma_{H_R}^2 + \sigma_{\hat{c}_p}^2 \cdot \sin(\theta_{inc,p})^2, \end{aligned} \quad (4.19)$$

where \underline{H}_R is the position (height above reference surface) of the reference point R (see Fig. 4.3), and its precision $\sigma_{H_R}^2$. $P = [x_P, y_P, z_P]$ is the position of scatterer in TRF, $\theta_{inc,P}$ is the incidence angle at P , and $\underline{f}_D(\underline{a}_P)$ is the Doppler frequency while imaging scatterer P at azimuth position \underline{a}_P . For products provided in zero-Doppler annotation, $\underline{f}_D(\underline{a}_P) = 0$. $\underline{S}(\underline{a}_P) = [\underline{s}_x(\underline{a}_P), \underline{s}_y(\underline{a}_P), \underline{s}_z(\underline{a}_P)]$, and $\underline{V}_{s/c}(\underline{a}_P) = [\underline{v}_x(\underline{a}_P), \underline{v}_y(\underline{a}_P), \underline{v}_z(\underline{a}_P)]$ are the respective position and velocity vectors of the spacecraft at the instant of imaging scatterer P at \underline{a}_P during the master acquisition. l and b are the semi-major and semi-minor axis of the reference ellipsoid, respectively.

Optionally, to ease identification and visualization of scatterers at the object level, the 3D TRF coordinates (x_P, y_P, z_P) are further projected into a national or local reference coordinate system (Fig. 4.4). This national or local 3D Cartesian coordinate system is usually defined by coordinates East (e), North (n) and Up or Height (h). Here, we project the 3D TRF coordinates using de Bruijne et al. (2005) into the Dutch National Triangulation system RD ('Rijksdriehoeksstelsel' in Dutch) and vertical NAP ('Normaal Amsterdams Peil') reference system, denoted as RDNAP.

Quality description

The 3D position uncertainty in radar Q_{rac} can be propagated to map geometry Q_{enh} by Monte-Carlo simulation, linearization, or in a geodetic manner by computing the transformation parameters between the radar and map coordinate systems. The geocoding (Eq. (4.19)), and projection (de Bruijne et al., 2005) steps form a complex non-linear process, thus the error propagation is not performed by linearization. Monte-Carlo simulation based approaches are not preferred, as they are relatively time consuming to apply for several (e.g. up to millions of) scatterers in a radar image. In this paper, we use the geodetic approach for error propagation. We know that the geocoding and subsequent projection steps provide point clouds in both the radar $[a_i, r_i, c_i]$ and local map $[e_i, n_i, h_i]$ coordinates, $\forall i \in \{1, 2, \dots, N\}$ scatterers. Therefore, the available point clouds in both radar and local map coordinates are exploited to form the following S-transformation (Baarda, 1981):

$$E\left\{\begin{bmatrix} e_1 \\ n_1 \\ h_1 \\ \vdots \\ e_N \\ n_N \\ h_N \end{bmatrix}\right\} = F \begin{bmatrix} d_{3 \times 1} \\ --- \\ \text{vec}\{R_{3 \times 3}\} \end{bmatrix} \quad (4.20)$$

$$\text{with } F = \begin{bmatrix} 1 & 0 & 0 & a_1 & r_1 & c_1 & 0 & 0 & 0 & 0 & 0 & 0 \\ 0 & 1 & 0 & 0 & 0 & 0 & a_1 & r_1 & c_1 & 0 & 0 & 0 \\ 0 & 0 & 1 & 0 & 0 & 0 & 0 & 0 & 0 & a_1 & r_1 & c_1 \\ \vdots & & & & & & & \vdots & & & & \\ 1 & 0 & 0 & a_N & r_N & c_N & 0 & 0 & 0 & 0 & 0 & 0 \\ 0 & 1 & 0 & 0 & 0 & 0 & a_N & r_N & c_N & 0 & 0 & 0 \\ 0 & 0 & 1 & 0 & 0 & 0 & 0 & 0 & 0 & a_N & r_N & c_N \end{bmatrix},$$

where d is the translation vector, R is the rotation matrix and operator $\text{vec}\{\cdot\}$ is the vector of a matrix. For a given area of interest, transformation parameters S and R are estimated

using BLUE (Teunissen et al., 2005). Then the 3D position error ellipsoid (or VC matrix) can be propagated from radar geometry to a given local map geometry (Fig. 4.4) and vice-versa. From Eq. (4.18) and the variance propagation law, the VC matrix in local map geometry is given by

$$Q_{enh} = R_{3 \times 3} \cdot Q_{rac} \cdot R_{3 \times 3}^T = \begin{bmatrix} \sigma_e^2 & \sigma_{en}^2 & \sigma_{eh}^2 \\ \sigma_{en}^2 & \sigma_n^2 & \sigma_{nh}^2 \\ \sigma_{eh}^2 & \sigma_{nh}^2 & \sigma_h^2 \end{bmatrix}, \quad (4.21)$$

where the diagonal ($\sigma_e^2, \sigma_n^2, \sigma_h^2$) and non-diagonal ($\sigma_{en}^2, \sigma_{eh}^2, \sigma_{nh}^2$) entries are the variances and covariances in east, north and up coordinates, respectively. Then, for each coherent scatterer, from the eigenvalues of Q_{enh} , a 3D error ellipsoid is drawn with the estimated position as its center. The error ellipsoid can be described by its size, shape and orientation:

- The dimensions of the error ellipsoid are given by the eigenvalues of Q_{enh} , which are the diagonal elements of Q_{rac} . Therefore, σ_{rp} , σ_{ap} , and σ_{cp} describe the three semi-axis lengths of the ellipsoid.

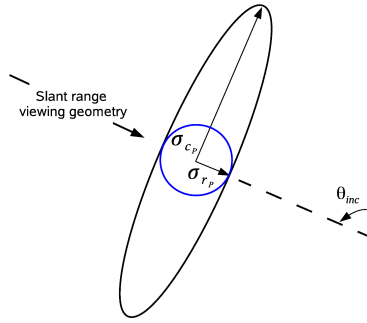


Figure 4.5: A cross-section of error ellipsoid in range and cross-range dimensions. Error ellipse for the cases $\gamma_1 \ll \gamma_2$ (prolate ellipsoid) and $\gamma_1 \approx \gamma_2$ (spheroid) are drawn in black and blue, respectively.

- The shape the ellipsoid is derived from the ratio of their axis lengths, given by $(1/\gamma_1/\gamma_2)$, where $\gamma_1 = \frac{\sigma_{ap}}{\sigma_{rp}}$, and $\gamma_2 = \frac{\sigma_{cp}}{\sigma_{rp}}$, see Tab. 4.2.
- The orientation (inclination) of an error ellipsoid is dependent on the local incidence angle of the radar beam at the target. A cross-section of an error ellipsoid for $\gamma_1 \ll \gamma_2$ (in black) and $\gamma_1 \approx \gamma_2$ (in blue) is shown in Fig. 4.5.

Table 4.2: Depending on the values of γ_1 and γ_2 , the shape of the error ellipsoid will vary from a prolate ellipsoid to a spheroid.

Case	Shape
$1 \lesssim \gamma_1 \ll \gamma_2$	a prolate (cigar-shaped) ellipsoid elongated in cross-range direction
$\gamma_1 \approx \gamma_2 \approx 1$	a spheroid

4.3. Scatterer position validation

Here, the position obtained in the previous section is assessed in 2D and 3D with the ground truth position measurements. Scatterer positioning accuracy or error is defined as the difference between the ground truth and measured (or estimated) positions. The measured position, retrieved from the image, is obtained by performing complex FFT oversampling and detecting the sub-pixel location of a target in a given SLC image and correcting for the higher-order positioning terms as stated in the previous section. The ground truth position, used for validation, is obtained with the aid of an external terrestrial measurement technique such as DGPS. The DGPS instrument is used to measure the phase center of a target of interest such as a trihedral corner reflector.

4.3.1. 2D accuracy

The position accuracy in 2D is computed in radar geometry as the difference between the ground truth and measured positions for azimuth and range coordinates. In 2D, two outcomes are produced:

1. Similar to Small et al. (2004a); Schubert et al. (2010); Eineder et al. (2011), the accuracy is computed without taking into account the stochastic properties of the measurements and the higher-order positioning terms. This computation will serve as an independent validation of the results reported in Schubert et al. (2010); Eineder et al. (2011); Small et al. (2004a,b) for TSX SM images.
2. Then, 2D accuracy is computed taking into account all the stochastic properties as described below.

Let $[\underline{a}_{1,E}, \underline{a}_{2,E}, \dots, \underline{a}_{m,E}]$ and $[\sigma_{a_{1,E}}^2, \sigma_{a_{2,E}}^2, \dots, \sigma_{a_{m,E}}^2]$ be the measured azimuth positions and their respective precisions in m images. If the target is measured with DGPS and then radar-coded by range-Doppler positioning (Meier et al., 1993; Small et al., 1996) to obtain the ground truth positions in m images $[\underline{a}_{1,T}, \underline{a}_{2,T}, \dots, \underline{a}_{m,T}]$ with its precision given by $[\sigma_{a_{1,T}}^2, \sigma_{a_{2,T}}^2, \dots, \sigma_{a_{m,T}}^2]$, then the functional and stochastic models for the azimuth position error (accuracy) can be written as

$$E\{\underline{y}\} = A \underline{\mu}_a, \quad \text{with } \underline{y} = \begin{bmatrix} \underline{a}_{1,T} - \underline{a}_{1,E} \\ \underline{a}_{2,T} - \underline{a}_{2,E} \\ \vdots \\ \underline{a}_{m,T} - \underline{a}_{m,E} \end{bmatrix}, \quad A = \begin{bmatrix} 1 \\ 1 \\ \vdots \\ 1 \end{bmatrix}, \quad \text{and } Q_y = \begin{bmatrix} \kappa_1 & & & \\ & \kappa_2 & & \\ & & \ddots & \\ & & & \kappa_m \end{bmatrix}, \quad (4.22)$$

where κ_i is the part of the *a priori* Q_y matrix representing i -th image, defined as:

$$\kappa_i = \sigma_{a_{i,T}}^2 + \sigma_{a_{i,E}}^2, \quad \forall i \in \{1, 2, \dots, m\}. \quad (4.23)$$

Taking into account Q_y , the first ($\hat{\underline{\mu}}_a$) and second ($\hat{\sigma}_a^2$) moments of azimuth position error are given by:

$$\hat{\underline{\mu}}_a = (A^T Q_y^{-1} A)^{-1} A^T Q_y^{-1} \underline{y}, \quad \text{and } \hat{\sigma}_a^2 = \frac{m}{m-1} \cdot \frac{\hat{\underline{e}}^T Q_y^{-1} \hat{\underline{e}}}{\text{Tr}\{Q_y^{-1}\}}, \quad \text{with residue } \hat{\underline{e}} = \underline{y} - A \hat{\underline{\mu}}_a, \quad (4.24)$$

where operator $\text{Tr}\{\cdot\}$ is the trace of a matrix. If $\hat{\underline{\mu}}_a \neq 0$ then it represents the existence of a systematic bias in the azimuth position estimate, which might have been left uncompensated during the satellite's (geometric) calibration phase.

Similar to Eq. (4.22), given the ground truth range positions in m images by $[\underline{r}_{1,T}, \underline{r}_{2,T}, \dots, \underline{r}_{m,T}]$ and their precisions $[\sigma_{r_{1,T}}^2, \sigma_{r_{2,T}}^2, \dots, \sigma_{r_{m,T}}^2]$, the functional and stochastic models of the range position error is written by,

$$E\{\underline{y}\} = A \underline{\mu}_r, \quad \text{with } \underline{y} = \begin{bmatrix} \underline{r}_{1,T} - \underline{r}_{1,E} \\ \underline{r}_{2,T} - \underline{r}_{2,E} \\ \vdots \\ \underline{r}_{m,T} - \underline{r}_{m,E} \end{bmatrix}, \quad A = \begin{bmatrix} 1 \\ 1 \\ \vdots \\ 1 \end{bmatrix}, \quad \text{and } Q_y = \begin{bmatrix} \kappa_1 & & & \\ & \kappa_2 & & \\ & & \ddots & \\ & & & \kappa_m \end{bmatrix}, \quad (4.25)$$

where $[\underline{r}_{1,E}, \underline{r}_{2,E}, \dots, \underline{r}_{m,E}]$ and $[\sigma_{r_{1,E}}^2, \sigma_{r_{2,E}}^2, \dots, \sigma_{r_{m,E}}^2]$ are the measured range positions and their precisions in m images. κ_i is the part of the Q_y matrix representing i -th image, defined as:

$$\kappa_i = \sigma_{r_{i,T}}^2 + \sigma_{r_{i,E}}^2, \quad \forall i \in \{1, 2, \dots, m\}. \quad (4.26)$$

The first ($\hat{\underline{\mu}}_r$) and second ($\hat{\sigma}_r^2$) moments of range position error is computed by substituting Eq. (4.25) in Eq. (4.24). Similarly, when $\hat{\underline{\mu}}_r \neq 0$, it represents the existence of a systematic bias in the range position estimate. It is an estimate of the residual range timing offset, left uncorrected during calibration.

4.3.2. 3D accuracy

The 3D position accuracy proposed in our study, expressed as the difference between the ground truth and estimated positions, is computed in 3D Cartesian coordinates. For targets with known effective phase centers such as CR, the ground truth position is obtained by measuring it with DGPS. But, for non-CR targets such as PS, the effective phase center is neither known precisely nor can it necessarily be measured per individual scatterer. For such targets, the 3D position accuracy was validated using external 3D building and city models. For 3D positioning, we demonstrate three key results:

1. The improved absolute 3D positioning capability with its precision drawn as an error ellipsoid.
2. Validation of 3D positioning accuracy and the error ellipsoid concept using a hypothesis testing procedure for scatterers whose phase center can be precisely measured (such as CR).

We assume the null hypothesis H_0 that the 3D position estimated $P_E = [\underline{e}_E, \underline{n}_E, \underline{h}_E]$ with uncertainty $Q_{enh,E}$ and the ground truth position (obtained from DGPS) $P_T = [\underline{e}_T, \underline{n}_T, \underline{h}_T]$ with uncertainty $Q_{enh,T}$ measure the same position $[e, n, h]$ of a scatterer. Therefore, the functional and stochastic models of our observations are given by:

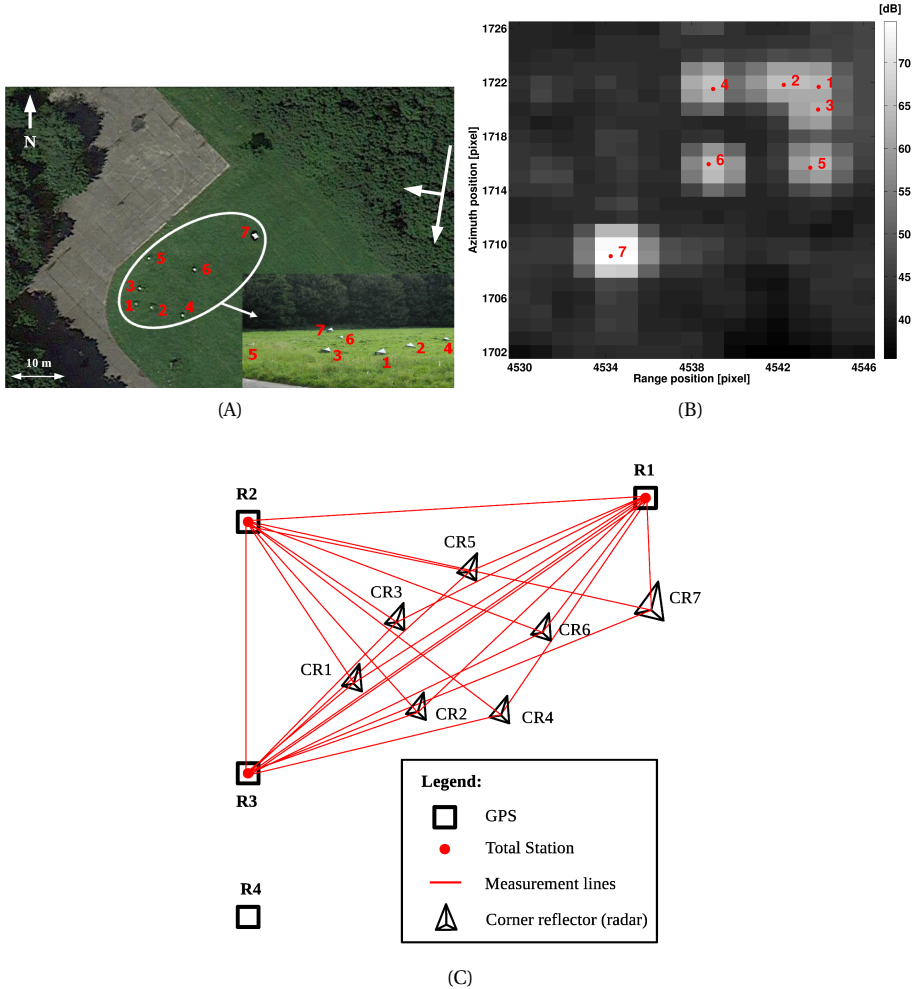


Figure 4.6: Delft corner reflector experiment setup. (A) Delft corner reflector experiment site. Six small (CR 1 to 6) and one big (CR 7) corner reflectors were imaged with TSX SM descending pass acquisitions. (B) Mean intensity image (from 45 acquisitions) covering seven corner reflectors. The colorbar represents the intensity expressed in dB. Subpixel locations are marked with red dots along with their CR numbers. (C) Ground truth measurement setup using DGPS and tachymetry.

$$H_0 : \begin{bmatrix} e^E \\ n^E \\ h^E \\ e^T \\ n^T \\ h^T \end{bmatrix} = \begin{bmatrix} I \\ I \end{bmatrix} \begin{bmatrix} e \\ n \\ h \end{bmatrix} + \underline{\epsilon}, \text{ with } Q_{enh,ET} = \begin{bmatrix} Q_{enh,E} & \\ & Q_{enh,T} \end{bmatrix}, \quad (4.27)$$

where I is the identity matrix, $\underline{\hat{\epsilon}} = y - \hat{y}$ is the vector of residues, and $Q_{enh,ET}$ is the a

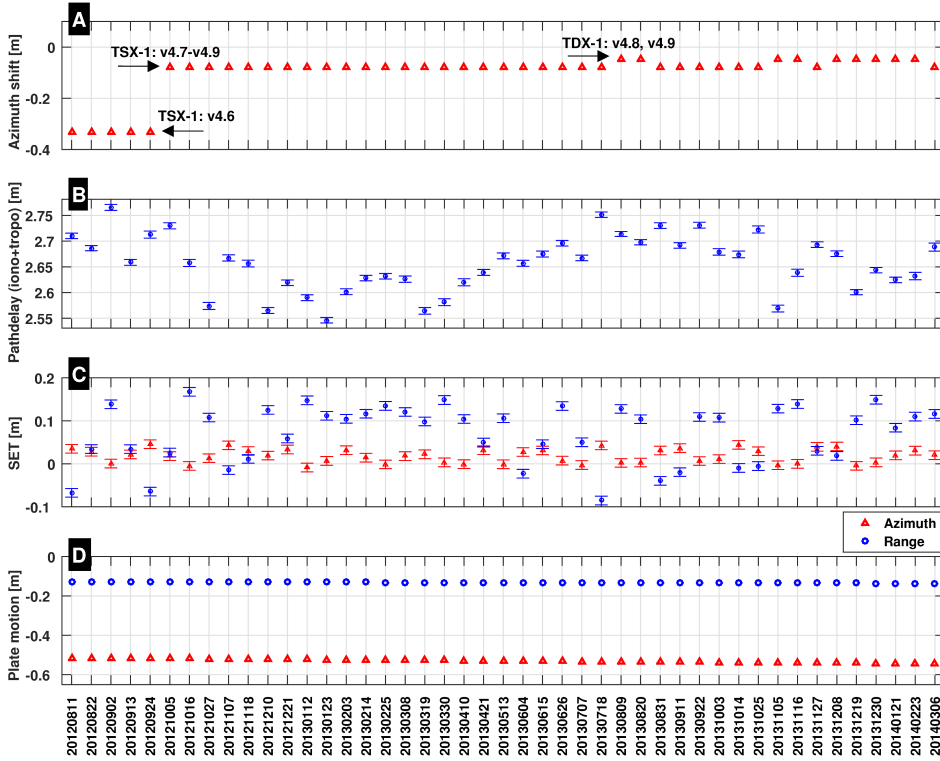


Figure 4.7: Position correction factors for Delft test site computed for TSX SM acquisitions: (A) Azimuth time shift, (B) Total path delay (ionosphere and troposphere) in slant range direction, (C) SET component in azimuth and slant range directions, and (D) Impact of plate motion in azimuth and slant range dimensions. Error bars in (B) and (C) are drawn with 1σ confidence.

priori VC matrix.

$$t_{omt} = \frac{\hat{\epsilon}^T \cdot Q_{enh,ET}^{-1} \cdot \hat{\epsilon}}{3} \quad (4.28)$$

The Overall Model Test (OMT) statistic given by Eq. (4.28) is then applied to infer whether the null hypothesis is accepted at a given confidence level (Teunissen et al., 2005). The higher the confidence at which H_0 is accepted, the lower the false rejection rate and the better the position accuracy validation.

3. Identification of potential radar scatterers by the intersection of the 3D position error ellipsoid with real-life objects.

4.4. Experiment setup

4.4.1. Configuration

Six small (45 cm sides) and one big (1 m sides) trihedral corner reflectors were deployed near Delft in August 2012, see Fig. 4.6A, and oriented for TSX stripmap descending pass

Table 4.3: Precision of ground truth CR position measurements in East, North, and Up coordinates.

	Local position (Tachymetry)			Final position (DGPS and Tachymetry)		
	σ_e [mm]	σ_n [mm]	σ_h [mm]	σ_e [mm]	σ_n [mm]	σ_h [mm]
CR6	2.0	2.2	1.4	10.2	10.2	20.1
CR7	6.4	0.9	0.7	11.9	10.0	20.0

4 acquisitions. The mean intensity image with the corner reflectors is shown in Fig. 4.6B. 45 SM images acquired by a combination of TSX and TDX satellites from Aug 2012 to March 2014 were used in our study. We concentrated on the results of one small (CR6) and one big (CR7) reflector, since they were least interfered by the side-lobes of other reflectors. The CR's ground truth position was measured using a DGPS and tachymetry setup as shown in Fig. 4.6C. Trimble R7 GPS receivers were placed at reference locations marked R1, R2, and R3 for 40 minutes and at R4 for 5 hours. Station R4 served as a local GPS reference. The Total Station (TOPCON GPT-7003i) was placed at R1, R2, and R3 to measure the apex of the CR with respect to R1, R2 and R3 respectively as illustrated by the measurement lines (in red) in Fig. 4.6C. The local positions were found to exhibit a better than 1 cm precision as shown in Tab. 4.3. The GPS data was processed using the Netherlands Positioning Service (NETPOS, 2015). The total station local measurements were then combined with GPS coordinates to get coordinates in ETRS89. From the final position estimates, the overall precision was found to be ~ 1 cm in the horizontal (e and n) and ~ 2 cm in the vertical (h) directions (see Tab. 4.3).

Table 4.4: Change in external azimuth time shift for TSX and TDX processor versions.

Satellite	Processor version	Azimuth shift
		$ a_{\text{shift}} $ [cm]
TSX-1	v4.6	~ 33.34
TSX-1	v4.7,v4.8,v4.9	~ 7.94
TDX-1	v4.8,v4.9	~ 4.81

4.4.2. Computation of the higher-order positioning terms

The higher-order positioning components (Appendix A) were computed for the Delft experiment site. Fig. 4.7 (A) shows the azimuth timing shift values retrieved from the TSX and TDX metadata for the experiment period. During our experiment's time span, the TSX and TDX processors were updated a few times with new (radiometric and geometric) calibration constants. As a result, the azimuth time shift value changed depending on the processor version with which the image was processed and the satellite, as shown in Tab. 4.4. The precision of the timing offset is given in nanoseconds (resulting in < 1 mm standard deviation), hence the stochasticity of this term was neglected. Atmospheric slant range one-way path delay at the time of satellite pass along with its 1σ uncertainty in meters

is plotted in Fig. 4.7 (B). The ionospheric path delay contribution retrieved from Global Ionosphere Maps was given with a precision in the order of 5 to 10 mm. The tropospheric delay was obtained from a GNSS station located in Delft, ~ 7 km from the test site. The use of GPS phase measurements provided tropospheric delays with a precision < 5 mm (Baltink et al., 2002; Bender et al., 2008). Taking the flat topography of the terrain into account, it is assumed that the troposphere contribution at the test site was not significantly different from the location of the GNSS station. Fig. 4.7 (C) shows the SET at the time of image acquisition projected in azimuth and range directions. For our Delft test site, SET was computed using a Fortran program by Milbert (2011). That tidal model was validated by Schubert et al. (2012a) to have 1 cm precision, representing 1σ of the estimated SET. Finally, the corrections due to plate tectonics were computed for each epoch of the satellite pass using the EUREF (the AG (International Association of Geodesy) Regional Reference Frame sub-commission for Europe) permanent network services (Bruyninx, 2004; Bruyninx et al., 2009) and applied before comparing the estimated and ground truth positions. The impact of plate motion in azimuth and range is plotted in Fig. 4.7 (D). The precision of GNSS station velocities was in the order of 1 mm/year, hence the stochasticity of this effect is ignored.

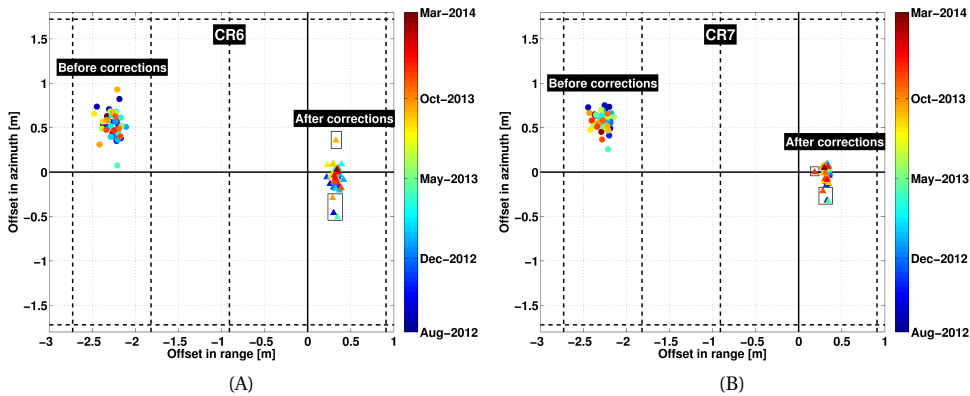


Figure 4.8: Delft experiment site: 2D absolute position accuracy of small CR6 (A) and big CR7 (B) for TSX SM descending mode acquisitions. Dashed lines indicate the azimuth and range pixel spacings. Color represents the variation of position accuracy over time. Images affected by strong wind or heavy rain are marked with black rectangles and were removed in the error computations. (A) Small reflector CR6 with accuracy of -6.1 ± 8.7 cm in azimuth and 32.7 ± 4.2 cm in range. (B) Big reflector CR7 with accuracy of -1.8 ± 6.9 cm and 32.3 ± 2.2 cm in azimuth and range, respectively.

4.5. Results

4.5.1. 2D absolute CR position accuracy

CR phase center positions measured with DGPS and tachymetry were radar-coded and compared with image pixels which were FFT oversampled by a factor of 128×128 . The higher-order positioning terms such as SET, azimuth time shift, path delay and plate tectonics were computed as shown in Fig. 4.7, and mitigated for CR6 and CR7.

Fig. 4.8 shows the 2D absolute position error as a function of time, before and after applying the listed corrections. After applying the corrections, CR6 exhibited a positional

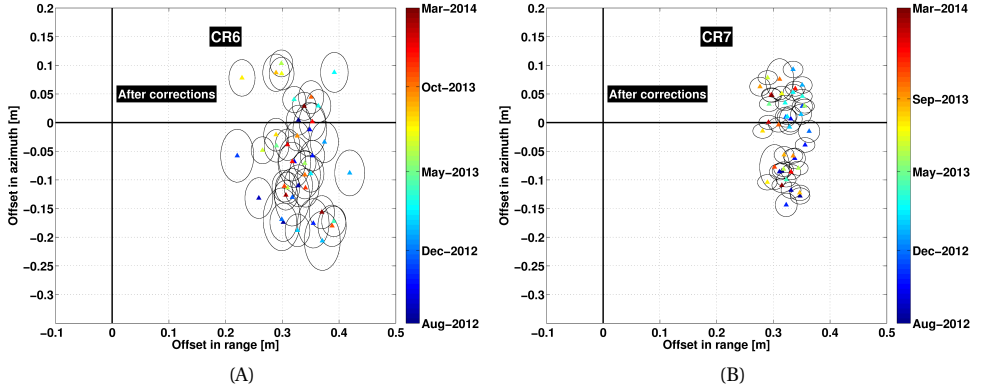


Figure 4.9: Delft experiment site: 2D absolute position accuracy of CR6 (top) and CR7 (bottom) taking stochastic properties into account. Color represents variations in position over time. Error ellipses scaled down to 25% confidence interval (0.32σ) for clear visualization. (A) Small reflector CR6 with accuracies of -4.8 ± 8.6 cm in azimuth and 32.6 ± 4 cm in range. (B) Big reflector CR7 with accuracies of -1.7 ± 6.8 cm and 32.3 ± 2.2 cm in azimuth and range, respectively.

offset of -6.1 ± 8.7 cm in azimuth and 32.7 ± 4.2 cm in range directions, while CR7 showed an offset of -1.8 ± 6.9 cm and 32.3 ± 2.2 cm in azimuth and range, respectively. The bigger CR7 showed slightly better positional accuracy in comparison to its small sized counterpart CR6. Using the results from CR7, one can say that the bias of $\hat{\mu}_a \approx 2$ cm in azimuth and $\hat{\mu}_r \approx 32$ cm in range were due to residual azimuth and range timing errors. Taking the SM mode into account, these 2D position accuracies are comparable to the results from Schubert et al. (2010); Eineder et al. (2011); Balss et al. (2013) and will serve as a benchmark for future SM mode validations.

The amplitude response of CR's impacted by adverse weather conditions (marked with black rectangles in Fig. 4.8) were considered outliers and removed in the error computations. The meteorological data, obtained from the Royal Netherlands Meteorological Institute, were used to understand the outliers. Due to strong wind gusts up to ~ 40 km/h and ~ 90 km/h on days before the acquisitions 24-Sep-2012 and 21-Apr-2013, respectively, CR6 and CR7 appear to be affected. For images dated 11-Sep-2013 and 22-Sep-2013, CR6 showed a 5 to 10 dB dip in SCR due to the accumulation of rain water in the reflector. Heavy rainfall of up to ~ 14 mm was recorded days before the satellite pass. Similarly, CR7 showed a decrease in SCR of about 16 dB on 05-Nov-2013 and 27-Nov-2013 due to strong wind (~ 60 km/h) and rainfall (~ 5 mm). During the experiment timespan, after detecting abnormal amplitude changes, field inspections were carried out to repair (fix the screws or clean the drainage hole of) the affected CR.

It is to be noted (refer the color coding in Fig. 4.8) that the position was not found to systematically drift over time, which could signal either an excellent performance of the onboard local oscillator or that the relevant corrections were being implicitly performed regularly for the respective timing parameters in the metadata. Similar reasoning holds for CoM changes of the satellite.

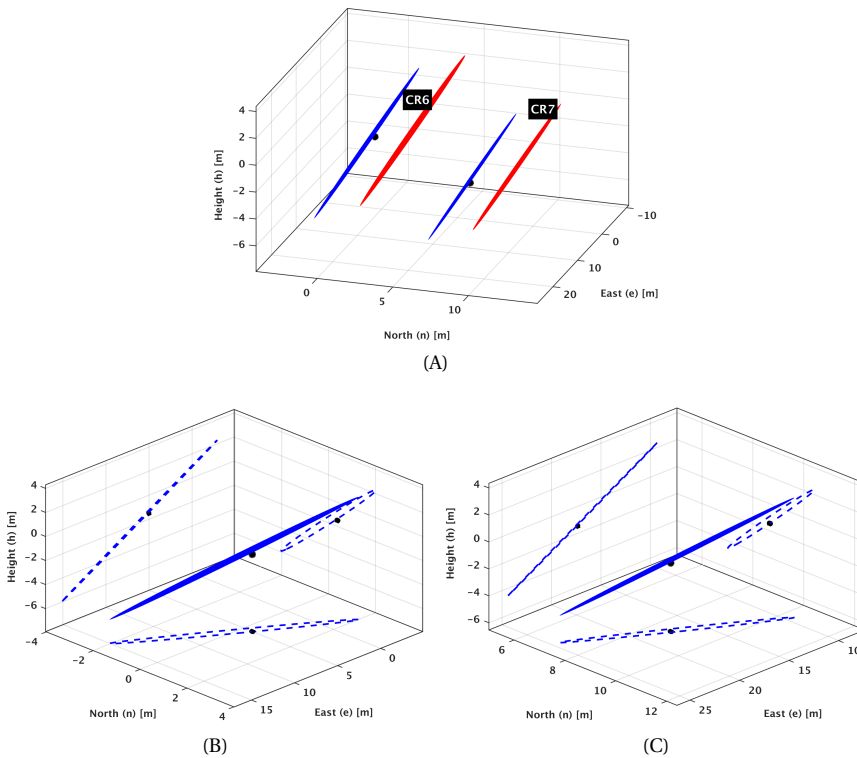


Figure 4.10: Demonstration of 3D position accuracy of corner reflectors with its 3D uncertainty expressed using error ellipsoids. All error ellipsoids are drawn with 1σ confidence intervals. (A) 3D absolute position accuracy with its quality drawn as an error ellipsoid. CR6 and CR7 are plotted before (with red ellipsoid) and after corrections (with blue ellipsoid), both with respect to the ground truth given by its GPS position (indicated with a black dot). (B) The 3D accuracy of CR6 was 1.12 m. It exhibited a cigar-shaped error ellipsoid with a ratio of axis lengths $1/2/129$. (C) The 3D accuracy of CR7 was 0.66 m. It exhibited a cigar-shaped error ellipsoid with a ratio of axis lengths $1/3/213$. With a 0.01 level of significance, the estimated 3D position of CR6 and CR7 with error ellipsoid (in blue) represented the ground truth position (in black). The error ellipsoids in (B) and (C) are projected in *en*, *nh*, and *he* planes (indicated with dashed lines) to illustrate their intersection with the ground truth position.

4.5.2. 2D absolute position accuracy of CR using stochastic information

Here, the 2D accuracy was computed by taking into account the stochastic properties of position estimates, ground truth and the higher-order positioning terms, as described in Eq. (4.13), Eq. (4.14), and sec. 4.3.1. As a result, every azimuth and range position was now associated with a 2×2 diagonal VC matrix and represented by an error ellipse as depicted in Fig. 4.9 for CR6 and CR7. CR6 exhibited position offset of -4.8 ± 8.6 cm in azimuth and 32.6 ± 4 cm in range, while CR7 showed -1.7 ± 6.8 cm and 32.3 ± 2.2 cm in azimuth and range, respectively.

Comparing Fig. 4.9 with Fig. 4.8, the accuracy estimates were slightly improved (for CR6 in azimuth), because the stochastic characteristics of the higher-order terms estimates and the quality of the azimuth and range position estimates did not vary significantly.

4.5.3. 3D absolute positioning and its uncertainty for CR

During PSI and geocoding, CR1, whose height in ETRF89 was known *a priori*, was taken as a reference point, so that the estimated scatterer heights were interpretable. Azimuth and range corrections were applied with respect to the master image (30-Mar-2013). 3D position error modeling and error propagation were applied as described in sec. 4.2.4 and sec. 4.2.5 respectively. The resulting error ellipsoids for CR6 and CR7 before (in red) and after (in blue) the higher-order positioning term corrections are drawn in comparison to their ground truth position (in black) obtained from GPS and tachymetry (Fig. 4.10A).

An offset between the estimated and ground truth 3D positions was computed to be 1.12 m for CR6 and 0.66 cm for CR7. CR6 and CR7 exhibited a prolate error ellipsoid with a ratio of axis lengths 1/2/129 and 1/3/213, respectively. With the precision of height estimated to be $\sigma_{\hat{h}} = 1 \text{ m}$, the cross-range precision $\sigma_{\hat{c}}$ was about 2.5 m. Therefore, the case of $\gamma_1 \ll \gamma_2$ (see Tab. 4.2 and Fig. 4.5) was observed for both reflectors. Hence, the error ellipsoids were cigar-shaped and elongated along the cross-range direction. The orientation of the error ellipsoids was attributed to the steep incidence angle of about 24° for the TSX descending pass acquisitions over Delft. Hypothesis testing (OMT) was carried out as stated in sec. 4.3.2, and as a result, the estimated positions of CR6 and CR7 were found to represent their ground truth positions with a 0.01 level of significance (Figs. 4.10B and 4.10C).

CR7 exhibited better positioning capability (with smaller error ellipsoid) compared to CR6 due to its higher signal-to-noise ratio as seen in Fig. 4.8B. The ground truth 3D position of corner reflectors was plotted in black for comparison. It can be seen that the error ellipsoid (in blue) intersects with the ground truth position (in black), demonstrating our proposed methodology. Hence, providing position corrections along with 3D error modeling helps to identify where the radar reflections originate, in this case a known trihedral corner reflector object.

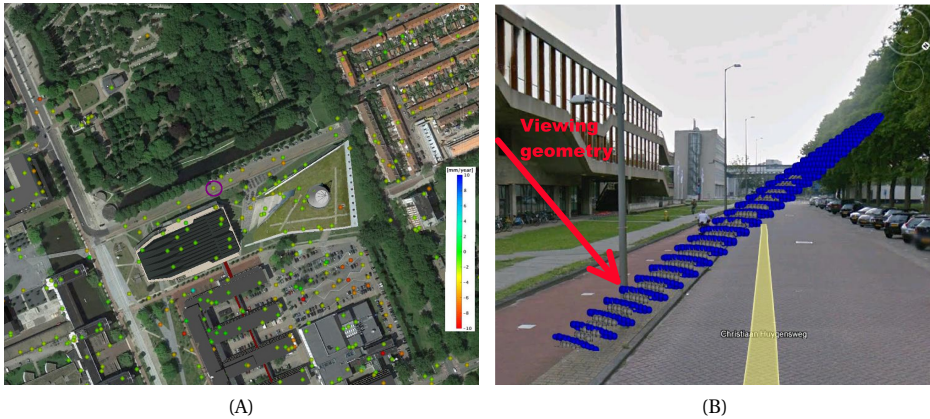
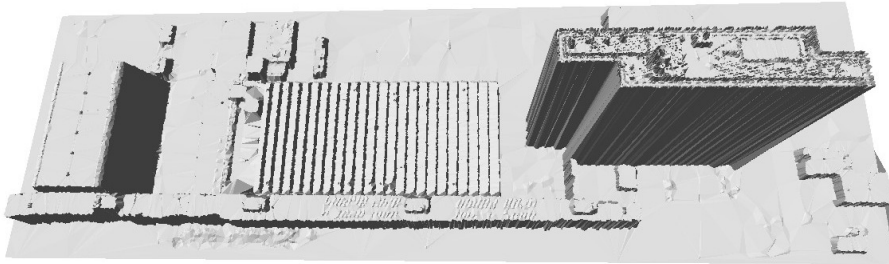


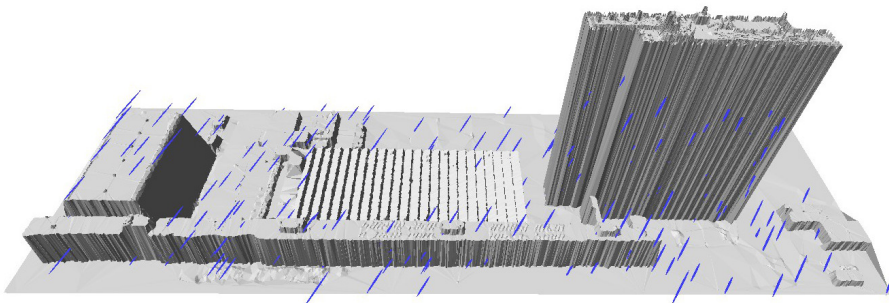
Figure 4.11: Demonstration of 3D absolute positioning and error ellipsoid concept for a coherent scatterer (a metal pole in this case) in a Google Earth Street View map (GoogleInc., 2015). (A) PS deformation rate (in mm/year) map. The scatterer of interest (a PS on a lamp pole) is highlighted in magenta. (B) 3D absolute position with error ellipsoids (blue: 3σ and gray: 1σ). The slant range (line of sight) viewing geometry is marked in red. Here, the error ellipsoid is drawn with point clouds to ease visualization.



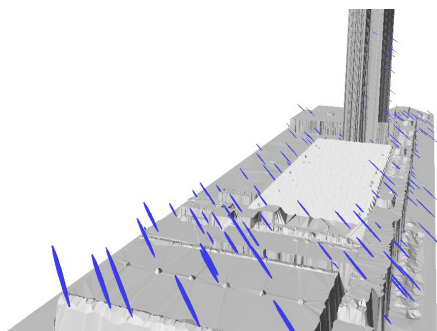
(A)



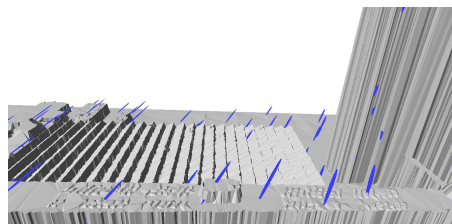
(B)



(C)



(D)



(E)

Figure 4.12: Demonstration of 3D absolute positioning and error ellipsoid concept for coherent scatterers using 3D building model. (A) Geometry of a building of interest in a Google Earth map (GoogleInc., 2015). (B) 3D building model constructed from LiDAR data. (C) Coherent scatterers along with their error ellipsoids drawn in blue with 1σ confidence. (D) Error ellipsoids seen from the side. (E) Zoomed to visualize scatterers with ellipsoids intersecting at roof level.

4.5.4. 3D absolute positioning and its uncertainty for (non-CR) coherent scatterers

The proposed methodology was also applied to all coherent scatterers in the image and the results are presented for: i) an isolated target such as a pole, and ii) an urban region with a 3D building model.

i) A single radar target was selected and its improved (after corrections) 3D position with error ellipsoids (blue: 3σ and gray: 1σ) are drawn over a Google Earth Street View map as illustrated in Fig. 4.11. From its 3D position and error ellipsoid, based on its intersection with a lamp post, we are able to associate the radar scatterer to an object, in this case a lamp post

ii) A complex urban environment (see Fig. 4.12A) with a 3D building model as shown in Fig. 4.12B was selected. The 3D building model was constructed using high quality LiDAR data from Lesparre and Gorte (2012). The improved 3D positions along with the error ellipsoid are drawn (in blue color) for a set of coherent scatterers in the area, see Fig. 4.12C, and from a side view perspective in Fig. 4.12D. Each coherent scatterer had different ellipsoid dimensions, especially visible in the cross-range direction due to different precisions in the cross-range dimension for each scatterer.

Similar to corner reflectors, the error ellipsoids of coherent scatterers were also cigar-shaped, and elongated in cross-range direction. These error ellipsoids (drawn with 1σ confidence interval) not only represent the quality of the 3D position but also its intersection with objects such as a surface, the roof of buildings, ground surface, etc. as shown in Fig. 4.12E and 4.12D, helping to identify and associate the effective phase center of the radar scatterers to real world objects.

4.6. Summary and conclusions

In this study, we set out to demonstrate a systematic geodetic procedure to precisely estimate the radar scatterer position and quality description in a geodetic datum. The proposed method was assessed in 2D and 3D with DGPS, tachymetry, and 3D building models.

In the 2D case, the absolute positioning offset for TSX SM images was found to be approximately 1.8 cm in azimuth and 32.3 cm in range. By removing these decimeter-level position biases, we were able to achieve a 1σ position accuracy of 6.9 cm in azimuth and 2.2 cm in range. It is inferred that, one tie point (a CR target) is mandatory to demonstrate centimeter accuracy positioning capability. Taking the stochastic properties of measurements, models and noise into account, an improvement of up to 1.3 cm was demonstrated. The results improved mainly for the reflector with low SNR (CR6) in azimuth with an offset of approximately 4.8 cm and a standard deviation of 4 cm in range. These independent 2D accuracy estimates were found to be comparable with results from other groups reported and should serve as a benchmark for future TSX SM mode images.

In the 3D case, the position and its error ellipsoids were validated for trihedral corner reflectors. For the CR, absolute positioning offset of 1.12 m for CR6 and 0.66 m for CR7 were achieved. Their error ellipsoids were cigar-shaped with the ratio of axis lengths 1/2/129 (CR6) and 1/3/213 (CR7) were obtained. The CR estimated 3D positions were in accordance with the ground truth positions given by DGPS and tachymetry at a 0.01 level of significance. The intersection of the reflector reference positions with the error ellipsoids justifies the proposed method. Further, the proposed technique was also shown to apply equally well

for any (non-CR) coherent scatterer in an urban environment.

In the current experimental setup, a single tropospheric delay (from GNSS stations) was used for all the scatterers, introducing small errors in the range component, impacting both the 2D and 3D positioning. In the future, combining the relative atmosphere from PSI with GNSS could be used to generate target-specific path delay estimates. It should be noted that the 3D positioning results could be further enhanced by improving the cross-range component estimation. In our study, the scatterer identification was done by visual inspection. In the future, when a complete 3D city model is available, automated algorithms could be implemented to identify intersections and their associated radar counterparts.

5

Positioning and target association in medium resolution imagery

Associating a radar scatterer to a physical object is crucial for the correct interpretation of Interferometric Synthetic Aperture Radar (InSAR) measurements. Yet, especially for medium resolution imagery, this is notoriously difficult, and dependent on the accurate 3D positioning of the scatterers. Here we investigate the 3D positioning capabilities of ENVISAT medium resolution data. We find that the data are perturbed by range-and-epoch-dependent timing errors and calibration offsets. Calibration offsets are estimated to be about 1.58 m in azimuth and 2.84 m in range, and should be added to ASAR products to improve geometric calibration. The timing errors involve a bistatic offset, atmospheric path delay, solid earth tides, and local oscillator drift. This way, we achieve an unbiased positioning capability in 2D, while in 3D, a scatterer was located at a distance of 28 cm from the true location. 3D precision is now expressed as an error ellipsoid in local coordinates. Using the Bhattacharyya metric, we associate radar scatterers to real-world objects. Interpreting deformation of individual infrastructure is shown to be feasible for this type of medium-resolution data.

5.1. Introduction

PSI is well applicable to reflections from man-made objects, such as civil infrastructure. However, complications arise in linking radar reflections (PS) to specific objects (or locations on objects) on the ground in order to unambiguously interpret the estimated line-of-sight (LOS) deformation. Here we attempt to improve the geodetic capacity of PS for infrastructure monitoring using medium resolution SAR imagery. In our analysis, we assume that the SAR resolution cells contain one dominant scatterer.

Associating PS to infrastructure has recently gained more attention, especially using high-resolution sensors such as TerraSAR-X (TSX) or Cosmo-Skymed (CSK). Centimeter-level 2D (radar coordinates) positioning accuracy was successfully demonstrated using corner reflectors in very high-resolution TSX satellite images, see e.g. Eineder et al. (2011); Schubert et al. (2010). Ray-tracing was applied to simulate geometric scattering, and was

This chapter has been published in the IEEE Transactions on Geoscience and Remote Sensing, 2018 (Dheenathayalan et al., 2018).

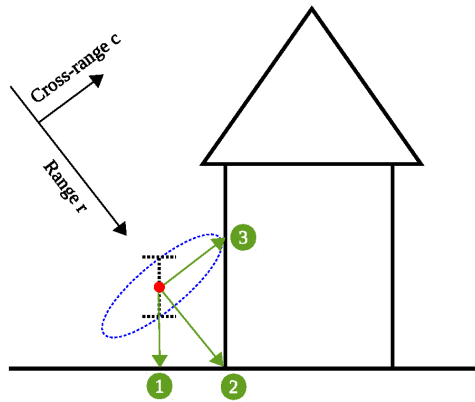


Figure 5.1: Linking a scatterer (red dot) to the ground (1), curb-to-wall interface (2), or a building facade (3). A cross-section of the confidence (error) ellipsoid in the range/cross-range plane is shown in blue. The azimuth (flight) direction is perpendicular to the plane. The scatterer height error is shown in dotted black. In this case, the scatterer is linked to the facade (3) based on the error ellipsoid, instead of the position with the shortest Euclidean distance (or by using only height) (1), or the position in the radar look-direction (2).

5

helpful in the interpretation of TSX spotlight SAR images (Auer et al., 2010). PS were geometrically registered to buildings in a city model with 3D terrestrial coordinates. Factors influencing PS density such as surface structure, shadowing, aspect dependency, and quasi-random effects were discussed in Schunert and Soergel (2016). A systematic procedure to fix positioning errors in radar coordinates, i.e., before geocoding to avoid non-linear distortions in the 3D terrestrial coordinates, was proposed (Dheenathayalan et al., 2013, 2014, 2016). This procedure results in a high positioning quality, and can link the phase center of a radar scatterer to an object, see Fig. 5.1. This was demonstrated using a TSX stripmap dataset in Dheenathayalan et al. (2016). In Zhu et al. (2016) and Gisinger et al. (2015) stereo-SAR radar acquisitions were used from multiple tracks to obtain precise 3D geodetic coordinates of scatterers. However, this approach is not always possible as (i) often only one track with time series is available, and (ii) it requires the same physical scatterer to be visible in both imaging geometries, which is unlikely aside from isolated poles. In contrast to high resolution SAR imagery, medium and low resolution variants feature wide swaths, large volumes of archived imagery, cover a larger area per resolution cell and yield a relatively poor point density. This makes interpretation of coherent scatterers difficult, and hampers the monitoring of individual objects.

Scatterer positions in the radar coordinates azimuth a , range r^1 and cross-range c , are converted to terrestrial coordinates by a non-linear transformation known as geocoding (Schreier, 1993b; Small et al., 1996).

The terrestrial coordinates are converted to local coordinates east e , north n , and height h by a datum transformation. As a result, a constant shift in radar coordinates (a, r, c) will translate into a varying shift in local coordinates (e, n, h). The influence of range, azimuth and cross-range on the local coordinates depends on the local incidence angle θ_{inc} and the heading angle α_h , see Tab. 5.1 and Fig. 5.2. Due to the large scene extent in medium and low resolution imagery, a variety of radar timing offsets (in range and azimuth) further

¹Range always refers to the slant-range radar imaging coordinate, unless explicitly stated otherwise.

Table 5.1: Impact of error in radar coordinates (r, a, c) on the local coordinates (e, n, h) of a target with a local incidence angle θ_{inc} and heading angle α_h .

	$\kappa = r$	$\kappa = a$	$\kappa = c$
$\frac{\partial e}{\partial \kappa}$	$\cos(\alpha_h)\sin(\theta_{\text{inc}})$	$\sin(\alpha_h)$	$\cos(\alpha_h)\cos(\theta_{\text{inc}})$
$\frac{\partial n}{\partial \kappa}$	$-\sin(\alpha_h)\sin(\theta_{\text{inc}})$	$\cos(\alpha_h)$	$-\sin(\alpha_h)\cos(\theta_{\text{inc}})$
$\frac{\partial h}{\partial \kappa}$	$-\cos(\theta_{\text{inc}})$	0	$\sin(\theta_{\text{inc}})$

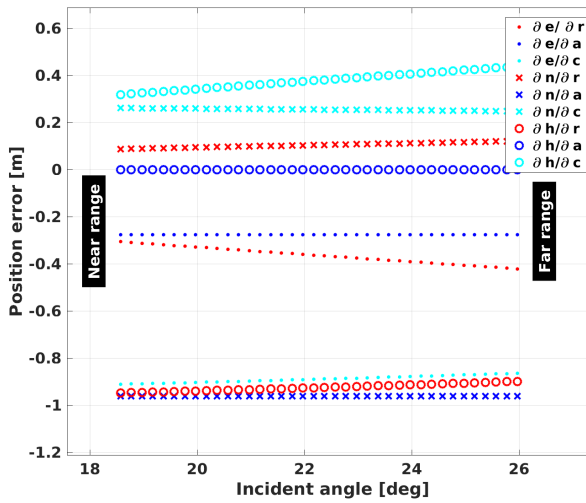


Figure 5.2: Non-linear variation of position error in local coordinates (e, n, h) across the scene for a constant-and-unit change in (r, a, c) when applied to Tab. 5.1. Here, θ_{inc} variation represents a typical ASAR IMS (Imaging Mode Single Look Complex) scene; a heading of $\alpha_h = 196^\circ$ was used.

distorts the positioning capability. Therefore, a systematic procedure needs to be applied, per scatterer, before applying a geocoding procedure to achieve precise positioning to aid interpretation. The procedure proposed by Dheenathayalan et al. (2016) is studied here for the medium resolution case, using ENVISAT ASAR data as an example. Although the ENVISAT sensor stopped acquiring new data after 10 years, ASAR C-band imagery is still widely being processed to understand geodynamic changes of the Earth during the period from 2002 to 2012, and can serve as an example for other medium resolution sensors, such as ERS-1/2, RADARSAT-2, and Sentinel-1A/1B.

In this chapter, Section 5.2 is devoted to the 3D radar scatterer positioning, its dominant error sources, and linking scatterers to real-world objects. The experimental setup and the positioning results are described in Section 5.3, for corner reflectors and other coherent scatterers. Section 5.4 draws the main conclusions.

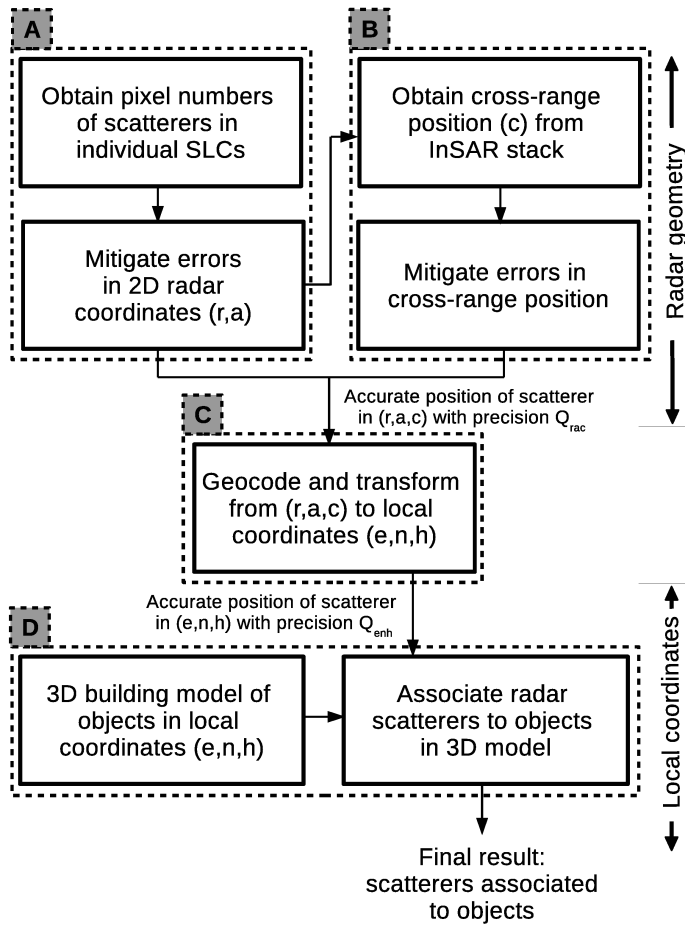


Figure 5.3: Procedure to obtain an accurate 3D position and perform target association to an object.

5.2. Positioning and target association

A 2D SAR image with range and azimuth coordinates (r, a) shows scatterers with (local) 3D coordinates (e, n, h) . Transforming the position of the scatterer from radar geometry to local coordinates, and subsequently linking it to objects is performed in four steps, see sections 5.2.1, 5.2.2, 5.2.3, and 5.2.4, as well as Fig. 5.3.

5.2.1. Mitigate errors in 2D position of radar scatterers

The position of a radar scatterer P in 2D radar coordinates $(a_P$ and $r_P)$ is measured by performing complex FFT (Fast Fourier Transform) oversampling and detecting the sub-pixel location of its amplitude peak. Thus, the 2D position in radar coordinates can be obtained solely from a single SLC (Single Look Complex) image. The stronger the scatterer's SCR (Signal to Clutter Ratio), the smaller its variance in position, $\sigma_{r_P}^2$ and $\sigma_{a_P}^2$.

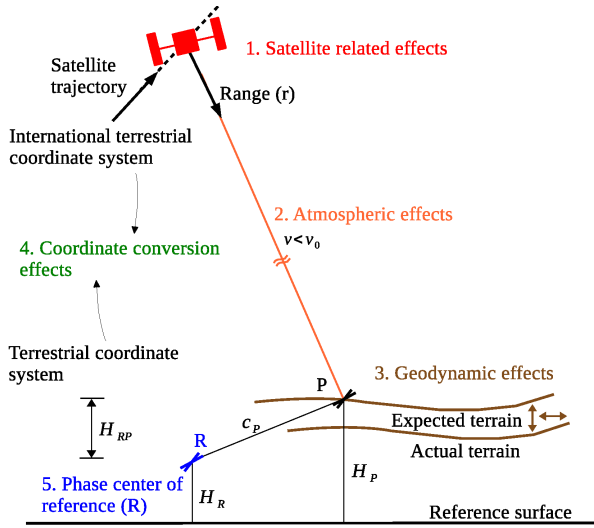


Figure 5.4: Components (1 to 5) impacting scatterer positioning. H_R , and H_P are the respective heights of reference point R and target P from a reference surface. H_{RP} and c_P are the height and cross-range position of scatterer P relative to reference point R , respectively. v is the actual propagation velocity of the radio waves between the radar antenna and the scatterer, while v_0 is the velocity in vacuum.

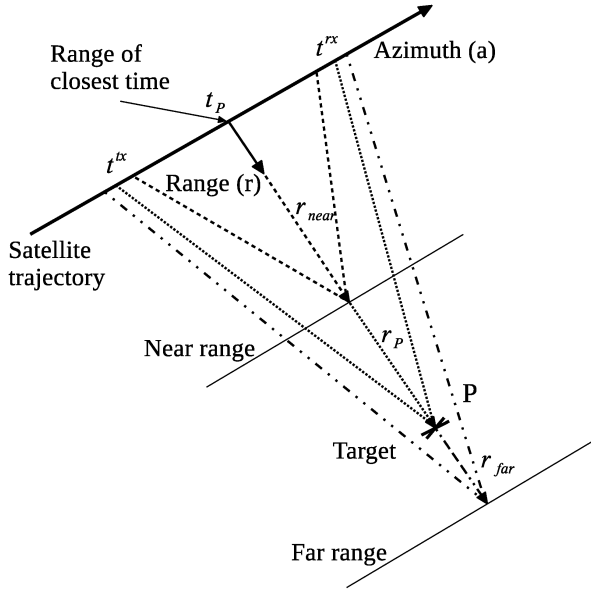


Figure 5.5: The bistatic effect scales with the range of the target r_P from the sensor at zero-Doppler (range of closest) time. r_{near} and r_{far} are the distances to the near and far range swath extremes.

The 2D position of a scatterer P in radar coordinates (r_P, a_P) follows from

$$\begin{aligned}
 r_P &= \frac{v_0}{2} \left(\tau_0 + \mu_P (\Delta \tau + \tau_{l_0}) + \tau_{p d_P} + \tau_{set_P} + \tau_{tect} \right) + r_{cal}, \\
 a_P &= v_{s/c} \left(t_0 + v_P (\Delta t + t_{l_0}) + t_{bi_P} + t_{set_P} + t_{tect} \right) + a_{cal},
 \end{aligned}
 \tag{5.1}$$

where

ν_0 velocity of microwaves in vacuum,

$\nu_{s/c}$ local velocity of the spacecraft,

t_0 time of transmission of first pulse of focused image,

τ_0 time to the first range pixel,

$\Delta\tau$ range sampling interval,

Δt azimuth pulse repetition interval,

t_{lo}, τ_{lo} corrections applied to Δt and $\Delta\tau$ due to local-oscillator drift,

τ_{set_p}, t_{set_p} timing correction factors due to Solid Earth Tides (SET) in range and azimuth, respectively,

τ_{tect}, t_{tect} corrections due to plate tectonics, in range and azimuth, respectively,

τ_{pd_p} range path delay,

t_{bi_p} azimuth bistatic correction,

r_{cal}, a_{cal} residual unmodeled calibration offsets.

These last offsets are unmodeled, and need to be empirically estimated and removed during calibration campaigns. While they are location and epoch independent, they are sensor dependent.

Below we elaborate on the various components in Eq. (5.1), see also Fig. 5.4, subdivided in four classes:

1. satellite-related timing corrections ($\tau_{lo}, t_{lo}, t_{bi_p}$),
2. atmospheric (τ_{pd_p}), and geodynamic (τ_{set_p}, t_{set_p}) corrections,
3. coordinate transformation effects (τ_{tect}, t_{tect}), and
4. unmodeled calibration offsets (r_{cal}, a_{cal}).

Satellite corrections

Here, we discuss the impact of three factors: the target-specific bistatic timing correction (t_{bi_p}), the sensor local oscillator drift (τ_{lo} and t_{lo}), and the center-of-mass (CoM) changes of the satellite during its lifetime.

The raw radar signal is transmitted at t^{tx} and recorded at the time of reception, t^{rx} , of the back-scattered (echo) return from the target P , see Fig. 5.5. During SAR image focusing, the received time of the echo should be converted to zero-Doppler time, i.e., t_p . If this time difference (see t_{bi_p} in Eq. (5.1)) is not compensated for, the azimuth timing error leads to a geolocation shift in azimuth. Note that this azimuth timing error scales proportionally with range, cf. Fig. 5.5, between r_{near} and r_{far} . This problem was observed in ENVISAT ASAR data, and is known as the “bistatic” effect, see Small et al. (2004b). The bistatic azimuth offset varies between ~ 18.5 m in near range and ~ 19.5 m in far range, see Figs. 5.5 and

5.10. Though this azimuth bias is strictly an annotation convention issue, it has to be compensated for to achieve optimal positioning accuracy.

Marinkovic and Larsen (2015) reported a systematic frequency decay over the lifetime of the ENVISAT ASAR instrument, which was assumed to originate from the deterioration of the Local Oscillator (LO) performance over time. The LO could introduce a systematic drift in the range position of about 0.04 pixels per year (Marinkovic and Larsen, 2015). Hence, the range position can drift about 3 m over the 10 years lifetime of the mission. Based on an analysis over a set of $\sim 10,000$ ASAR images, the impact of the LO oscillator drift expressed in ppm (parts per million) was given by Marinkovic and Larsen (2015):

$$\text{LO}_{\text{drift}} = \left[a + b \Delta t - c \Delta t^2 + d \Delta t^3 \right] \cdot 10^{-6},$$

with $a = 0.7037$, $b = 0.3266$, $c = 0.0148$, and $d = 0.0035$, (5.2)

where Δt is the relative time of acquisition in years since 01-Jan-2008. Here, the constant term in Eq. (5.2) is obtained after removing the calibration offsets from Eq. (5.1) in Marinkovic and Larsen (2015). Based on Eq. (5.2), a new set of azimuth and range timing parameters ($\Delta\tau + \tau_{l_o}$ and $\Delta t + t_{l_o}$ in Eq. (5.1)) are to be replaced with their corresponding annotated values in the header files to mitigate the effect of this drift.

It is expected that the center-of-mass (CoM) of the satellite changes during the 10-year ENVISAT mission due to the consumption of fuel (hydrazine). This could cause a drift over time in azimuth and/or range coordinates. Unfortunately, no information could be retrieved to model this behavior. Here we assume that the effects of CoM changes will be absorbed implicitly by the other drift corrections.

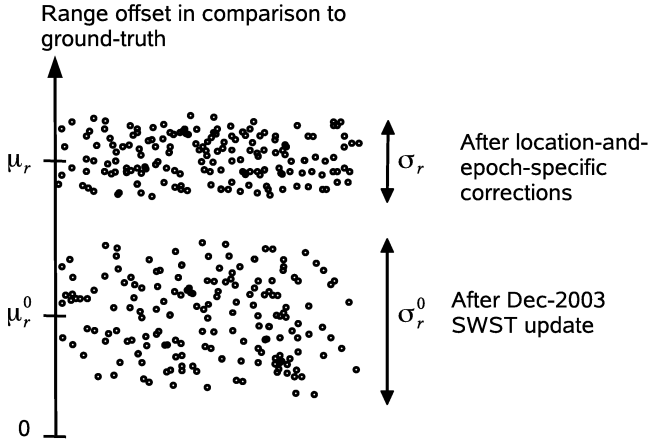


Figure 5.6: Expected impact of location-and-epoch-specific corrections (μ_r, σ_r) over a one-time SWST bias range update (μ_r^0, σ_r^0) for ASAR range position.

Atmospheric and geodynamic effects

Radio waves are delayed by the Earth's ionosphere and the troposphere (Hanssen et al., 1999a). This delay is caused by a reduced propagation velocity of the radio waves ($v < v_0$) and the bending of the ray path due to refraction. The latter is negligible for SAR

acquisitions with $\theta_{\text{inc}} < 87^\circ$ (Bean and Dutton, 1968). Hence, the change in propagation velocity is the only factor attributed to the atmospheric delay.

In the case of the TerraSAR-X satellite, average ionospheric and tropospheric time delays are specifically annotated², enabling users to decide on a tailor made atmospheric correction (Fritz, 2007). In the case of ASAR, such specific annotations are lacking. During the ENVISAT commissioning phase, a mean range position offset (dominated by atmospheric effects) was computed from several calibration targets (transponders and corner reflectors) located at several locations (Flevoland, the Netherlands and Dübendorf, Switzerland). This offset was subsequently absorbed in an update of the SWST (Sampling Window Start Time) for all ASAR products from 12-Dec-2003 onwards (Small et al., 2004a). Thus, instead of annotating all individual corrections, as in TerraSAR-X, ASAR has many physical effects lumped together in one parameter, through which they are not easily separable. These involve timing, atmospheric (ionosphere + troposphere), geodynamic (SET, etc), and tectonic plate motion effects. Moreover, these values are only based on the situation at a few specific locations and times of the calibration campaign. As the atmospheric delay at the time of the calibration is already lumped in the SWST, doing another full atmospheric correction for a specific location and epoch means that effectively the dominant part of the atmospheric delay will be added again to the data. Thus, it will introduce an increased range position offset, from μ_r^0 to μ_r , as shown in Fig. 5.6. However, location-and-epoch-specific corrections will decrease the dispersion of the offsets, i.e., the standard deviation decreases from σ_r^0 to σ_r , see Fig. 5.6. A similar explanation holds for the azimuth position.

5

Empirical estimation of residual 2D offsets

After removing the modeled corrections in Eq. (5.1), unmodeled offsets r_{cal} and a_{cal} in range and azimuth positions remain. In range, r_{cal} is attributed to a residual internal electronic instrument delay (after internal instrument calibration based upon calibration pulses), the state vector estimation inaccuracies, and range bias between near-field calibration measurements made on the ground pre-launch and actual end-to-end far-field measurements made over calibration site(s) during commissioning. In azimuth, a_{cal} is associated to a potential bias between the ASAR instrument radar time and the time coordinate used in the DORIS (Doppler Orbitography and Radio-positioning Integrated by Satellite) orbit determination. These residual offsets, assumed to be common and constant for all ASAR products, need to be estimated using calibration targets. These calibration constants can be considered as a refinement to the Dec-2003 SWST bias update (r_{cal} for range), and a_{cal} as an additional offset in azimuth. For this purpose, calibration targets such as corner reflectors (CR) or transponders (TR) need to be deployed in the scene and their ground truth position needs to be measured using an independent technique. Empirically estimated calibration offsets and precisions in azimuth (a_{cal}, σ_a) and range (r_{cal}, σ_r) are given by

$$\hat{a}_{\text{cal}} = E\{\underline{a}_{i,T} - \underline{a}_{i,E}\}, \quad (5.3)$$

$$\sigma_a^2 = D\{\underline{a}_{i,T} - \underline{a}_{i,E}\}, \quad (5.4)$$

$$\hat{r}_{\text{cal}} = E\{\underline{r}_{i,T} - \underline{r}_{i,E}\}, \quad (5.5)$$

$$\sigma_r^2 = D\{\underline{r}_{i,T} - \underline{r}_{i,E}\}, \quad (5.6)$$

²In the *GEOREF.xml* file.

where $E\{\cdot\}$, and $D\{\cdot\}$ are the expectation and dispersion operators, respectively. The underline (e.g., $\underline{r}_{i,T}$, $\underline{a}_{i,E}$) denotes that the quantities are stochastic in nature. \underline{a}_E and \underline{r}_E are the measured azimuth and range positions of a scatterer in the i^{th} SLC image after correcting for model errors such as bistatic effect, local oscillator drift, path delay, SET, and plate tectonics. The 3D ground truth position of a scatterer is radar-coded by range-Doppler positioning to obtain 2D radar coordinates $\underline{a}_{i,T}$ and $\underline{r}_{i,T}$ in the i^{th} SLC image (Meier et al., 1993; Small et al., 1996).

5.2.2. Cross-range positioning of radar scatterers

In order to find the position of a scatterer in the third dimension, namely cross-range c_P , the interferometric phase is exploited. Unlike azimuth and range, the cross-range component is estimated using a series of interferometric SAR acquisitions in a relative manner, *i.e.* with respect to a reference point R at a reference epoch (master image) (Hanssen, 2001a):

$$c_P = r_P \cdot \theta_{PR}, \quad (5.7)$$

where θ_{PR} is the change in look angle estimated from PSI. The precision in cross-range (σ_{c_P}) is dictated by the phase quality driven by SCR, the perpendicular baseline distribution of the stack, the error in baseline due to orbits, the phase unwrapping (assumed to be error-free), and the precise position of reference point R . The precision of the cross-range position can be written by,

$$\sigma_{c_P}^2 = \sigma_{c_{P,\text{orb}}}^2 + \sigma_{c_{P,\text{SCR}}}^2 + \sigma_{c_R}^2, \quad (5.8)$$

where the terms $\sigma_{c_{P,\text{orb}}}^2$, $\sigma_{c_{P,\text{SCR}}}^2$, and $\sigma_{c_R}^2$ are explained in the following sections.

Impact of orbits

The change in cross-range position Δc_P of a point P obtained from an interferometric pair (see Fig. 5.7) can be given by (Hanssen, 2001a, pp. 113–130),

$$\begin{aligned} \Delta c_P &= -c_P^0 \cdot \frac{|\mathcal{E}| \cos(\theta - \beta)}{B_{\perp}^0}, \\ &= -c_P^0 \cdot \frac{\mathcal{E}_{\perp}}{B_{\perp}^0}, \end{aligned} \quad (5.9)$$

where c_P^0 is the initial cross-range position computed with perpendicular baseline B_{\perp}^0 , ignoring the residual perpendicular baseline \mathcal{E}_{\perp} caused by the orbit error \mathcal{E} . θ is the look-angle. Assuming a Gaussian distributed perpendicular baseline error with a standard deviation $\sigma_{\mathcal{E}_{\perp}}$, the uncertainty in cross-range $\sigma_{c_{P,\text{orb}}}$ can be written by,

$$\sigma_{c_{P,\text{orb}}} = \frac{c_P^0}{B_{\perp}^0} \cdot \sigma_{\mathcal{E}_{\perp}}. \quad (5.10)$$

The larger the perpendicular baseline, the lower the impact of the state vector errors on the cross-range computation.

Non-parallel orbits might cause decorrelation (a small reduction in SCR due to viewing angle differences) and a phase ramp in azimuth direction in the interferograms. The

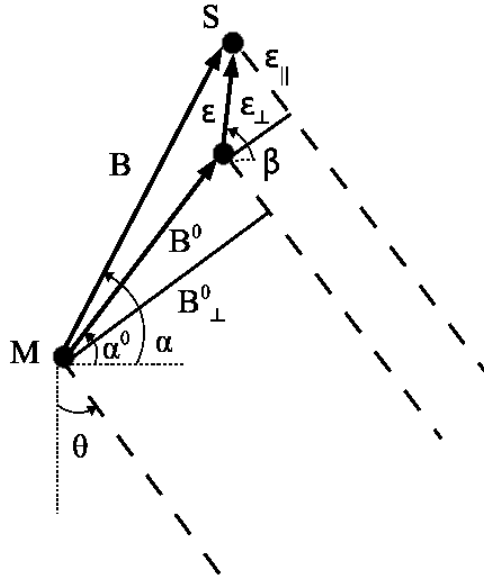


Figure 5.7: Propagation of orbit errors to baseline errors. $B(B^0 + \mathcal{E})$ and $B_{\perp}(B_{\perp}^0 + \mathcal{E}_{\perp})$ are the baseline and perpendicular baseline with orbit error \mathcal{E} , respectively, between a master M and a slave S acquisition. \mathcal{E}_{\perp} and \mathcal{E}_{\parallel} are the residual perpendicular, and parallel baseline error components, respectively. α is the orientation angle of baseline B . β is the orientation of orbit error \mathcal{E} . Superscript zero indicates the corresponding values without taking the error in the state vector (\mathcal{E}) into account.

decorrelation can be neglected for our case since we work with persistent scatterers (point-like targets). In our PSI stack processing, a phase de-ramping operation is performed to remove the phase-trend.

Impact of the SCR of scatterers

Given the SCR of a target (P), the impact of interferometric phase variance σ_{ϕ_P} on the precision of cross-range $\sigma_{c_{PSCR}}$ can be approximated (for SCR > 1 dB) by (Dheenathayalan et al., 2017), (Hanssen, 2001a, pp. 34–50),

$$\begin{aligned} \sigma_{c_{PSCR}} &= \frac{\lambda r_P}{4\pi B_{\perp}} \cdot \sigma_{\phi_P} \\ &\approx \frac{\lambda r_P}{4\pi B_{\perp}} \cdot \sqrt{\frac{2}{2 \text{ SCR} - 0.55}}, \end{aligned} \quad (5.11)$$

where λ is the radar wavelength.

Phase-center of the reference point

The position of a reference point R plays a role during the geocoding when radar coordinates are transformed to TRF (Terrestrial Reference Frame) coordinates. The bias and precision in the cross-range position of the reference point R impacts the 3D position and

precision of the rest of the scatterers. The impact of cross-range error is listed in the terms $\left(\frac{\partial e}{\partial c}, \frac{\partial n}{\partial c}, \frac{\partial h}{\partial c}\right)$ in Tab. 5.1 (column $\kappa = c$) and Fig. 5.2.

The cross-range bias of the reference point R can be mitigated in two ways. First, a mean ground height of the area (we assume most of the PS are from the ground level) is obtained from the mode of the histogram of PS heights (which is relative to a reference point). Similarly, a mode computed from the histogram of heights from a high-precision Digital Elevation Model (DEM) gives an alternate estimate of the same ground level. A difference in these two mode values provides the height of the reference point R above the reference surface (Dheenathayalan and Hanssen, 2013). The second approach is to measure *in situ* the phase-center of a reference scatterer. A convenient approach would be to use a known geometric structure with well-defined phase-center such as a CR or TR as a reference point (Ferretti et al., 2007; Mahapatra et al., 2014; Dheenathayalan et al., 2014). The uncertainty in the cross-range position of reference point ($\sigma_{c_R}^2$) can be given by,

$$\sigma_{c_R} = \frac{\sigma_{H_R}}{\sin(\theta_{\text{inc},R})}, \quad (5.12)$$

where σ_{H_R} is the precision of reference point height H_R above a reference surface (see Fig. 5.4), and $\theta_{\text{inc},R}$ is the incidence angle at the location of the reference point R .

5.2.3. Geocoding and datum transformation from radar to local coordinates

Geocoding is applied on the corrected (r_p, a_p, c_p) coordinates (from Eqs. (5.1), and (5.7)) to transform to TRF coordinates (Schreier, 1993b; Small et al., 1996). The datum transformation between TRF coordinates and the local (Dutch) coordinates (e_p, n_p, h_p) (expressed in North, East and Height) were performed using the RDNAPTRANS procedure (de Bruijne et al., 2005). This procedure employs a geoid model for the vertical component. The position error (assumed diagonal) variance-covariance (VC) matrix Q_{rac} in radar coordinates is given by,

$$Q_{rac} = \begin{bmatrix} \sigma_{r_p}^2 & & \\ & \sigma_{a_p}^2 & \\ & & \sigma_{c_p}^2 \end{bmatrix}. \quad (5.13)$$

Then, using a S-transformation (described in Dheenathayalan et al. (2016)) the 3D position VC matrix in radar, Q_{rac} , is propagated to the VC matrix in local coordinates, Q :

$$\begin{aligned} \underline{\hat{P}} &\sim \mathcal{N}(\mu, Q) \text{ with} \\ \mu &= \begin{bmatrix} e_p \\ n_p \\ h_p \end{bmatrix} \text{ and } Q = \begin{bmatrix} \sigma_e^2 & \sigma_{en}^2 & \sigma_{eh}^2 \\ \sigma_{en}^2 & \sigma_n^2 & \sigma_{nh}^2 \\ \sigma_{eh}^2 & \sigma_{nh}^2 & \sigma_h^2 \end{bmatrix}, \end{aligned} \quad (5.14)$$

where μ , and Q are the estimated 3D position in local coordinates and its VC matrix, respectively. The diagonal $(\sigma_e^2, \sigma_n^2, \sigma_h^2)$ and non-diagonal $(\sigma_{en}^2, \sigma_{eh}^2, \sigma_{nh}^2)$ entries are the variances and covariances in east, north and height coordinates, respectively.

5.2.4. Linking radar scatterers to objects

Scatterer-to-object linking is a step to associate a scatterer with a 3D position and a VC matrix to a position on a real-world object, or a point from a set of K potential points from e.g. a scan of the environment. This step is facilitated by using point cloud data from the objects, with its quality expressed by a 3×3 VC matrix for each point along with its position. A radar scatterer can be linked to the nearest point, in the metric defined by both VC matrices. The VC matrix not only represents the radar acquisition geometry but is also very helpful in constraining the 3D search space to link a scatterer to a point from a point set.

To perform this linking, we exploit a similarity (closeness) measure (\mathbb{B}) between a radar scatterer position \underline{P} and the position \underline{P}_i of the i^{th} point of a 3D object model, e.g., a building facade, building roof, bridge, or pole. Similarity between two populations with associated probability density functions (PDF) is given by (Mahalanobis, 1936; Bhattacharyya, 1946; Matusita, 1955; Duda et al., 2012, pp. 20–65):

$$\int \sqrt{\text{pdf}(\underline{P})} \sqrt{\text{pdf}(\underline{P}_i)} df, \quad (5.15)$$

where f is the 3D space defined by (e, n, h) . The positions $\underline{P} \sim \mathcal{N}(\mu, Q)$ and $\underline{P}_i \sim \mathcal{N}(\mu_i, Q_i)$ are trivariate Gaussian distributed. For the case of Gaussian PDFs, the above integral can be evaluated by an exponential function (Duda et al., 2012, pp. 20–65),

$$e^{g(\omega)} \text{ with } \omega = 0.5, \quad (5.16)$$

and

$$g(\omega) = \frac{\omega(1-\omega)}{2} (\mu_i - \mu)^T \left[\omega Q + (1-\omega) Q_i \right]^{-1} (\mu_i - \mu) + \frac{1}{2} \ln \left(\frac{|\omega Q + (1-\omega) Q_i|}{|Q|^\omega |Q_i|^{1-\omega}} \right), \quad (5.17)$$

where $|\cdot|$ is the determinant of a matrix. Then, the Bhattacharyya measure \mathbb{B}_i between \underline{P} and \underline{P}_i can be written as (Bhattacharyya, 1946; Kailath, 1967),

$$\mathbb{B}_i(\underline{P}, \underline{P}_i) = \frac{1}{8} \left[(\mu_i - \mu)^T \left(\frac{Q + Q_i}{2} \right)^{-1} (\mu_i - \mu) \right] + \frac{1}{2} \left[\ln \left(\left| \frac{Q + Q_i}{2} \right| \right) - \frac{1}{2} \ln(|Q|) - \frac{1}{2} \ln(|Q_i|) \right],$$

for $i = 1, \dots, K$

(5.18)

The measure \mathbb{B}_i compares two distributions rather than just their means. In this aspect the similarity measure is preferred over the weighted squared norm $\|\underline{P} - \underline{P}_i\|_{Q+Q_i}$ (chi-squared test statistic) (Teunissen, 2000; Aherne et al., 1998).

The radar scatterer with position \underline{P} is then associated to an object i located at $\underline{P}_{i,T}$ with the minimum Bhattacharyya measure:

$$\min_{\text{find } i \in (1, K)} \left\{ \mathbb{B}_i(\underline{P}, \underline{P}_i) \right\}, \quad (5.19)$$

where K is the number of possible real-world points in the vicinity of a radar scatterer.

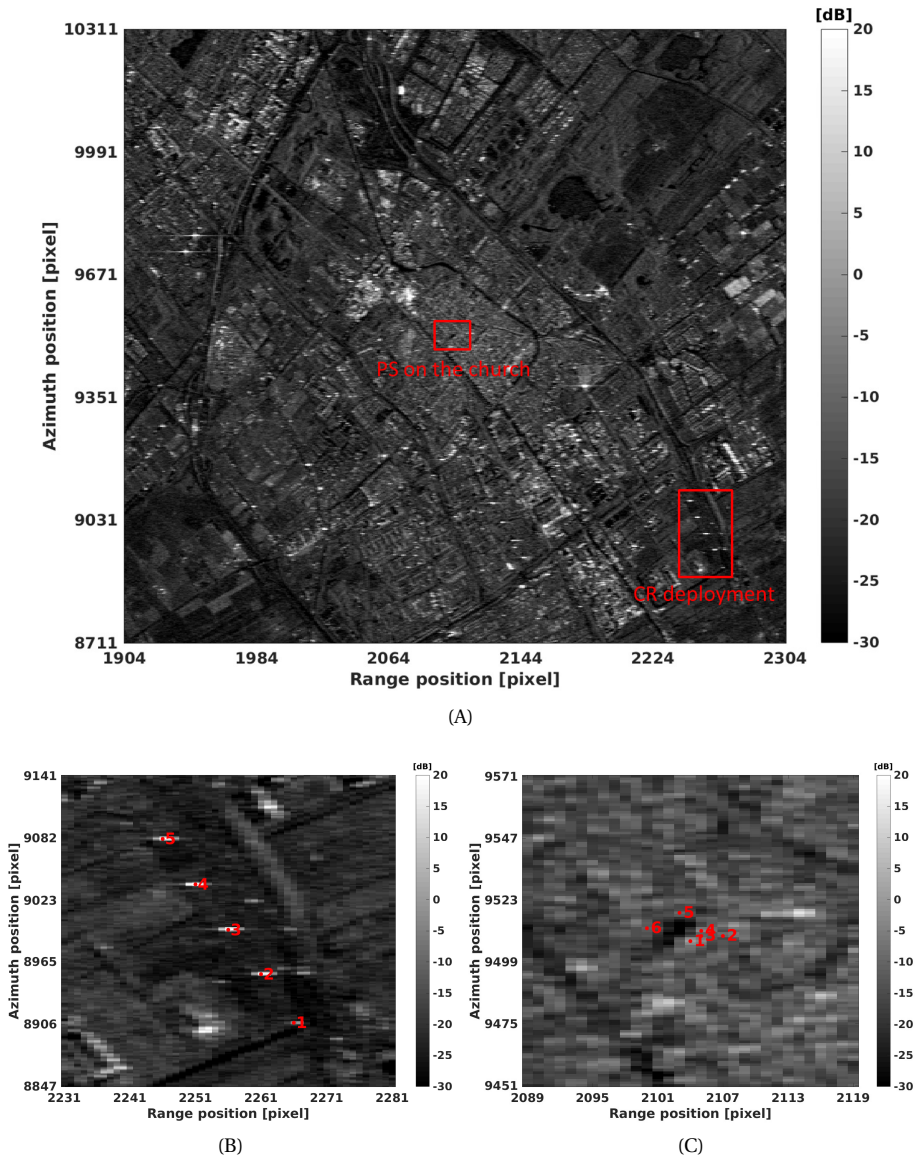


Figure 5.8: Mean backscatter image (averaged 44 ASAR IMS images and expressed in dB) covering Delft. (A) Shows the CR deployment and the infrastructure of regions of interest highlighted in red. (B) Shows a mean backscattering response of CRs deployed at a test site (for optical image see Fig. 5.9). (C) Location of the six PSs detected on the infrastructure of interest shown in Fig. 5.15. The results of PSs linked to targets are demonstrated in Fig. 5.16.

5.3. Experiment setup and results

We investigated the positioning performance of medium resolution SLC images covering Delft, the Netherlands. The mean intensity image from ASAR over Delft is shown in Fig. 5.8. The procedure described in the previous section was tested with CRs from a field



Figure 5.9: Delft CR experiment setup for ENVISAT ASAR descending acquisitions. CR and their numbers are marked in red as shown in the GoogleEarth (optical image date: 19-May-2004) (GoogleInc., 2017).

experiment (see Fig. 5.8B) and “natural” coherent scatterers from PSI, see, e.g., Fig. 5.8C. In both cases, the scatterer positions estimated from SAR were compared with the ground truth position. The ground truth position, the phase center of a scatterer, was obtained with the aid of DGPS (Differential Global Positioning System) for the CRs, and LiDAR for validating natural coherent scatterers.

5.3.1. Setup

Five trihedral corner reflectors (1.43 m sides) oriented (see Fig. 5.9) towards ENVISAT ASAR IM IS2 swath descending acquisitions from Nov-2003 to Jun-2008 were used. CR1, and CR2 were later destroyed and stolen, respectively, and did not serve the whole experiment period, therefore CR3, CR4, and CR5 were used in this study. The CRs were oriented for 44 IM mode IS2 swath acquisitions with an incidence angle of 24.2° , and a heading angle of 196.2° . The IMS (SLC) products have a pixel spacing of approximately 4 m and 8 m in azimuth and (slant) range, respectively. They were acquired in VV polarization and came

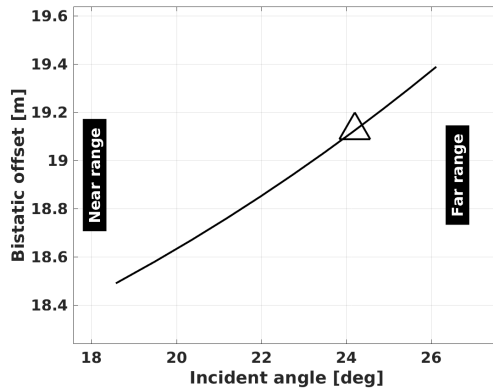


Figure 5.10: The azimuth bistatic offset computed along the swath of a ENVISAT ASAR descending acquisition (21-Feb-2007). The magnitude of bistatic offset at the location of the CR5 is marked with a triangle.

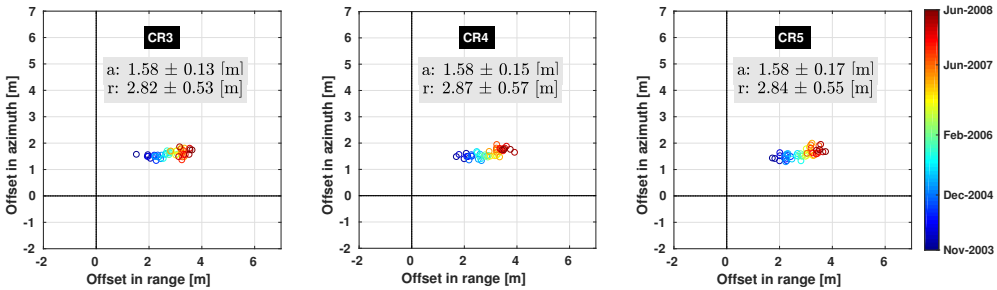


Figure 5.11: 2D position offsets of CR with azimuth bistatic (as shown in Fig. 5.10), SET, atmosphere (with respect to mean), and plate tectonics corrections. The position errors are reported with respect to the desired offset of (0, 0), highlighted with bold lines. The estimated azimuth and range one-time calibration offsets are: $\hat{a}_{cal} = 1.58$ m and $\hat{r}_{cal} = 2.84$ m.

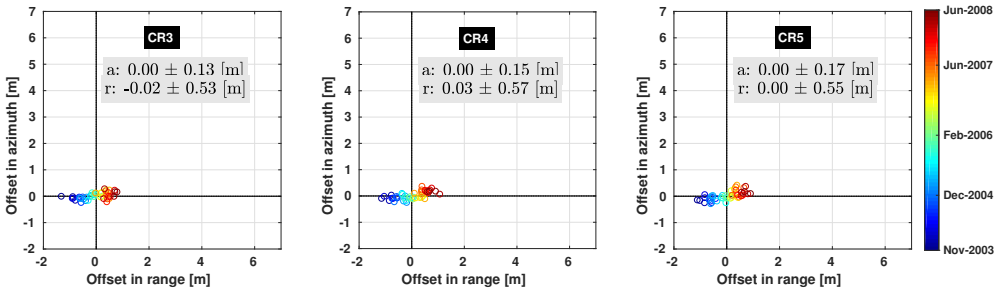


Figure 5.12: 2D position offsets of CR with the bistatic, SET, atmospheric path delay, plate motion, and calibration offset corrections. The azimuth (a) and range (r) offsets and the resulting precisions are indicated in the plot for each CR.

with a geometric resolution of ~ 9 m in slant range and 6 m in azimuth. The image pixels were oversampled by a factor of 128×128 , using a FFT, to detect the sub-pixel positions. The chosen oversampling factor introduced a quantization error of approximately 1 cm in

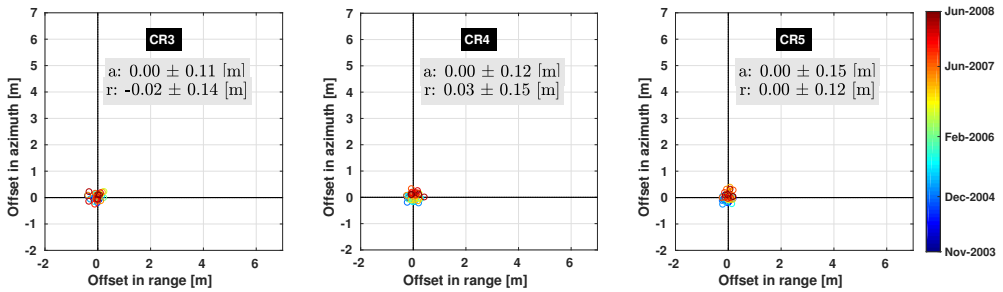


Figure 5.13: An unbiased 2D positioning capability of ENVISAT ASAR products. The overall corrections applied were the bistatic, SET, path delay (ionosphere and troposphere), plate motion, calibration offsets and LO drift.

azimuth and 2 cm in range in determining the pixel peak. For validation, the CR ground truth positions were measured with DGPS RTK (Real Time Kinematic) in ETRF89 (European Terrestrial Reference Frame 1989), provided with a 1–2 cm 3D precision.

5

5.3.2. Empirical computation of 2D residual calibration offsets

The error sources in azimuth and range (see Sec. 5.2) were mitigated step by step; the results are shown in Figs. 5.11, 5.12, and 5.13. The impact of the bistatic effect in the ASAR IMS imagery is shown in Fig. 5.10. The bistatic azimuth shift at the location of the CR (around 19 m) has been computed and removed in Fig. 5.11. In addition, the plate motion corrections were performed in order to compare the ground truth CR measurements (given in ETRF89) with ASAR data (with orbits provided in ITRF (International Terrestrial Reference Frame)). The residual position errors were dominated by the existence of unmodeled calibration offsets, see Sec. 5.2.1, and Eq. (5.1). These azimuth and range residual calibration offsets were estimated to be $\hat{a}_{\text{cal}} = 1.58$ m and $\hat{r}_{\text{cal}} = 2.84$ m, respectively. The SLC images used in this study already included the 13-Dec-2003 SWST bias updates. Therefore, as explained in Sec. 5.2.1, the variability with respect to their mean path delay and SET were mitigated. After application of calibration offsets in Fig. 5.12, it can be clearly seen that the position is drifting in range as discussed in Sec. 5.2.1. Finally, the corrections due to LO drift from Eq. (5.2) were incorporated in PRF (Pulse Repetition Frequency) and SWST; the results are presented in Fig. 5.13. LO drift compensation provided a significant improvement of about 460% (CR5) in the range positioning, and a minor 1% improvement in azimuth. The above corrections result in improved 2D positioning and led to an accuracy of 11 cm in azimuth (CR3) and 12 cm in range (CR5), see Fig. 5.13. Compared to earlier studies, which reached a position accuracy in the order of metres, see Small et al. (2007); Miranda et al. (2013); Schubert et al. (2012b), the achieved accuracy is an order of magnitude better. Similar improvements were demonstrated for the case of Sentinel-1A/1B (Schubert et al., 2017).

5.3.3. 3D position accuracy for reflectors

For the cross-range position, PSI was applied on a set of 44 ASAR IMS (swath IS2) descending mode acquisitions covering Delft. The image acquired on 21-Feb-2007 was used as a master image. The position corrections in azimuth and range, as mentioned in Sec. 5.3.2, were performed with respect to the master image pixels. The LO drift corrections from

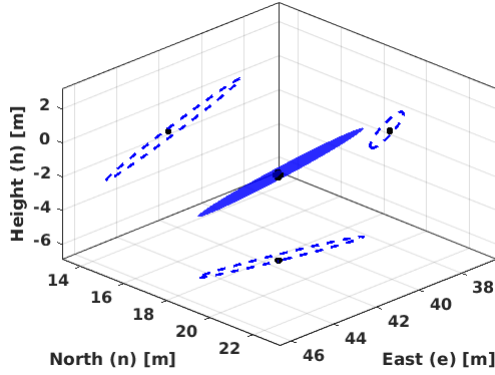


Figure 5.14: The 3D accuracy of CR4 was 0.28 m with its 3D uncertainty drawn using error ellipsoid (1σ confidence interval) relative to the ground truth indicated by the black dot. It exhibited an elongated (prolate) error ellipsoid with a ratio of axis lengths $1/0.8/12$ (with $\sigma_r = 0.15$ m). The ratio of axis lengths represents the precision in range, azimuth, and cross-range relative to range, respectively. The error ellipsoid is projected onto the en , nh , and he planes (indicated with dashed lines) to illustrate their intersection with the ground truth position (black dot).

Eq. (5.2) were applied to the master image timing parameters. CR3 was used as reference R , see Fig. 5.4. Fixing the phase-center of reference point R to the apex of CR3 with centimeter accuracy eliminates the cross-range bias in the 3D position estimation. The position of the other two CR was transformed into (e, n, h) coordinates, cf. Sec. 5.2.3, and the positioning VC matrix was propagated from radar (Q_{rac}) to local (Q_{enh}) coordinates (Dheenathayalan et al., 2016).

The corner reflectors used in this study had an average SCR of about 35 dB and exhibited a normalized amplitude dispersion of ~ 0.05 . If we consider an orbit precision of $\sigma_{\mathcal{E}_\perp} = 10$ to 20 cm, and an average perpendicular baseline of the stack of about 450 m (as observed in our time-series), a cross-range precision of $\sigma_{c_{p\text{orb}}} = 3$ to 5 cm was noticed for a target of 50 m height. We used a CR with a known position as reference, and a σ_{c_R} of ~ 2 cm was observed. In our InSAR stack processing, the impact of $\sigma_{c_{p\text{SCR}}}$ was found to be a dominant factor in σ_{c_p} , see Eqs. (5.11) and (5.8). The application of position corrections resulted in the 3D position accuracy of 0.28 m (CR4) and 0.53 m (CR5) with the quality of 3D position expressed as an error ellipsoid with a ratio of axis lengths $(1/\frac{\sigma_{a_p}}{\sigma_{r_p}} / \frac{\sigma_{c_p}}{\sigma_{r_p}})$ $1/0.8/12$ (with $\sigma_r = 15$ cm) (CR4) and $1/1/15$ (with $\sigma_r = 12$ cm) (CR5), respectively. The results of CR4 and CR5 are in the same order of magnitude, therefore we plot only the results of CR4 in Fig. 5.14. The estimated position of CR4 (in blue) is drawn in comparison to its ground truth position (in black) along with its respective error ellipsoid. The position error ellipsoids for ASAR are elongated in the cross-range direction, resembling a cigar-shaped ellipsoid. The intersection of the scaled error ellipsoid (in blue) with the ground truth position (in black) shows that the geolocalization corrections were successful.

5.3.4. Linking coherent scatterers to objects

In this section, we present the 3D positioning results of opportunistic coherent scatterers from ENVISAT ASAR IMS acquisitions covering Delft. A normalized amplitude dispersion threshold of 0.5 was used to detect PS (opportunistic coherent scatterers) in our PSI

Table 5.2: SCR and amplitude dispersion (D_A) values exhibited by the PSs detected over the church.

PS #	SCR (dB)	D_A
1	18.9	0.43
2	17.1	0.26
3	14.0	0.32
4	16.4	0.25
5	14.7	0.24
6	13.1	0.37



Figure 5.15: Infrastructure of interest (a church) in Delft region shown in GoogleEarth (optical image date: 19-May-2004) (GoogleInc., 2017).

processing (Kampes, 2005). The scatterers from the church (see Figs. 5.15 and 5.8C) were detected as PSs. They exhibited an average SCR of about 13–19 dB and an amplitude dispersion of 0.2–0.4, see Tab. 5.2.

The error correction, PSI processing and the position ellipsoid per scatterer was computed as in Sec. 5.3.3 for a church, see Fig. 5.15. The coherent scatterers with their VC-matrix drawn as error ellipsoids (2σ confidence level) are shown with a 3D model in Fig. 5.16A (left). A 3D city model was constructed using high quality LiDAR data as described in Lesparre and Gorte (2012). The quality of LiDAR point positions is considered to have a VC matrix, $Q_i = \sigma^2 I$ (see Eq. (5.18)) with $\sigma = 0.1$ m, and I is a 3×3 identity matrix (der Zon, 2011; van der Sande et al., 2010). Then, using Eq. (5.18), the radar scatterers were linked (associated) to positions on the church, see Fig. 5.16A (right). The scatterer's error ellipsoid (Fig. 5.16A (left)) and intersection point on the church (Fig. 5.16A (right)) are colored based on their deformation rate. For validation, the associated scatterers were individually visualized with optical images, see Fig. 5.16B. From these visualizations, it is considered that the scatterers ①, ④, and ⑤ were trihedral corner reflectors while object ⑥ is a single-bounce reflector. Objects ②, and ③ are either single-bounce or multi-bounce reflectors. Here, the scatterers ① to ③ were from the church; ④ and ⑤ were from church and ground interaction; and ⑥ from the ground. Even after applying position error

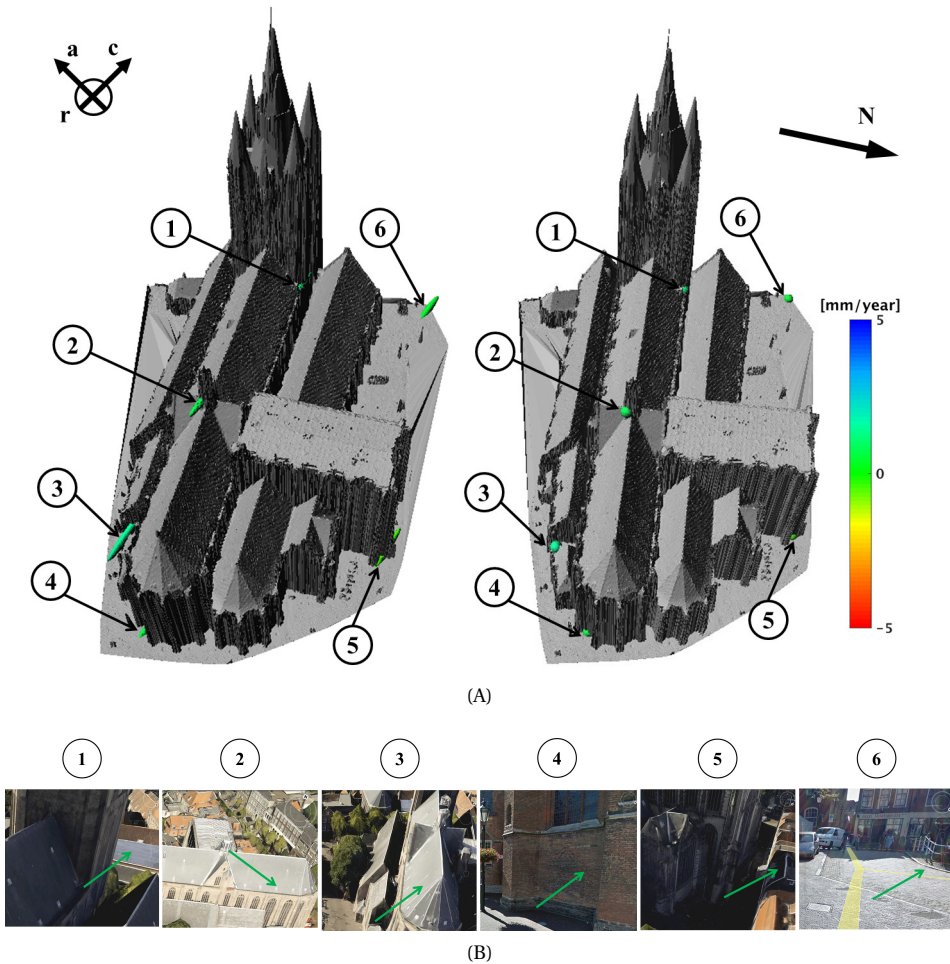


Figure 5.16: Results of linking radar scatterers from ENVISAT ASAR to a church in Delft using a 3D city model (in gray). Here, the opportunistic coherent scatterers of the church are presented. (A, left) shows the scatterers with position error ellipsoids (2σ confidence level). (A, right) shows the results of scatterers after linking to objects on the church as a dot (size scaled just to ease visualization). The color coding of ellipsoids and dots is based on their deformation rate in mm/year. (B) Optical image showing each of the linked objects. It is hypothesized that the scatterers ①, ④, and ⑤ are trihedral reflectors while object ⑥ is a single-bounce reflector. Objects ②, and ③ are either single-bounce or multi-bounce reflectors. Here, the scatterers ① to ③ are from the church; ④ and ⑤ are from church and ground interaction; and ⑥ is from the ground. Interpretation: the reflections from the church (① to ⑤) and the ground (⑥) were found to exhibit no significant linear deformation, see Fig. 5.17.

corrections, some of the scatterer phase centers were found inside buildings and below ground level, see ①, ⑤, and ⑥ in Fig. 5.16A (left). Similar scenarios were also observed by Auer et al. (2011) and Schunert and Soergel (2016). We believe this behavior is due to the influence of signal contributions from the scatterers in the (urban) neighborhood. In spite of this, we were able to associate scatterers to their geometrically most probable position in the 3D model as shown in Fig. 5.16A (right), based on the exploitation of the position

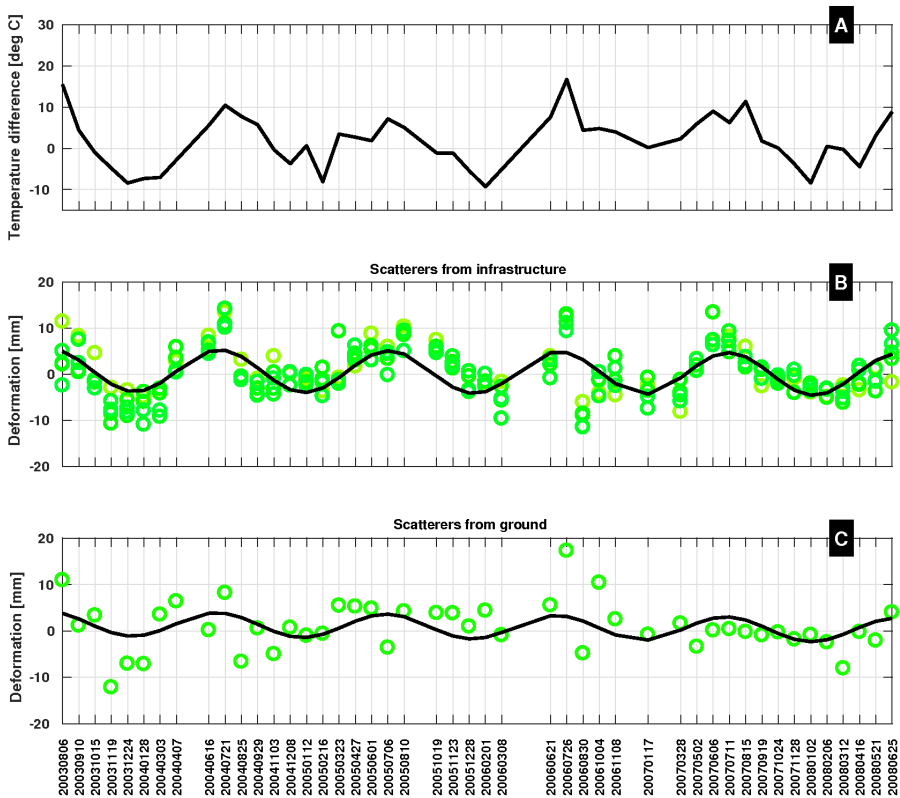


Figure 5.17: Interpreting the deformation of scatterers after linking to objects in Fig. 5.16. LOS deformation in (B) and (C) are drawn with color circles. Their colors are based on their linear deformation rate identical to Fig. 5.16. In (A) the black line shows 24 h average temperature from a meteorological station at the time of satellite acquisition with respect to the master image. (B) and (C) show the kinematic time-series of scatterers linked to the infrastructure and the ground, respectively. The black line in (B) and (C) represents a seasonal deformation model for the scatterers from the infrastructure (① to ⑤ in Fig. 5.16) and the ground (⑥ in Fig. 5.16), respectively. Here, the seasonal signal (due to temperature) from the infrastructure (black line in (B)) was stronger than the ground (black line in (C)).

error ellipsoids and the availability of LiDAR data. For the case when the phase center (in case of multiple reflections) is not present in a 3D model, our approach will associate the scatterer to an object (in a 3D model) depending on the position error ellipsoid's orientation and proximity. From this linking, it was evident that the main tower of this church was not measured by PS from the ASAR track and the scatterers from the other parts of the church showed seasonal deformation patterns (see Figs. 5.17 (A) and (B)), while the reflections from the ground showed a weak seasonal pattern as shown in Fig. 5.17 (C). The deformation pattern of the ground and the infrastructure is attributed to temperature and ground water level variability (van Leijen and Hanssen, 2008). Fig. 5.17 (A) shows the one-day average temperature during each ASAR acquisition relative to the master acquisition. The meteorological data was obtained from a weather station located approximately 8 km from this location.

By associating the scatterer's phase center to objects, each scatterer's estimated deformation can be interpreted to a depth necessary for a certain application. Such linking could improve our understanding and pave the way for applications such as infrastructure specific monitoring and stability analysis, relative stress on underground infrastructure (Dheenathayalan et al., 2011; Arsénio et al., 2014), and designing construction of new infrastructure (cities, buildings, dikes, etc) to enhance InSAR measurement sampling.

5.4. Summary and conclusions

We applied a systematic procedure to precisely estimate the radar scatterer position and subsequent quality description for medium resolution SAR imagery, and demonstrated a method for radar scatterer to object linking. The method was assessed using 5 years of ASAR imagery for a test site in Delft using DGPS, and LiDAR.

As mean atmospheric and geodynamic corrections were implicitly incorporated in the 2003 SWST bias update, these corrections are not necessary. Therefore, only epoch-dependent atmosphere and SET corrections with respect to their mean value were applied here. Further, the application of plate motion and bistatic corrections helped us in identifying the existence of residual calibration offsets, see Fig. 5.11. These residual calibration offsets, considered as a refinement to the 12-Dec-2003 SWST bias update, were empirically computed to be about 1.58 m in azimuth and 2.84 m in range. The application of LO drift corrections showed significant improvements from 55 cm to 12 cm (CR5) in the range precision, see Fig. 5.13. This proposed procedure (consisting of bistatic, path delay, SET, LO and calibration corrections) is "tie-point free" and can be applied to all ASAR products in order to deliver a more accurate 2D positioning capability as shown in Fig. 5.13. From our CR experiment site, we showed that we were able to accomplish an accuracy of up to 11 cm (CR3), and 12 cm (CR5) in azimuth and range, respectively. These improvements should serve as a reference for other medium resolution sensors, such as, ERS-1/2, RadarSAT-2 and Sentinel-1A/B.

In 3D, the trihedral corner reflector's position and error ellipsoid were validated using DGPS measurements and absolute positioning of about 0.28 m for CR4 and 0.53 m for CR5 were achieved. The error ellipsoids were cigar-shaped; their intersection with GPS positions justified the method of linking the scatterer's phase center to objects. The method was also applied to other non-CR coherent scatterers and using their error ellipsoids, scatterers were associated to objects (points) in a 3D city model. The results of linking and interpretation were demonstrated over a building in Delft (Figs. 5.16 and 5.17). In spite of using medium resolution ASAR IMS imagery, the results established the capability of monitoring (parts of) individual infrastructure.

6

Distributed Corner Reflectors - an alternative method to introduce PS

In recent years, Synthetic Aperture Radar Interferometry (InSAR) has become a recognized geodetic tool for observing ground motion. For monitoring areas with low density of coherent targets, artificial corner reflectors are usually introduced. The required size of a reflector depends on radar wavelength and resolution, and on the required deformation accuracy. Corner reflectors have been traditionally used to provide a high signal-to-clutter ratio (SCR). However, large dimensions can make the reflector bulky, difficult to install and maintain. Furthermore, if a large number of reflectors is needed, e.g., for long infrastructure such as vegetation covered dikes, the total price of the reflectors can become unaffordable. On the other hand, small reflectors have the advantage of easy installation and low cost. In this work, we design and study the use of small reflectors with low SCR for ground motion monitoring. In addition, we propose a new closed-form expression to estimate the interferometric phase precision of resolution cells containing a (strong or weak) point target and clutter. Through experiments, we demonstrate that the small reflectors can also deliver displacement estimates with an accuracy of a few mm. To achieve this, we apply a filtering method for reducing clutter noise.

6.1. Introduction

The limitation of InSAR to monitor ground displacement in non-urban areas is usually solved by introducing coherent targets. Although originally designed for calibration purposes, artificial CR (corner reflectors) are traditionally used as coherent targets in InSAR applications due to their large radar cross section (RCS) and wide RCS pattern, see e.g., Sarabandi and Chiu (1996); Small et al. (2004a); Qin et al. (2013); Dheenathayalan et al. (2016). With corner reflectors, measurements with accuracy in the order of 1 mm have been demonstrated, see e.g., Ferretti et al. (2007). Traditionally, corner reflectors have been designed to provide a very strong, dominant reflection compared to the background signal, which assures a high signal-to-clutter ratio (SCR) signal (Freeman, 1992). Small reflectors do

This chapter has been published in the IEEE Transactions on Geoscience and Remote Sensing, 2017 (Dheenathayalan et al., 2017).

not provide such high SCR values, but they are appealing for other reasons. First, their costs are lower. In the cases where a large number of reflectors is needed e.g., for monitoring long infrastructures, such as oil pipe lines or grass covered dikes, very low cost reflectors are preferable. Second, their small dimensions make installation easier, particularly for infrastructure with reduced space. Third, small reflectors have a low visual impact on the landscape. In this contribution, we study small reflectors and derive an expression for phase precision covering high and low SCR targets. Furthermore, we provide a design of a small bidirectional reflector tile (RT), and show how reduced size reflectors can deliver accurate observations when correctly filtered. Preliminary results of this work has been presented in Cuenca et al. (2014). This manuscript is arranged as follows. In Section 6.2, we briefly discuss and derive a new theoretical expression for phase variance as a function of its SCR and we present a formula to calculate the RCS of reflector tiles used in this study. In Section 6.3, we provide a design of small bidirectional reflectors that can be used for both ascending and descending passes. We also show a filtering approach that can deliver an increase in the SNR directly proportional to the square root of the number of corner reflectors used in the filter. In Section 6.4, we describe the result of testing these small, bidirectional reflectors in a real situation. The formation scheme for measuring deformation is shown and measurement results are demonstrated using TerraSAR-X data acquired over a test site in the Netherlands.

6

6.2. Signal to clutter ratio and the phase statistics

6.2.1. Phase precision of radar targets

Signal-to-clutter ratio is a common metric for describing the quality of a radar observation (Skolnik, 1962, pp. 403–423). When using SCR for quality description, it is generally assumed that a target inside a resolution cell is the only object providing coherent information whereas all other reflecting objects -the clutter- change randomly, which causes speckle, see e.g., Frery et al. (1997). In this publication the term clutter noise is used to refer to the magnitude of the speckle (in power units). SCR is defined as:

$$SCR = \frac{P_P}{P_C} \quad (6.1)$$

where P_P is the power reflected by the reflector (point target) and P_C the clutter. The phase value of the reflector, which is required in interferometric applications, is disturbed by the clutter to an extent depending on the magnitude of SCR . For high SCR objects, the influence of clutter variations is small because P_P dominates over P_C . For traditional radar applications, such as target detection, a threshold of 13 dB SCR is commonly used (Skolnik, 1962). For InSAR applications such as subsidence monitoring, SCR has been used as indicator for the standard deviation of the interferometric phase, which is directly linked to the accuracy of the measurement, e.g. ground displacements (Kampes, 2006). For high SCR values the interferometric phase standard deviation is given by (Goodman, 1975; Just and Bamler, 1994),

$$\sigma_\phi \approx \frac{1}{\sqrt{SCR}}. \quad (6.2)$$

σ_ϕ can be converted to the standard deviation of deformation σ_d by:

$$\sigma_d = \sigma_\phi \cdot \frac{\lambda}{4\pi}, \quad (6.3)$$

where λ is the radar wavelength. In this contribution, we are mostly interested in reflectors that have a low SCR values, but greater than 1. To test the validity of Eq. (6.2) for low SCR reflectors, we simulated a target plus random clutter as a coherent summation of point scatterers and compared the result to Eq. (6.2). Fig. 6.1 shows the result of this simulation. We find that Eq. (6.2) represents very well the standard deviation of the interferometric phase for values of SCR above 10 dB. Below this value, Eq. (6.2) underestimates the experimentally derived standard deviation. Larger differences between Eq. (6.2) and simulations are found as the SCR decreases with a maximum of about 0.28 rad at SCR of 0 dB. For this purpose, a new closed-form expression covering the phase precision of low and high SCR targets is derived in this paper. Although, in radar applications a SCR threshold of 13 dB is usually applied for target detection (Skolnik, 1962), we find from simulations that interferometric phases for resolution cells with a SCR below this threshold are not strongly disturbed by clutter and information contained in their reflections can still be extracted, despite the fact that such targets are hardly visible in a radar image. However, we have to take into account that Eq. (6.2) represents only clutter noise. Thermal receiver noise and other noise types, e.g. atmospheric, system and processing noise are not considered. The actual interferometric phase standard deviation in a real measurement will therefore be higher than the value shown in Fig. 6.1.

For a single-look complex (SLC) SAR image, the complex return y (with amplitude $|y|$ and phase Ψ_y) from a resolution cell containing a dominant scatterer and a fully developed clutter can be written by:

$$y = A_P \cdot e^{j\Psi_P} + c, \quad (6.4)$$

where c is a complex number (with amplitude $|c|$ and a uniform distributed phase) representing a fully developed clutter (noise), and $|\cdot|$ is the magnitude operator. For homogeneous areas *i.e.*, the case of a fully-developed speckle, the clutter exhibits a circular Gaussian distribution (Dainty, 1975; Goodman, 1976; Madsen, 1986; Davenport and Root, 1987; Molesini et al., 1990; Bamler and Hartl, 1998). A_P and Ψ_P are the amplitude and phase of a point scatterer, respectively. The impact of one realization of clutter is shown in Fig. 6.2. Fig. 6.2A shows the impact for a high SCR case, and the phase of the resolution cell is less-dependent on the clutter for high SCR values. For a low SCR resolution cell, the impact of clutter on phase is inevitable, as shown in Fig. 6.2B. From Fig. 6.2, the phase contribution of (a realization of) clutter in a resolution cell can be written geometrically as,

$$\Psi = \arccos\left(\frac{A_P^2 + |y|^2 - |c|^2}{2A_P|y|}\right). \quad (6.5)$$

In general, the clutter contribution c is treated as a stochastic process. Therefore, the probability density function (PDF) of the SLC phase of a resolution cell in Fig. 6.2 can be written as (Middleton, 1960, pp. 396–437):

$$p_\Psi(\Psi) = \frac{e^{-SCR}}{2\pi} \left(1 + \beta\sqrt{\pi} \cdot e^{\beta^2} \cdot (1 + \text{erf}(\beta))\right) \\ \text{with } \beta = \sqrt{SCR} \cdot \cos(\Psi - \Psi_P), \forall -\pi \leq \Psi - \Psi_P \leq \pi, \quad (6.6)$$

where $\text{erf}(\cdot)$ is the Gauss error function defined by $\text{erf}(\alpha) = \frac{2}{\sqrt{\pi}} \int_0^\alpha e^{-x^2} dx$. Here, the choice of dominant scatterer phase Ψ_P is arbitrary and hence set to zero as shown in

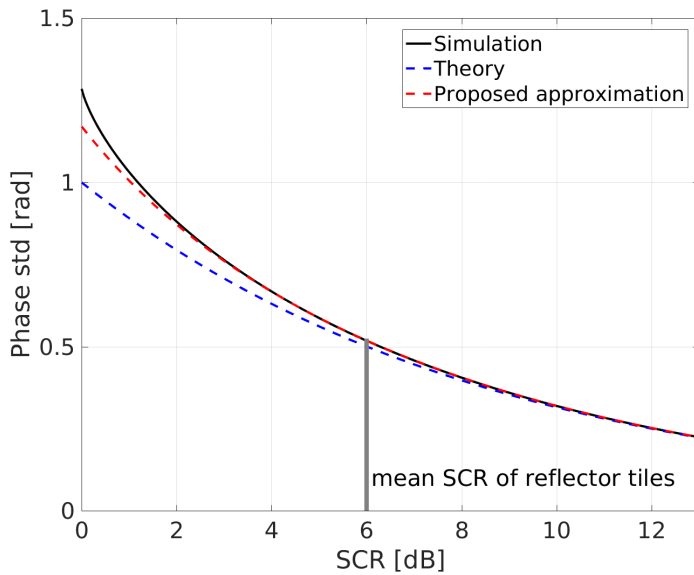


Figure 6.1: Standard deviation of interferometric phases (single differences) determined using Eq. (6.2) (dashed blue line), our approximation Eq. (6.9) (dashed red line) and simulations (black solid line). The approximation given by Eq. (6.9) provides a good match with the simulations for $SCR > 1$ dB. The SCR of the reflector tiles used in this study is also indicated. We simulated SCR for values down to 0 dB. Smaller values are possible, but considered of no interest because the clutter power will dominate the cell.

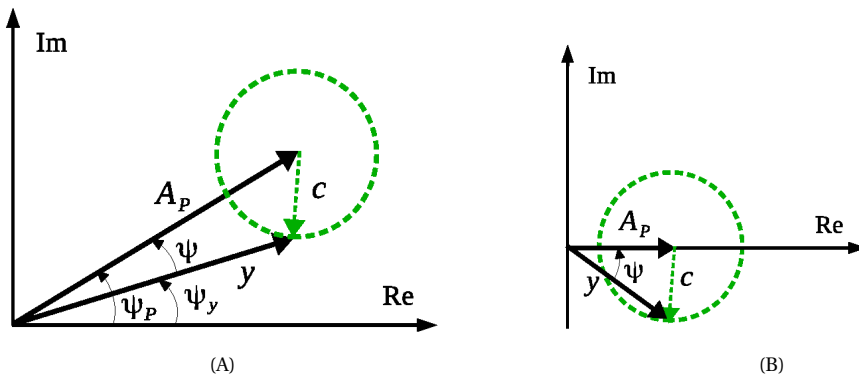


Figure 6.2: The impact of clutter c (in green) in a resolution cell with a dominant point scatterer (with amplitude A_p and phase Ψ_p) drawn in real (Re) and imaginary (Im) planes. (A) A high SCR case, the stronger the point target A_p , the weaker the impact of clutter c on the phase $\Psi_y = \Psi - \Psi_p$. (B) Shows the impact of the clutter on phase for a lower SCR case. The choice of point target phase is arbitrary and here, kept at $\Psi_p = 0$ for convenience.

Fig. 6.2B. Therefore, substitute $\beta = \sqrt{SCR} \cdot \cos(\Psi)$ in Eq. (6.6). The PDF of single-look phase for several values of SCR are plotted as colored lines in Fig. 6.3, and the colored crosses represent their Gaussian equivalents. It can be noted that the mean of the PDF is centered at $\Psi_p = 0$. When the signal contribution from the dominant scatterer vanishes

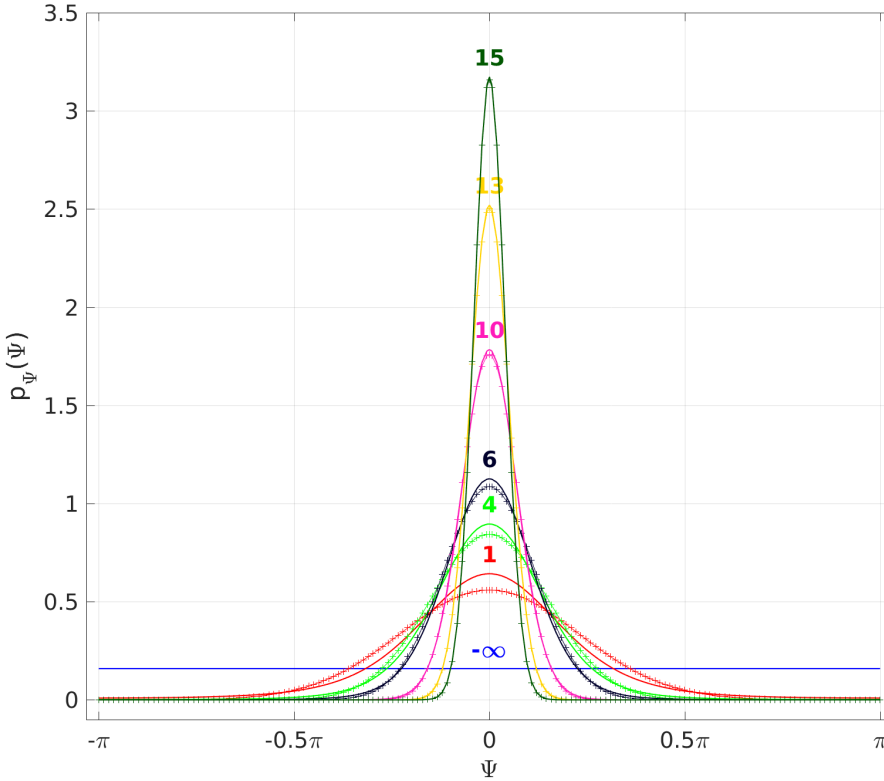


Figure 6.3: Probability density function $p_{\Psi}(\Psi)$ of the SLC phase Ψ (in radians). The color lines represent the PDF (Eq. (6.6)) for different SCR values (in dB) and the crosses are their respective approximations given by Eq. (6.7). When SCR = 0 *i.e.*, $-\infty$ dB (resolution cell with only clutter), the PDF becomes an uniform distribution (blue line). The phase PDF given by Eq. (6.7) provides a reasonable approximation for a range of SCR > 1 dB.

(SCR = $-\infty$ dB), the resolution cell has only the clutter part and the phase PDF approaches a uniform distribution, see blue line in Fig. 6.3. The PDF in Eq. (6.6) can be numerically approximated by,

$$p_{\Psi}(\Psi) \approx \frac{1}{\sqrt{4\pi \text{SCR} - \sqrt{3}}} \cdot e^{\frac{-\pi\Psi^2}{4\pi\text{SCR} - 2\sqrt{3}}}, \quad \forall -\pi \leq \Psi \leq \pi, \text{ and } \text{SCR} > \frac{\sqrt{3}}{2\pi}. \quad (6.7)$$

Eq. (6.6) is a zero mean ($\Psi_p = 0$) Gaussian phase PDF with variance given by,

$$\sigma_{\Psi}^2 = \frac{\pi}{2\pi \text{SCR} - \sqrt{3}}. \quad (6.8)$$

The approximated PDF of Eq. (6.7) is plotted against the full PDF (Eq. (6.6)) in Fig. 6.3. From Fig. 6.3 we see that PDF approximation given by Eq. (6.7) (colored crosses) matches very well with the true PDF of Eq. (6.6) for values of SCR > 1 dB. But, for the case of SCR \leq 1 dB, the PDF approximation cannot fully describe the PDF (Eq. (6.6)). However, the proposed approximation is more than sufficient for the small reflector tiles proposed in this study, as their SCR is in the order of 5 to 6 dB. Now, for the reflectors with SCR > 1 dB the standard

deviation of the interferometric phase ϕ of a resolution cell for the single-look case can be written from Eq. (6.8):

$$\sigma_\phi = \sqrt{2} \sigma_\Psi = \sqrt{\frac{2}{2SCR - \sqrt{3}/\pi}} \approx \sqrt{\frac{2}{2SCR - 0.55}}. \quad (6.9)$$

The proposed expression for σ_ϕ is plotted in dashed red line in Fig. 6.1. Comparing the red line (proposed expression, Eq. (6.9)) and blue line (theory, Eq. (6.2)) with the black line (simulated) in Fig. 6.1. One realizes that, Eq. (6.9) provides an improved estimation of the interferometric phase precision for both low and high SCR targets when compared to the high-SCR approximation given by Eq. (6.2). In this study, we used Eq. (6.9) to obtain the phase precision of the low-SCR targets such as RT.

The estimation of a reflector SCR prior to its installation is a basic requirement in order to optimize design and resources. We estimate SCR of a (point target) reflector tile, $S_{\text{reflector}}$, from the ratio of RCS of the reflector to the expected RCS of the background clutter at the RCS location:

$$\langle SCR_{\text{reflector}} \rangle = \frac{\text{RCS}_{\text{reflector}}}{\langle \text{RCS}_{\text{clutter}} \rangle}, \quad (6.10)$$

where $\langle \rangle$ is used to indicate the estimator operator and $\text{RCS}_{\text{reflector}}$ is deterministic.

In the next subsections, we describe how to determine RCS for both the reflector tiles and the clutter.

6

6.2.2. Radar cross-section of reflector tiles

For simple objects, the RCS can be calculated from their geometry. In our study, we use a triangular trihedral reflector whose aperture forms an isosceles triangle, as shown in Fig. 6.4. Note that the sides b and a are different, with $b > a$. This is a design choice we made to optimize the angular reflection pattern (the maximum reflection is required in the direction of the satellite) and the available space, while maximizing the RCS, see Section 6.3.1.

The effective aperture of a triangular trihedral reflector, A_{effec} , is determined from the portions of the surface that participate in the triple bounce mechanisms (Knott et al., 1985). A_{effec} is shown in Fig. 6.4 as a gray irregular hexagon. The relationship between RCS and A_{effec} is given by:

$$\text{RCS}_{\text{reflector}} = \frac{4\pi \cdot A_{\text{effec}}^2}{\lambda^2}. \quad (6.11)$$

The effective aperture can be calculated as follows

$$A_{\text{effec}} = \frac{a \cdot h}{2} - \frac{a \cdot h}{6} = \frac{a \cdot h}{3}, \quad (6.12)$$

where a and h are as indicated in Fig. 6.4. Note that h and b are related through Pythagoras's theorem but we use h for convenience. The reflector RCS now becomes:

$$\text{RCS}_{\text{reflector}} = \frac{4\pi \cdot a^2 \cdot h^2}{9\lambda^2}. \quad (6.13)$$

It is worth noting that in the case where the sides are equal $h = a\sqrt{3}/2$ and the RCS is given by:

$$\text{RCS}_{\text{reflector}} = \frac{\pi \cdot a^4}{3\lambda^2}, \quad (6.14)$$

which is the well-known RCS of a triangular trihedral reflector (Knott et al., 1985).

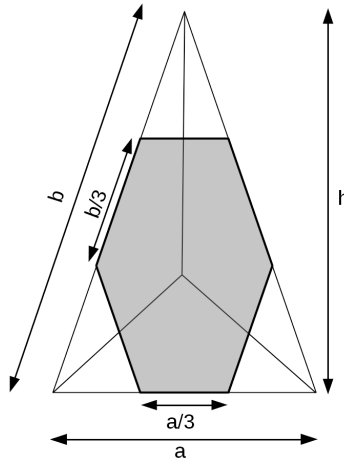


Figure 6.4: Triangular trihedral reflector used in this study, with $b > a$. The effective aperture, A_{effec} , is shown as a gray irregular hexagon.

6.2.3. Radar cross-section of the background

The clutter RCS, depends on the resolution of the radar and on the radar backscatter coefficient of the area:

$$\text{RCS}_{\text{clutter}} = \sigma_0 \cdot A, \quad (6.15)$$

where A is the ground area equal to the resolution cell, and σ_0 the radar backscatter coefficient.

Models of σ_0 for different terrain types are reported in Ulaby and Dobson (1989), which includes rocky terrain, and short vegetation, among others. We have also access to the Dutch ROVE dataset (de Loor et al., 1982), which comprises many measurements of agricultural crops, grasses and bare soils at X-band and Ka-band. We estimate the clutter RCS using the scattering model that was estimated in Ulaby and Dobson (1989) for the case of terrain with short vegetation. The modeled σ_0 is given in dBm^2 per m^2 for different incidence angles, which can be easily adapted to the resolution and incidence angle provided by TerraSAR-X.

6.3. Small reflectors for ground motion monitoring

In this section we provide the design of a small reflector that is optimized for ground motion monitoring. In subsection 6.3.1 the small bidirectional reflector is described. The expected SCR for these reflectors is analyzed in subsection 6.3.2.

Next we investigate the challenges that are posed by the use of small reflectors due to their low SCR. In particular, we face two challenges for the case applying InSAR to ground motion monitoring. First, a small reflector is difficult to detect from a single image, especially if its SCR is less than 13 dB (Skolnik, 1962). Second, system noise plus clutter noise may dominate the radar returns, so the signal of interest such as the ground motion may not be observed. To overcome those two limitations, we provide a method that consists of a deployment strategy and a filter, see subsections 6.3.3 and 6.3.4.

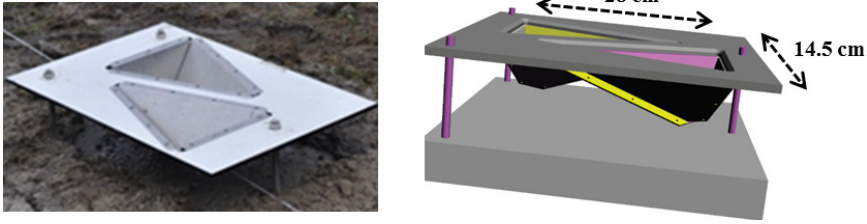


Figure 6.5: Bidirectional reflector tile, during the installation (left) and the original design (right).

6.3.1. Bidirectional reflector tiles design

The reflector that we have designed for infrastructure monitoring is a bidirectional reflector tile as shown in Fig. 6.5. The tile includes two small trihedral corner reflectors. One reflector is oriented to the ascending pass direction, and the other to the descending. Since they are connected to a unique tile structure, the reflectors are subject to the same ground displacement signal. Therefore, the reflector tile can be easily applied for the estimation of a 2-D vector displacement. Note also that the reflector's aperture has a horizontal orientation to ease installation. The reflector's orientation plays obviously a major role, since we want the maximum RCS direction to coincide with the incidence angle θ_i of the satellite radar. Fig. 6.6 shows a cross-cut of the reflector where the angles and dimensions are defined. Through the selection of the rib sizes c and d , we have some freedom in selecting the maximum RCS direction, while maintaining the horizontal aperture orientation. The ratio d/c determines the depression angle δ of the long rib c . The maximum RCS direction of the reflector with respect to rib c is θ . For a symmetrical corner reflector ($c = d$) $\theta = 54^\circ$. θ increases with the ratio d/c as demonstrated in Fig. 6.7.

The depression angle δ also increases with d/c . We may write the following relation:

$$\theta_i = 90^\circ - \delta - \theta. \quad (6.16)$$

Fig. 6.7 shows the variation of θ_i , the direction of maximum RCS of the reflector, on the d/c ratio. By tuning the d/c ratio and the depression angle, the incidence angle required for a given sensor can be achieved. It is worth noting that the majority of radars operate with incidence angles between 20° and 50° . We constrained further the design with a second requirement on the thickness. We kept the thickness of the reflector (measured from apex to aperture) limited to ~ 10 cm, so it would fit in a top layer of a road for instance, which is

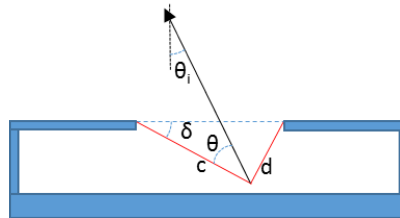


Figure 6.6: Cross-cut of the bidirectional reflector tile, with one corner reflector shown. The corner depression angle δ and the maximum RCS direction θ can both be influenced by the ratio of the corner ribs c and d .

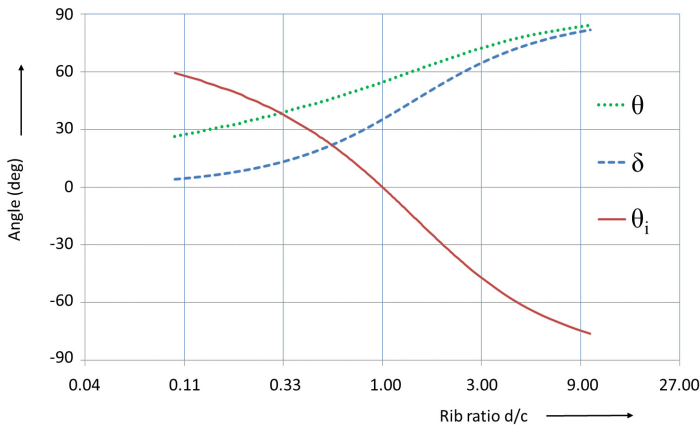


Figure 6.7: Three parameters that depend on the corner rib ratio d/c are plotted. The corner depression angle δ and the angle of maximum RCS both increase with d/c . The resulting maximum RCS direction of the bidirectional reflector tile decreases with d/c , spanning an angular range of more than 120° .

usually in the order of 10 to 20 cm.

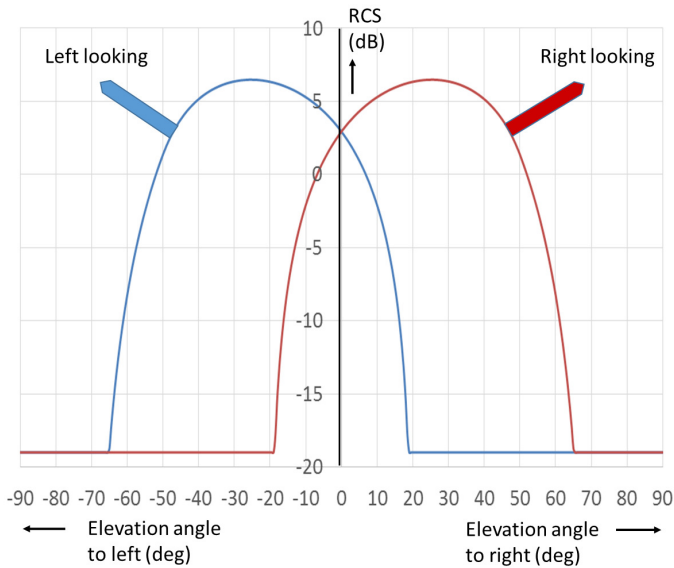


Figure 6.8: Elevation diagram for the bidirectional reflector. Vertical look direction is θ_0 . Left looking angles are negative, right looking positive. The responses of the two corner reflectors are plotted separately. For incidence angles > 20 degrees (left and right looking) only one corner reflector will respond to the radar, ensuring a well-defined phase centre for the reflector.

The bidirectional corner reflector tile used in our experiment has dimensions $c = 28.2$ cm and $d = 14.5$ cm, resulting in a ratio $d/c = 0.51$. Hence, $\theta_i = 25.3^\circ$. The wide elevation beamwidth of the corner reflector provides sufficient flexibility to cover practical

satellite radar incidence angle ranges. Fig. 6.8 displays the actual elevation diagrams for the bidirectional reflector. The beamwidth for each section is 45 degrees. Note that for satellite incidence angles over 20 degrees only one section will produce a reflection. This ensures a single reflection from the bidirectional tile, leading to a stable and well defined phase centre. For angles smaller than 20 degrees both reflectors would contribute, leading to erroneous phase signals. In the design process the minimum angle can be chosen as required. We have chosen the same d/c ratio for the two corners in the bidirectional reflector, but it would be possible to use different ratios for both corners, in order to optimize the incidence angles for ascending and descending tracks of the satellite radar.

The maximum RCS of each reflector is 6.4 dBm^2 , which is calculated using Eq. (6.13). The total dimensions of the tile are around $35 \text{ cm} \times 20 \text{ cm}$, with a height of 12 cm (excluding support base), similar to a pavement tile. The reflector tile was designed to monitor grass-covered dikes, which are very common in the Netherlands and other low land countries. A hole is drilled at the bottom of each reflector to drain rain water. Installing a radome is possible, but we did not test this. We expect that a radome will introduce a loss between 1 and 1.5 dB (Skolnik, 1962).

6.3.2. Expected SCR

As previously explained, we estimate the reflector SCR prior to its installation using a model of the backscattering coefficient σ_0 , of the background where the reflector will be placed. Our test will be executed with TerraSAR-X images, with resolution $3 \times 3 \text{ m}$, and the incidence angle varies between 24 and 39 degrees. The σ_0 of terrain with short grass observed with an X-band radar at an incidence angle of 20 to 40 degrees is around $-8 \text{ dBm}^2/\text{m}^2$ according to the Dutch ROVE dataset (de Loor et al., 1982) and (Ulaby and Dobson, 1989). Now, the background RCS can be found from Eq. (6.15). The result is 1.5 dBm^2 . Therefore, we expect a reflector SCR in the order of 4 to 5 dB. The value will not be the same for ascending and descending tracks, because the incidence angles are different and hence the σ_0 will change slightly. Furthermore, the RCS of the corner reflector at the satellite incidence angle of 39° is slightly reduced, as can be seen in Fig. 6.8.

Based on the estimated value of the SCR we derive a first indication on the expected standard deviation using Eq. (6.9). An SCR of 5 dB is equivalent to a phase standard deviation of 0.6 rad, which provides about 1.5 mm Line-Of-Sight (LOS) deformation precision (1σ confidence) for TerraSAR-X.

6.3.3. Reflector tiles deployment

We deploy the reflectors in a predefined and therefore recognizable pattern in order to precisely localize low SCR reflectors. The chosen pattern helps to both identify the reflectors within the SAR image and to yield an efficient method for spatial filtering. A matched filter can be used for fast and accurate localization of the reflectors within a SAR image. Fig. 6.9 (C) shows deployment patterns that are used in the experiment.

Fig. 6.9 (A) and 6.9 (B) display time averaged amplitude images for (A) descending (30 images averaged) and (B) ascending passes (20 images averaged). Small reflectors forming a quincunx-shaped pattern are marked with red arrows. Because of their low SCR, the reflectors are almost undistinguishable from the clutter. The predefined deployment pattern therefore helps in their detection. Other reflectors of larger size are deployed in an arrow-shaped pattern. They appear as a very bright points in the descending pass, see

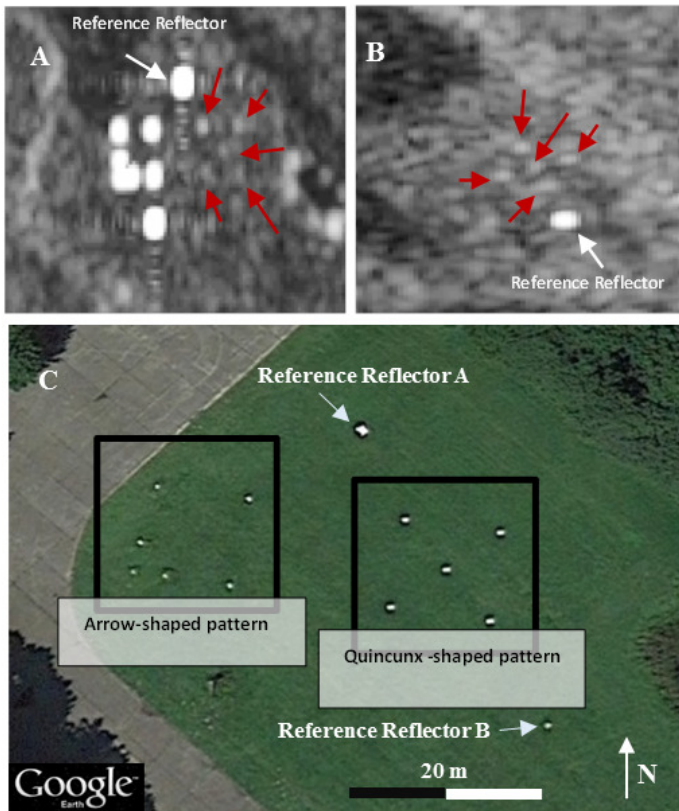


Figure 6.9: Incoherent time-averaged SAR images for (A) descending and (B) ascending passes. Reflector tiles are indicated with red arrows. White arrows indicate reference reflectors, which are larger trihedral corner reflectors. (C) Optical image (Google Earth (GoogleInc., 2017)) of the area. Reflector tiles are deployed in a quincunx shape pattern. Other reflectors (trihedral ones) are deployed in an arrow-shaped pattern. These reflectors were not used in this study and only visible in the descending pass, see (A).

Fig. 6.9 (A). The reflectors forming an arrow-shaped pattern are not used in this study.

6.3.4. Filtering

We filter the data by taking the coherent mean of the complex signal of the five selected pixels. This is similar to the coherent integration that is performed in classical radar technology (Skolnik, 1962) to improve the signal to noise ratio. For truly coherent signals in the presence of random noise, the SCR improvement is equal to the number of coherently summed samples. In the InSAR case, the coherent filter improves the SCR when all reflectors are subject to the same deformation signal. Furthermore, since the distance between them is short, the atmospheric delay experienced by the radar returns is negligible between the reflectors. With the complex mean, the signal that is common to all reflectors (i.e. ground deformation) adds up. However, the clutter noise reduces due to its random nature. Therefore, the increase in SCR is equal to the number of reflectors included in the filter, which is the same as the number of integrated radar returns. In Section 6.4, we

prove experimentally that, despite the low power returned by individual reflectors, coherent averaging greatly reduces phase noise.

6.4. Experimental results

To test the bidirectional reflectors, we deployed them forming a quincunx pattern, as shown in Fig. 6.9. The test site was located in the Netherlands, a TNO premises near to Delft with visibility from both ascending (incidence angle $\sim 39^\circ$) and descending (incidence angle $\sim 24^\circ$) passes. The reflectors were installed in a geophysically stable area in a grass field, thus resembling the setup for our final goal, which was monitoring dikes which have similar vegetated surfaces.

6.4.1. Setup

In order to place many small CRs in a predefined formation, the spatial distances between reflectors have to be carefully chosen. Distances should not be too short, to avoid interference between reflectors. We found that the distance between the reflectors should be *at least two resolution cells* to avoid mutual reflector interference. In addition to that, the maximum distance between the reflectors should be smaller than the decorrelation distance expected for both the deformation and the atmospheric signal, otherwise the spatial filter is not effective. Finally, the orientation of the pattern is chosen such that the interference due to side lobes (from the CRs in the formation) is minimal.

6.4.2. SCR estimation

There exist different methods to estimate the SCR (de Loor et al., 1982), our approach is as follows. First the clutter power is determined by measuring the mean radar power of a small, homogeneous area (with grass) before the reflector is installed. After the reflector is placed, we determine its response, which is the sum of the reflector and the clutter, and estimate the ratio of the two powers. Although clutter power will change over time, this method provides a reasonable approximation of the SCR, as the backscatter of the area is rather stable during wintertime when we performed this experiment. The power ratio determined this way, is

$$\frac{P_R + P_C}{P_C}. \quad (6.17)$$

The SCR was introduced in Eq. (6.1) as $S = P_R/P_C$, and can be easily calculated from the measured quantities. Clearly, the SCR will be smaller than the ratio in Eq. (6.17). After the tiles were installed, the received power at the corresponding pixel positions increased ~ 6 dB, see Fig. 6.10. As explained above, the SCR can now be estimated as 6 dB. This value is in agreement with the estimation in Section 6.3.1.

From radar detection theory it is known that reliable detection of a target requires an SCR of at least 13 dB (Skolnik, 1962); hence the tiles are ~ 7 dB below detection threshold. In principle, this makes the reflector tiles suitable for covert operations. To increase the RCS of the tiles to obtain an SCR of 13 dB, their size would have to be increased. Applying the same ratio, the sizes c and d in Fig. 6.6 would increase by a factor 1.6, from $14.5 \times 28.2 \text{ cm}^2$ to $23.2 \times 45.1 \text{ cm}^2$, which is considerably larger.

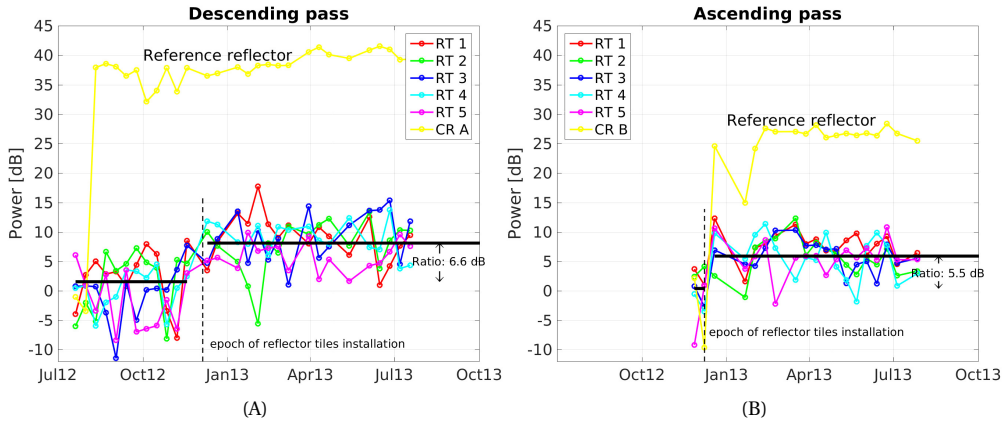


Figure 6.10: Estimated SCR for tile reflectors (RT 1 to RT 5) observed in the descending and ascending pass (red arrows in Fig. 6.9 (A,B)). The reference reflector (of sides 1 m in descending and 45 cm in ascending) are traditional trihedral corner reflectors (white arrows in Fig. 6.9). CR A and CR B were installed in August 2012 (for descending) and December 2012 (for ascending), respectively.

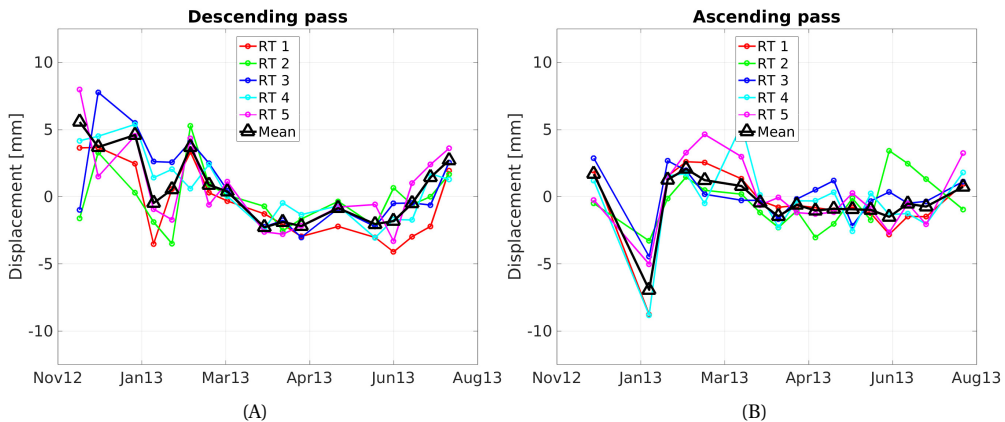


Figure 6.11: Displacements estimated from interferometric phases for (A) descending and (B) ascending. Values represent motion with respect to the reference reflector. Mean value is shown with black triangles. Only observations after the installation of reflectors are included.

6.4.3. LOS deformation results

After the interferograms are formed with respect to a common master image and the contribution of the reference surface (the WGS84 ellipsoid) is removed (Hanssen, 2001a), we calculate the interferometric phase differences of all reflector tiles with respect to a reference reflector. A reference reflector with a SCR of around 37 dB (1 m sides) and 27 dB (45 cm sides) are used in descending and ascending, respectively, to avoid the addition of extra noise when taking double differences. The resulting phase differences are converted to radar LOS displacements. Fig. 6.11 shows the displacements for descending (A) and

ascending (**B**) passes after the installation of the 5 reflector tiles on the 5th of December 2012. The phases of individual reflectors appear relatively stable, with the exception of the period around mid-January, when the reflectors were covered with snow. Note that, despite the low SCR of individual reflectors (~ 6 dB on average) the phase signal appears to be reasonably coherent. We reduce the phase noise by coherent averaging the five pixels in space as explained in Section 6.3.4. The mean values of the interferometric phases of the reflectors are shown in Fig. 6.11 as black triangles for every measurement day. From this figure it is clearly visible that the variability of the signal of the mean is considerably less than those of individual reflectors.

Next, we estimated the improvement obtained from the filter. It is worth noting that the filter only works optimally if the phases are aligned in the sense that all reflectors included in the filter observed the same signal. In other words, the filter is optimal when the signal of interest (e.g. ground deformation) is spatially correlated and noise is not. For noise variance estimation, we approximate the displacements with a linear plus seasonal model. After removal of the estimated model, we determine a noise standard deviation of 3 mm for individual reflectors, the sensor wavelength being 31 mm. After the complex mean operation, we estimate 1.5 mm standard deviation. The observations around the snow fall period (January 2013) are not used in the estimation of the standard deviation. The reduction in the standard deviation by a factor of 2 is in agreement with the expected theoretical improvement of \sqrt{N} , where N is the number of reflectors, equal to five in our case. We recall that the SCR improvement is a factor N , leading to a reduction in σ_ϕ of \sqrt{N} , see Eq. (6.9). The estimated noise variances determined for this dataset are probably overestimated since they include unmodeled deformation, and other signals that are not truly noise. In any case, this experimental setup measures the improvement obtained with the complex mean compared to their individual reflectors.

6

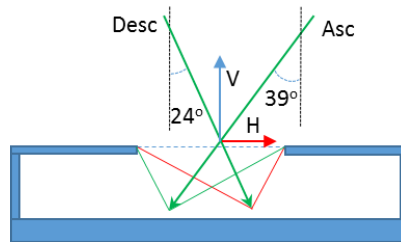


Figure 6.12: Geometry of the observations in the plane through the two radar lines of sight and their decomposition.

6.4.4. Decomposition of LOS deformation

The bidirectional tiles enable decomposition of the LOS deformation into horizontal and vertical displacement values. The TerraSAR-X observations were taken from two directions, ascending and descending passes at $\sim 39^\circ$ and $\sim 24^\circ$, respectively. To find the vertical and horizontal displacements we need to solve the following equations (Hanssen, 2001a):

$$\begin{bmatrix} d_{\text{desc}} \\ d_{\text{asc}} \end{bmatrix} = \begin{bmatrix} \cos(\theta_{\text{desc}}) & \sin(\theta_{\text{desc}}) \cdot \cos(\alpha_{\text{desc}}) \\ \cos(\theta_{\text{asc}}) & -\sin(\theta_{\text{asc}}) \cdot \cos(\alpha_{\text{asc}}) \end{bmatrix} \begin{bmatrix} V \\ H \end{bmatrix} \quad (6.18)$$

with d_{desc} , d_{asc} the displacement observed by the satellite in descending and ascending mode. θ_{desc} , and α_{desc} are incidence and heading angles in descending mode while θ_{asc} , and α_{asc} are incidence and heading angles in ascending mode. V , and H are the vertical and horizontal (East) components, respectively.

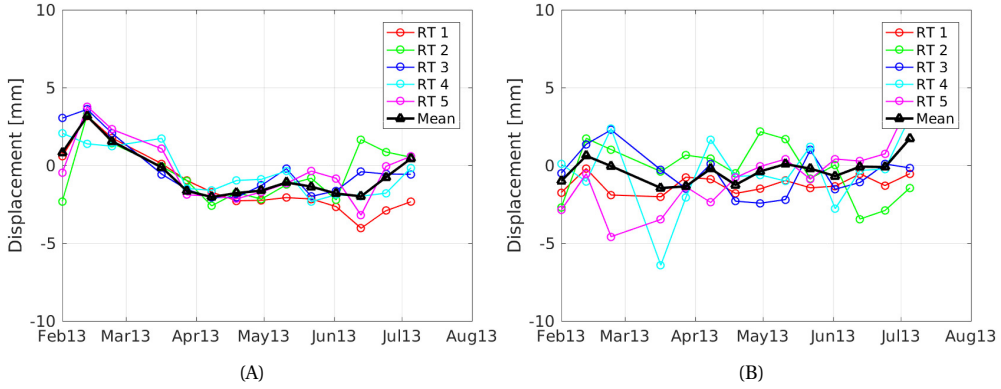


Figure 6.13: (A) vertical and (B) horizontal displacement of the 5 reflector tiles (RT1 to RT5) as a function of time in the first half year of 2013. Black line with triangles represent the displacements after signal is spatially filtered. Color lines with circles represent the estimations of vertical and horizontal displacement for individual reflector tiles RT1 to RT5.

The heading angles of the satellite are 350° ($\alpha_{\text{asc}} = 10^\circ$) for ascending mode and 192° ($\alpha_{\text{desc}} = 12^\circ$) for descending mode. Since the radar looks perpendicular to the satellite track, the horizontal displacement in East-West direction is the easiest to measure, whereas the one in North-South direction may experience low accuracy. The vertical accuracy is dependent on the incidence angles. Fig. 6.12 shows the situation in a diagram.

In this case study, the observed displacements are expected to be mostly in the vertical direction. However, discrepancies between the signals observed at ascending and descending passes may occur due to a difference in the incidence angle between passes ($\sim 39^\circ$ and $\sim 24^\circ$, respectively) and different reference reflectors for ascending and descending passes. Different sampling times can also produce large variations between these two time series. For example, the snow fall in the beginning of January 2013 was closer in time to the ascending acquisition than to the descending one, as can be seen by comparing Fig. 6.11 (A) and (B).

The estimated vertical and horizontal displacements are shown in Fig. 6.13. The plotted lines include both estimates, the ones obtained from individual reflectors (colored lines with circles) and also the estimate obtained after applying the complex mean filter (black line with triangles). The variances and co-variance of vertical (V) and horizontal (H) components of the complex means are (from Eq. (6.18)) $\sigma_V^2 = 1.3^2 \text{ mm}^2$, $\sigma_H^2 = 2.1^2 \text{ mm}^2$, and $\sigma_{VH}^2 = 0.6^2 \text{ mm}^2$, respectively. These values are smaller by a factor of N when compared to the individual tiles.

We observe a weak horizontal component. We attribute this to the noise floor, besides that we do not expect any motion of the reflector tiles in the horizontal plane (based on the local conditions). In the vertical plane we see a subsidence of the reflectors of several mm's in the first two months after installation. This could be a settling effect. The tiles were

simply placed on a 10 cm layer of sand, which was compressed manually.

6.4.5. Discussion

The reflector tiles that we propose in this research were designed for monitoring grass covered dikes and specifically developed for X-band satellites. We selected X-band satellites, because they provide high resolution data and have small wavelengths enabling to use small reflectors which are cheaper. Furthermore, there are a large number of X-band satellites, TerraSAR-X, Cosmo-SkyMed and KOMPSAT5, that can help to reduce the observation time and improve the monitoring strategy. The deployment of reflectors should aim at optimizing the sampling of the ground deformation, but also take into account that the distance between reflectors should be less than the decorrelation distance of atmospheric disturbances, i.e. around 800 m (Rocca, 2007). When monitoring infrastructures such as natural dikes (e.g. peat dikes) we suggest positioning the reflectors near the dike's crown, as the upper part of the dike experiences the largest fluctuations. The final precision of the LOS estimation will depend on the number of reflectors included in the filter. For example if the deformation signal does not change over an area where N reflectors are included in the spatial averaging filter, the expected precision is around $3/\sqrt{N}$ mm. Although developed for dike monitoring (e.g. grass, and vegetation covered dikes), these bidirectional tiles are also well suited for other types of infrastructure, such as large bridges and dams whose orientation is not optimal for the radar satellites.

6

6.5. Summary and conclusions

We have shown that small corner reflectors can be of use for interferometric applications. However, due to their low SCR they appear hidden in the clutter. By deploying the reflectors in predefined patterns, we were able to localize them in radar images, whereas the individual reflectors were invisible in a single image. They start to appear somewhat visible after applying a temporal filter on radar backscatter images. Despite their low SCR, we have proved that small reflectors contain coherent information and that they are valuable for interferometric applications. A combination of small reflectors can be used to reduce SCR induced errors in the interferometric phase or deformation signal. In addition, we have derived a new expression to estimate interferometric phase precision for resolution cells having a point target and clutter. From our experiments, we conclude that the complex mean of the interferometric signals improves the phase accuracy by a factor \sqrt{N} , where N is the number of reflectors in the ensemble. We estimated for each reflector tile ~ 3 mm standard deviation of the interferometric phase noise, compared to ~ 1.5 mm for the complex mean of 5 reflector tiles. Noise includes all signals that are not included in the deformation model. We were able to decompose the LOS deformation signals of ascending and descending passes in horizontal and vertical displacements of the reflector tiles with a standard deviation of about 2.1 mm and 1.3 mm, respectively. The structure of the reflector tiles enabled this application in a favorable way.

7

Conclusions and Recommendations

The goals of this research are (i) to develop methods to identify the object within the SAR resolution voxel that is responsible for the coherent reflection (decoding), and (ii) to design, deploy and test new reflecting objects in order to introduce a new coherent measurement (encoding). In this chapter, we present the key conclusions, list the main contributions, and recommend future research.

7.1. Conclusions

This study presents methodology to decode and encode spaceborne radar interferometry measurements in a systematic approach with experimental validations. The main conclusion is that radar measurements should be, and can be, linked to objects on the ground, which is possible using classification and/or precise point positioning. As a result, we are better able to interpret the estimated displacements and utilize these for infrastructure asset management.

In case no coherent reflection can be obtained at a desired location, we introduce a novel method to encode new coherent measurements using a distributed set of small radar reflectors, referred to as a Distributed Corner Reflector, which can be used as an alternative for large and bulky reflectors estimates with an accuracy of a few millimeters.

We defined three research questions and several sub-questions, as described in chapter 1. Secs. 7.1.1 and 7.1.2 are related to decoding and sec. 7.1.3 is related to encoding.

7.1.1. Decoding via target classification

The first research question, “*How can we identify each coherent radar scatterer on the ground and relate InSAR-derived displacements to stress on the infrastructure?*”, is addressed by the following three sub-questions.

Sub-question 1. How can we attribute radar scatterers to different types of infrastructure?

Infrastructure can be grouped into two types: above-ground (elevated) infrastructure and underground infrastructure. Relative deformation between these two might pose a safety risk. For example, underground cast-iron gas pipes are connected to houses, leading to an explosion risk in case of relative deformation between the two. PSI provides displacements of PSs, which are randomly distributed spatially. Identifying the ground-related PSs through classification is a vital step towards correctly interpreting the PS measurements. Combining (1) polarization, (2) amplitude and (3) phase measurements, scatterer classification was shown possible in literature.

In our approach, radar scatterers from elevated infrastructure and ground-level are separated using their height estimates, see chapter 3. This approach is favored over polarimetric and amplitude-based approaches, as large Doppler and perpendicular baseline variations are not always available. The height-based classification method estimates the local ground height distribution near each PS location in order to discriminate PSs at the ground level from those from elevated structures. This method is self-reliant on PS and it does not use require an external DEM.

The performance of our classification method is tested with simulated data and real data spanning 20 years. In the simulation, the success rate of classification is found to be above 80% when the number of scatterers from the ground level reaches 50% or higher. The InSAR satellites usually acquire images with moderately steep incidence angles which guarantee a substantial number of scatterers from the ground level, and therefore an adequate classification outcome. Applied on real data, our approach proves to be sufficiently reliable for practical applications, and is currently operationally applied for asset management by some of the main utility providers in the Netherlands. Finally, it is demonstrated that the DEM of the area obtained as a by-product of the height-based classification can be exploited for the classification performance analysis. The DEM obtained from the classification results of ERS, ENVISAT, and TerraSAR-X is compared with a high-quality lidar data (AHN2) and is found to be ~ 1 m accurate.

By segregating scatterers into above-ground and underground types, the classification method facilitates a first level interpretation of the estimated height and velocity, as the deformation of the ground and the buildings can be investigated separately. We present the results of our target classification in two ways — point based, and postcode based. From the classification results (sec. 3.3.3) it is demonstrated that our height-based methodology is reliable and can be used as a tool for localized and wide-scale deformation interpretation.

Sub-question 2. How can we classify different deformation phenomena in order to relate them to stress on underground infrastructure?

The next challenge is to classify the driving mechanisms so that the type of deformation experienced by a particular type of infrastructure can be identified. Relative deformation of infrastructure at a very-local scale — within itself and in relation with other infrastructure and underground utilities — may pose problems in terms of its stability and the safety of the people in the neighborhood.

The proposed deformation classification methodology uses the high-low separation per point, as discussed above, and combines it with the deformation of the neighboring PSs through a hypothesis testing procedure. The hypothesis testing procedure takes the

precision of PS deformation estimates into account and enables the end-user to set a significance level to detect anomalous differential deformation.

Relative deformation between two scatterers is classified into five regimes: autonomous structural motion, shallow compaction, local land subsidence, inter-structural deformation, and no relative motion, see Tab. 3.2. A 'no relative motion' regime is detected when there is no significant relative deformation. A 'shallow compaction' is identified when the ground shows a significant displacement relative to the elevated infrastructure and vice-versa for an 'autonomous structural motion'. A 'local land subsidence' captures relative motion between the ground while an 'inter-structural deformation' represent motion between buildings. The 'shallow compaction', and 'local land subsidence' types relate to the stress on the under-ground infrastructure such as gas pipes and water pipes. The 'autonomous structural motion' and 'inter-structural deformation' types represent the stress on the elevated infrastructure itself.

Sub-question 3. How can we detect, quantify, and analyze potential stress on infrastructure so that asset maintenance can be prioritized?

Subsidence is a global problem which has consequences to infrastructure, its maintenance and the people dependent on them. The Netherlands Environmental Assessment Agency (PBL) has provided an estimate of about €22 billion to fix the damage caused by land subsidence until 2050 in the Netherlands alone.

Accumulation of stress in the underground utilities infrastructure consisting of gas transportation pipes, electricity pipes, water pipes, and sewer pipes can result in severe accidents with economic damage and loss of lives. A fracture in gas pipe network had led to explosions in the past, see Fig. 3.34. Government agencies along with underground pipe network companies are working together to prioritize replacing the brittle pipes. For this goal, a deformation-based classification methodology is proposed using InSAR to quantify stress and prioritize the replacement of the vulnerable brittle pipes.

We propose a new parameter called the relative deformation index (RDI) to quantify and analyze potential stress on infrastructure. RDI, expressed in percentage, is defined as a ratio between a mean relative deformation at a PS location and a threshold critical displacement. RDI uses a user-definable deformation rate threshold to assist asset managers towards detecting and analyzing critically deformation regions. Since RDI combines all the relative deformation types such as autonomous structural motion, shallow compaction, local land subsidence, and inter-structural deformation into one parameter, it can be used to detect localized deformation of a scatterer in relation to its neighborhood. As RDI uses relative deformation, the actual deformation of the reference point (assumed stable in most cases) in the deformation interpretation can be eliminated.

We apply the RDI-based approach to a stack of TerraSAR-X interferograms over Amsterdam and using RDI we successfully demonstrate the monitoring of the underground assets for gas transportation pipe networks. The results obtained from RDI are validated using gas pipeline-failure data (sec. 3.5). The generated RDI map, serves as an infrastructure stress map, and is presented per region using the postcode as an example. Such a region based stress map can be used to strategize and prioritize regions for preventive maintenance and the brittle pipe replacement.

The challenge of maintaining and replacing older and brittle underground infrastructure is not just limited to gas pipelines, water pipeline network among others face a similar problem. In order to assess the impact of relative deformation on underground water pipeline network infrastructure, we study The Hague region using a TerraSAR-X dataset with our methodology. Application of RDI, provided us with a pipe replacement prioritization map, which establishes the value-addition of the proposed approach (Appendix B). The approach can be deployed at places where an InSAR data stack is available and it does not require any additional information about the reference point and the terrain (*i.e.* 3D city model). Our methodology for infrastructure stress monitoring derived from the radar satellite data is useful, cost-effective and can be extended to other applications such as underground tunnel monitoring, and building stability analysis.

7.1.2. Decoding via 3D positioning and target association

The second main research question is, “How can we precisely associate each coherent radar scatterer to a physical object on the ground?”, which is addressed by the following three sub-questions (highlighted in gray).

Sub-question 1. How can we pinpoint very-localized deformation?

7

In order to detect very-localized deformation, *e.g.* different parts of the same infrastructure, precise point positioning of radar scatterers is necessary. The relatively poor positioning accuracy of InSAR measurement points is a major roadblock in interpreting PSs on infrastructure. An error in the 3D position could result in mis-association of PSs to infrastructure and could therefore lead to mis-interpretation of deformation estimates.

By addressing positional errors in a mathematical model, we improve accuracy and precision of the 3D position. As a result, scatterers can be rightly associated to physical objects and achieve a very-localized deformation interpretation. In this approach, mitigation of the positional offsets and deriving a quality description are the key steps.

Scatterer positioning involves a set of steps that maps a position in radar image coordinates (in pixels) to a corresponding point in terrestrial coordinates (in meters). In chapter 4, we introduced a systematic geodetic procedure using a standard Gauss–Markov approach to account for position offsets and perform error propagation from the radar coordinates to a local Cartesian coordinate system. In the end, we derive an *accurate* estimated position and an associated *precision* expressed via the variance-covariance matrix in the local 3D coordinates.

The approach developed in chapter 4 is tested on high-resolution TSX stripmap data (in chapter 4) and medium-resolution ENVISAT data (in chapter 5). The Position improvement obtained from the step-by-step geodetic procedure for artificial corner reflectors and PSs is validated using the ground truth data such as DGPS, and 3D model. The results demonstrate that this procedure is applicable to a general purpose InSAR stack and can achieve improvements in the positioning capability of millions of radar scatterers.

Sub-question 2. How can we systematically model error contributions and estimate the 3D position of a radar scatterer, with a proper quality description?

Position error contributions can induce errors ranging from centimeters to several meters. Since timing errors such as bistatic offset can vary across image and the transformation from radar coordinates (range r , azimuth a , and cross-range c) to terrestrial coordinates (east e , north n , and height h) is non-linear, we found the position errors to vary across the scene. Hence, a point-level correction mechanism is necessary rather than at an image-level (chapters 4 and 5). For this purpose, we introduce the functional and stochastic models for each scatterer to facilitate precise point positioning, error propagation and quality assessment and control.

The functional model is found to be perturbed by several secondary components in azimuth and range. These are the components measured by the radar but considered as noise in the position estimation. It includes the dominant terms such as range path delay, tectonic plate motion, solid earth tides, orbit errors, and timing errors. External data such as GNSS and tide models are used to estimate these secondary components in the functional model. The stochastic model captures (i) unmodeled secondary components, (ii) quality of external data used for secondary components computation, and (iii) the error in the position determination due to the scatterer's signal-to-clutter ratio.

Using a TerraSAR-X and TanDEM-X stripmap dataset over the Netherlands the proposed method is assessed in 2D and 3D with DGPS, tachymetry, and 3D building models using an experiment. As a result, we achieve a 2D precision of about 7 cm for trihedral corner reflectors. In spite of correcting the secondary positional components, we observe a residual azimuth and range timing bias of ~ 2 cm in azimuth and ~ 32 cm in range, see sec. 4.5.1. In 3D, we are able to achieve an accuracy (Euclidean distance from the ground truth) in the order of decimeters, see sec. 4.5.3. Through error propagation, the position uncertainty in radar geometry is transformed into local reference coordinates and is represented by an error ellipsoid. The error ellipsoids are cigar-shaped and elongated in cross-range with a typical ratio of the axis lengths of 1/3/200 in range, azimuth, and cross-range, respectively.

An error in scatterer positioning is a serious problem in medium and low resolution SAR imagery when compared to the high and very-high resolution case. The medium and low resolution variants cover a larger area per resolution cell and yield a relatively poor point density. This makes monitoring parts of an infrastructure difficult. In chapter 5, we apply the procedure developed in chapter 4 and improve the positioning for medium resolution images using ENVISAT ASAR as an example. Here, we introduced the local oscillator drift, and the bistatic offset corrections in the functional model in addition to the existing ones in chapter 4.

Using trihedral corner reflectors installed between 2003 and 2008 in Delft, we have found that the ASAR imagery needs to be corrected for a calibration offset of about 1.58 m in azimuth and 2.84 m in range to achieve bias-free geometric calibration. In 3D, we are able to locate scatterer in the order of decimeters distance from the true location. Similar to chapter 4, the positional precision of scatterers is expressed as error ellipsoid and they are found elongated along the cross-range direction (with a ratio of the axis lengths of 1/0.8/12), representing a coarse precision in that direction, see Fig. 5.14.

The approach to obtain precise positioning, demonstrated for TerraSAR-X and ENVISAT, can be applied to other SAR sensors such as ERS-1/2, RadarSAT-2, Cosmo-Skymed, and Sentinel-1A/1B.

Sub-question 3. How can we establish a link between the radar scatterers and the physical objects on the ground?

By applying the above error modeling and geolocation correction steps, high-precision positioning of radar scatterers in 3D terrestrial coordinates can be integrated with other geodetic data. The object space on the ground can be represented by a 3D city or building model.

An accurate 3D building model serves as ground truth of the environment. The estimated scatterer position along with its error ellipsoid is used as a search space to look for points or objects in the 3D model. Exploiting the covariance matrices of SAR and the 3D building model, the radar scatterers are associated with objects in the 3D mode using the Bhattacharyya metric (chapter 5). Such linking of InSAR measurements with objects on the ground, significantly improves the operational capabilities of PSI by accurately interpreting the estimated deformation of millions of PSs. However, when there are multiple reflections the phase center may not be uniquely associated with the 3D model. In such cases our approach will link the scatterer to an object in the 3D model based on the position ellipsoid's orientation and proximity.

Association of scatterers with their geometrically most probable position in the 3D model is demonstrated for a high-resolution TerraSAR-X stripmap and a medium-resolution ENVISAT dataset in chapters 4 and 5, respectively. Interpretation of deformation from parts of individual infrastructure is shown to be feasible for these types of SAR imagery. This approach also helps in identifying infrastructure and parts of it which are not measured by the PSs approach, see, *e.g.*, the tower of the church in Fig. 5.16. By linking PSs to different types of infrastructure such as roads, power lines, bridges, railways, harbors, and so on, the proposed methodology will pave the way for numerous infrastructure monitoring applications.

7

7.1.3. Encoding via distributed corner reflectors

The final research question is, “*How can we monitor a specific infrastructure (or a point of interest) by artificially encoding coherent SAR measurements?*”, addressed by the following three sub-questions (highlighted in gray).

Sub-question 1. How can we distribute and detect small artificial reflectors for infrastructure monitoring?

InSAR is an opportunistic measurement technique, meaning that obtaining a measurement at a point of interest is not guaranteed. In order to guarantee measuring a specific point on interest, the object space on the ground can be modified by introducing coherent reflectors,

i.e., it needs encoding. To encode the object space artificial radar reflectors can be used, preferably passive reflectors due to their low cost and maintenance requirements.

Artificial reflector deployment for deformation monitoring often has contradicting requirements. To provide with high signal-to-clutter ratio (SCR) and avoid decorrelation noise, their size is required to be large, which obviously complicates their deployment and maintenance. These contradictions lead us to introduce a new concept of distributed corner reflectors in chapter 6.

Small reflectors do not provide high SCR values, but they offer low cost, easy installation, suitability for infrastructure with space constraints, and have a low visual impact on the landscape. To facilitate detection, we have distributed small reflectors in a predefined pattern such as quincunx and arrow shapes. In spite of their low SCR, the predefined pattern and temporal averaging helps in detecting the small reflectors in the SAR image. The reflectors are deployed such that the sampling of the ground deformation signal is optimal, and the distance between reflectors should be less than the decorrelation distance of atmospheric noise. In order to achieve decomposition of deformation signals, small reflectors are designed such that they can be seen in both ascending and descending satellite orbits, see Fig. 6.5. The distributed corner reflector concept that we propose in this research is successfully demonstrated for TerraSAR-X over a region in the Netherlands.

Sub-question 2. How can we describe the phase statistics of small artificial reflectors?

For InSAR applications, the SCR is typically used as an indicator for the standard deviation of the interferometric phase, which propagates to the precision of the ground displacements. In literature, the quality of phase for a point target in a low clutter environment has been derived. However, this closed form expression is only valid for very high SCR targets (SCR above 10 dB) and it underestimates the phase standard deviation for low-SCR targets.

In our case, we used small reflector tiles with a dimension of about $14.5 \times 28.2 \text{ cm}^2$. They exhibited a low SCR of about 6 dB. Therefore to describe the interferometric phase standard deviation for such low SCR targets, an improved closed-form expression is required. For this purpose, we propose a Gaussian approximation for the probability density function (pdf) of the SLC phase. From this approximated pdf, we obtain a closed-form expression for interferometric phase variance as a function of SCR. This expression matches the true pdf very well for the values of $\text{SCR} > 1 \text{ dB}$.

The proposed closed-form expression is able to estimate the interferometric phase precision for both low and high SCR radar targets. The expression provides a better estimate of the interferometric phase precision of $\sim 0.18 \text{ rad}$ compared to the existing one, see Fig. 6.1.

Sub-question 3. How do the distributed CRs perform over a vegetated region?

We provide a design of small reflector tiles and a strategy to distribute them such that it is optimized for ground motion monitoring. The reflector tiles are designed to monitor grass-covered dikes, which are very common in the Netherlands and other low-land countries.

A field experiment is conducted by distributing the reflector tiles in a grassy region in two spatial patterns over a region near Delft, the Netherlands. The data acquired from TerraSAR-X ascending and descending orbits are processed and the interferometric phase standard deviation of each individual small reflector is estimated to be ~ 3 mm. By spatially averaging N small reflectors, we are able to achieve a precision of about $3/\sqrt{N}$ mm. In our experiment, we distributed $N = 5$ small reflectors and we obtain a phase precision of about 1.5 mm after complex averaging. Decomposing ascending and descending tracks, horizontal and vertical deformation are estimated with a precision of ~ 2.1 mm and ~ 1.3 mm, respectively.

Although developed for dike monitoring (e.g. grass, and vegetation covered dikes), these small reflectors can also be used for other types of infrastructure, such as large bridges, arid/semi-arid fields, dams, and buildings, whose orientation is sub-optimal for the radar satellites.

7.2. Main contributions

The five main contributions (with sub-contributions) of this research are summarized as follows.

1. A height-based adaptive iterative methodology using hypothesis testing is designed and demonstrated to distinguish ground-level radar scatterers from those associated with elevated structures, see sec. 3.3.
 - The target classification methodology is applied to ERS, ENVISAT, and TerraSAR-X datasets (sec. 3.3.2). Results show successful separation of deformation behavior of the ground from the elevated structure, see sec. 3.3.3.
 - The methodology is introduced to estimate local ground height to create an accurate DEM of the ground using PSI. The generated DEM is found to be ~ 1 m accurate when compared to high quality lidar data, see Fig. 3.13.
2. A methodology is introduced to combine scatterer classification with displacement estimation to distinguish five relative deformation regimes: autonomous structural motion, shallow compaction, local land subsidence, inter-structural deformation, and no relative motion, see sec. 3.4.1.
 - A new parameter called the ‘Relative Deformation Index (RDI)’ to detect and quantify regions subject to differential land subsidence is proposed in order to prioritize asset management, see sec. 3.4.2.
 - The proposed scatterer and deformation classification methods are applied to monitor underground gas and water pipeline networks in the Netherlands. The results validate the use of spaceborne SAR as a tool for underground infrastructure monitoring, see sec. 3.5 and Arsénio et al. (2014). Based on the outcome of this work, industry has picked this up and the methodology is now applied for gas pipe network monitoring in practice (Ianoschi et al., 2013).
3. A mathematical model is introduced for scatterer positioning and the positional uncertainty is propagated from the radar geometry to local terrestrial coordinates, see chapter 4.

- The positioning capability of high-resolution TerraSAR-X stripmap and medium-resolution ENVISAT data is empirically assessed through corner reflector experiments, see chapters 4 and 5 (Dheenathayalan et al., 2016, 2018).
 - New geometric calibration constants are computed for TerraSAR-X stripmap imagery which are comparable to the results for very-high resolution spotlight data by other authors, see sec. 4.5.1.
 - New geometric calibration constants are computed for ENVISAT ASAR imagery to obtain a bias-free scatterer positioning in radar geometry, see sec. 5.3 and Dheenathayalan et al. (2018).
 - In 3D, scatterers are located with an offset in the order of decimeters from the ground truth for both TerraSAR-X stripmap and ENVISAT datasets (Dheenathayalan et al., 2016, 2018).
 - The position covariance matrix in local coordinates is represented by an error ellipsoid and an approach to link radar scatterers to objects/points in the 3D model is introduced, see secs. 5.2.4 and 5.3.4.
4. The linking of persistent radar scatterers in high and medium resolution imagery to parts of infrastructure is demonstrated to achieve very-localized deformation monitoring capability, see Fig. 4.12 and Fig. 5.16.
 5. A new ‘distributed corner reflector’ concept is introduced using small radar reflectors deployed in a pattern, for infrastructure monitoring and natural areas subject to decorrelation, see chapter 6 and Dheenathayalan et al. (2017).
 - A new pdf approximation and a closed-form expression of interferometric phase as a function of SCR is introduced to evaluate the second-order statistics of interferometric phases covering both weak and strong radar scatterers, see Fig. 6.3 and Eq. (6.9).
 - The distributed corner reflector is evaluated over a grassy terrain yielding a millimeter-level precision in ground motion monitoring, see sec. 6.4 and Dheenathayalan et al. (2017).

List of Publications

Journal articles:

- Yang, M., **Dheenathayalan, P.**, López-Dekker, P., van Leijen, F., Liao, M., and Hanssen, R. (2019). On the influence of sub-pixel position correction for PS positioning accuracy and time series quality. *ISPRS Journal of Photogrammetry and Remote Sensing*. (In preparation)
- Yang, M., López-Dekker, P., **Dheenathayalan, P.**, Liao, M., , and Hanssen, R. (2019). On the value of corner reflectors and surface models in precise point positioning of insar point clouds. *ISPRS Journal of Photogrammetry and Remote Sensing*. (Submitted in June 2019)

- Yang, M., López-Dekker, P., **Dheenathayalan, P.**, Biljecki, F., Liao, M., and Hanssen, R. (2019). Linking persistent scatterers to the built environment using ray-tracing on urban models. *IEEE Transactions on Geoscience and Remote Sensing*, 57(8):5764–5776.
- **Dheenathayalan, P.**, Small, D., and Hanssen, R. F. (2018). 3-D positioning and target association for medium-resolution SAR sensors. *IEEE Transactions on Geoscience and Remote Sensing*, 56(11):6841–6853.
- **Dheenathayalan, P.**, Cuenca, M. C., Hoogeboom, P., and Hanssen, R. (2017). Small reflectors for ground motion monitoring with InSAR. *IEEE Transactions on Geoscience and Remote Sensing*, PP(99):1–10.
- **Dheenathayalan, P.**, Small, D., Schubert, A., and Hanssen, R. F. (2016). High-precision positioning of radar scatterers. *Journal of Geodesy*, 90(5):403–422.
- Arsénio, A. M., **Dheenathayalan, P.**, Hanssen, R. F., Vreeburg, J., and Rietveld, L. (2014). Pipe failure predictions in drinking water systems using satellite observations. *Structure and Infrastructure Engineering*, 11(8):1102–1111.

Conference Proceedings:

- Hanssen, R. F., van Natiyne, A., Lindenbergh, R. C., **Dheenathayalan, P.**, Yang, M., Chang, L., and others (2018). Scatterer identification and analysis using combined InSAR and laser data. Abstract from *EGU General Assembly*, Vienna, Austria, April 2018.
- Yang, M., **Dheenathayalan, P.**, Biljecki, F., and Hanssen, R. F. (2017). On the Predictability of PS occurrence and location based on 3D Ray-tracing models. In *the 10th International Workshop on “Advances in the Science and Applications of SAR Interferometry and Sentinel-1 InSAR”, ‘Fringe 2017’, Helsinki, Finland, Jun 2017.*
- Yang, M., **Dheenathayalan, P.**, Chang, L., Wang, J., Lindenbergh, R. C., Liao, M., and Hanssen, R. F. (2016). High-precision 3D geolocation of persistent scatterers with one single-Epoch GCP and LIDAR DSM data. In L. Ouwehand (Ed.), *Proceedings of Living Planet Symposium 2016* (Vol. SP-740, pp. 398–398), Prague, Czech Republic, May 2016.
- **Dheenathayalan, P.**, Small, D., and Hanssen, R. F. (2014). 3D geolocation capability of medium resolution SAR sensors. **Invited session** In *Proceedings of International Geoscience and Remote Sensing Symposium (IGARSS 2014), 35th Canadian Symposium on Remote Sensing (35th CSRS)*, Quebec, Canada, July 2014.
- Cuenca, M. C., **Dheenathayalan, P.**, van Rossum, W., and Hoogeboom, P. (2014). Deployment and design of bi-directional corner reflectors for optimal ground motion monitoring using insar. In *Proceedings of 10th European Conference on Synthetic Aperture Radar (EUSAR 2014)*, pages 1–4, Berlin, Germany, June 2014.

- **Dheenathayalan, P.**, Schubert, A., Small, D., and Hanssen, R. F. (2013). 3D Geolocation Error of Radar Pixels: Modeling, Propagation and Mitigation. In *Proceedings of the 2013 European Space Agency Living Planet Symposium*, Edinburgh, United Kingdom, September 2013.
- Ianoschi, R., Schouten, M., Leezenberg, P. B., **Dheenathayalan, P.**, and Hanssen, R. F. (2013). Satellite Radar Interferometry For Risk Management Of Gas Pipeline Networks. In *Proceedings of the 2013 European Space Agency Living Planet Symposium*, Edinburgh, United Kingdom, September 2013.
- Chang, L., **Dheenathayalan, P.**, and Hanssen, R. F. (2013). Precise geolocation of persistent scatterers aided and validated by a lidar DSM. In *Proceedings of the 2013 European Space Agency Living Planet Symposium*, Edinburgh, United Kingdom, September 2013.
- **Dheenathayalan, P.** and Hanssen, R. F. (2013). Radar target type classification and validation. In *IEEE International Geoscience and Remote Sensing Symposium*, page 4 pp., Melbourne, Australia, July 2013.
- **Dheenathayalan, P.**, Cuenca, M. C., and Hanssen, R. F. (2011). Different approaches for psi target characterization for monitoring urban infrastructure. In *8th International Workshop on "Advances in the Science and Applications of SAR Interferometry", 'FRINGE 2011'*, page 8., Frascati, Italy, September 2011.
- Mahapatra, P.S., Hanssen, R.F., Samiei-Esfahany, S., **Dheenathayalan, P.**, Holley, R., Komac, M., Fromberg, A. (2011). Compact Active Transponders for SAR Interferometry: Experimental Validation. In *proceedings of Advances in Science and Applications of SAR Interferometry, Fringe 2011 workshop*, Frascati, Italy, September 2011.
- **Dheenathayalan, P.** and Hanssen, R. F. (2011). Target characterization and interpretation of deformation using persistent scatterer interferometry and polarimetry. In *5th International Workshop on Science and Applications of SAR Polarimetry and Polarimetric Interferometry, 'POLInSAR 2011'*, page 8., Frascati, Italy, January 2011.

7.3. Recommendations for future work

The work presented towards the exploitation of PSs provides a scope for new improvements and research directions. Eight recommendations for further investigation are presented as follows.

(i) We have demonstrated target classification and interpretation of deformation phenomenon over urban areas. By a full scale application of the developed methods at national level using Sentinel-1 and/or RadarSAT-2 data, one can create a wealth of information, e.g., a database or a map that can be used for wide and local scale infrastructure monitoring. By applying the improved positioning capability, the data processed from different SAR sensors can be integrated to improve the deformation analysis at the infrastructure level.

(ii) Precise 3D positioning is achieved using a systematic procedure involving a tie-point installation to perform geometric calibration for TerraSAR-X and ENVISAT. Geolocation

precision versus cost analysis should be conducted to minimize or even substitute the tie-point installations with a lidar-based open access digital surface model data. Moreover, the positioning performance in 2D and 3D should be analyzed using SAR images from the more recent Sentinel-1 satellites (Yang et al., 2019c).

(iii) Sub-pixel position estimation is conducted per scatterer to improve the azimuth and range pixel positions. Yet, the flat earth phase and topographic phase are computed at pixel level, which might introduce a phase bias in the time-series when the sub-pixel positions are not considered. Hence, a complete study is necessary to analyze the impact of the sub-pixel position in the phase time-series and the parameter estimation (Yang et al., 2019a). In addition, sub-pixel determination requires significant oversampling for each of millions of PSs, which is a computationally expensive operation. Hence, this step needs to be optimized using, *i.e.*, parallel processing and 2D quadratic interpolation (Press et al., 1992; Hanssen and Bamler, 1999) and must be integrated into the Delft PSI software (Kampes and Usai, 1999; Kampes, 2006; van Leijen, 2014).

(iv) Radar scatterers are associated to 3D models in chapters 4 and 5 based on the minimum norm in the metric defined by covariance matrices. However, the 3D model is not entirely visible by the radar during the imaging process. Therefore, a detection (including multi-bounce scenario) and/or removal of non-imaged points and surfaces from 3D models may improve the quality of the target association. In addition, the fusion of laser scanning from terrestrial and mobile systems with airborne lidar data should be carried out to improve the facade and spatial sampling of the 3D model. Doing so the precision of points or voxels in the 3D model should also be updated before the linking step.

(v) At present, we associate PSs to points in a 3D model (serving as an independent reference information) and ignore the bias between the PS position and the reference information. The position offset between the PS and the 3D model can be used as a feedback to correct the interferometric phase and thereby we might improve unwrapping and deformation estimation.

(vi) Alternate methods to find a link between PSs and objects can be explored using ray-tracing like approaches. Using ray-tracing simulation, PSs occurrence and location are predicted and can be compared with real SAR data for validation. For those scatterers identified by ray-tracing and matched with real data, the object type and nature of the reflection exhibited by PSs can be inferred (Yang et al., 2019b). 3D city models with different levels of detail are available in practice. A 3D model with a certain level of detail needs to be selected based on its performance in PS identification.

(vii) In this study, it is assumed that the resolution cells detected with PS contain only one dominant scatterer. This assumption should be tested using tomographic processing techniques. Tomography is expected to improve the positioning of existing PSs and also add a new set of measurement points which would otherwise not be detected as PS. Once tomography is applied and scatterer contributions can be separated, then scatterer positioning, scatterer-to-object linking, and deformation classification can be performed to refine the interpretation.

(viii) Distributed corner reflectors were tested over a vegetation region. A similar experiment is to be deployed and validated when deployed over a large scale infrastructure such as dams, dikes, and large/tall buildings. In our approach, these weak reflectors are distributed in simple pattern and detected visually. Methods need to be developed to optimally distribute reflectors in a pattern such that it provides a better estimation of

deformation signal on the ground. In addition, for a large scale deployment a methodology for automatic detection of reflectors in radar images needs to be developed.

Bibliography

- (2012). De Basisregistratie adressen en gebouwen (BAG). <https://www.amsterdam.nl/stelselpedia/bag-index>. Accessed 18 Apr 2019.
- (2014). Lat/Lon converter: Yellowstone National Park Research.
- Achache, J., Fruneau, B., and Delacourt, C. (1996). Applicability of SAR interferometry for monitoring of landslides. In *Ers Applications*, volume 383, page 165.
- Adam, N., Kampes, B. M., and Eineder, M. (2004). Development of a scientific persistent scatterer system: Modifications for mixed ERS/ENVISAT time series. In *ENVISAT & ERS Symposium, Salzburg, Austria, 6–10 September, 2004*, page 9.
- Adam, N., Zhu, X., and Bamler, R. (2009). Coherent stacking with TerraSAR-X imagery in urban areas. In *2009 Joint Urban Remote Sensing Event*, pages 1–6.
- Aherne, F. J., Thacker, N. A., and Rockett, P. I. (1998). The bhattacharyya metric as an absolute similarity measure for frequency coded data. *Kybernetika*, 34(4):363–368.
- Al-Adeeb, A. and Matti, M. (1984). Leaching corrosion of asbestos cement pipes. *International Journal of Cement Composites and Lightweight Concrete*, 6(4):233–240.
- Alberda, J. E. (1973). Planning and optimisation of networks: Some general considerations. In *Symposium on Computational Methods in Geometric Geodesy*, Oxford. International Association of Geodesy.
- Alberga, V. (2007). A study of land cover classification using polarimetric SAR parameters. *International Journal of Remote Sensing*, 28(17):3851–3870.
- Amelung, F., Galloway, D. L., Bell, J. W., Zebker, H. A., and Lacznik, R. J. (1999). Sensing the ups and downs of Las Vegas: InSAR reveals structural control of land subsidence and aquifer-system deformation. *Geology*, 27(6):483–486.
- Ansari, H. (2019). *Efficient High-Precision Time Series Analysis for Synthetic Aperture Radar Interferometry*. PhD thesis, Technische Universität München, German Aerospace Center (DLR).
- Argenti, F., Lapini, A., Bianchi, T., and Alparone, L. (2013). A tutorial on speckle reduction in synthetic aperture radar images. *Geoscience and Remote Sensing Magazine, IEEE*, 1(3):6–35.
- Arikan, M., van Leijen, F., Guang, L., and Hanssen, R. (2008). Improved image alignment under the influence of elevation. In *Fifth International Workshop on ERS/Envisat SAR Interferometry, 'FRINGE07', Frascati, Italy, 26 Nov-30 Nov 2007*, page 4 pp.

- Arsénio, A. M., Dheenathayalan, P., Hanssen, R. F., Vreeburg, J., and Rietveld, L. (2014). Pipe failure predictions in drinking water systems using satellite observations. *Structure and Infrastructure Engineering*, 11(8):1102–1111.
- Arsénio, A. M., Pieterse, I., Vreeburg, J., de Bont, R., and Rietveld, L. (2013). Failure mechanisms and condition assessment of pvc push-fit joints in drinking water networks. *Journal of Water Supply: Research and Technology-AQUA*, 62(2):78–85.
- Askne, J. and Hagberg, J. O. (1993). Potential of interferometric SAR for classification of land surfaces. In *International Geoscience and Remote Sensing Symposium, Tokyo, Japan, 18–21 August 1993*, pages 985–987.
- Asnaashari, A., McBean, E. A., Gharabaghi, B., and Tutt, D. (2013). Forecasting watermain failure using artificial neural network modelling. *Canadian Water Resources Journal*, 38(1):24–33.
- Auer, S., Gernhardt, S., and Bamler, R. (2011). Ghost persistent scatterers related to multiple signal reflections. *IEEE Geoscience and Remote Sensing Letters*, 8(5):919–923.
- Auer, S., Hinz, S., and Bamler, R. (2010). Ray-tracing simulation techniques for understanding high-resolution SAR images. *IEEE Transactions on Geoscience and Remote Sensing*, 48(3):1445–1456.
- Baarda, W. (1981). *S-Transformations and Criterion Matrices*, volume 5 of *Publications on Geodesy, New Series*. Netherlands Geodetic Commission, Delft, 2 edition.
- Baarda, W., Commission, N. G., et al. (1967). *Statistical concepts in geodesy*, volume 2. Rijkscommissie voor Geodesie.
- Bähr, H. (2013). *Orbital Effects in Spaceborne Synthetic Aperture Radar Interferometry*. KIT Scientific Publishing, Germany.
- Bakker, K. and Bezuijen, A. (2008). Ten years of bored tunnels in the netherlands: Part i, geotechnical issues. In *Proceedings of the 6th Int. Symposium on Geotechnical Aspects of Underground Construction in Soft Ground*, page 243.
- Balss, U., Cong, X. Y., Brcic, R., Rexer, M., Minet, C., Breit, H., Eineder, M., and Fritz, T. (2012). High precision measurement on the absolute localization accuracy of TerraSAR-X. In *Geoscience and Remote Sensing Symposium (IGARSS), 2012 IEEE International*, pages 1625–1628. IEEE.
- Balss, U., Gisinger, C., Cong, X. Y., Brcic, R., Steigenberger, P., Eineder, M., Pail, R., and Hugentobler, U. (2013). High resolution geodetic earth observation with TerraSAR-X: Correction schemes and validation. In *IEEE International Geoscience and Remote Sensing Symposium, Melbourne, Australia, 21–26 July 2013*.
- Baltink, H., Marel, H. V. D., and van der Hoeven, A. (2002). Integrated atmospheric water vapor estimates from a regional gps network. *Journal of Geophysical Research: Atmospheres (1984–2012)*, 107(D3):ACL–3.

- Bamler, R., Adam, N., Davidson, G. W., and Just, D. (1998). Noise-induced slope distortion in 2-d phase unwrapping by linear estimators with application to SAR interferometry. *IEEE Transactions on Geoscience and Remote Sensing*, 36(3):913–921.
- Bamler, R. and Eineder, M. (2005). Accuracy of differential shift estimation by correlation and split-bandwidth interferometry for wideband and delta-k SAR systems. *Geoscience and Remote Sensing Letters, IEEE*, 2(2):151–155.
- Bamler, R. and Hartl, P. (1998). Synthetic aperture radar interferometry. *Inverse Problems*, 14:R1–R54.
- Bamler, R. and Schättler, B. (1993). SAR data acquisition and image formation. In Schreier (1993b), pages 53–102.
- Barzaghi, R., Cazzaniga, N. E., De Gaetani, C. I., Pinto, L., and Tornatore, V. (2018). Estimating and comparing dam deformation using classical and GNSS techniques. *Sensors*, 18(3).
- Bean, B. R. and Dutton, E. J. (1968). *Radio Meteorology*. Dover, New York.
- Bender, M., Dick, G., Wickert, J., Schmidt, T., Song, S., Gendt, G., Ge, M., and Rothacher, M. (2008). Validation of GPS slant delays using water vapour radiometers and weather models. *Meteorologische Zeitschrift*, 17(6):807–812.
- Bennett, W. (1948). Spectra of quantized signals. *Bell System Technical Journal*, 27(3):446–472.
- Berardino, P., Casu, F., Fornaro, G., Lanari, R., Manunta, M., Manzo, M., and Sansosti, E. (2004). A quantitative analysis of the SBAS algorithm performance. *International Geoscience and Remote Sensing Symposium, Anchorage, Alaska, 20–24 September 2004*, pages 3321–3324.
- Berardino, P., Fornaro, G., Lanari, R., and Sansosti, E. (2002). A new algorithm for surface deformation monitoring based on small baseline differential SAR interferograms. *IEEE Transactions on Geoscience and Remote Sensing*, 40(11):2375–2383.
- Bhattacharyya, A. (1946). On a measure of divergence between two multinomial populations. *Sankhyā: The Indian Journal of Statistics (1933-1960)*, 7(4):401–406.
- Bolter, R. (2000). Reconstruction of man-made objects from high resolution sar images. In *Aerospace Conference Proceedings, 2000 IEEE*, volume 3, pages 287–292. IEEE.
- BORN, G. H., DUNNE, J. A., and LAME, D. B. (1979). Seasat mission overview. *Science*, 204(4400):1405–1406.
- Born, M., Wolf, E., and Bhatia, A. B. (1959). *Principle of optics; electromagnetic theory of propagation, interference and diffraction of light*. Pergamon Press, New York.
- Breen, J. (2006). Expected lifetime of existing pvc water systems: Summary. *Eindhoven: TNO*.

- Brus, D. J. and Van Den Akker, J. J. (2018). How serious a problem is subsoil compaction in the netherlands? a survey based on probability sampling. *Soil*, 4(1):37.
- Bruyninx, C. (2004). The EUREF Permanent Network: a multi-disciplinary network serving surveyors as well as scientists. *GeoInformatics*, 7(5):32–35.
- Bruyninx, C., Altamimi, Z., Boucher, C., Brockmann, E., Caporali, A., Gurtner, W., Habrich, H., Hornik, H., Ihde, J., Kenyeres, A., Mäkinen, J., Stangl, G., van der Marel, H., Simek, J., Söhne, W., Torres, J., and Weber, G. (2009). The European Reference Frame: Maintenance and Products. In Drewes, H., editor, *Geodetic Reference Frames*, volume 134 of *International Association of Geodesy Symposia*, pages 131–136. Springer Berlin Heidelberg.
- Budhu, M. (2008). *SOIL MECHANICS AND FOUNDATIONS, (With CD)*. John Wiley & Sons.
- Burgherr, P., Eckle, P., and Hirschberg, S. (2012). Comparative assessment of severe accident risks in the coal, oil and natural gas chains. *Reliability Engineering & System Safety*, 105:97–103. ESREL 2010.
- Burgherr, P. and Hirschberg, S. (2014). Comparative risk assessment of severe accidents in the energy sector. *Energy Policy*, 74:45–56. Nuclear Energy and Sustainable Development: Selected Topics.
- Carver, K. R., Elachi, C., and Ulaby, F. T. (1985). Microwave remote sensing from space. *Proceedings of the IEEE*, 73(6):970–996.
- Cascini, L., Ferlisi, S., Peduto, D., Fornaro, G., and Manunta, M. (2007). Analysis of a subsidence phenomenon via dinstar data and geotechnical criteria. *Italian Geotechnical Journal*, 41(4):50–67.
- Chang, L. (2015). *Monitoring civil infrastructure using satellite radar interferometry*. PhD thesis, Delft University of Technology, Delft, the Netherlands.
- Chen, C. W. (2001). *Statistical-cost network-flow approaches to two-dimensional phase unwrapping for radar interferometry*. PhD thesis, Stanford University.
- Cloude, S. and Pottier, E. (1996). A review of target decomposition theorems in radar polarimetry. *Geoscience and Remote Sensing, IEEE Transactions on*, 34(2):498–518.
- Colesanti, C., Ferretti, A., Novali, F., Prati, C., and Rocca, F. (2003). SAR monitoring of progressive and seasonal ground deformation using the permanent scatterers technique. *IEEE Transactions on Geoscience and Remote Sensing*, 41(7):1685–1701.
- Colesanti, C. and Wasowski, J. (2006). Investigating landslides with space-borne synthetic aperture radar (SAR) interferometry. *Engineering geology*, 88(3-4):173–199.
- Colwell, R. N., Simonett, D. S., and Ulaby, F. T., editors (1983). *Manual of Remote Sensing*, volume 1, Theory, Instruments and Techniques. American Society of Photogrammetry, Falls Church, Virginia, 2 edition.

- Crosetto, M., Monserrat, O., Cuevas-González, M., Devanthéry, N., and Crippa, B. (2016). Persistent scatterer interferometry: A review. *{ISPRS} Journal of Photogrammetry and Remote Sensing*, 115:78 – 89. Theme issue 'State-of-the-art in photogrammetry, remote sensing and spatial information science'.
- Cuenca, M. C., Dheenathayalan, P., van Rossum, W., and Hoogeboom, P. (2014). Deployment and design of bi-directional corner reflectors for optimal ground motion monitoring using insar. In *EUSAR 2014; 10th European Conference on Synthetic Aperture Radar; Proceedings of*, pages 1–4. VDE.
- Cuenca, M. C., Hooper, A. J., and Hanssen, R. F. (2011). A new method for temporal phase unwrapping of persistent scatterers insar time series. *IEEE Transactions on Geoscience and Remote Sensing*, 49(11):4606–4615.
- Cumming, I. and Wong, F. (2005). *Digital Processing Of Synthetic Aperture Radar Data: Algorithms And Implementation*. Artech House Publishers, New York. ISBN 1580530583.
- Curlander, J. C. and McDonough, R. N. (1991). *Synthetic aperture radar: systems and signal processing*. John Wiley & Sons, Inc, New York.
- Dainty, J., editor (1975). *Laser Speckle and Related Phenomena*, volume 9 of *Topics in Applied Physics*. Springer-Verlag, Heidelberg.
- Davenport, W. and Root, W. (1987). *An Introduction to the Theory of Random Signals and Noise*. IEEE Press, New York.
- Davis, J. L., Herring, T. A., Shapiro, I. I., Rogers, A. E. E., and Elgered, G. (1985). Geodesy by radio interferometry: Effects of atmospheric modelling errors on estimates of baseline length. *Radio Science*, 20(6):1593–1607.
- de Bruijne, A., van Buren, J., Kösters, A., and van der Marel, H. (2005). *Geodetic reference frames in the Netherlands. Definition and specification of ETRS89, RD and NAP, and their mutual relationships*. Netherlands Geodetic Commission, Delft.
- De Lange, G., Bakr, M., Gunnink, J., and Huisman, D. (2012). A predictive map of compression-sensitivity of the dutch archaeological soil archive. *Conservation and Management of Archaeological Sites*, 14(1-4):284–293.
- de Loor, G. P., Hoogeboom, P., and Attema, E. P. W. (1982). The dutch rove program. *IEEE transactions on Geoscience and Remote Sensing*, (1):3–11.
- De Silva, D., Burn, L., and Eiswirth, M. (2001). Joints in water supply and sewer pipelines: an australian perspective.
- Dell'Acqua, F. and Gamba, P. (2001). Detection of urban structures in sar images by robust fuzzy clustering algorithms: the example of street tracking. *Geoscience and Remote Sensing, IEEE Transactions on*, 39(10):2287–2297.
- Dell'Acqua, F. and Gamba, P. (2003). Texture-based characterization of urban environments on satellite sar images. *Geoscience and Remote Sensing, IEEE Transactions on*, 41(1):153–159.

- Dell'Acqua, F., Gamba, P., and Lisini, G. (2003). Improvements to urban area characterization using multitemporal and multiangle sar images. *Geoscience and Remote Sensing, IEEE Transactions on*, 41(9):1996–2004.
- der Zon, N. V. (2011). Kwaliteitsdocument AHN-2. *Rijkswaterstaat & Waterschappen, Technical Report (in Dutch)*, 1:1.
- Dheenathayalan, P., Cuenca, M. C., and Hanssen, R. F. (2011). Different approaches for psi target characterization for monitoring urban infrastructure. In *In 8th International Workshop on "Advances in the Science and Applications of SAR Interferometry"*, 'FRINGE 2011', Frascati, Italy, 19-23 Sep 2011, page 8. ESA.
- Dheenathayalan, P., Cuenca, M. C., Hoogeboom, P., and Hanssen, R. (2017). Small reflectors for ground motion monitoring with InSAR. *IEEE Transactions on Geoscience and Remote Sensing*, PP(99):1–10.
- Dheenathayalan, P. and Hanssen, R. F. (2011). Target characterization and interpretation of deformation using persistent scatterer interferometry and polarimetry. In *5th International Workshop on Science and Applications of SAR Polarimetry and Polarimetric Interferometry*, 'POLInSAR 2011', Frascati, Italy, 24–28 Jan 2011, page 8. ESA.
- Dheenathayalan, P. and Hanssen, R. F. (2013). Radar target type classification and validation. In *IEEE International Geoscience and Remote Sensing Symposium, Melbourne, Australia, 21–26 July 2013*, page 4 pp.
- Dheenathayalan, P., Schubert, A., Small, D., and Hanssen, R. F. (2013). 3D Geo-location Error of Radar Pixels: Modeling, Propagation and Mitigation. In *Proceedings of the 2013 European Space Agency Living Planet Symposium, 9-13 September 2013, Edinburgh, United Kingdom*.
- Dheenathayalan, P., Small, D., and Hanssen, R. F. (2014). 3D geolocation capability of medium resolution SAR sensors. In *Proceedings of International Geoscience and Remote Sensing Symposium (IGARSS 2014), 35th Canadian Symposium on Remote Sensing (35th CSRS), 13-18 July 2014, Quebec, Canada*. IEEE.
- Dheenathayalan, P., Small, D., and Hanssen, R. F. (2018). 3-D positioning and target association for medium-resolution SAR sensors. *IEEE Transactions on Geoscience and Remote Sensing*, 56(11):6841–6853.
- Dheenathayalan, P., Small, D., Schubert, A., and Hanssen, R. F. (2016). High-precision positioning of radar scatterers. *Journal of Geodesy*, 90(5):403–422.
- Dingus, M., Haven, J., and Austin, R. (2002). *Nondestructive, noninvasive assessment of underground pipelines*. American Water Works Association.
- Dobson, M. C., Ulaby, F. T., and Pierce, L. E. (1995). Land-cover classification and estimation of terrain attributes using synthetic aperture radar. *Remote Sensing of Environment*, 51(1):199 – 214. Remote Sensing of Land Surface for Studies of Global Change.
- Dong, Y. and Ticehurst, B. F. C. (1997). Radar backscatter analysis for urban environments. *International journal of remote sensing*, 18(6):1351–1364.

- Duda, R., Hart, P., and Stork, D. (2012). *Pattern Classification*. John Wiley & Sons.
- Eineder, M. and Holzner, J. (1999). Phase unwrapping of low coherence differential interferograms. In *International Geoscience and Remote Sensing Symposium, Hamburg, Germany, 28 June–2 July 1999*, pages cdrom, 4 pages.
- Eineder, M., Minet, C., Steigenberger, P., Cong, X., and Fritz, T. (2011). Imaging geodesy – toward centimeter-level ranging accuracy with TerraSAR-X. *Geoscience and Remote Sensing, IEEE Transactions on*, 49(2):661–671.
- Elachi, C. (1988). *Spaceborne radar remote sensing: applications and techniques*. Institute of Electrical and Electronics Engineers, New York.
- Evans, D., Farr, T., van Zyl, J., and Zebker, H. (1988). Radar polarimetry: analysis tools and applications. *Geoscience and Remote Sensing, IEEE Transactions on*, 26(6):774–789.
- Even, M. and Schulz, K. (2018). InSAR deformation analysis with distributed scatterers: A review complemented by new advances. *Remote Sensing*, 10(5).
- Farr, T. G., Rosen, P. A., Caro, E., Crippen, R., Duren, R., Hensley, S., Kobrick, M., Paller, M., Rodriguez, E., Roth, L., Seal, D., Shaffer, S., Shimada, J., Umland, J., Werner, M., Oskin, M., Burbank, D., and Alsdorf, D. (2007). The shuttle radar topography mission. *Rev. Geophys.*, 45:33.
- Feinberg, E. (1944). On the propagation of radio waves along an imperfect surface. *J. Phys. (Moscow)*, 8:317–330.
- Ferretti, A., Fumagalli, A., Novali, F., Prati, C., Rocca, F., and Rucci, A. (2011). A new algorithm for processing interferometric data-stacks: SqueeSAR. *IEEE Transactions on Geoscience and Remote Sensing*, 49(9):3460–3470.
- Ferretti, A., Prati, C., and Rocca, F. (1999). Permanent scatterers in SAR interferometry. In *International Geoscience and Remote Sensing Symposium, Hamburg, Germany, 28 June–2 July 1999*, pages 1–3.
- Ferretti, A., Prati, C., and Rocca, F. (2001). Permanent scatterers in SAR interferometry. *IEEE Transactions on Geoscience and Remote Sensing*, 39(1):8–20.
- Ferretti, A., Savio, G., Barzaghi, R., Borghi, A., Musazzi, S., Novali, F., Prati, C., and Rocca, F. (2007). Submillimeter accuracy of InSAR time series: Experimental validation. *IEEE Transactions on Geoscience and Remote Sensing*, 45(5):1142–1153.
- Fisher, R. A. et al. (1925). Applications of “student’s” distribution. *Metron*, 5(3):90–104.
- Folkman, S. (2012). Water main break rates in the USA and Canada: A comprehensive study, April 2012.
- Fornaro, G. and Serafino, F. (2006). Imaging of single and double scatterers in urban areas via SAR tomography. *IEEE Transactions on Geoscience and Remote Sensing*, 44(12):3497–3505.

- Foster, M. R. and Guinzy, N. J. (1967). The coefficient of coherence: its estimation and use in geophysical data processing. *Geophysics*, 32(4):602–616.
- Franceschetti, G., Iodice, A., and Riccio, D. (2002). A canonical problem in electromagnetic backscattering from buildings. *Geoscience and Remote Sensing, IEEE Transactions on*, 40(8):1787–1801.
- Freeman, A. (1992). Polarization effects and multipolarization SAR. In *Fundamental and Special Problems of Synthetic Aperture Radar (SAR)*, number 182 in AGARD Lecture Series, pages 5/1–5/13. Agard, Neuilly-sur-Seine.
- Frery, A. C., Muller, H. J., Yanasse, C. C. F., and Sant’Anna, S. J. S. (1997). A model for extremely heterogeneous clutter. *IEEE Transactions on Geoscience and Remote Sensing*, 35(3):648–659.
- Fritz, T. (2007). TerraSAR-X ground segment level 1b product format specification. *TerraSAR-X ground segment level 1b product format specification*, (TX-GS- DD-3307). Issue 1.3.
- Fruneau, B., Achache, J., and Delacourt, C. (1996). Observation and modelling of the saint-etienne-de-tinée landslide using SAR interferometry. *Tectonophysics*, 265(3-4):181–190.
- Fukushima, Y., Cayol, V., and Durand, P. (2005). Finding realistic dike models from interferometric synthetic aperture radar data: The february 2000 eruption at piton de la fournaise. *Journal of Geophysical Research: Solid Earth*, 110(B3).
- Fung, A. (1994). *Microwave Scattering and Emission Models and Their Applications*. Artech House remote sensing library. Artech House.
- Gabriel, A. K., Goldstein, R. M., and Zebker, H. A. (1989). Mapping small elevation changes over large areas: differential radar interferometry. *Journal of Geophysical Research*, 94(B7):9183–9191.
- Gamba, P., Houshmand, B., and Sacconi, M. (2000). Detection and extraction of buildings from interferometric sar data. *Geoscience and Remote Sensing, IEEE Transactions on*, 38(1):611–617.
- Gatelli, E., Monti Guarnieri, A., Parizzi, F., Pasquali, P., Prati, C., and Rocca, F. (1994). The wavenumber shift in SAR interferometry. *IEEE Transactions on Geoscience and Remote Sensing*, 32(4):855–865.
- Gernhardt, S. (2010). Potential of very high resolution sar for persistent scatterer interferometry in urban areas. *Annals of GIS*, 16(2):103–111.
- Geudens, P. (2012). Dutch drinking water statistics 2012. *Rijswijk: Fivewin*.
- Geudtner, D., Winter, R., and Vachon, P. W. (1996). Flood monitoring using ERS-1 SAR interferometry coherence maps. Presented at IGARSS’96.
- Ghiglia, D. C. and Pritt, M. D. (1998). *Two-dimensional phase unwrapping: theory, algorithms, and software*. John Wiley & Sons, Inc, New York.

- Gisinger, C., Balss, U., Pail, R., Zhu, X. X., Montazeri, S., Gernhardt, S., and Eineder, M. (2015). Precise three-dimensional stereo localization of corner reflectors and persistent scatterers with TerraSAR-X. *IEEE Transactions on Geoscience and Remote Sensing*, 53(4):1782–1802.
- Goel, K. and Adam, N. (2014). A distributed scatterer interferometry approach for precision monitoring of known surface deformation phenomena. *IEEE Transactions on Geoscience and Remote Sensing*, 52(9):5454–5468.
- Goldstein, R. (1995). Atmospheric limitations to repeat-track radar interferometry. *Geophysical Research Letters*, 22(18):2517–2520.
- Goldstein, R. M., Engelhardt, H., Kamp, B., and Frolich, R. M. (1993). Satellite radar interferometry for monitoring ice sheet motion: Application to an antarctic ice stream. *Science*, 262:1525–1530.
- Goldstein, R. M., Zebker, H. A., and Werner, C. L. (1988). Satellite radar interferometry: Two-dimensional phase unwrapping. *Radio Science*, 23(4):713–720.
- Goodman, J. (1976). Some fundamental properties of speckle. *JOSA*, 66(11):1145–1150.
- Goodman, J. (2007). *Speckle Phenomena in Optics: Theory and Applications*. Roberts & Company.
- Goodman, J. W. (1975). Statistical properties of laser speckle patterns. In Dainty (1975), chapter 2, pages 9–75.
- GoogleInc. (2015). Google earth (version 6.0.3.2197). Website: <http://www.earth.google.com>.
- GoogleInc. (2017). Google earth (version 7.1.5.1557). Website: <http://www.earth.google.com>.
- Grafarend, E. W. and Sansò, F. (2012). *Optimization and design of geodetic networks*. Springer Science & Business Media.
- Guarnieri, A. M. and Tebaldini, S. (2008). On the exploitation of target statistics for SAR interferometry applications. *IEEE Transactions on Geoscience and Remote Sensing*, 46(11):3436–3443.
- Guillaso, S., Ferro-Famil, L., Reigber, A., and Pottier, E. (2005). Building characterization using L-band polarimetric interferometric SAR data. *Geoscience and Remote Sensing Letters, IEEE*, 2(3):347–351.
- Hajduch, G., Bourbigot, M., Johnsen, H., Piantanida, R., Poullaouec, J., et al. (2018). Sentinel-1 product specification. Technical Report S1-RS-MDA-52-7441, ESA.
- Hanssen, R. and Bamler, R. (1999). Evaluation of interpolation kernels for SAR interferometry. *IEEE Transactions on Geoscience and Remote Sensing*, 37(1):318–321.
- Hanssen, R. F. (2001a). *Radar Interferometry: Data Interpretation and Error Analysis*. Kluwer Academic Publishers, Dordrecht.

- Hanssen, R. F. (2001b). *Radar Interferometry: Data Interpretation and Error Analysis*. PhD thesis, Delft University of Technology.
- Hanssen, R. F., Weckwerth, T., Zebker, H., and Klees, R. (1999a). High-resolution water vapor mapping from interferometric radar measurements. *Science*, 283(5406):1297–1299.
- Hanssen, R. F., Weckwerth, T. M., Zebker, H. A., and Klees, R. (1999b). High-resolution water vapor mapping from interferometric radar measurements. *Science*, 283:1295–1297.
- Hartl, P., Thiel, K. H., Wu, X., Doake, C., and Sievers, J. (1994). Application of SAR interferometry with ERS-1 in the Antarctic. *Earth Observation Quarterly*, 43:1–4.
- Haynes, M., Smart, S., and Smith, A. (2004). Compact active transponders for operational sar interferometry applications. In *Proc. ENVISAT Symp*, pages 6–10.
- Helmert, F. R. (1880). *Die mathematischen und physikalischen theorieen der höheren geodäsie*, volume 1. BG Teubner.
- Helmert, F. R. (1884). *Die mathematischen und physikalischen theorieen der höheren geodäsie*, volume 2. BG Teubner.
- Hoekman, D. H. and Quiñones, M. J. (1998). Forest type classification by airborne SAR in the Columbian Amazon. In *Second Int. Workshop on "Retrieval of Bio- and Geophysical Parameters from SAR Data for Land Applications" 21-23 Oct, Noordwijk, The Netherlands*. ESTEC.
- Hooper, A., Zebker, H., Segall, P., and Kampes, B. (2004). A new method for measuring deformation on volcanoes and other non-urban areas using InSAR persistent scatterers. *Geophysical Research Letters*, 31:L23611, doi:10.1029/2004GL021737.
- Hooper, A. and Zebker, H. A. (2007). Phase unwrapping in three dimensions with application to insar time series. *JOSA A*, 24(9):2737–2747.
- Hu, Y., Vu, H. Q., and Lotfian, K. (2008). *Instrumentation of a Section of AC Pipe in Expansive Soil*, pages 1–10.
- Huynen, J. (1970). *Phenomenological theory of radar targets*. PhD thesis, TU Delft, Delft University of Technology.
- Ianoschi, R., Schouten, M., Bas Leezenberg, P., Dheenathayalan, P., and Hanssen, R. (2013). Satellite radar interferometry for risk management of gas pipeline networks. In *ESA Living Planet Symposium*, volume 722, page 60.
- Inglada, J., Henry, C., and Souyris, J. (2004). Assessment of ASAR/IMS multipolarization images phase difference in the framework of persistent scatterers interferometry. In *ENVISAT & ERS Symposium, Salzburg, Austria, 6–10 September, 2004*, page 4 pp.
- Jensen, J. R. and Cowen, D. C. (1999). Remote sensing of urban/suburban infrastructure and socio-economic attributes. *Photogrammetric engineering and remote sensing*, 65:611–622.

- Jiang, M., Ding, X., Hanssen, R. F., Malhotra, R., and Chang, L. (2015). Fast statistically homogeneous pixel selection for covariance matrix estimation for multitemporal InSAR. *IEEE transactions on geoscience and remote sensing*, 53(3):1213–1224.
- Just, D. and Bamler, R. (1994). Phase statistics of interferograms with applications to synthetic aperture radar. *Applied Optics*, 33(20):4361–4368.
- Kailath, T. (1967). The divergence and bhattacharyya distance measures in signal selection. *IEEE Transactions on Communication Technology*, 15(1):52–60.
- Kampes, B. (1999a). Delft object-oriented radar interferometric software. VMSG Symposium, Utrecht, the Netherlands.
- Kampes, B. (1999b). *Delft Object-Oriented Radar Interferometric Software: Users manual and Technical Documentation*. Delft University of Technology, Delft, 1.2 edition.
- Kampes, B. (2005). *Displacement Parameter Estimation using Permanent Scatterer Interferometry*. PhD thesis, Delft University of Technology, Delft, the Netherlands.
- Kampes, B. and Hanssen, R. F. (2004a). Ambiguity resolution for permanent scatterer interferometry. *Geoscience and Remote Sensing, IEEE Transactions on*, 42(11):2446–2453.
- Kampes, B. and Usai, S. (1999). Doris: the Delft Object-oriented Radar Interferometric Software. In *2nd International Symposium on Operationalization of Remote Sensing, Enschede, The Netherlands, 16–20 August, 1999*.
- Kampes, B. M. (2006). *Radar interferometry: Persistent scatterer technique*. Springer.
- Kampes, B. M. and Hanssen, R. F. (2004b). Ambiguity resolution for permanent scatterer interferometry. *IEEE Transactions on Geoscience and Remote Sensing*, 42(11):2446–2453.
- Kampes, B. M., Hanssen, R. F., and Perski, Z. (2003). Radar interferometry with public domain tools. In *Third International Workshop on ERS SAR Interferometry, 'FRINGE03', Frascati, Italy, 1-5 Dec 2003*, page 6 pp.
- Karila, K., Karjalainen, M., Hyypä, J., Koskinen, J., Saarinen, V., and Rouhiainen, P. (2013). A comparison of precise leveling and persistent scatterer sar interferometry for building subsidence rate measurement. *ISPRS International Journal of Geo-Information*, 2(3):797–816.
- Ketelaar, G. and Hanssen, R. (2006). Monitoring subsidence due to gas extraction in Groningen using satellite radar interferometry. 8ste Nederlands Aardwetenschappelijk Congres 24-25 April, 2006, Veldhoven.
- Ketelaar, G., Zeijlmaker, L., and Hanssen, R. (2006). Monitoring subsidence due to gas extraction using satellite radar interferometry in Groningen, the Netherlands. *Shell EP Journal of Technology*, 7004:35–38.
- Ketelaar, V. B. H. (2008). *Monitoring surface deformation induced by hydrocarbon production using satellite radar interferometry*. PhD thesis, Delft University of Technology, Delft, the Netherlands.

- Knott, E. F., Shaeffer, J. F., and Tuley, M. T. (1985). Radar cross section, norwood, ma: Artech house.
- Kozma, A. and Christensen, C. (1976). Effects of speckle on resolution*. *J. Opt. Soc. Am.*, 66(11):1257–1260.
- Kult, A., Barstow, R., Ramsbottom, D., and Peake, G. (2007). ENVISAT-1 Products Specifications. Volume 8: ASAR Products Specifications. Technical Report PO-RS-MDA-GS-2009, ESA. Issue 4. Revision B dated 05.08.2007.
- Laakso, T. I., Välimäki, V., Karjalainen, M., and Laine, U. K. (1996). Splitting the unit delay. *IEEE Signal processing magazine*, pages 30–60.
- Lan, H., Li, L., Liu, H., and Yang, Z. (2012). Complex urban infrastructure deformation monitoring using high resolution PSI. *IEEE Journal of Selected Topics in Applied Earth Observations and Remote Sensing*, 5(2):643–651.
- Lanari, R., Mora, O., Manunta, M., Mallorquí, J. J., Berardino, P., and Sansosti, U. (2004). A small-baseline approach for investigating deformations on full-resolution differential SAR interferograms. *IEEE Transactions on Geoscience and Remote Sensing*, 42(7):1377–1386.
- Lee, J., Hoppel, K., Mango, S., and Miller, A. (1994). Intensity and phase statistics of multilook polarimetric and interferometric sar imagery. *IEEE Transactions on Geoscience and Remote Sensing*, 32(5):1017–1028.
- Lee, J.-S. (1983). Digital image smoothing and the sigma filter. *Computer vision, graphics, and image processing*, 24(2):255–269.
- Lesparre, J. and Gorte, B. (2012). Simplified 3d City Models from LiDAR. *ISPRS-International Archives of the Photogrammetry, Remote Sensing and Spatial Information Sciences*, 1:1–4.
- Lillesand, T., Kiefer, R. W., and Chipman, J. (2014). *Remote sensing and image interpretation*. John Wiley & Sons.
- Liu, S. (2012). *Satellite radar interferometry: estimation of atmospheric delay*. PhD thesis, Delft University of Technology, Delft, the Netherlands.
- Liu, Z., Kleiner, Y., Rajani, B., Wang, L., and Condit, W. (2012). Condition assessment technologies for water transmission and distribution systems. *United States Environmental Protection Agency (EPA)*, 108.
- Lombardini, F. (2005). Differential tomography: A new framework for SAR interferometry. *IEEE Transactions on Geoscience and Remote Sensing*, 43(1):37–44.
- Madsen, S. (1986). *Speckle Theory: Modelling, analysis, and applications related to Synthetic Aperture Radar Data*. PhD thesis, Technical University of Denmark.
- Madsen, S. N., Zebker, H. A., and Martin, J. (1993). Topographic mapping using radar interferometry: Processing techniques. *IEEE Transactions on Geoscience and Remote Sensing* 31(1):246–255.

- Maffett, J. C. J. A. (1965). Radar cross-section estimation for simple shapes. *Proceedings of the IEEE*, 53(8):833–848.
- Mahalanobis, P. (1936). On the generalized distance in statistics. *Proceedings of the National Institute of Sciences (Calcutta)*, 2:49–55.
- Mahapatra, P. S., Samiei-Esfahany, S., van der Marel, H., and Hanssen, R. F. (2014). On the use of transponders as coherent radar targets for sar interferometry. *IEEE Transactions on Geoscience and Remote Sensing*, 52(3):1869–1878.
- Marinkovic, P. and Larsen, Y. (2013). On the long term stability of ASAR LO frequency - empirical study of 10 years of data. *IEEE Transactions on Geoscience and Remote Sensing*. Submitted.
- Marinkovic, P. and Larsen, Y. (2015). Consequences of the Local Oscillator Drift model for ENVISAT ASAR - significant improvement of the localization accuracy. In *CEOS Calibration and Validation Workshop, 27-29 October 2015, Noordwijk, the Netherlands*.
- Marinkovic, P. S., van Leijen, F., Ketelaar, G., and Hanssen, R. F. (2005). Recursive data processing and data volume minimization for PS-InSAR. In *International Geoscience and Remote Sensing Symposium, Seoul, Korea, 25–29 July 2005*, pages 2697–2700.
- Massonnet, D. (1997). Satellite radar interferometry. *Scientific American*, pages 32–39.
- Massonnet, D. and Feigl, K. L. (1998). Radar interferometry and its application to changes in the earth's surface. *Reviews of Geophysics*, 36(4):441–500.
- Massonnet, D., Rogron, B., and Rossi, M. (1995). SAR image quality and interferometric potential for digital terrain model derivation. In *Final Report of JERS-1/ERS-1 System Verification Program, Volume II*, pages 627–638. National Space Development Agency of Japan.
- Massonnet, D., Rossi, M., Carmona, C., Adagna, F., Peltzer, G., Feigl, K., and Rabaute, T. (1993). The displacement field of the Landers earthquake mapped by radar interferometry. *Nature*, 364(8):138–142.
- Massonnet, D. and Vadon, H. (1995). ERS-1 internal clock drift measured by interferometry. *IEEE Transactions on Geoscience and Remote Sensing*, 33(2):401–408.
- Matsuoka, M. and Yamazaki, F. (2004). Use of satellite sar intensity imagery for detecting building areas damaged due to earthquakes. *Earthquake Spectra*, 20(3):975–994.
- Matusita, K. (1955). Decision rules, based on the distance, for problems of fit, two samples, and estimation. *The Annals of Mathematical Statistics*, 26(4):631–640.
- Meier, E., Frei, U., and Nüesch, D. (1993). *Precise terrain corrected geocoded images*, chapter 7, pages 173–185. ed. G. Schreier, Herbert Wichmann, Verlag GmbH, Karlsruhe, Germany.
- Melchior, P. (1974). Earth tides. *Geophysical surveys*, 1(3):275–303.

- Mendes, V. B. (1999). *Modeling the neutral-atmosphere propagation delay in radio-metric space techniques*. PhD thesis, University of New Brunswick.
- Meyer, F., Bamler, R., Jakowski, N., and Fritz, T. (2006). The potential of low-frequency sar systems for mapping ionospheric TEC distributions. *IEEE Geoscience and Remote Sensing Letters*, 3(4):560–564.
- Middleton, D. (1960). *An introduction to statistical communication theory*, volume 960 of *International series in pure and applied physics*. McGraw-Hill New York.
- Milbert, D. (2011). Solid earth tide, fortran computer program. <http://home.comcast.net/~dmilbert/softs/solid.htm>. Accessed 1 Apr 2014.
- Miranda, N., Rosich, B., Meadows, P. J., Haria, K., Small, D., Schubert, A., Lavalle, M., Collard, F., Johnsen, H., Guarneri, A. M., et al. (2013). The ENVISAT ASAR mission: A look back at 10 years of operation. In *ESA Special Publication*, volume 722, page 41.
- Molesini, G., de Souza, M. P., Quercioli, F., and Trivi, M. (1990). Experimental statistics of fully developed speckle fields by phase-shifting interferometry. *Optics Communications*, 77(2):129–134.
- Mora, O., Mallorqui, J. J., and Broquetas, A. (2003). Linear and nonlinear terrain deformation maps from a reduced set of interferometric SAR images. *IEEE Transactions on Geoscience and Remote Sensing*, 41(10):2243–2253.
- Moser, A. P. and Folkman, S. L. (2008). *Buried pipe design (3rd ed.)*. McGraw-Hill New York.
- Nasr, J. and Vidal-Madjar, D. (1991). Image simulation of geometric targets for spaceborne synthetic aperture radar. *Geoscience and Remote Sensing, IEEE Transactions on*, 29(6):986–996.
- NETPOS (2015). Netherlands Positioning Service (NETPOS). <https://zakelijk.kadaster.nl/netpos>. Accessed 1 Jul 2019.
- Nitti, D. O., Hanssen, R. F., Refice, A., Bovenga, F., and Nutricato, R. (2011). Impact of DEM-assisted coregistration on high-resolution SAR interferometry. *IEEE Transactions on Geoscience and Remote Sensing*, 49(3):1127–1143.
- NSSDCA (1978). NASA Space Science Data Coordinated Archive. <https://nssdc.gsfc.nasa.gov/nmc/spacecraft/display.action?id=1978-020A>. Accessed 4 Jun 2019.
- Ohtsubo, J. and Asakura, T. (1977). Statistical properties of the sum of partially developed speckle patterns. *Optics letters*, 1(3):98–100.
- Olliff, J., Rolfe, S., Wijeyesekera, D., and Reginold, J. (2001). Soil-structure-pipe interaction with particular reference to ground movement induced failures. *BOOK-INSTITUTE OF MATERIALS*, 759:941–950.
- O'Rourke, T. (2010). Geohazards and large, geographically distributed systems. *Géotechnique*, 60(7):505.

- O'rourke, T., Jezerski, J., Olson, N., Bonneau, A., Palmer, M., Stewart, H., O'rourke, M., and Abdoun, T. (2008). Geotechnics of pipeline system response to earthquakes. In *Geotechnical Earthquake Engineering and Soil Dynamics IV Congress 2008-Geotechnical Earthquake Engineering and Soil Dynamics*.
- Papoulis, A. (1991). *Probability, Random variables, and stochastic processes*. McGraw-Hill series in Electrical Engineering. McGraw-Hill, New York.
- Parizzi, A. and Brcic, R. (2011). Adaptive insar stack multilooking exploiting amplitude statistics: A comparison between different techniques and practical results. *IEEE Geoscience and Remote Sensing Letters*, 8(3):441–445.
- Pepe, A., Yang, Y., Manzo, M., and Lanari, R. (2015). Improved EMCF-SBAS processing chain based on advanced techniques for the noise-filtering and selection of small baseline multi-look DInSAR interferograms. *IEEE Transactions on Geoscience and Remote Sensing*, 53(8):4394–4417.
- Perissin, D. (2006). *SAR super-resolution and characterization of urban targets*. PhD thesis, Politecnico di Milano, Italy.
- Perissin, D. (2008). Validation of the sub-metric accuracy of vertical positioning of PS's in C band. *Geoscience and Remote Sensing Letters*, 5(3):502–506.
- Perissin, D. and Ferretti, A. (2007). Urban-target recognition by means of repeated spaceborne sar images. *Geoscience and Remote Sensing, IEEE Transactions on*, 45(12):4043–4058.
- Prati, C., Ferretti, A., and Perissin, D. (2010). Recent advances on surface ground deformation measurement by means of repeated space-borne SAR observations. *Journal of Geodynamics*, 49(3-4):161–170.
- Press, W., Flannery, B., Teukolsky, S., and Vetterling, W. (1992). *Numerical Recipes in C: The Art of Scientific Computing*. Cambridge University Press, Cambridge, 2 edition.
- Pritchard, M. E. and Simons, M. (2002). A satellite geodetic survey of large-scale deformation of volcanic centres in the central andes. *Nature*, 418(6894):167.
- Qin, Y., Perissin, D., and Lei, L. (2013). The design and experiments on corner reflectors for urban ground deformation monitoring in hong kong. *International Journal of Antennas and Propagation*, 2013.
- Rajani, B. and Kleiner, Y. (2001). Comprehensive review of structural deterioration of water mains: physically based models. *Urban water*, 3(3):151–164.
- Rajani, B., Zhan, C., and Kuraoka, S. (1996). Pipe soil interaction analysis of jointed water mains. *Canadian Geotechnical Journal*, 33(3):393–404.
- Raney, R. (1998). Radar fundamentals: Technical perspective. In Henderson, F. M. and Lewis, A. J., editors, *Principles and applications of Imaging Radar*, volume 2 of *Manual of Remote Sensing*, chapter 2, pages 9–130. John Wiley & Sons, Inc., New York, 3 edition.

- Reigber, A. and Moreira, A. (2000). First demonstration of airborne SAR tomography using multibaseline L-band data. *IEEE Transactions on Geoscience and Remote Sensing*, 38(5):2142–2152.
- Rice, S. (1951). Reflection of electromagnetic waves from slightly rough surfaces. *Communications on Pure and Applied Mathematics*, 4(2-3):351–378.
- Rietveld, H. (1984). Land subsidence in the netherlands. In *Proceedings of the Third International Symposium on Land Subsidence*, pages 455–464.
- Rijkswaterstaat-AGI (1996). AHN: Actueel Hoogtebestand Nederland. Meetkundige Dienst, Rijkswaterstaat.
- Rocca, F. (2007). Modeling interferogram stacks. *IEEE Transactions on Geoscience and Remote Sensing*, 45(10):3289–3299.
- Rodriguez, E. and Martin, J. M. (1992). Theory and design of interferometric synthetic aperture radars. *IEE Proceedings-F*, 139(2):147–159.
- Rosen, P. A., Hensley, S., Zebker, H. A., Webb, F. H., and Fielding, E. J. (1996). Surface deformation and coherence measurements of Kilauea volcano, Hawaii, from SIR-C radar interferometry. *Journal of Geophysical Research*, 101(E10):23109–23125.
- Rott, H., Stuefer, M., Siegel, A., Skvarca, P., and Eckstaller, A. (1998). Mass fluxes and dynamics of Moreno Glacier, Southern Patagonia Icefield. *Geophysical Research Letters*, 25(9):1407–1410.
- Ruck, G. (1970). *Radar cross section handbook*. Number v. 1 in Radar Cross Section Handbook. Plenum Press.
- Russo, P., Rosa, A., and D’ippolito, A. (2005). Transponder having high phase stability, particularly for synthetic aperture radar, or sar, systems. US Patent 6,861,971.
- Salman, B. (2010). *Infrastructure management and deterioration risk assessment of wastewater collection systems*. PhD thesis, University of Cincinnati.
- Samiei Esfahany, S. (2017). *Exploitation of distributed scatterers in synthetic aperture radar interferometry*. PhD thesis, Delft University of Technology, Delft, the Netherlands.
- Sarabandi, K. and Chiu, T. C. (1996). Optimum corner reflectors for calibration of imaging radars. *IEEE Transactions on Antennas and Propagation*, 44(10):1348–1361.
- Schmidt, D. A. and Bürgmann, R. (2003). Time-dependent land uplift and subsidence in the Santa Clara valley, California, from a large interferometric synthetic aperture radar data set. *Journal of Geophysical Research*, 108(B9):doi:10.1029/2002JB002267.
- Schmitt, G. (1982). Optimization of geodetic networks. *Reviews of Geophysics*, 20(4):877–884.
- Schreier, G. (1993a). Geometrical properties of SAR images. *SAR geocoding: Data and Systems*, pages 103–134.

- Schreier, G. (1993b). *SAR Geocoding: data and systems*. Wichmann Verlag, Karlsruhe.
- Schubert, A., Jehle, M., Small, D., and Meier, E. (2010). Influence of atmospheric path delay on the absolute geolocation accuracy of TerraSAR-X high-resolution products. *Geoscience and Remote Sensing, IEEE Transactions on*, 48(2):751–758.
- Schubert, A., Jehle, M., Small, D., and Meier, E. (2012a). Mitigation of atmospheric perturbations and solid earth movements in a TerraSAR-X time-series. *Journal of Geodesy*, 86(4):257–270.
- Schubert, A., Miranda, N., Geudtner, D., and Small, D. (2017). Sentinel-1A/B combined product geolocation accuracy. *Remote Sensing*, 9(6).
- Schubert, A., Small, D., Jehle, M., and Meier, E. (2012b). COSMO-SkyMed, TerraSAR-X, and RADARSAT-2 geolocation accuracy after compensation for earth-system effects. In *2012 IEEE International Geoscience and Remote Sensing Symposium*, pages 3301–3304.
- Schubert, A., Small, D., Meier, E., Miranda, N., and Geudtner, D. (2014). Spaceborne SAR product geolocation accuracy: a Sentinel-1 update. In *Proceedings of International Geoscience and Remote Sensing Symposium (IGARSS 2014), 35th Canadian Symposium on Remote Sensing (35th CSRS), 13-18 July 2014, Quebec, Canada*, pages 2675–2678. IEEE.
- Schunert, A. and Soergel, U. (2016). Assignment of persistent scatterers to buildings. *IEEE Transactions on Geoscience and Remote Sensing*, 54(6):3116–3127.
- Schwäbisch, M. (1995a). Die SAR-Interferometrie zur Erzeugung digitaler Geländemodelle. Forschungsbericht 95-25, Deutsche Forschungsanstalt für Luft- und Raumfahrt, Oberpfaffenhofen.
- Schwäbisch, M. (1995b). *Die SAR-Interferometrie zur Erzeugung digitaler Geländemodelle*. PhD thesis, Stuttgart University.
- Seymour, M. S. and Cumming, I. G. (1994). Maximum likelihood estimation for SAR interferometry. In *International Geoscience and Remote Sensing Symposium, Pasadena, CA, USA, 8–12 August 1994*, pages 2272–2275.
- Shinozuka, M., Ghanem, R., Houshmand, B., and Mansouri, B. (2000). Damage detection in urban areas by sar imagery. *Journal of Engineering Mechanics*, 126(7):769–777.
- Sigmundsson, F., Vadon, H., and Massonnet, D. (1997). Readjustment of the Krafla spreading segment to crustal rifting measured by satellite radar interferometry. *Geophysical Research Letters*, 24(15):1843–1846.
- Skolnik, M. (2002). Role of radar in microwaves. *IEEE Transactions on microwave theory and techniques*, 50(3):625–632.
- Skolnik, M. I. (1962). *Introduction to Radar Systems*. McGraw-Hill Kogakusha, Ltd., Tokyo.
- Skolnik, M. I. (1980). *Introduction to radar systems*. McGraw Hill Book Co., New York.

- Small, D., Pasquali, P., and Fuglistaler, S. (1996). A comparison of phase to height conversion methods for SAR interferometry. In *International Geoscience and Remote Sensing Symposium, Lincoln, Nebraska, USA, 27–31 May 1996*, volume 1, pages 342–344 vol.1.
- Small, D., Rosich-Tell, B., Meier, E., and Nüesch, D. (2004a). Geometric calibration and validation of ASAR imagery. In *CEOS WGCV SAR Calibration & Validation Workshop, Ulm Germany, 27–28 May 2004*, page 8.
- Small, D., Rosich-Tell, B., Schubert, A., Meier, E., and Nüesch, D. (2004b). Geometric validation of low and high-resolution ASAR imagery. In *ENVISAT & ERS Symposium, Salzburg, Austria, 6–10 September, 2004*, page 9.
- Small, D., Schubert, A., Rosich-Tell, B., and Meier, E. (2007). Geometric and radiometric correction of ESA SAR products. In *ESA ENVISAT Symposium, Montreux, Switzerland, 23–27 April 2007*, page 6.
- Soergel, U., Thoennessen, U., and Stilla, U. (2003). Reconstruction of buildings from interferometric sar data of built-up areas. *INTERNATIONAL ARCHIVES OF PHOTOGRAMMETRY REMOTE SENSING AND SPATIAL INFORMATION SCIENCES*, 34(3/W8):59–64.
- Soergel, U., Thoennessen, U., Stilla, U., and Brenner, A. (2004). New opportunities for analysis of urban areas in high resolution SAR data. In *European Conference on Synthetic Aperture Radar, Ulm, Germany, 25–27 May 2004*, pages 415–418.
- Stein, S. (1981). Algorithms for ambiguity function processing. *Acoustics, Speech and Signal Processing, IEEE Transactions on*, 29(3):588–599.
- Stilla, U., Michaelsen, E., Soergel, U., and Schulz, K. (2003a). Perceptual grouping of regular structures for automatic detection of man-made objects. In *Geoscience and Remote Sensing Symposium, 2003. IGARSS'03. Proceedings. 2003 IEEE International*, volume 6, pages 3525–3527. IEEE.
- Stilla, U., Soergel, U., and Thoennessen, U. (2003b). Potential and limits of insar data for building reconstruction in built-up areas. *{ISPRS} Journal of Photogrammetry and Remote Sensing*, 58(1–2):113 – 123. Algorithms and Techniques for Multi-Source Data Fusion in Urban Areas.
- Stramondo, S., Bozzano, F., Marra, F., Wegmuller, U., Cinti, F., Moro, M., and Saroli, M. (2008). Subsidence induced by urbanisation in the city of Rome detected by advanced InSAR technique and geotechnical investigations. *Remote Sensing of Environment*, 112(6):3160–3172.
- Strozzi, T., Farina, P., Corsini, A., Ambrosi, C., Thüring, M., Zilger, J., Wiesmann, A., Wegmüller, U., and Werner, C. (2005). Survey and monitoring of landslide displacements by means of l-band satellite SAR interferometry. *Landslides*, 2(3):193–201.
- Strozzi, T., Teatini, P., and Tosi, L. (2009). Terrasar-x reveals the impact of the mobile barrier works on venice coastland stability. *Remote Sensing of Environment*, 113(12):2682–2688.

- Strozzi, T., Wegmuller, U., Tosi, L., Bitelli, G., and Spreckels, V. (2001). Land subsidence monitoring with differential sar interferometry. *Photogrammetric engineering and remote sensing*, 67(11):1261–1270.
- Taket, N., Howarth, S., and Burge, R. (1991). A model for the imaging of urban areas by synthetic aperture radar. *Geoscience and Remote Sensing, IEEE Transactions on*, 29(3):432–443.
- Tebaldini, S. (2010). Single and multipolarimetric SAR tomography of forested areas: A parametric approach. *IEEE Transactions on Geoscience and Remote Sensing*, 48(5):2375–2387.
- Teunissen, P., Simons, D., and Tiberius, C. (2005). *Probability and observation theory*. Delft Institute of Earth Observation and Space Systems (DEOS), Delft University of Technology, The Netherlands.
- Teunissen, P. J. G. (2000). *Testing theory; an introduction*. Delft University Press, Delft, 1 edition.
- Tur, M., Chin, K., and Goodman, J. (1982). When is speckle noise multiplicative? *Applied optics*, 21(7):1157–1159.
- Tuthill, T., Sperry, R., and Parker, K. (1988). Deviations from rayleigh statistics in ultrasonic speckle. *Ultrasonic imaging*, 10(2):81–89.
- Ulaby, F. and Elachi, C. (1990). *Radar Polarimetry for Geoscience Applications*. Artech House remote sensing library. Artech House.
- Ulaby, F. T. and Dobson, M. C. (1989). Handbook of radar scattering statistics for terrain. ARTECH HOUSE, 685 CANTON STREET, NORWOOD, MA 02062(USA), 1989, 500.
- Ulaby, F. T., Moore, R. K., and Fung, A. K. (1982). *Microwave remote sensing: active and passive. Vol. 2. Radar remote sensing and surface scattering and emission theory*. Addison-Wesley, Reading.
- United Nations, Department of Economic and Social Affairs, Population Division (2015). *World Urbanization Prospects: The 2014 Revision, (ST/ESA/SER.A/366)*. UN.
- Usai, S. and Hanssen, R. F. (1997). Long time scale INSAR by means of high coherence features. In *Third ERS Symposium—Space at the Service of our Environment, Florence, Italy, 17–21 March 1997*, pages 225–228.
- Usai, S. and Klees, R. (1999). SAR interferometry on very long time scale: A study of the interferometric characteristics of man-made features. *IEEE Transactions on Geoscience and Remote Sensing*, 37(4):2118–2123.
- Van-Camp, L., Bujarrabal, B., Gentile, A. R., Jones, R. J. A., Montanarella, L., and Olazabal (2004). *Reports of the technical working groups established under the Thematic Strategy for Soil Protection*, volume 21319. Office for Official Publications of the European Communities, Luxembourg.

- Van den Born, G., Kragt, F., Henkens, D., Rijken, B., Bommel, B. v., van der Sluis, S., Polman, N., Bos, E., Kuhlman, T., Kwakernaat, C., et al. (2016). Dalende bodems, stijgende kosten: mogelijke maatregelen tegen veenbodemdaling in het landelijk en stedelijk gebied: beleidsstudie.
- van der Sande, C., Soudarissanane, S., and Khoshelham, K. (2010). Assessment of relative accuracy of ahn-2 laser scanning data using planar features. *Sensors*, 10(9):8198–8214.
- van Leijen, F. and Hanssen, R. F. (2008). Ground water management and its consequences in Delft, the Netherlands as observed by persistent scatterer interferometry. In *Fifth International Workshop on ERS/Envisat SAR Interferometry, 'FRINGE07', Frascati, Italy, 26 Nov-30 Nov 2007*, pages 1–6.
- van Leijen, F. J. (2014). *Persistent scatterer interferometry based on geodetic estimation theory*. PhD thesis, Delft University of Technology, Delft, the Netherlands.
- van Leijen, F. J., Hanssen, R. F., Marinkovic, P. S., and Kampes, B. M. (2006). Spatio-temporal phase unwrapping using integer least-squares. In *Fourth International Workshop on ERS/Envisat SAR Interferometry, 'FRINGE05', Frascati, Italy, 28 Nov-2 Dec 2005*, page 6 pp.
- van Outeren, E. (2009). Subway headaches: Amsterdam metro line sinks deeper into trouble. <http://www.spiegel.de/international/europe/subway-headaches-amsterdam-metro-line-sinks-deeper-into-trouble-a-617894.html>. Accessed 18 Apr 2019.
- van Vollenhoven, P., Hulsenbek, J. A., Brouwer-Korf, A., Mertens, F., and Visser, J. (2009). Grijs gietijzeren gasleidingen - Een onderzoek naar aanleiding van de gasexplosie Haarlemmer Houttuinen Amsterdam, 9 maart 2008. Technical report, De Onderzoeksraad voor Veiligheid, The Hague, The Netherlands. Project number M2008BL0309-01.
- van Vollenhoven et. al., P. (2002). Gasexplosie na breuk van gasdistributieleiding - Brosse breuk grijs gietijzeren gasdistributieleiding veroorzaakt gasexplosie op 15 augustus 2001 in Amsterdam. Technical report, De Onderzoeksraad voor Veiligheid, The Hague, The Netherlands. Reference CB-4-02.060.
- Van Zyl, J. J. (1986). *On the importance of polarization in radar scattering problems*. PhD thesis, California Institute of Technology.
- Van Zyl, P. (1989). Unsupervised classification of scattering behavior using radar polarimetry data. *IEEE Transactions on GRS*, -(-):-.
- Vaniček, P. and Krakiwsky, E. (1982). *Geodesy, the concepts*. North-Holland Pub. Co.
- Vloerbergh, I., Thienen, P. v., Schipdam, R., et al. (2012). Pipe fitters assist to predict investment needs for water main rehabilitation. *Water Asset Management International*, 8(3):12–18.
- Wang, Y. and Moore, I. D. (2014). Simplified design equations for joints in buried flexible pipes based on hetényi solutions. *Journal of Geotechnical and Geoenvironmental Engineering*, 140(3):04013020.

- Wertheimer, M. (1938). Laws of organization in perceptual forms. first published as *untersuchungen zur lehre von der gestalt ii. psychologische forschung*, 4, 301–350. translation published in ellis, w.(1938).
- Wiley, C. A. (1954). Pulsed Doppler radar methods and apparatus. *United States Patent, No. 3196436*.
- Yang, M., Dheenathayalan, P., López-Dekker, P., van Leijen, F., Liao, M., and Hanssen, R. (2019a). On the influence of sub-pixel position correction for ps positioning accuracy and time series quality. *ISPRS Journal of Photogrammetry and Remote Sensing*.
- Yang, M., López-Dekker, P., Dheenathayalan, P., Biljecki, F., Liao, M., and Hanssen, R. (2019b). Linking persistent scatterers to the built environment using ray-tracing on urban models. *Geoscience and Remote Sensing, IEEE Transactions on*, pages 1–13.
- Yang, M., López-Dekker, P., Dheenathayalan, P., Liao, M., , and Hanssen, R. (2019c). On the value of corner reflectors and surface models in precise point positioning of insar point clouds. *ISPRS Journal of Photogrammetry and Remote Sensing*.
- Zebker, H. and Goldstein, R. (1986). Topographic mapping from Interferometric Synthetic Aperture Radar observations. *Journal of Geophysical Research*, 91(B5):4993–4999.
- Zebker, H., van Zyl, J., and Held, D. (1987). Imaging radar polarimetry from wave synthesis. *Journal of Geophysical Research: Solid Earth*, 92(B1):683–701.
- Zebker, H. A., Rosen, P. A., Goldstein, R. M., Gabriel, A., and Werner, C. L. (1994a). On the derivation of coseismic displacement fields using differential radar interferometry: The Landers earthquake. *Journal of Geophysical Research*, 99(B10):19617–19634.
- Zebker, H. A. and Villasenor, J. (1992). Decorrelation in interferometric radar echoes. *IEEE Transactions on Geoscience and Remote Sensing*, 30(5):950–959.
- Zebker, H. A., Werner, C. L., Rosen, P. A., and Hensley, S. (1994b). Accuracy of topographic maps derived from ERS-1 interferometric data. *IEEE Transactions on Geoscience and Remote Sensing*, 32(4):823–836.
- Zhu, X. X. and Bamler, R. (2010). Very high resolution spaceborne SAR tomography in urban environment. *IEEE Transactions on Geoscience and Remote Sensing*, 48(12):4296–4308.
- Zhu, X. X., Montazeri, S., Gisinger, C., Hanssen, R. F., and Bamler, R. (2016). Geodetic sar tomography. *IEEE Transactions on Geoscience and Remote Sensing*, 54(1):18–35.

A

Higher-order positioning terms

The higher-order positioning terms are the secondary components measured by the radar and considered as noise (with $E\{\text{noise}\} \neq 0$) in the position estimation process. They are broadly divided into 4 groups: i) Radar satellite instrument effects, ii) Signal propagation effects, iii) Geodynamic effects, and iv) Coordinate conversion effects. In the following, we will discuss the parameterization of each of these correction factors, followed by a quality description.

A.0.1. Radar satellite instrument effects

During the in-orbit geometric calibration phase, the radar system is corrected for the pixel positions in the SAR image for the internal delays in the satellite, particularly, cable lengths, and frequency offsets. This results in an azimuth time shift, denoted as $\underline{t}_{\text{sys}}$ expressed in meters as:

$$\underline{a}_{\text{shift}} = \underline{v}_{s/c} \cdot \underline{t}_{\text{sys}}, \quad (\text{A.1})$$

For satellite missions such as TSX and TDX, an external azimuth timing offset is provided per image. This offset accounts for the range and frequency dependent azimuth shifts which result from the relativistic Doppler effect and instrument timing errors, see Fritz (2007).

Quality description

The quality of the azimuth shift depends on the precision of the time shift ($\sigma_{\underline{t}_{\text{sys}}}^2$) and velocity of spacecraft ($\sigma_{\underline{v}_{s/c}}^2$). For TSX *science orbit products*, state vector velocities are given with 5 mm/s 3D RMS (root mean square) value (Fritz, 2007). Linearising Eq. (A.1) with initial values ($\underline{t}_{\text{sys}}^o, \underline{v}_{s/c}^o$), the precision is given by

$$\sigma_{\underline{a}_{\text{shift}}}^2 = \begin{bmatrix} \underline{t}_{\text{sys}}^o & \underline{v}_{s/c}^o \end{bmatrix} \begin{bmatrix} \sigma_{\underline{v}_{s/c}}^2 & \\ & \sigma_{\underline{t}_{\text{sys}}}^2 \end{bmatrix} \begin{bmatrix} \underline{t}_{\text{sys}}^o & \underline{v}_{s/c}^o \end{bmatrix}^T. \quad (\text{A.2})$$

This appendix has been published in the Journal of Geodesy, 2016 (Dheenathayalan et al., 2016).

A.0.2. Signal propagation effects: Atmospheric path time delay

The total path length (or time delay) of radio signal propagation increases due to the refractivity of the atmosphere, mainly from ionosphere and troposphere (Hanssen, 2001a). In addition, due to the side looking SAR imaging geometry, this time delay scales with the looking angle of the radar satellite.

The ionosphere component of path delay is approximated via the vertical Total Electron Content (νTEC) from Global Ionosphere Maps. According to the ionospheric refraction equation, the one way zenithal ionospheric delay in seconds is given by

$$\tau_{\text{iono}} = \frac{K \cdot H}{f^2} \cdot \nu TEC, \quad (\text{A.3})$$

where $K = 40.28 \text{ m}^3 / \text{s}^2$ is a refractive constant, νTEC is the Total Electron Content in zenith direction expressed in $10^{16} \frac{\text{electrons}}{\text{m}^2}$, H is a factor due to flying height of satellite with respect to the total extend of ionosphere, and f is the radar signal center frequency. For TSX, $H \approx 0.75$ is reported (Balss et al., 2012).

The troposphere component (τ_{tropo}) of the path delay is very difficult to estimate due to the strong spatio-temporal variability of refractivity, but a first-order estimate can be obtained from collocated GNSS (Global Navigation Satellite System) delays or even from numerical weather models. In this study, the tropospheric component is obtained from the permanent GNSS station (within the scene). The total path delay in the radar line of sight direction expressed in meters is then obtained as:

$$r_{\text{pd}} = v_0 \cdot \frac{(\tau_{\text{iono}} + \tau_{\text{tropo}})}{\cos(\theta_{\text{inc}})}, \quad (\text{A.4})$$

where v_0 is speed of light in vacuum, θ_{inc} is the incidence angle, and $\frac{1}{\cos(\theta_{\text{inc}})}$ is the mapping function.

Quality description

The quality of the path delay

$$\sigma_{r_{\text{pd}}}^2 = \left(\frac{v_0}{\cos(\theta_{\text{inc}})} \right)^2 \cdot (\sigma_{\tau_{\text{iono}}}^2 + \sigma_{\tau_{\text{tropo}}}^2) \quad (\text{A.5})$$

depends on the precision of ionospheric ($\sigma_{\tau_{\text{iono}}}^2$) and tropospheric ($\sigma_{\tau_{\text{tropo}}}^2$) delays.

A.0.3. Geodynamic effects

The Earth as a whole reacts to external forces as an elastic body due to several geodynamic phenomena resulting in surface displacements. These phenomena vary from solid earth tides, ocean pole tides, pole loading, ocean tidal loading, atmospheric pressure loading to ocean pole loading. All these factors yield an integrated surface displacement at the time of satellite data acquisition. Here, only the major contributor, namely ‘‘Solid Earth Tide’’ is computed and mitigated.

When the Earth rotates within the gravitational fields of the Sun and Moon, due to the Earth’s elasticity the Earth’s surface experiences displacements of up to 40 cm in vertical direction and a few tens of cm in horizontal direction. This response to lunisolar gravitational attraction is called as Solid Earth tide or body tide (Melchior, 1974). SET for

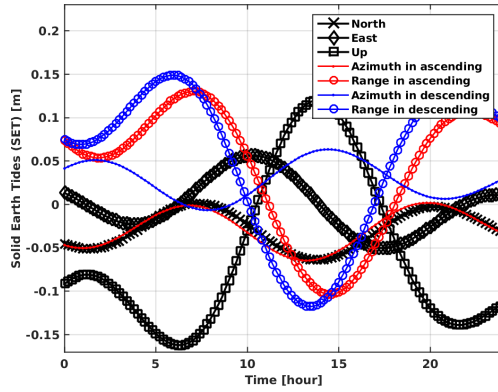


Figure A.1: SET displacements for one full day (30-Mar-2013) at Delft, and their impact in azimuth and range directions for a ascending and descending satellite pass.

one full day (30-Mar-2013) is shown in Fig. A.1. For the Delft test site, the SET shows a displacement of ± 15 cm in radial (\underline{d}_h) and ± 5 cm in horizontal (\underline{d}_n and \underline{d}_e) directions. Using Eq. A.6, the radial and horizontal displacements are projected into azimuth (\underline{a}_{set}) and line of sight (\underline{r}_{set}) range directions for ascending and descending orbits as shown in Fig. A.1.

$$\begin{aligned} \underline{r}_{set} &= -\underline{d}_h \cdot \cos(\theta_{inc}) + \sin(\theta_{inc}) \cdot (-\underline{d}_n \cdot \sin(\alpha_h) + \underline{d}_e \cdot \cos(\alpha_h)) \\ \underline{a}_{set} &= \underline{d}_n \cdot \cos(\alpha_h) + \underline{d}_e \cdot \sin(\alpha_h), \end{aligned} \quad (\text{A.6})$$

where α_h is the azimuth heading angle. The displacement and hence the corrections will be significant in range when compared to azimuth direction in Sec. 4.2.3.

Quality description

Given the precision of SET in North ($\sigma_{d_n}^2$), East ($\sigma_{d_e}^2$) and Up ($\sigma_{d_h}^2$) components, the quality of the SET in radar coordinates ($\sigma_{r_{set}}^2$ and $\sigma_{a_{set}}^2$) can be given by

$$\begin{aligned} \sigma_{r_{set}}^2 &= \sigma_{d_h}^2 \cdot \cos(\theta_{inc})^2 + \sin(\theta_{inc})^2 \cdot (\sigma_{d_n}^2 \cdot \sin(\alpha_h)^2 + \sigma_{d_e}^2 \cdot \cos(\alpha_h)^2) \\ \sigma_{a_{set}}^2 &= \sigma_{d_n}^2 \cdot \cos(\alpha_h)^2 + \sigma_{d_e}^2 \cdot \sin(\alpha_h)^2. \end{aligned} \quad (\text{A.7})$$

A.0.4. Coordinate conversion effects: Tectonic plate motion

When a measurement in one coordinate reference system is to be compared with an another measurement in second reference system, the changes in reference systems have to be taken into account.

In the end, we want scatterer position in a local map geometry defined by a TRF, e.g., in ETRF89 (European Terrestrial Reference Frame 1989) reference. But, the satellite orbit state vectors are given in the ITRF (International Terrestrial Reference Frame). The ITRF and ETRF are linked relative to epoch 1989.0, since then ETRF89 has been drifting north-east at a rate of ~ 2.44 cm/year as shown in Fig. A.2A. This drift in reference frames, when neglected leads to a palpable position error of approximately 60 cm (for a period of 25 years from 1989.0 to 2014.0) along north-east direction as depicted in Fig. A.2B.

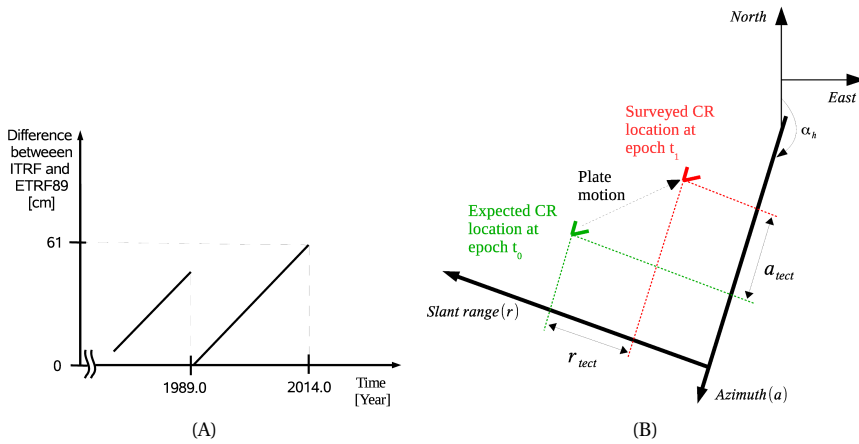


Figure A.2: Impact of mismatch between ETRF89 and ITRF reference frames. (A) Connection between a scatterer in ETRF89 and satellite state vector in ITRF reference frames. (B) The effect of tectonic plate motion in azimuth (a_{tect}) and range (r_{tect}) for a descending right-looking satellite pass.

Quality description

The quality of plate motion corrections in range ($\sigma_{r_{tect}}^2$) and azimuth ($\sigma_{a_{tect}}^2$) are obtained by substituting the precision of plate motion corrections in North, East and Up components in Eq. (A.7) instead of respective SET components.

B

Pipe failure predictions in drinking water systems using satellite radar interferometry

Soil deformation is believed to play a crucial role in the onset of failures in the underground infrastructure. This article describes a method to generate a replacement-prioritization map for underground drinking water pipe networks using ground movement data. A segment of the distribution network of a Dutch drinking water company was selected as the study area. Failure registration data comprising 868 failures registered over 40 months and geographical network data were obtained from the water utility. Ground movement was estimated using radar satellite data. Two types of analyses were performed: cell- and pixel-based. For the cell-based analysis, asbestos cement (AC) pipes exhibited the highest failure rates. Older AC pipes were also shown to fail more often. Conversely, failure rates for PVC were the lowest. For the pixel-based analysis, ground movement was demonstrated to play a role in the failure of all materials combined. Therefore, a replacement-prioritization map for AC was generated which combined ground movement data and pipe-age data. This method can be a beneficial resource for network managers for maintenance and continuous monitoring.

B.1. Introduction

Drinking water supply networks are part of a myriad of underground infrastructures that underpin modern civilization. Because much of this infrastructure is located underground, its fate is intimately related to that of the surrounding soil (O'Rourke, 2010). A factor expected to play a role in the failure of drinking water pipes is non-uniform ground movement, also referred to as differential ground movement (Budhu, 2008). In this process, ground movement creates stress on the pipe and may lead to its failure. Damage to one

This appendix has been published in the Structure and Infrastructure Engineering, 2014 (Arsénio et al., 2014).

facility (e.g., water main) can culminate in damage to surrounding facilities (e.g., gas or telecommunications) with system-wide consequences (O'Rourke, 2010).

Ground movement can be especially damaging to older pipelines (Olliff et al., 2001) and older, rigid joints (De Silva et al., 2001). Hu et al. (2008) argued that changes in soil volume can induce differential ground movement that could subsequently cause the development of stresses in asbestos cement (AC) pipes. The effect of ground movement can also impact pipes whose integrity may have already been compromised by other factors, for example, a chemical attack from water inside the pipe and/or from soil outside the pipe (Hu et al., 2008). According to Breen (2006), provided that PVC pipes are properly manufactured, installed, and free of scratches of more than 1 mm depth, they can endure for more than 100 years in operation. However, the same authors argued that non-uniform soil settling can cause enormous local stresses in a PVC pipe and lead to preliminary failure, and such conditions can decrease the lifetime of a PVC pipe to just 10 years.

Dingus et al. (2002) surveyed 46 of the largest AwwaRF member utilities. For their distribution systems, according to 25% of the survey respondents, frost heave/ground motion was the number one problem. Folkman (2012) surveyed 188 North American utilities. According to the author, 55.3% of respondents identified cast iron (CI) as the most common failing pipe material, followed by asbestos cement (AC) at 17.0%.

Furthermore, the utilities were asked to choose the most common type of failure in their networks; 50% answered that circumferential cracks were the primary failure mode for CI, concrete and AC. Corrosion was the primary failure mode for ductile iron and steel pipes. A longitudinal crack was the primary failure mode for PVC. One of the causes for circumferential breaks is longitudinal loading (Rajani and Kleiner, 2001) that can originate from ground movement (Moser and Folkman, 2008). According to O'Rourke (2010), geohazards (e.g., soil subsidence, earthquakes, hurricanes) have generated substantial interest in lifeline systems (e.g., water, gas and telecommunications). Keeping this in mind, O'Rourke et al. (2008) examined the response of the Los Angeles water supply network during the 1994 Northridge earthquake, which was the beginning point for developing a decision support model for the city's distribution network. More recently, O'Rourke (2010) expanded the previous work, analyzed and modeled the response of three North American networks to earthquakes (San Francisco and Los Angeles), the effect of Katrina in New Orleans, and in the Mississippi River and the Gulf of Mexico.

In centuries past, the Netherlands has not been affected by earthquakes or hurricanes. However, according to Rietveld (1984), "There is no stable rock on the surface of the country and approximately half of its surface is covered by Holocene sediments of clay, sand, and peat which attain thicknesses up to 20 m. In these areas, soil compaction can be relatively significant in relation to tectonic movements". Thus, in the country, the role of ground movement in water pipe failures is expected to be noticeable.

Therefore, the objective of this article is twofold. The first is to study the influence of ground movement on failures occurring in a Dutch drinking water network. While failure-related data was provided by a water utility, the ground movement data was obtained from satellite-borne radar surveys. The second objective is to create a replacement-prioritization map for network management from these conclusions. This map will assist the utility in addressing potential problems created by soil movement-related failures and in pinpointing pipes installed in high priority replacement areas. Finally, the pipes installed in these areas can be inspected using non-destructive evaluation tools as discussed in

Arsénio et al. (2013). It should be mentioned that ground movement can have several origins, for example, soil compaction, ground water level changes, and/or anthropogenic activities. Nevertheless, in this work, quantitatively quantifying ground movement is the main goal, not defining its origin.

B.2. Materials and methods

B.2.1. Soil deformation data

Persistent scatterer points

Interferometric Synthetic Aperture Radar (InSAR) measures the changes in distance between a satellite and the Earth's surface over a given time frame. Given the satellite's position, changes in the surface (ground movement) are measured along the line of sight (viewing direction) of the satellite (Hanssen, 2001a). When compared to other measuring techniques (e.g., leveling or GPS), InSAR possesses a relatively high temporal and spatial sampling, which is a significant advantage of this technology. InSAR is also shown beneficial in modeling the signal source at a few kilometers beneath the surface (Fukushima et al., 2005; Pritchard and Simons, 2002). In our study, we used movement of the soil surface, measured from a satellite, to study the impact on underground water pipes installed at depths of around 1 m, which is typical in the Netherlands.

In the late 1990s, the Persistent Scatterer Interferometry (PSI) technique was introduced to process stacks of images and extract ground movement by exploiting coherent pixels known as Persistent Scatterer (PS) points (Ferretti et al., 2001). These PS points are usually manmade objects (e.g., buildings, bridges, lamp posts). In this work, PS points are also referred to as pixels. PSI is an opportunity-based technique, therefore, the settling estimation at any desired, specific location or object cannot be guaranteed. However, this technique provides relatively high density of such coherent pixels in urban regions and millimeter precision in surface movement estimation. In fact, the number of PS points per square kilometer (PS density) varies from area to area and depends on the satellite used. In general, a density from 100-1000 PS points km^{-2} in urban environments can be expected.

The PSI technique requires a reference in time and space to estimate ground movement. The reference in time is solved by selecting a reference image, referred to as the master image, and comparing other images to the master to estimate changes in the surface. The reference in space is obtained by taking a point in the master image as a reference point. All of the estimations are then provided with a reference to this reference point, and the most stable point in the image is normally chosen as the reference point.

For this analysis, 99 TerraSAR-X strip-map ascending mode images of the study area were processed employing PSI techniques to estimate the ground movement rate (expressed in mm year^{-1}) per pixel. For this satellite, a pixel, or PS point, indicates an area of 3×3 m (approximately). The satellite data used in this work encompass the period from February 2009 until May 2012.

Probability of differential motion

The probability of differential motion (PDM), expressed in a percentage, is defined as the probability that a given PS point experiences relative motion with respect to its surrounding PS points (Dheenathayalan et al., 2011; Dheenathayalan and Hanssen, 2011). Thus, PDM is a derived metric obtained from the deformation estimates. To calculate PDM, every PS point is compared with the surrounding PS points (within 200 m) to detect relative

motion above a certain threshold. The value of 200 m was selected in order to guarantee enough PS points in the vicinity. The threshold for the ground movement rate employed in this work was 1 mm year^{-1} . This low threshold was selected to ensure that even a very minimal ground movement difference between two points was detected. Fig. B.1 illustrates an example of the PDM computation for a PS point of interest.

Therefore, by comparing a given PS point with other neighboring PS points, the probability of the given point experiencing relative ground movement is computed (the PDM). This procedure is repeated for every PS point so that the PDM is obtained per PS. Then, following the work of Dheenathayalan and Hanssen (2013), PS points are classified to ascertain those lying on the ground's surface; these represent the differential ground movement signals. In our study of underground water pipe network analyses, only the PDM for PS points lying on the ground surface were considered.

B.2.2. Failure registration data

The failure registration data set consisted of 868 failures comprising all available data for this utility. The exploited failure data set encompasses the period from January 2009 until April 2012 which is consistent with the period covered by the satellite data. During this period, there was no occurrence of natural hazards (e.g., earthquakes or landslides) in the study area. For each failure, the date, longitude and latitude, and pipe material were known. These data were obtained from USTORE (Vloerbergh et al., 2012). USTORE also provides additional information, for example, regarding the origin of the failure (ground movement, inner/outer corrosion, etc.), diameter, type of soil, or presence of trees in the vicinity. Nevertheless, the reliability of these data have not yet been assessed, hence these data were not exploited.

B.2.3. Study area

This work had the participation of a Dutch drinking water company. This company supplies more than 1.2 million people in a region of 601 km^2 , which is equivalent to a population density of $\sim 2000 \text{ people km}^{-2}$ (Geudens, 2012). As a comparison the water company that serves the region of Groningen (in the northeast of the country) serves 592,000 customers spread throughout 2403 km^2 , which is equivalent to $\sim 246 \text{ people km}^{-2}$. This part of the country was selected for the following reasons:

1. Availability of failure registration data;
2. Anticipated ground movement above the national level (De Lange et al., 2012); and,

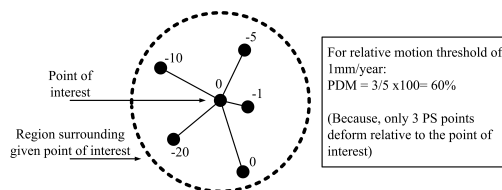


Figure B.1: An example of PDM computation for a point of interest (located in the center). Bold points represent PS points and values next to them represent deformation estimates in mm per year. Dotted circle represents the surrounding region (within 200 m radial distance) from the point of interest.

3. Availability of high resolution radar-borne satellite data during the period of failure registration data.

The study area used in this work covers approximately 144 km² of this company's supply region. In this area, water is supplied through 4309 km of distribution network; with PVC (~57%), AC and CI (both ~15%) being the most common materials (tab.B.1). Inside the study area is the city of The Hague (in the west of the country), which is the biggest city supplied by this water company and the third largest city in the Netherlands.

B.2.4. Data analysis

To produce the replacement-prioritization map, it is possible to follow a pixel-based approach or a cell-based approach. Each approach will now be presented and discussed. For both approaches, the available data is analyzed, and the conclusions of these analyses are used in the implementation of the map. Irrespective of the approach, it is expected that the failure rate increases with the level of ground movement.

Pixel-based approach

This approach analyzes the vicinity of PS points. The vicinity is expected to be affected by the local differential ground movement, quantified by the PDM. In the Netherlands, drinking water pipes are usually 10 m long. Two pipes are connected with stand-alone pieces referred to as joints that feature two rubber gaskets. These gaskets keep the system sealed and are expected to sustain some of the ground movement. According to Wang and Moore (2014), for flexible pipes, surface loads in the vicinity of a joint connecting two shallow buried pipe segments influence that joint, but the deformations become negligible at the other ends of the two pipe segments. Therefore, for the present situation, if two flexible pipe segments (e.g., PVC) are involved, it is assumed that the vicinity is 20 m. For rigid pipes (e.g., AC), it is assumed that two adjacent pipe segments are also influenced, in addition to the pipe segment where differential ground motion is exerted; thus, vicinity is defined as 30 m. Furthermore, it is also assumed that for longer distances the effect of ground movement will be dissipated by the joints.

It can be argued that ground movement may be the result of pipe failure (e.g., leakage) and not the cause. It cannot be concluded as to what occurred first - ground movement or pipe failure. Therefore, in this work, it is assumed that ground movement is the cause of failure and not the result. This assumption may lead to conservative decisions that imply the replacement of pipes that are in good condition. In order to minimize this, the utility should inspect the pipes before replacement using non-destructive evaluation tools (e.g. Liu et al. (2012)). Thus, for this approach, the distribution of the PDM values in the vicinity of failures will be compared with the distribution of the PDM values away from failures. To produce the replacement-prioritization map, detailed GIS data is required, i.e., the exact coordinates of the pipe network. However, these data were not available. Thus, the analysis was conducted, but the replacement map could not be produced.

Cell-based approach

The study area was divided into a virtual matrix (451×320 cells). Each cell represents an area of 100×100 m (approximately 144 km²). This cell size was selected to obtain cells with 20-30 pixels each to allow significant results in the subsequent calculations. It can be expected that pipes installed in different backfills will respond differently to ground movement.

Nevertheless, the soil in each cell is considered to possess homogeneous characteristics. This cell-based approach was followed due to the lack of more detailed soil data; Dutch water companies do not register the characteristics of the soil where the pipes are installed. In this approach, the ground movement in a cell is hypothesized to play a role in the cell's failure rate.

All PS points within a cell can be collectively calculated for an average PDM:

$$\overline{PDM}_i = \frac{\sum PDM_j}{n}, \quad (\text{B.1})$$

where \overline{PDM}_i is the average PDM in cell i [%], PDM_j is the PDM of pixel j in cell i [%] and n is the number of pixels in cell i . Furthermore, each failure was assigned to the specific cell where it occurred and the failure rate per cell was calculated:

$$\Omega_{i,m} = \frac{\sum F_{j,m}}{\sum L_{i,m} \times \Delta t}, \quad (\text{B.2})$$

where $\Omega_{i,m}$ is indicative of the failure rate [$\# \text{km}^{-1} \text{year}^{-1}$] in cell i for material m ; $F_{j,m}$ is the j^{th} failure in cell i ; $\sum L_{i,m}$ is the total pipe length [km] of pipe material m in cell i , assumed constant during Δt ; and Δt is the duration of the registration data [years]. O'Rourke (2010) used a similar parameter referred to as the repair rate [$\# \text{repairs km}^{-1}$]. This formulation, solely normalized in reference to network length, is of use in episodic situations such as earthquakes. However, for the long-term analysis of the network's performance, normalization with respect to time becomes necessary.

The average pipe age per cell was calculated using:

$$\overline{\text{Age}}_{i,m} = \frac{\sum \text{age}_{j,m} \times \sum L_{j,m}}{\sum L_{i,m}}, \quad (\text{B.3})$$

where $\overline{\text{Age}}_{i,m}$ is the average age [years] of pipe material m in cell i ; $\sum \text{age}_{j,m}$ is the average of age bin k (5-year bins) of material m ; and $\sum L_{j,m}$ is the length [km] of material m of age k . In this analysis, cells for which radar estimations are unavailable or that have no drinking water network were not considered in the analysis. For this approach, a correlation between ground movement and pipe failures at a cell level was researched. To produce the cell-based replacement-prioritization map, GIS data, as detailed as for the pixel-based analysis, was not necessary. In fact, knowing the total length of pipes and the number of failures per cell was enough. These data were available, and a replacement map was produced.

B.3. Results and discussion

Exploiting satellite observations, an analysis of failures in drinking water networks was conducted. Based on that analysis, the replacement-prioritization map will be presented and analyzed.

B.3.1. Failure registration data

In the study area, asbestos cement (AC) experienced the highest failure rate followed by cast iron (CI) and then PVC (tab. B.1). Subsequent analyses were conducted without failures originating from third-party damage since, *a priori*, these failures are considered

independent from ground movement. In total, 589 failures were included. Additionally, in this study, the linear velocity from ground movement over the observation period was used. This signifies that the area experiencing a gradual ground movement pattern over a period is being taken into consideration on its own. Thus, short and local ground movement-related activities such as road work, seasonal effects, etc. were not considered in our analyses.

The failure registration data set was analyzed in order to study the existence of age-related trends in the failure rate for various pipe materials. Thus, fig. B.2A depicts the failure rate for the three materials per decade of installation. While PVC has an unexpected spike during the 1950s and CI during the 1970s, the failure rates for both materials remain under $0.06 \text{ \#km}^{-1}\text{year}^{-1}$. As a comparison, according to Rajani et al. (1996), a failure rate above $0.05 \text{ \#km}^{-1}\text{year}^{-1}$ can be considered “undesirably high”. Very little CI has been installed in the Netherlands since the 1970s (Geudens, 2012), which explains the absence of data points these past decades.

AC pipes experienced the two highest failure rates (0.13 and $0.18 \text{ \#km}^{-1}\text{year}^{-1}$) for pipes installed before the 1960s, which indicates that these older pipes are more prone to failure than the newer ones. Comparable results have been presented by Vloerbergh et al. (2012) for the complete USTORE database (five Dutch water companies) for the failures registered in 2009 and 2010. A common problem with AC pipes is leaching corrosion, which is related to the free lime content $\text{Ca}(\text{OH})_2$, and leads to a consequent loss of structural strength (Al-Adeeb and Matti, 1984), which makes these pipes very vulnerable to pressure burst and ground movement. Throughout the rest of the analysis, we assumed that all of these pipes are older than 50 years.

In fig. B.2B the cumulative number of failures per month is depicted. Whereas CI has the highest failure rates during colder months, as described by other authors (Asnaashari et al., 2013), no seasonal tendency was found for AC or PVC.

B.3.2. Pixel-based analysis

Distribution of the PDM in relation to the distance from failures

It was hypothesized that, if failures are caused due to ground movement, the distribution of the PDM in the vicinity of failures ($< 25 \text{ m}$) could be skewed to positive values (higher PDM). This analysis was conducted by including all available failures (without third-party) collectively from all materials. A normalized histogram of the PDM for all pixels in the study area and for the pixels in the vicinity of the failures (distance $< 25 \text{ m}$) is presented in fig. B.3 (top and bottom). While complete histograms are presented on the left, zoomed details of

Table B.1: Pipe length, number of failures (total and due to third party damage) and failure rate (Ω) per pipe material within the study area. In this table *All mat* indicates all materials used by the water company.

	Length [km]	Failures [#]	Ω [# fail- ures/km/year]	Third-party damage [#]
All mat	4309	868	0.060	279
PVC	2479	421	0.054	194
AC	656	235	0.10	51
CI	659	165	0.072	19

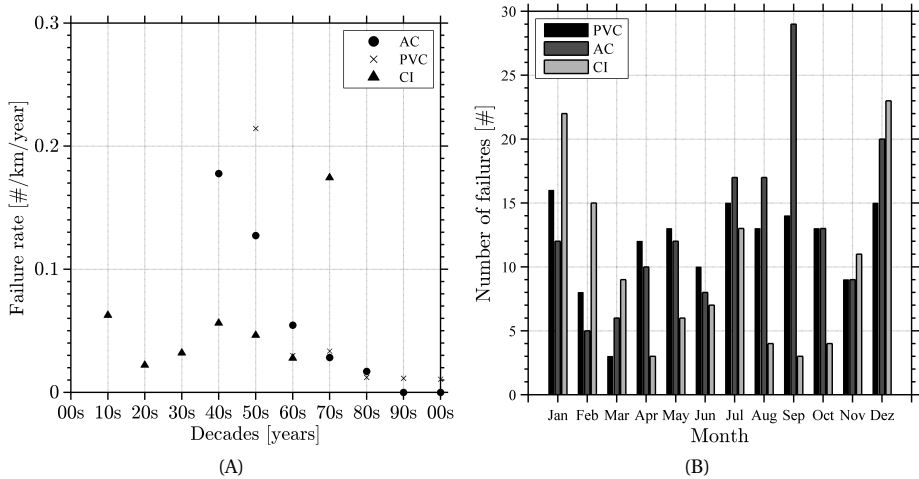


Figure B.2: (A) Failure rate per material and decade from 1900 until 2000. (B) Cumulative number of failures per month.

the histograms (PDM > 50%) are depicted on the right.

The complete histograms show little difference between the entire area (fig. B.3, top left) and the vicinity of the failures (fig. B.3, bottom left). However, it is evident from the detailed histograms that, in the vicinity of failures (fig. B.3, bottom right), there is a greater percentage of PS points with a higher PDM (above 90%) than in the entire area (fig. B.3, bottom left), indicating the role of differential motion in the failures of pipes.

Replacement-prioritization map for pixel-based analysis

Despite a trend being identified, the GIS data required to produce the map were not available. Thus, the pixel-based map was not produced.

B.3.3. Cell-based analysis

Analysis of the PDM

Given the size of the study area and the relative minimal number of failures, ground movement data were divided into bins. Three bins were created including low movement (LM), medium movement (MM) and high movement (HM). A histogram of the PDM per cell is illustrated in fig. B.4. The boundaries are represented in fig. B.4 by dashed vertical lines. Boundaries between the bins are percentiles 33 (PDM=25.6%) and 67 (PDM=46.4%). While LM is below the PDM=25.6%, HM is above the PDM=46.4%. These boundaries were selected to allow having an equal number of counts (PDM) in each bin. An alternative to this approach could have been the definition of a threshold condition following laboratory tests using new or exhumed pipe specimens. However, given the wide variety of pipe materials and even the physical/chemical differences between pipes of the same material, the variety of barrel lengths and the different types of joints in the study area, the authors decided to follow the percentile approach.

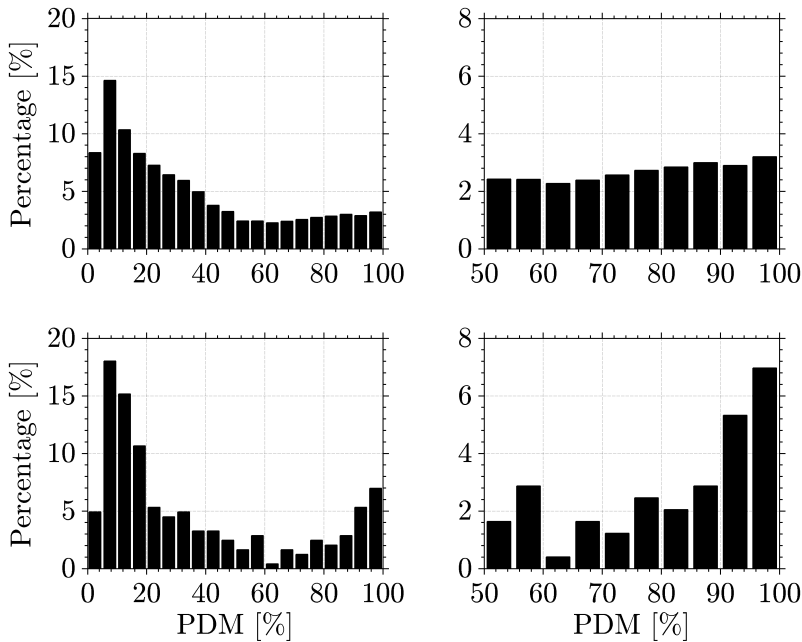


Figure B.3: Histograms of the PDM for the complete study area and in the vicinity of registered failures (< 25 m) for all pipe materials. Top left: the PDM for all pixels in the study area. Bottom left: maximum the PDM of pixels close to the failures. Top and bottom right: zoomed details of histograms on the left, presented for the PDM>50%.

Age distribution

Mean age per pipe material is calculated using eq. (B.3). Age distribution indicates no variation across different areas (fig. B.5). In fig. B.5, the error bars represent the standard deviation of the age. For this area, PVC is the youngest material (15 years) followed by AC (45 years), with CI being the oldest (70 years).

Length distribution

Areas with increased ground movement also have a higher percentage of PVC and lower percentages of AC and CI (fig. B.6). In stable areas (sand), the infrastructure was mostly installed in the late 19th Century and early 20th Century when cast iron was the preferred material. Due to the expansion of the population, unstable areas (peat) began to be urbanized beginning in the 1960s. Since that time, the use of PVC has been increasing among Dutch water companies (Geudens, 2012).

Given these results, it could be expected that the average pipe age in areas of high movement was lower than in the other areas, which actually was not the case (fig. B.5) given that this water company does not use ground movement data to prioritize their pipe replacements.

Failure rate

In fig. B.7, the aggregated failure rate for all areas with a certain level of ground movement is plotted against the level of ground movement. In fig. B.8, the same data is presented in a scatter plot so that the slopes can be calculated. The x coordinates are the average between

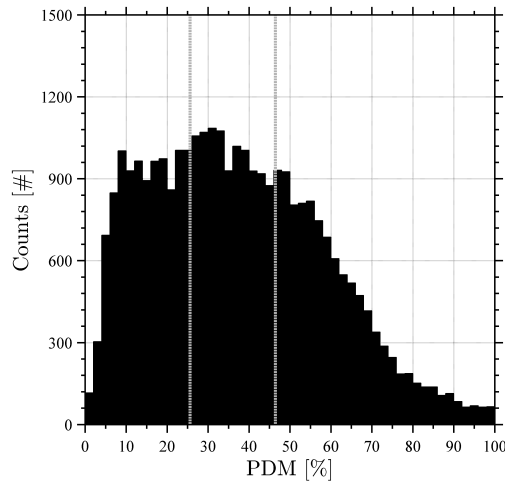


Figure B.4: Histogram of the PDM. The two grey dashed vertical lines (gray) represent the boundaries for ground movement: percentiles 33rd (PDM=25.6%) and 67th (PDM=46.4%). While LM is for the PDM<25.6%, HM is for the PDM>46.4%.

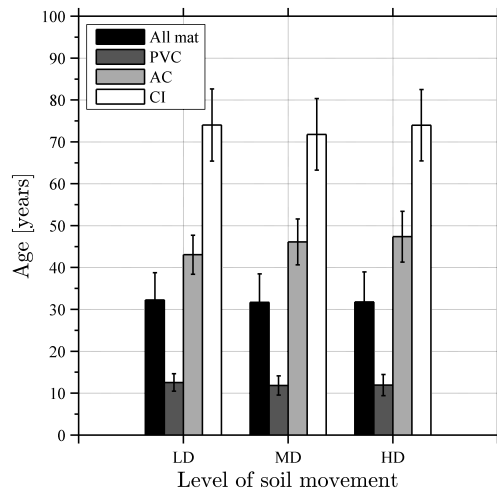


Figure B.5: Distribution of pipe age per level of ground movement. In this figure “All mat” represents all materials taken as a whole. The error bars represent the standard deviation of the age.

the corresponding bins. A positive slope indicates that the failure rate increases with the level of ground movement. The material most sensitive to ground movement will have the highest slope.

By observing Figs. B.7 and B.8, it is evident that PVC experienced the lowest failure rate values and was the least influenced by ground movement (slope= 2.1×10^{-4} , lowest). This was expected because PVC pipes are both the youngest and the most flexible in the network. The failure rates of both CI (slope= 1.1×10^{-3} , highest) and AC (slope= 8.5×10^{-4}) increase with the increase in ground movement (fig. B.8). Also, CI has the highest slope, which indicates

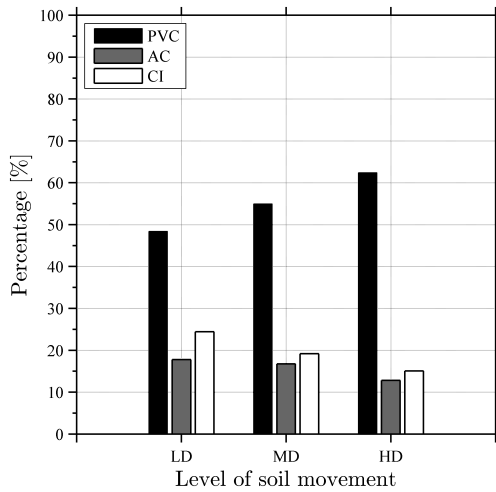


Figure B.6: Distribution of pipe lengths per level of ground movement.

that, in this area, CI is the most sensitive material to ground movement. Overall, the failure rates of AC are the highest in the study area: always at least four times higher than those of PVC.

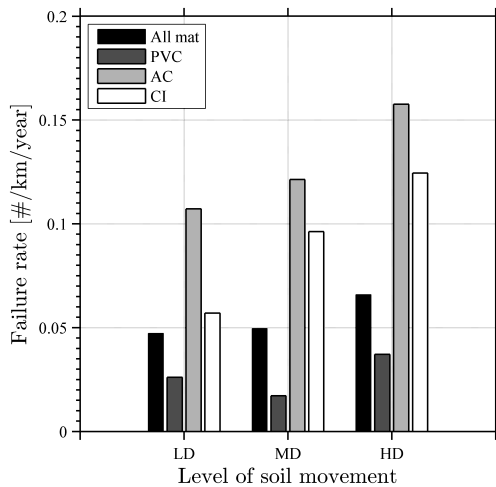


Figure B.7: An example of PDM computation for a point of interest (located in the center). Bold points represent PS points and values next to them represent deformation estimates in mm per year. Dotted circle represents the surrounding region (within 200 m radial distance) from the point of interest.

Replacement-prioritization map for cell-based analysis

For AC pipes, two factors exhibited a role in the failures: age and ground movement. On the one hand, a clear difference can be determined between the pipes older and younger than 50 years (fig. B.2A). On the other hand, the failure rate for AC pipes increases with the

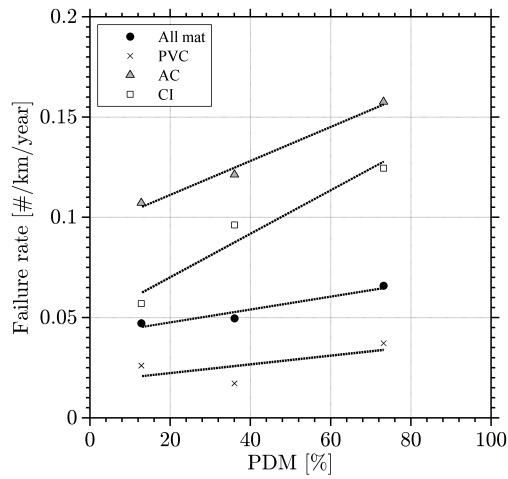


Figure B.8: Failure rate per pipe material against the PDM. In this figure “All mat” represents all materials taken collectively.

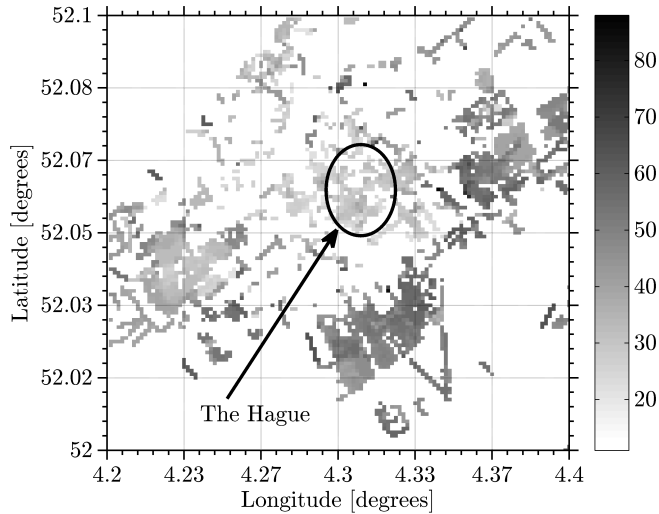


Figure B.9: Age distribution of AC pipes in the study area (10×10 km). The scale, illustrated in years, varies from light grey for cells (100×100 m) where the pipes are, on average younger pipes, to black for cells with older pipes (on average). A white dot indicates the non-existence of an AC network in that cell. Notes: Each degree of latitude is equivalent to ~111 km from the Equator to the Poles. A degree of longitude is widest at the Equator (~111 km) and becomes zero at the Poles. In this area of the Netherlands, one degree of longitude is ~68 km (mon, 2014).

level of ground movement (fig. B.7 and fig. B.8). In fig. B.9, the age distribution of AC pipes in the study area is depicted. In fig. B.10, the distribution of ground movement data in the study area is demonstrated. In both figures, white indicates the non-existence of a network. While there are two clusters of older pipes, 52.02° N, 4.3° E and 52.07° N, 4.37° E (fig. B.9), the distribution of ground movement data is random across the study area (fig. B.10).

Both AC pipe age and level of ground movement were employed to create a priority

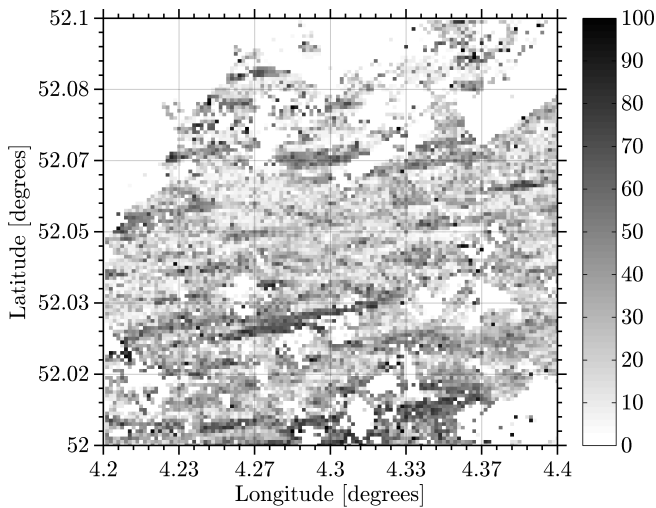


Figure B.10: Distribution of ground movement in the study area (10×10 km). The scale, given in a percentage (PDM), varies from light grey for more stable cells (100×100 m) to black for more unstable cells. A white dot indicates the non-existence of ground movement data within that cell.

Table B.2: Priority matrix for AC pipes created to produce the replacement-prioritization map. A higher grade indicates higher priority areas. Each cell matrix is determined by adding the area points (top) and age points (left).

	Area points		
	LD (0 points)	MD (1 point)	HD (2 points)
Age points			
< 50 years (0 points)	0	1	2
50 years (1 point)	1	2	3

matrix (tab. B.2) based on the approaches described in order to produce risk matrices to manage wastewater networks (Salman, 2010). This was the foundation for the replacement-prioritization map. For this approach, a cell is given age points and area points; a higher score indicates that pipes in this area should be given priority for inspection or replacement. Thus, zero age points were assigned to AC pipes younger than 50 years (lowest priority) and one age point to AC pipes that are older (highest priority). Similarly, zero area points were assigned to pipes installed in LM areas (lowest priority), one area point in MM areas (higher priority), and two area points in HM areas (highest priority). The total score per cell was determined by adding the age points and the area points. Therefore, the lowest replacement priority (0 points, light grey) was assigned to cells with a majority of young AC pipes in areas of LM; the highest priority (3 points, black) was assigned to cells with a majority of old AC pipes installed in HM areas. Pipes installed in high replacement-priority areas should be replaced or, preferably, inspected in a shorter time frame.

Using the priority matrix, the replacement-prioritization map was produced for AC pipes (fig. B.11A). To validate the assumptions of the map, the distribution of failure rates

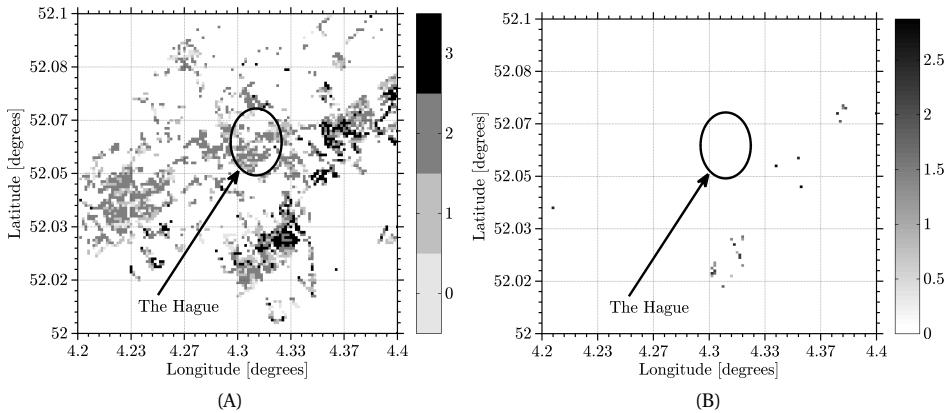


Figure B.11: (A) Replacement-prioritization map for AC for part of the study area (10×10 km). The scores vary from low priority (light grey) to high priority (black). (B) Failure rate distribution in the same area, the scale ($\# \cdot \text{km}^{-1} \cdot \text{year}^{-1}$) varies from light grey for cells with low failure rate to black for cells with a higher failure rate. In both plots, a dot represents a cell (100×100 m) in which there is a pipe network and for which ground movement data were available. A white dot indicates a cell without an AC network and/or failures.

in the study area for AC pipes is depicted in fig. B.11B. While in fig. B.11A white indicates the non-existence of a pipe network and/or soil ground movement data, in fig. B.11B, white indicates the absence of failures and of a pipe network.

It should be noted that Figs. B.9-B.11 depict part of the study area (10×10 km) with the highest number of satellite reflections. Furthermore, there is only data in fig. B.11A where there is a pipe network (fig. B.9) and ground movement data (fig. B.10). Finally, all failures used in the work (fig. B.11B) were registered in cells where there is a pipe network (fig. B.9).

The cells that contain older pipes (fig. B.9 in black) are also cells containing pipes of high replacement priority (fig. B.11A in black). Furthermore, the most failures (fig. B.11B) were registered inside or close to high replacement-priority cells. Therefore, despite needing further validation, this work suggests that the areas that are presented in fig. B.11A in black, could be selected by the water utility to be inspected as discussed in Arsénio et al. (2013a) as they represent a greater risk of failure for the pipes installed inside or within their vicinity.

B.4. Conclusions

In this work, it was hypothesized that ground movement leads to stresses on pipes, which increases the number of pipe failures. Therefore, areas with more ground movement would indicate zones that are likely areas of high risk for pipe failure. The analysis of the failure registration data together with the ground movement data clearly demonstrated that the failure rate of all materials increases with the level of ground movement; this relationship being obvious for both CI and AC. Additionally, it was also demonstrated that AC pipes installed prior to the 1960s fail more frequently than younger pipes. For the pixel-based analysis, it was discovered that, for all materials in the vicinity of failures, there were relatively more pixels with high PDM ($> 90\%$) than for the entire study area. This further demonstrates the role played by differential soil motion on the failures in an underground infrastructure.

A cell-based replacement-prioritization map for AC was produced. The map takes into consideration both the age of the material and the level of ground movement in the soil where it was installed. This approach can be extrapolated to similar situations. It can be assumed that older, rigid pipes (e.g., AC older than 50 years) installed in areas with high probability of ground movement (PDM>46.4 %) are more prone to failure. The utilities should pay greater attention to these pipes, which are the ideal candidates i) for routine replacement or to minimize conservative decisions that replace pipes actually in good condition, ii) for condition-assessment programs.

Finally, for this work, a total of 589 registered failures were exploited. More robust analysis will require having access to more failure registration data. For example, with access to more failure registration data, analyses can also focus on the impact of ground movement in smaller and larger diameter pipes. This emphasizes the significance of failure data registration and its importance for the management of (water) utilities.

About the author

Prabu Dheenathayalan was born in Madurai, Tamil Nadu, India on July 05, 1982.

Prabu Dheenathayalan received the B.E. (Sandwich) degree in electrical and electronics engineering in 2005 from PSG College of Technology, Coimbatore, India. He was with Honeywell Technology Solutions, Bangalore, India from 2005 to 2007. He obtained his M.Sc. degree in Electrical Engineering and Information Technologies from Karlsruhe Institute of Technology (KIT), Karlsruhe, Germany in 2009. During his master's degree he worked with The Research Center for Information Technology (FZI), Karlsruhe and The Institute for Information Processing Technology (ITIV), Karlsruhe Institute of Technology.

He has also worked with Harman Becker Automotive Systems GmbH, Karlsbad, Germany. He was with the German Aerospace Center (DLR), Oberpfaffenhofen, Germany for his Master's thesis work.

He is currently a Researcher with the Department of Geoscience and Remote Sensing, Delft University of Technology, Delft, The Netherlands. He holds two granted patents. His current research interests include remote sensing, SAR interferometry, data science, and image/signal processing.



